

**Faculty of Engineering and Science**

**A Novel Semi-Passive Turbulence Enhancement Method: A Flexible  
Vortex Generator**

**Chan Hiang Bin**

**This thesis is presented for the Degree of  
Master of Philosophy  
of  
Curtin University**

**May 2016**

## **Declaration**

To the best of my knowledge and belief this thesis contains no material previously published by any other person except where due acknowledgement has been made.

This thesis contains no material which has been accepted for the award of any other degree or diploma in any university.

Signature:

Date: 14 June 2016

## Abstract

Numerical studies – Fluid-Structural Interaction (FSI) simulations were performed to investigate the turbulence generation ability of the flexible vortex generator (FVG), which was proposed to overcome the weaknesses associated with the conventional rigid vortex generator (RVG). The numerical model used in the study was validated with published results. The main objective of the study is to show that the FVG is able to create more turbulence compared to the RVG. The shear production (shear rate,  $\partial u_i / \partial x_j$ ) was investigated to evaluate turbulence. Ideally, a greater shear rate is preferred as it indicates a greater turbulence production.

In the study, circular and flat plate R/FVG (cantilever-liked VG) with various aspect ratios (ARs) were involved. In addition, the local Reynolds Number within the subcritical flow range ( $10^2 < Re_D < 10^5$ ) was considered in the study. In the case of circular VGs, the study covers circular RVG and FVG with AR=6, 8 or 10 that was individually submerged in a flow with  $Re_D \sim 3500$ . In the case of flat plate VGs, the study covers flat plate RVG and FVG with AR=4, 5 or 6 that was individually submerged in a flow with  $Re_D \sim 11500$ .

The spatial properties of the wake behind the RVG and FVG were investigated. The results show that the FVG generates a larger (taller) wake compared to the RVG's wake; the wake of the circular FVG is  $1.5D \sim 2.3D$  taller than its respective RVG's wake, whereas the wake of flat plate FVG is  $0D \sim 1D$  taller than its respective RVG's wake. Besides, it was found that the wake height increment in the FVG case is the result of vanishing/weakening downwash caused by the deflection of the FVG. The weakening effect is escalated with greater deflection and it is independent of the motion of the FVG.

Next, the shear rate of the flow around the VGs was examined to determine the turbulence generation ability. The first part of this study investigated the wall shear stress ( $\tau_w$ ). The results show that the FVG produces greater  $\tau_w$  compared to the RVG; the  $\tau_w$  on the circular FVG has increased ranging from 9.3%~75% compared to its respective RVG, whereas the  $\tau_w$  on the flat plate FVG has increased ranging from 5.0%~66.7% compared to its respective RVG. A flow model was proposed, based on the current understanding of fluid dynamics, to explain the observed results. Based on the flow model, the cause of the increasing  $\tau_w$  is scaled with the structural velocity.

With a greater  $\tau_w$ , it is expected that the FVG is capable of producing a stronger vortex. In the second part of shear rate study, the circulation ( $\Gamma$ ) was used to quantify the strength of a vortex, which is fundamentally related to the shear rate within a vortex. The results show that the vortex generated from the FVG has higher  $\Gamma$  than those generated from the RVG. The improvement differs at different spanwise locations. Besides, the results have confirmed that the circulation enhancement scales with structural velocity, which was predicted by the flow model proposed previously.

The heat transfer performance of the FVG was briefly examined as well. Based on the previous findings, it is anticipated that the FVG will have a better heat transfer performance than the RVG. Two cases (heat source on VG and heat source on the ground plate) were studied. The heat transfer performance was examined through plotting the Nusselt Number (Nu) contour and streamwise temperature profiles. All the obtained results (higher Nu and downstream temperature) indicates that the FVG has better heat transfer performance than the RVG.

In conclusion, all the analyses conducted in the present study have demonstrated that the FVG can generate greater turbulence, in both spatial and qualitative aspects, compared to the RVG. Besides, throughout the study, the structural velocity has been identified to be playing an important role in turbulence enhancement via any passively-oscillating structure.

## **Acknowledgement**

First of all, I would like to give my sincere acknowledgement to my thesis committees, especially to my supervisor – Associate Professor Dr. Sharul Sham, for giving me the opportunity to work under him. I am grateful towards his endless guidance, advice and motivation throughout my MPhil candidature. Most importantly, I have learned so much, in both technical knowledge and philosophy, from him that I consider priceless throughout this journey.

Secondly, I would like to thank my co-supervisor, Dr. Wee Siaw Khur who continue to provide valuable supports and inspiration throughout my MPhil candidature. I am especially grateful to her continuous supervision during the one-year period when she was away from Curtin.

Also, I would like to extend my gratitude to Associate Professor Dr. Perumal Kumar, my co-supervisor who has provided useful advice and assistance that have critically improved the quality of my work.

Next, I would like to thank all my HDR friends for their supports and the encouragement throughout my MPhil candidature. This journey will not be such delightful without them.

I gratefully acknowledge the financial (tuition fee) support – Higher Degree by Research Scholarship I received from Curtin University, Sarawak Malaysia.

Last but not least, I would like to thank my parents for their endless support and encouragement during my study.

Thank you all!

Chan Hiang Bin

# Table of Contents

<b>Declaration</b> .....	<b>I</b>
<b>Abstract</b> .....	<b>II</b>
<b>Acknowledgement</b> .....	<b>IV</b>
<b>Nomenclatures</b> .....	<b>IX</b>
<b>List of Figures</b> .....	<b>XII</b>
<b>List of Tables</b> .....	<b>XVII</b>
<b>Chapter 1: Introduction</b> .....	<b>1</b>
1.1 Vortex Generation.....	1
1.2 Proposed Method – The Flexible Vortex Generator .....	3
1.3 Aim, the Research Questions and the Objectives.....	5
1.4 Thesis Structure.....	6
Summary of chapter .....	7
<b>Chapter 2: Backgrounds and Theories</b> .....	<b>8</b>
2.1 Reynolds Number.....	8
2.2 Turbulence and Kinetic Budget Equations .....	9
2.3 The Technical Aspects of the Downsides of Conventional Vortex Generator (VG) .....	11
2.3.1 Energy Loss on Vortex Generator .....	11
2.3.2 Pressure Loss (Penalty) on Vortex Generator .....	13
2.4 Flow Separation, Vortex Formation and Vortex Shedding.....	15
2.5 Vortex Generation Methods.....	18
2.6 Vortex-Induced Vibration .....	20
2.6.1 Lock-in.....	21
2.7 The Flexible Vortex Generator (FVG) .....	24
2.7.1 The Working Principle of the FVG .....	25
Summary of Chapter .....	28
<b>Chapter 3: Literature Review</b> .....	<b>29</b>

3.1	Flow Past a Cantilever.....	29
3.1.1	The Flow Field around the Cantilever .....	29
3.1.2	Drag Reduction on Cantilever .....	33
3.1.3	Vortex Shedding.....	34
3.1.4	Span of Free End Effect and Critical Aspect Ratio .....	35
3.2	Flow Past an Oscillating Object.....	39
3.2.1	Wake Structure behind an Oscillating Object.....	39
3.2.2	Velocity Field and Turbulence Characteristic behind an Oscillating Object	45
3.3	Role of Vortex and Vortex Generator on Heat Transfer .....	47
3.4	Effects of Oscillating Structure on the Heat Transfer Performance .....	49
3.5	Numerical Approaches and Modelling .....	51
	Summary of chapter .....	56
<b>Chapter 4: Numerical Modelling .....</b>		<b>57</b>
4.1	Governing Equations .....	57
4.1.1	Structural Model.....	57
4.1.2	Fluid Flow Model .....	57
4.1.3	Turbulence Model.....	58
4.1.4	Heat Transfer Model.....	60
4.1.5	The Coupling – Fluid-Structural Interaction (FSI).....	61
4.2	Numerical Model.....	64
4.2.1	Simulation Domain .....	64
4.2.2	Mesh .....	67
4.2.3	Time-step size.....	71
4.2.4	Model Validations .....	71
	Summary of chapter .....	80
<b>Chapter 5: Numerical Visualisation.....</b>		<b>82</b>
5.1	Wake of the FVG and RVG ( $x$ - $z$ plane) .....	82
5.1.1	Wake of the Circular VGs ( $x$ - $z$ plane) .....	83
5.1.2	Wake of the Flat Plate VGs ( $x$ - $z$ plane) .....	86
5.1.3	Effects of Oscillation and Deflection on the Wake Structure ( $x$ - $z$ plane)	89

5.2	Wake of the FVG and RVG ( $x$ - $y$ plane)	97
5.3	Vortical Activities Analysis	99
	Summary of Chapter	105
<b>Chapter 6: Turbulence Characteristics</b>		<b>107</b>
6.1	The shear rate in boundary layer: Wall shear stress	107
6.1.1	Wall Shear Stress on the Circular RVG and FVG	108
6.1.2	Wall Shear Stress on the Flat Plate VG and FVG	111
6.1.3	Effects of Oscillation and Deflection on Wall Shear Stress Magnitude and Distribution	113
6.3	The Shear Rate in a Vortex: Circulation	119
6.3.1	$z$ -circulation ( $\Gamma_z$ )	123
6.4	The Pressure Loss on the FVG	133
	Summary of Chapter	136
<b>Chapter 7: FVG's Heat Transfer Performance</b>		<b>138</b>
7.1	Heat Source on the FVG	138
7.1.1	Case Description	139
7.1.2	Results and Discussion	140
7.2	Heat Source on the Ground Plate	147
7.2.1	Case Description	147
7.2.2	Results and Discussion	148
	Summary of Chapter	153
<b>Chapter 8: Conclusions and Recommendations</b>		<b>155</b>
8.1	The Wake Size behind a FVG	155
8.2	Turbulence Characteristics behind a FVG	156
8.3	Heat Transfer Performance of a FVG	157
8.4	Significance of the Current Work	158
8.5	Recommendations	159
<b>References</b>		<b>161</b>
<b>Appendix I: Structural Parameters Calculation</b>		<b>170</b>



**Appendix II: Displacement Responses of FVGs..... 171**

## Nomenclatures

### Symbols

$A$	Amplitude	m
$A_v$	Vortex area	m <sup>2</sup>
$A/D$	Amplitude to diameter ratio	-
$C_D$	Drag Coefficient	-
$D$	Diameter	m
$d$	Deflection or displacement	m
$E$	Elastic or Young's Modulus	Pa
$f$	Vortex shedding frequency	Hz
$F$	Force	N
$f_n$	Natural frequency	Hz
$\overline{h_w}$	Average wake height	m
$h$	Convective heat transfers coefficient	W/(m <sup>2</sup> ·K)
$I$	Second moment of Inertia	m <sup>4</sup>
$k$	Elastic stiffness	N/m
$k_h$	Thermal conductivity	W/(m·K)
$L$	Length	M
$n_{\Delta t}$	Number of time step per vortex shedding	-
$\dot{m}$	Mass flow rate	kg/s
$m$	Mass	kg
$m^*$	Mass ratio ( $m_{osc}/m_{disp}$ )	-
$m_{disp}$	Mass of displaced fluid	kg
$m_{osc}$	Mass of oscillating object	kg
$Nu$	Nusselt Number	-
$P$	Instantaneous pressure	Pa
$p'$	Fluctuating component of pressure	Pa
$Q$	Volumetric flow rate	m <sup>3</sup> /s
Re	Reynolds Number	-
$q$	Damping coefficient	N·s/m
St	Strouhal Number	-
$T$	Temperature	K
$U$	Instantaneous velocity	m/s
$u$	Velocity in $x$ -direction	m/s

$u'$	Fluctuating component of $x$ -velocity	m/s
$U_\infty$	Mean flow velocity	m/s
$U_s$	Structural velocity	m/s
$v$	Velocity in $y$ -direction	m/s
$v'$	Fluctuating component of $y$ -velocity	m/s
$w$	Velocity in $z$ -direction	m/s
$w'$	Fluctuating component of $z$ -velocity	m/s
$x$	Location in the $x$ -direction	m
$y$	Location in the $y$ -direction	m
$y^+$	Dimensional wall distance	-
$z$	Location in the $z$ -direction	m

### Greeks

$\Gamma$	Circulation or vortex strength	$\text{m}^2/\text{s}$
$\lambda_2$	Lambda2 Criterion	$\text{Pa}\cdot\text{s}$
$\mu$	Dynamic Viscosity	-
$\mu_\tau$	Turbulent Viscosity	$\text{Pa}\cdot\text{s}$
$\rho$	Density	$\text{kg}/\text{m}^3$
$\tau_w$	Wall shear stress	$\text{Pa}$
$\nu$	Kinematic Viscosity	$\text{m}^2/\text{s}$
$\omega$	Vorticity	$1/\text{s}$

### Abbreviations

ALE	Arbitrary Lagrangian Eulerian
AR	Aspect ratio (L/D)
CFD	Computational Fluid Dynamics
DES	Detached Eddy Simulation
DoF	Degree of freedom
DPIV	Digital Particle Image Velocimetry
DVM	Discrete Vortex Method
FEM	Finite Element Method
FSI	Fluid-structure interaction
FVG	Flexible vortex generator

FVM	Finite Volume Method
KHI	Kelvin-Helmholtz Instability
LES	Large Eddy Simulation
PIV	Particle Image Velocimetry
RANS	Reynolds Averaged Navier-Stokes
RVG	Rigid vortex generator
SMA	Shape-memory alloy
SST	Shear stress transport
URANS	Unsteady Reynolds Averaged Navier-Stokes
VG	Vortex generator
VIV	Vortex-induced Vibration
VIVACE	Vortex-induced Vibration Aquatic Clean Energy

### **Subscripts**

$s$	Structural parameter
$f$	Fluid parameter
$c$	Characteristic parameter
$x, y \text{ or } z$	In either $x, y$ or $z$ direction

## List of Figures

Figure 1.1: Shell-tube heat exchanger (Leruth, 2012). .....	1
Figure 2.1: Schematic of energy transfer in turbulent flow. ....	11
Figure 2.2: Adverse Pressure Gradient and separation point (White & Corfield, 2006). .....	16
Figure 2.3: Illustration of the discontinuous velocity in the shear layers that leads to vortex sheet roll-up. ....	16
Figure 2.4: (a) Vortex formation on circular cylinder; (b) zoomed-view at the location of separation where Vortex A (in (a)) forms (Sumer & Fredsøe, 1997). .....	17
Figure 2.5: Vortex shedding from a circular cylinder (Sumer & Fredsøe, 1997). .....	18
Figure 2.6: (Left) Protuberance based generators (Gentry & Jacobi, 1995); (right) protrusion based generator. ....	19
Figure 2.7: (Top) In-line VIV by symmetric vortex shedding; (bottom) cross-flow VIV by non-symmetric vortex shedding. (Bai & Bai, 2005). .....	21
Figure 2.8: The amplitude plot of a cylinder that undergoes VIV versus the reduced velocity (Blevins & Coughran, 2009). .....	22
Figure 2.9: Bending of a cantilever beam with applied force $F$ . ....	24
Figure 2.10: Schematic of the energy transfer between the fin and the flow. ....	27
Figure 3.1: Schematic of flow structures around a circular cantilever (Sumner, 2013). .....	30
Figure 3.2: The inclined vortex tube model (Heseltine, 2003). .....	31
Figure 3.3: An instantaneous velocity field that demonstrates the upwash and downwash region near the free end of a cantilever (Park & Lee, 2000). ....	33
Figure 3.4: The vortex trajectories behind the oscillating cylinder in various amplitude. (a) Small amplitude oscillation; (b-c) large amplitude oscillation; (d) unstable configuration (Angrilli <i>et al.</i> , 1972). .....	40
Figure 3.5: Map of vortex pattern at different amplitude responses ( $A/D$ ) and reduced velocity ( $U/fD$ ) – the W-R’s map (William & Roshko, 1988). ....	41
Figure 3.6: Vortex pattern along a cantilever. ....	43
Figure 3.7: Vortex pattern behaviour of an oscillating cantilever. Modified from Figure 3.5. (Check the unmodified figure for the covered details). ....	44
Figure 3.8: A sketch of the hybrid (2P+2S) vortex pattern behind an oscillating tapered cylinder (Techet <i>et al.</i> , 1998). .....	44

Figure 4.1: The flowchart of one-way FSI simulation (for a single time step).....	62
Figure 4.2: The flowchart of two-way FSI simulation (for a single time step). ...	62
Figure 4.3: Flowchart of the strongly coupled two-way FSI simulation used in the present study.....	63
Figure 4.4: Schematic of the fluid domain (Not to scale). ....	64
Figure 4.5: The mesh independency study: (i) the drag coefficient ( $C_D$ ); (ii) The $x$ - component velocity ( $u$ ) profile at $x/D=0.75$ downstream from the cantilever; (iii) The static pressure profile at $x/D=0.75$ downstream from the cantilever. .....	69
Figure 4.6: The selected mesh (Mesh 4) on the simulation domain: (a) side view on the plane of symmetry ( $y=0$ ) and (b) top view on the cross-sectional plane.....	69
Figure 4.7: The structured mesh on the (left) circular FVG and (right) flat plate FVG. ....	70
Figure 4.8: Schematic of the experiment setup with dimensions (Not to scale)..	72
Figure 4.9: The instantaneous flow field comparison (at the plane of symmetry) of the CFD result with the experimental result: (i) Streamline from CFD ( $k-\omega$ (SST) – Mesh 4); (ii) experimental visualisation (Park & Lee, 2000).	75
Figure 4.10: Flow field comparison of the recirculation zone above the free end surface (at the plane of symmetry). (Left) Instantaneous velocity field computed by CFD approach ( $k-\omega$ (SST) – Mesh 4); (Right) Mean Streamlines obtained through experimental approach done by Sumner <i>et al.</i> (2013).....	76
Figure 4.11: The velocity profile at the plane-of-symmetry( $y/D=0$ ), located at $x/D=6$ .....	77
Figure 4.12: The bending of the flexible flat plate in a cross flow. ....	80
Figure 5.1: The lambda2 ( $\lambda_2$ ) iso-surface, $\lambda_2=-100$ , in the $z-x$ plane, of the circular RVG with (a) AR=6, (b) AR=8, and (c) AR=10. ....	84
Figure 5.2: The lambda2 ( $\lambda_2$ ) iso-surface, $\lambda_2=-100$ , in the $z-x$ plane, of the circular FVG with (a) AR=6, (b) AR=8, and (c) AR=10. ....	85
Figure 5.3: The lambda2 ( $\lambda_2$ ) iso-surface, $\lambda_2=-100$ , in the $z-x$ plane, of the flat plate RVG with (a) AR=4, (b) AR=5, and (c) AR=6.....	87
Figure 5.4: The lambda2 ( $\lambda_2$ ) iso-surface, $\lambda_2=-100$ , in the $z-x$ plane, of the flat plate FVG with (a) AR=4, (b) AR=5, and (c) AR=6.....	88

Figure 5.5: The streamlines of the normalised mean velocity magnitude at the plane of symmetry ( $y/D=0$ ) of the circular RVG with (a) AR=6, (b) AR=8, and (c) AR=10.....	91
Figure 5.6: The streamlines of the normalised mean velocity magnitude at the plane of symmetry ( $y/D=0$ ) of the flat plate RVG with (a) AR=4, (b) AR=5, and (c) AR=6.....	92
Figure 5.7: The streamlines of the normalised mean velocity magnitude at the plane of symmetry ( $y/D=0$ ) of circular FVG with (a) AR=6, (b) AR=8, and (c) AR=10.....	93
Figure 5.8: The streamlines of the normalised mean velocity magnitude at the plane of symmetry ( $y/D=0$ ) of flat plate FVG with (a) AR=4, (b) AR=5, and (c) AR=6.....	94
Figure 5.9: The streamlines plot at the plane of symmetry ( $y/D=0$ ) of AR=6 flat plate FVG at (top) $t = 3.63s$ and (bottom) $t = 3.83s$ .....	96
Figure 5.10: The lambda2 ( $\lambda_2$ ) iso-surface, $\lambda_2=-100$ , in the $x$ - $y$ plane, of the circular RVG with (a) AR=6, (b) AR=8, and (c) AR=10.....	98
Figure 5.11: The lambda2 ( $\lambda_2$ ) iso-surface, $\lambda_2=-100$ , in the $x$ - $y$ plane, of the circular FVG with (a) AR=6, (b) AR=8, and (c) AR=10.....	99
Figure 5.12: The instantaneous streamlines at the plane of symmetry ( $y/D=0$ ) of circular RVG with (a) AR=6, (b) AR=8, and (c) AR=10.....	100
Figure 5.13: The streamlines at the plane of symmetry ( $y/D=0$ ) of flat plate RVG with (a) AR=4, (b) AR=5, and (c) AR=6.....	101
Figure 5.14: The instantaneous streamlines at the plane of symmetry ( $y/D=0$ ) of circular FVG with (a) AR=6, (b) AR=8, and (c) AR=10.....	102
Figure 5.15: The streamlines at the plane of symmetry ( $y/D=0$ ) of flat plate FVG with (a) AR=4, (b) AR=5, and (c) AR=6.....	103
Figure 5.16: (a) Streamline plot behind a stationary circular cylinder; (b) Instantaneous vorticity behind a stationary cylinder; (c) Streamline plot behind a rotating circular cylinder; (d) Instantaneous vorticity behind a rotating cylinder. (a) to (d) are adapted from Dol <i>et al.</i> (2008). .....	105
Figure 6.1: Instantaneous wall shear stress magnitude (Pa) contour on (a) the circular RVG and (b) the circular FVG with (i) AR=6, (ii) AR=8 and (iii) AR=10.....	109
Figure 6.2: Labels of flow zones based on wall shear stress contour.....	110

Figure 6.3: Wall shear stress magnitude (Pa) contour on (a) the flat plate RVG and (b) the flat plate FVG with (i) AR=4, (ii) AR=5 and (iii) AR=6. ....	112
Figure 6.4: The change of wall shear stress contour on an AR=8 circular FVG as it deflects. ....	114
Figure 6.5: The change of wall shear stress contour on an AR=6 flat plate FVG as it vibrates. ....	115
Figure 6.6: Velocity gradient on the surface of a submerged structure: (a) stationary (b) moving against the flow with velocity $U_s$ . ....	116
Figure 6.7: The size difference between the wall shear stress contours of the (left) RVG and (right) FVG: (top) AR=10 circular VG and FVG and (bottom) AR=6 flat plate RVG and FVG. ....	118
Figure 6.8: (a) The $\Lambda_2$ contour; (b) the $x$ -velocity ( $u$ ) contour; (c) the $y$ -velocity ( $v$ ) contour; and (d) the $z$ -velocity ( $w$ ) contour that covers the newly shed vortex and a downstream vortex. ....	122
Figure 6.9: The (a) negative and (b) positive initial $z$ -circulation for (i) AR=6, (ii) AR=8 and (iii) AR=10 circular RVG and FVG ( marks the location where tip vortices are partially involved in the calculation). ....	124
Figure 6.10: Tip vortices and Kármán vortices behind a RVG. ....	125
Figure 6.11: Time series of $\Lambda_2$ – vortex forming and shedding: (1-3) vortex formation; (4-6) shedding of tip vortex and; (7-12) “peeling” of Kármán vortex. Dashed arrows denote the direction that the vortex tube/filament travels; solid arrows denote the direction that the circular FVG moves. .	127
Figure 6.12: The normalised structural velocity in the $y$ -direction ( $U_{s,y}/U_\infty$ ) of the circular FVG with different AR. The solid line represents the instantaneous component; dash line represents its r.m.s. ....	129
Figure 6.13: The normalised structural velocity in the $x$ -direction ( $U_{s,x}/U_\infty$ ) of the circular FVG with different AR. The solid line represents the instantaneous component; dash line represents its r.m.s. ....	129
Figure 6.14: The (a) negative and (b) positive initial $z$ -circulation for (i) AR=5 and (ii) AR=6 flat plate RVG and FVG. ....	130
Figure 6.15: The normalised structural velocity in the $x$ -direction ( $U_{s,x}/U_\infty$ ) of the flat plate FVG with different AR. The solid line represents the instantaneous component; dash line represents its r.m.s. ....	133



Figure 6.16: The mean pressure profile, at different spanwise location, in the plane-of-symmetry ( $y=0$ ) of the circular (a) RVG and (b) FVG with (i) AR=6, (ii) AR=8 and (iii) AR=10. ....	134
Figure 6.17: The mean pressure profile, at different spanwise location, in the plane-of-symmetry ( $y=0$ ) of the flat plate (a) RVG and (b) FVG with (i) AR=4, (ii) AR=5 and (iii) AR=6. ....	136
Figure 7.1: Mean Nusselt Number on the frontal surface of the flat plate (a) RVG and (b) FVG. ....	141
Figure 7.2: Mean Nusselt Number on the rear surface of the flat plate (a) RVG and (b) FVG. ....	141
Figure 7.3: The temperature profile (T), along the $x/D$ direction. (a) to (e) represent different spanwise locations, <i>i.e.</i> $z/D=2, 4, 6, 8$ and $10$ respectively.....	144
Figure 7.4: The vortex structures ( $\lambda_2 < -100$ ) behind the heated (top) RVG and (bottom) FVG.....	145
Figure 7.5: Temperature contour at the plane of symmetry ( $y=0$ ) of the (top) RVG and (bottom) FVG. The line probes used are also included.....	146
Figure 7.6: The mean Nusselt Number ( $\overline{Nu}$ ) on the ground plate of (top) the RVG and (bottom) FVG.....	148
Figure 7.7: The temperature profile (T), along the $x/D$ direction. (a) to (c) represent different spanwise locations, <i>i.e.</i> $z/D=1/6, 1/3$ and $1/2$ respectively. ....	150
Figure 7.8: Schematic that illustrates the relationship between the Nusselt Number and the flow temperature. ....	152
Figure 8.1: The proposed flow model – showing the velocity gradient on the surface of a submerged structure: (a) stationary, (b) moving against the flow with velocity $U_s$ (Taken from Chapter 6). ....	156

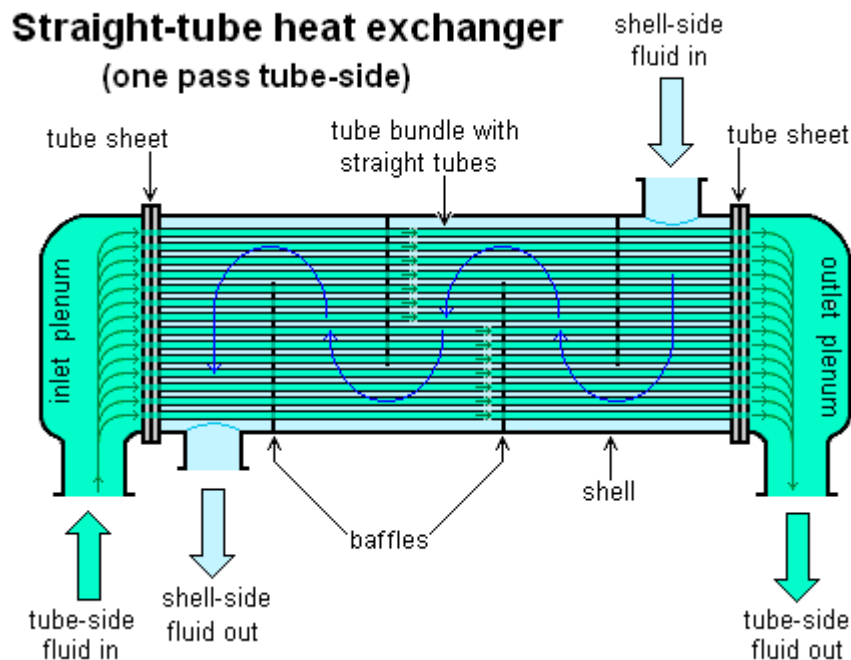
## List of Tables

Table 2.1: Summary of the performances of wing-type vortex generators (Gentry & Jacobi, 1995).....	14
Table 2.2: The features, vortex generation ability and the applicability of protrusion-based and protuberance-based VG.....	20
Table 3.1: The type of wake visualisation method(s) that confirm the validity of the second theory. ....	32
Table 3.2: The summary of the span of free end effect and the critical AR.....	38
Table 4.1: List of boundary conditions.....	65
Table 4.2: The fluid, flow and structural properties used in circular R/FVG simulation.....	66
Table 4.3: The fluid, flow and structural properties used in flat plate R/FVG simulation.....	67
Table 4.4: Summary of meshes and its respective information. ....	68
Table 4.5: Details of experimental and CFD comparison.....	73
Table 4.6: Structural and Fluid flow properties of the FSI-coupling validation. ....	79
Table 4.7: Comparison between the results of the CFD simulation and the benchmark.....	79
Table 5.1: The summary of wake height ( $\overline{h_w}$ ) behind the circular VGs. ....	86
Table 5.2: The summary of wake height ( $\overline{h_w}$ ) behind the flat plate VGs.....	89
Table 6.1: The normalised mean $z$ -circulation ( $\Gamma_{z,FVG}$ ) at the highest considering plane and the normalised r.m.s. of structural velocity ( $U_{s,(rms)}$ ) associated to the 6 <sub>CF</sub> , 8 <sub>CF</sub> and 10 <sub>CF</sub> .....	128
Table 6.2: The normalised mean $z$ -circulation ( $\Gamma_{z,FVG}$ ) at the highest considering $z/D$ and the normalised r.m.s. of structural velocity ( $U_{s,(rms)}$ ) associated to the 5 <sub>PF</sub> and 6 <sub>PF</sub> .....	132

# Chapter 1: Introduction

## 1.1 Vortex Generation

The study of turbulent flow has always been a popular topic in fluid dynamics due to its useful characteristics (such as diffusion, three-dimensional vorticity – curl of velocity, randomness, and dissipation) that are beneficial to many industrial applications. The most common role of turbulent flow in engineering applications is to facilitate mixing and/or heat transfer through stimulating the rate of momentum and mass transfer. A typical engineering application example that harnesses the benefit of turbulent flow is the heat exchanger, where its heat transfer and mixing ability is highly dependent on the turbulence generated by an array of tubes or fins, as shown in Figure 1.1. As a result, turbulence enhancement has become an important aspect that persistently caught the interest of industries.



**Figure 1.1: Shell-tube heat exchanger (Leruth, 2012).**

On the other hand, turbulent flow can also be thought as a flow filled with vortices in a wide spectrum of scales. Vortices play an important role in turbulent flow by stimulating the mass, momentum and energy transport in the

flow. Hence, the studies of vortex dynamics are closely linked to the understanding of turbulent flow phenomenon.

Vortices (turbulence) can be generated easily via either active or passive methods. Active methods require external energy to generate vortex; in contrast to that, passive methods require no external energy and are of simple design (it is often regarded as static method due to its non-moving design). Passive methods are widely used in a variety of engineering applications due to the relatively simple structure and ease of implementation. Among a variety of passive methods, vortex generator (VG) has shown promising turbulence enhancement ability. Typical VGs include protruded structures such as winglets, rigid blocks, cylinders, bumps and plates. The tubes in the heat exchanger as depicted in Figure 1.1 can also be considered as one of these VGs. Therefore, the studies of VG's performance in a wide variety of applications are still a popular topic today (Kaci *et al.*, 2009; Lemenand *et al.*, 2003; Gorji *et al.*, 2011; Viktorov & Nimafar, 2013; Erikson & Liao, 2007).

However, many studies have reported an undesirable pressure loss (penalty) associated with VGs (Fiebig *et al.*, 1986; Fiebig *et al.*, 1995; Wu & Tao, 2008; Chen *et al.*, 1998) despite its promising performance. According to Gentry and Jacobi (1995), the pressure loss is proportional to the turbulence enhancement ability of the VG. Hence, compromise between turbulence enhancement and pressure loss is often needed; otherwise, pressure recovery strategies have to be implemented. The pressure loss penalty will be reviewed and discussed further in Chapter 2.

Jacobi and Shah (1996) have suggested the implementation of the active method, such as a pump, that supplies additional energy to the system to provide pressure recovery. Nevertheless, active methods require additional energy, caution, and are sometimes confined to spatial and geometrical limitations in some applications. Therefore, there is a need to replace current technologies with an alternative method that is self-sustainable and energy-saving.

In addition, the conventional VG is often featuring and/or exhibiting rigid body characteristics. Although placing a protruded structure in a flow is essential for generating vortices, its presence can also dissipate the energy of the flow in various ways. First, it promotes viscous dissipation by extending the

region where the boundary layer is formed (the details and technical aspects of this dissipation will be covered in Chapter 2).

Secondly, when a flow “hits” a rigid VG, a portion of its kinetic energy is absorbed by the VG (the VG acts like a stiff structural-spring). The absorbed energy is then released and damped through tiny, little motion (usually vibration). This type of interaction is known as the Fluid-Structure Interaction (FSI). However, to be specific, rigid vortex generator only experiences one-way FSI: the flow can affect the structural dynamics but the structural changes are incapable of inducing significant influences to the flow. Therefore, the motion is normally assumed to be insignificant in most studies, so it is neglected. In short, the energy loss from the flow is wasted in a form of motion that has no significance towards the flow, hence reducing the efficiency of vortex generator.

## 1.2 Proposed Method – The Flexible Vortex Generator

There is a need to resolve the aforementioned problems associated with a rigid vortex generator, *i.e.* (i) improve the turbulence generation without sacrificing additional pressure loss and (ii) resolve the energy loss due to rigid structure characteristics and/or viscous effects. However, in light of the fact that current approaches in the studies of VG commonly focus on rigid structures, the problem of energy being damped by the tiny motion will not have a chance to be overcome (it is also because less attention has been invested in this area). So, an innovative solution is required!

Regardless of the suggestion from Jacobi and Shah (1996), some innovative ideas have been proposed instead of employing an already-known active/passive method to counter the pressure loss and other issues. For example, Aris *et al.* (2007) used shape memory alloy (SMA) that changes the angle of attack of the vortex generator passively based on the surrounding temperature to attain an optimal flow condition that eliminates unnecessary pressure loss. This is considered as one breakthrough in the study of vortex generation/generators, where an out-of-the-box solution is proposed. The SMA-vortex generator offers a non-static vortex generation strategy that does not require external energy supply, which has violated the definition of both active and passive methods. In other words, it has opened up a new door for vortex generators – a semi-passive method.

Inspired by the work of Aris *et al.*, the present work proposes to replace a typical rigid vortex generator (RVG) to a flexible one that can deform passively with response to the incoming flow. Through adopting this additional property, the Flexible Vortex Generator (FVG) is able to return the absorbed energy via an amplified motion that can modify the flow dynamics. Therefore, it is offering a semi-passive vortex generation strategy without an external energy supply. Besides, the problem of wasted energy due to the insignificant motion of RVGs can be resolved as well.

The FVG utilises the infamous Vortex-Induced Vibration (VIV) to drive a vibration/oscillation motion in the hope of modifying the flow dynamics to tackle the identified problems. VIV happens, unavoidably, whenever periodic vortex shedding is present. It has always been considered as fatal for fluid-interacting structures especially when the structure is vibrating in a locked-in state (resonance in VIV term). This vibration mode is well-known as one of the contributors of the Tacoma Narrow Bridge incident in 1940, as it induces a large-amplitude vibration that has led to the destruction of the bridge. Therefore, up until now, the studies of VIV mainly focus on its structural dynamics to gain an understanding of VIV and/or suppress its destructive effects on any fluid-interacting structure.

Apart from the efforts to suppress VIV, researchers have started to look into the positive potential and capability of VIV recently. A good example will be the VIVACE project lead by Professor Bernitsas (Bernitsas *et al.*, 2008), where a system – the VIVACE module – is designed to harness energy from VIV. This project offers great inspiration to the public, including the present work, that VIV can be utilised for better purposes.

Despite its potential in the structural dynamics as demonstrated in the VIVACE project, it is foreseen that VIV can be beneficial in the flow dynamics as well. While most VIV studies (Raghavan & Bernitsas, 2011; So *et al.*, 2008; Lee & Bernitsas, 2011; Singh & Chatterjee, 2014) including Professor Bernitsas's VIVACE studies mainly focus on the structural aspect of VIV, the study on the fluid dynamics and the vortex dynamics behind a vortex-induced vibrating object, to the best of the author's knowledge, receives relatively less attention.

### 1.3 Aim, the Research Questions and the Objectives

This research is designed to fill the research gap that has been identified earlier, namely the effect of a moving object – the FVG – on the flow dynamics; specifically, on the turbulence generation. The research focuses specifically on the mean flow component to identify the turbulence enhancement through evaluating the shear within the mean flow (will be further explained in Section 2.3.1). The purpose of studying the mean (shear) flow, instead of the classical statistical analysis on the fluctuating flow, is to identify the physics (*i.e.* vortex dynamics) and the mechanism of FVG-induced turbulence enhancement. If fluctuating components were studied instead, only a statistically description of the turbulence generated from the FVG can be obtained without understanding its physics. As a result of this research, the turbulence enhancement ability of the FVG with respect to the conventional RVG will be identified.

This leads to the definition of a set of research questions where answers are needed to prove that this proposed solution is useful to accomplish the task. These questions are:

1. How does a FVG influences the turbulence characteristic (in term of mean flow shear -  $\frac{dU_i}{dx_j}$ )?
2. What is the underlying physics that allows a FVG to improve turbulence level?

In addition to that, the ability of FVG in other applications should be studied as well. The most relevant application will be the heat transfer system as it is directly influenced by the turbulence characteristics. Thus, leading to the third research question:

3. If the usage of FVG is extended to other applications; for instance, heat transfer system, what is its influence on the heat transfer performance?

To answers, these questions, a set of research objectives are defined. The main objectives of this research are:

1. To investigate the turbulence enhancements (in term of flow shear) of a single-phase flow caused by a FVG, with the Reynolds Number range within the subcritical external flow ( $10^2 < Re_D < 10^5$ ). In this study, the subcritical flow is selected as the regime of interest because it is commonly involved in most engineering applications. Therefore, among the wide

spectrum of flow regime, it always draws more attention from the community.

2. To study the effects of varying aspect ratio (AR), which defines the ratio of VG's spanwise length ( $L$ ) to its characteristic length ( $D$ ), on the flow dynamics. By varying the AR, it is hoped that the physics and mechanism of VIV-induced turbulence enhancement can be understood better. This is also important to understand the governing parameters that play roles in FVG-enhanced turbulence. As a result, it provides useful insight for design and control in future applications.
3. To determine the heat enhancement caused by the enhanced turbulence generated by the FVG. The purpose of achieving this objective is to extend the effect of FVG to a heat transfer application. This study allows one to understand the effects of FVG in heat transfer processes.

These objectives are achieved through Fluid-Structural Interaction (FSI) simulation, a numerical method that integrates Computational Fluid Dynamics (CFD) and Finite Element Analysis (FEA) into a single model. The model used is validated with published experimental results. Besides, two of the simplest geometries are used as the VG: the circular cantilever and the flat plate cantilever.

## 1.4 Thesis Structure

**Chapter Two** covers the fundamental backgrounds and theories that provide essential understanding towards the research. Most importantly, it covers the technical descriptions of the research gaps that have been highlighted in this chapter.

**Chapter Three** reviews literature that provides insights regarding the current progress and/or findings of various relevant research areas. Apart from gaining the understanding of the physics, part of the review also highlighted the analysis techniques and methodologies that were used previously. This review covers topics such as flow past a cantilever, flow past an oscillating object, the role of vortex in heat transfer and lastly, the numerical approaches and modelling method used by other researchers.

**Chapter Four** outlines the numerical models to be used in the study. Besides, the validation of the model and the mesh independency study will be presented and discussed in this chapter as well.



**Chapter Five** discusses and compares the wake structure between the FVG and RVG via numerical visualisation. Throughout the discussion, the wake/flow modifications by employing the FVG and its cause are identified. Several preliminary predictions are made at the end of the chapter and the predictions will be justified in Chapter 5.

**Chapter Six** studies the shear in the flow field. Two specific regions have been targeted in the study, the boundary layer and the vortex. In the boundary layer, vorticity is formed through shearing and the formed vorticity is eventually fed to the forming vortex to aid its growth. The study of shear in the boundary layer provides an insight into the strength of the shed vortex. Next, as the result suggests that the vortex strength may have changed, and this leads to the second part of the chapter – the study of the vortex’s shear.

**Chapter Seven** investigates the extended application of the FVG, *i.e.* its heat transfer performance.

**Chapter Eight** covers the overall conclusion based on the conducted studies. Besides, future work and recommendations are also presented according to the experiences and knowledge that the author gained throughout the period of the research.

## **Summary of chapter**

In this chapter, the motivation behind this research work is presented and the missing puzzle – the research gap – of our current understanding in this field is identified. However, the presented information is, still, lack of technical and literature support. Thus, background theories and literature review shall be presented in the next chapter to clarify and identify the core information that is essential to comprehend the current research work.

## Chapter 2: Backgrounds and Theories

Chapter 1 has only introduced the research, lightly, without relating or discussing the underlying physics. Therefore, in this chapter, the essential information, principles and the technical aspects that formulate the research scope are discussed, in-depth, in the hope of deepening the understanding of the present work. Plus, literature is reviewed accordingly to enrich the discussion. Finally, the working principle of the proposed flexible vortex generator (FVG) is presented and discussed.

### 2.1 Reynolds Number

When dealing with fluid flow problems, it is primarily important to identify the flow properties, *i.e.* the flow regime. In this sense, the Reynolds Number,  $Re$ , is used to describe the flow properties. It is expressed by the following equation:

$$Re = \frac{U_c D_c}{\nu} = \frac{\rho U_c D_c}{\mu} \quad (2.1)$$

where  $U_c$  is the characteristic flow velocity,  $D_c$  is the characteristic length,  $\mu$  is the dynamic viscosity of the fluid,  $\nu$  is the kinematic viscosity of the fluid and  $\rho$  is the density of the fluid. From this expression, the Reynolds Number increases with the velocity of the flow. This denotes that the inertia force is dominating the flow at high Reynolds Numbers and the viscous force (effect) plays a less dominant role in the flow. This flow condition is known as the turbulent flow.

Equation 2.1 represents the general expression for Reynolds Number, where the  $D_c$  and  $U_c$  can be replaced by a specific value to represent the properties of a particular flow region. For instance, if the diameter of a cylinder,  $D$ , and the incoming flow velocity,  $U$ , are used as the characteristic length and velocity, then the Reynolds Number identifies the flow properties around the cylinder's surface. This identification of Reynolds numbers is often known as the local Reynolds Number ( $Re_D$ ). In this research,  $Re_D$  is used to identify the flow condition of the case.

## 2.2 Turbulence and Kinetic Budget Equations

It is understood that turbulence is an eddy motion which describes the chaotic changes in fluid flow. Due to this motion, turbulence gives rise to vigorous mixing and effective turbulence stress.

Turbulent flow can be described mathematically via decomposing the fluid flow properties, as shown in Equation 2.2.

$$\phi(t) = \bar{\phi} + \phi'(t) \quad (2.2)$$

where the  $\phi$  can be any flow property such as pressure, velocity and others;  $\bar{\phi}$  represents the mean value of any flow property while  $\phi'$  represents the fluctuation component. This description method is known as the Reynolds Decomposition Method. The equation also reflects the fact that a turbulent flow consist of two main regimes: the mean flow ( $\bar{\phi}$ ) and the fluctuating flow ( $\phi'$ ), indicating a close relationship between both regimes.

The energy transfer that describes turbulent flow is expressed by the Kinetic Energy Budget, which consists of two equations that are closely coupled (Kundu & Cohen, 2008). The energy transfer of the main flow is described by the Kinetic Energy Budget of Mean Flow:

$$\frac{D}{Dt} \left( \frac{1}{2} U_i^2 \right) = \frac{\partial}{\partial x_j} \left( \underbrace{-\frac{PU_j}{\rho_o}}_1 + \underbrace{2\nu U_i E_{ij}}_2 - \underbrace{\overline{u'_i u'_j U_i}}_3 \right) - \underbrace{2\nu \overline{E_{ij} E_{ij}}}_4 + \underbrace{\overline{u'_i u'_j}}_5 \frac{\partial U_i}{\partial x_j} - \underbrace{\frac{g}{\rho_o} \bar{\rho} U_3}_6 \quad (2.3)$$

The left-hand side represents the rate of change of the mean kinetic energy. For the right-hand side, the first three terms (inside the bracket) are the transportation terms, which describe the transportation of energy via the mean pressure, the mean viscous stresses and the Reynolds stresses, respectively. The fourth term represents the loss of kinetic energy due to the viscous effect, which is known as viscous losses. The fifth term represents the loss of kinetic energy due to turbulent (the sign of the term is positive because  $u'_i u'_j$  is usually negative due to the anisotropic character of turbulence). Besides, it is also important to note that this term will reappear in the Kinetic Energy Budget of Turbulent Flow, which signifies that the lost energy is transferred to the turbulent regime. The last term represents the loss of energy due to gravity in the vertical direction. In the mean flow, the loss due to viscous (fourth term) and

gravity (sixth term) can be neglected due to its relatively small scale losses compared to the shear losses (fifth term) (Kundu & Cohen, 2008).

Next, the kinetic energy in the turbulent regime is described by the Kinetic Energy Budget of Turbulent Flow:

$$\frac{D}{Dt} \left( \frac{1}{2} \overline{u_i'^2} \right) = - \frac{\partial}{\partial x_j} \left( \underbrace{-\frac{\overline{p u_j'}}{\rho_o}}_1 + \underbrace{\frac{1}{2} \overline{u_i'^2 u_j'}}_2 - \underbrace{2 \overline{\nu u_i' e_{ij}}}_3 \right) - \underbrace{2 \overline{\nu e_{ij} e_{ij}}}_4 - \underbrace{\overline{u_i' u_j'} \frac{\partial U_i}{\partial x_j}}_5 + \underbrace{g \alpha \overline{\omega T^n}}_6 \quad (2.4)$$

Similar to Kinetic Energy Budget of Mean flow, the first three terms on the right-hand side represent the energy transportation. The fourth term represents viscous dissipation. The fifth term represents the shear production, which is the gain of energy that has been lost from the mean flow that mentioned previously. In other words, it represents the generation of turbulent kinetic energy. The final term represents the buoyant production. Unlike the viscous dissipation in the mean flow, which can be neglected, the turbulence viscous dissipation cannot be neglected because it has a comparable order with the shear production (fifth term) (Kundu & Cohen, 2008). Apart from that, as depicted in Equation 2.4, the viscous loss term (fourth term) is the only term that dissipates turbulent kinetic energy. Therefore, if it is neglected, turbulent kinetic energy is not conserved (Energy in  $\neq$  Energy out) and it violates the Second Law of Thermodynamic.

The Kinetic Energy Budget Equations are useful in examining and evaluating the nature of turbulence. It is also applicable to any perturbed laminar system because it exhibits similar properties with the turbulent flow where the fluctuating components arise from perturbation. The later application was discussed by Dol *et al.* (2014), where the forced unsteadiness on a laminar flow over a back-faced step was examined through calculating the terms in the Turbulent (fluctuating) Kinetic Budget Equation.

In the present work, the Kinetic Energy Budget Equations will not be evaluated directly. Instead, the key ideas of the turbulent flow, such as its formation and dissipation, are extracted from the equations, so that the identified problem can be resolved by developing a fundamental understanding of the flow. This will be covered in the next section, Section 2.3.

## 2.3 The Technical Aspects of the Downsides of Conventional Vortex Generator (VG)

In Chapter 1, the pressure loss issue and the energy loss issue are discussed briefly. This section covers the technical aspects of those problems. Furthermore, it will further discuss those problems based on the underlying physics in the hope of resolving those issues based on the fundamental understanding.

### 2.3.1 Energy Loss on Vortex Generator

First of all, the Kinetic Budget Equations discussed in the previous section, show that the turbulent flows gain its energy from the mean flow via the shear production term. The idea of energy transfer of the flow is illustrated in Figure 2.1. The kinetic energy is lost from the mean flow in the form of shear loss. However, this loss of energy enters the turbulent regime as the shear production. The turbulent flow will consume this energy throughout its lifetime until it is eventually dissipated, via viscous effect, as heat (this part is not particularly important in the current study because it happens at the smallest scale of turbulence – Kolmogorov microscale, and the heat released is negligible on the macroscopic scale).

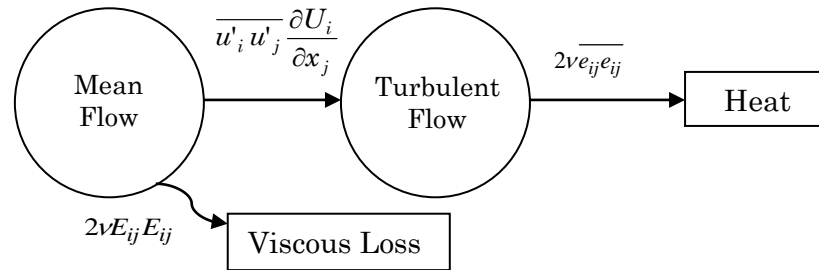


**Figure 2.1: Schematic of energy transfer in turbulent flow.**

The Kinetic Budget Equations also provide a mathematical impression on the viscous dissipation that has been discussed briefly in Chapter 1, which is accounted by the viscous loss term (fourth term) in Equation 2.4. As suggested by its name, the viscous loss arises whenever and wherever the viscous effect takes place. This means that whenever an obstacle (such as the vortex generator) is present in a flow, it promotes the formation of the boundary layer, in which this viscous effect is heavily involved. To put it differently, the obstacle produces a larger region where the viscous loss occurs, hence escalating the viscous loss.

Since forcing the formation of boundary layer and shear layer in the flow is essential for turbulence generation, the viscous loss is normally unavoidable and it is often not compromised. With reference to this loss, the efficiency of energy transfer from mean flow to turbulent flow can be expressed as Equation 2.5 (if the gravity loss is neglected).

$$efficiency = \frac{-\overline{u'_i u'_j} \frac{\partial U_i}{\partial x_j}}{\left( -\overline{u'_i u'_j} \frac{\partial U_i}{\partial x_j} + 2\nu E_{ij} E_{ij} \right)} \quad (2.5)$$

It expresses the ratio of *the energy loss to turbulence* to *the total energy loss from mean flow*. In order to improve the efficiency, the shear production has to be improved. In other words, the efficiency will be improved if and only if the turbulence generation is enhanced under the same flow condition.

From the above efficiency ratio, it is clear that the turbulence can be enhanced once the shear production (Equation 2.6) is enhanced.

$$\overline{u'_i u'_j} \frac{\partial U_i}{\partial x_j} \quad (2.6)$$

The expression clearly shows that the shear production that governs the turbulence formation, is a product of the Reynolds stresses ( $\overline{u'_i u'_j}$ ) and the shear rate ( $\partial U_i / \partial x_j$ ). These two components, however, represent a different aspect of the turbulence, *i.e.* the Reynolds stresses (it covers Reynolds normal and shear stresses) expresses the shear generated at the fluctuation part of the turbulence (hence  $u'_i$  and  $u'_j$ ); whereas, the shear rate symbolises the shear occurred at main flow component of the flow (hence  $U_i$ ). The present work focuses on the shear generated at the level of main flow component, *i.e.* the shear rate ( $\partial U_i / \partial x_j$ ).

In a flow, the shear rate is presented in the form of velocity gradient. It denotes and describes a change of velocity along the direction that is perpendicular to its flowing direction. So, in order to examine the shear production in the main flow, the region where velocity gradient arises; for example the boundary layer, the vortex, the separated flow and the wake; should be studied. In this study, the boundary layer around a VG – where a vortex gains its strength from; and the wake – where vortices play its role in turbulence events are investigated.

### 2.3.2 Pressure Loss (Penalty) on Vortex Generator

Aside from the viscous loss as discussed in Section 2.3.1, vortex generator (VG) is also accompanied by pressure loss. As mentioned in Chapter 1, many studies have reported an undesirable pressure loss associated with vortex generation, despite its promising turbulence enhancement ability. This finding is not limited to protrusion-based vortex generator but also appears in other passive turbulence enhancement techniques (Erikson & Liao, 2007; Ağra *et al.*, 2011; Laohalertdecha *et al.*, 2007). Therefore, it is believed that the pressure loss is induced whenever the flow is obstructed by any blunt object, which is similar to the formation of pressure drop behind a cylinder that is submerged in a flow.

Chen *et al.* (1998) had observed the pressure drop in their study on the performance of the winglet VGs. They attributed that the occurrence of pressure loss to the formation of drag behind the VGs due to the deficit in streamwise velocity. However, according to the principles of flow dynamics, the drag is a product of pressure drop; the drag force is exerting on the VG due to a pressure difference between the upstream and downstream of the VG. In fact, this pressure drop is formed once the boundary layer is separated from the VG. The most famous and relevant example will be the golf ball, where the drag can be reduced significantly when the flow separation is delayed by the dimples. This example has strongly evident that the formation of pressure drop is caused by the flow separation. Therefore, the argument of Chen *et al.* is incorrect.

Since flow separation is essential and crucial for vortex formation, it means that the pressure drop has become an unavoidable feature of VG. This is because the only strategy to reduce pressure drop on a VG is to suppress the flow separation. If so, the vortex formation is suppressed as well.

According to the review that was done by Gentry and Jacobi (1995), as shown in Table 2.1, the pressure drop penalty is proportional to its turbulence enhancement ability (it is referred as heat transfer enhancement in the original context. Since heat transfer is closely related to turbulence generation, it is regarded as turbulence enhancement in this discussion); greater enhancement is always accompanied by great pressure loss.

**Table 2.1: Summary of the performances of wing-type vortex generators (Gentry & Jacobi, 1995).**

Geometry	Reynolds Number	Overall Turbulence Enhancement	Pressure drop Penalty
Full Scale Plate-Fin Heat exchanger <sup>a</sup>	300-2200	50%	20-30%
Rectangular channel with delta winglet pair <sup>b</sup> :			
No hole under wing	500	34%	79%
Hole under wing	500	10%	48%
Rectangular channel <sup>c</sup> :			
Delta Wings	1000-2000	50%	45%
Multiple pairs(inline)	4600	60%	145%
Multiple pairs(staggered)	4600	52%	129%
Three Tube Rows <sup>d</sup> :			
Inline Round	600-3000	55-65%	20-44%
Staggered Round		9%	3%
Flat Tubes		100%	100%

a: Russel *et al.*, 1982

b: Biswas *et al.*, 1989; Biswas & Chattopadhyay, 1992

c: Fiebig *et al.*, 1991; Tiggelbeck *et al.*, 1992; Mitra & Fiebig, 1993

d: Valencia *et al.*, 1993; Fiebig *et al.*, 1993; Fiebig *et al.*, 1994

This indicates the need for compensation between the enhancement and the pressure drop penalty in order to achieve the optimal condition. For instance, in order to achieve a higher heat transfer rate, the pressure drop has to be sacrificed – a large pressure drop will be present in the system and it will slow down the flow. Consequently, a greater amount of input energy might be needed to drive the flow, thus, affecting the efficiency. Thus, the pressure loss is often called as the flow loss as well (Valencia *et al.*, 1993).

The consequences caused by the pressure drop penalty are, by some means, similar to the minor losses in pipe flow (the pressure losses caused by the pipe's components). By considering the Bernoulli's equation of a pipe flow, a greater pump power is required when the system has high minor losses (this example is used as an analogy to allow better understanding, so it will not be discussed in detail). This scenario is applicable in the case of flow past a vortex generator. Therefore, the pressure loss penalty associated with a vortex generator can be a major concern for both flow control and economy aspect.

Therefore, in order to evaluate the performance of a VG, the ratio of pressure loss to its turbulence generation can be checked. This ratio can be seen as the performance ratio of a system.



## 2.4 Flow Separation, Vortex Formation and Vortex Shedding

Aside from increasing the inertia force (increasing  $Re$ ), turbulent flow can be generated by creating vortex – a product of flow separation that undergoes a roll-up process due to Kelvin-Helmholtz instability. This is a common phenomenon that can be observed when a bluff body is immersed in flowing fluid. This vortex formation process is started with boundary layer separation.

As commonly known, when fluid flows around a bluff body, a boundary layer is formed on its surface. In such situation, the energy in the boundary layers dissipates due to the viscous effect or other possible reason, which leads to an insufficient energy state for the boundary layer to stay on the surface. As a result, a separation occurs. By “separation”, it means the *departure or breakaway, or the breakdown of boundary layer flow* (Simpson, 1989).

There are two possible causes of separation. The point of discontinuity such as sharp corner typically causes separation. At the point of discontinuity, the local flow changes drastically that will lead to the separation. For example, a large velocity gradient and a strong adverse pressure gradient is normally present at the point of discontinuity. Apart from this, separation can also be caused by the point with adverse pressure ( $\partial P/\partial y > 0$ ;  $\partial U/\partial y < 0$ ) and at the point where the wall shear stress vanished (equals to zero), as shown in Figure 2.2. Besides, the ability of the boundary layer to “stay” on the surface is also depending on whether the boundary layer is laminar or turbulent. A turbulent boundary layer normally contains a greater energy (or momentum) that allow it to withstand the adverse pressure gradient (Kundu & Cohen, 2008).

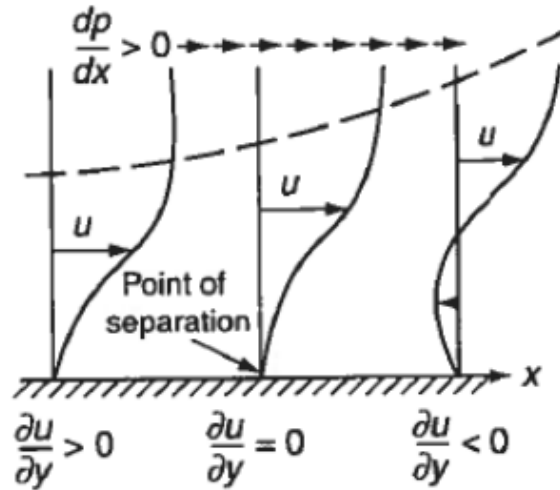


**Figure 2.2: Adverse Pressure Gradient and separation point (White & Corfield, 2006).**

After the boundary layer is separated, the flow is behaving as a free shear layer, with velocity gradient lies within the whole layer. It is because of the velocity gradient, the shear layer is highly unstable and it has the tendency to roll up due to Kelvin-Helmholtz Instability (KHI). In KHI, the flow is divided into many layers, which the velocity profiles are considered uniform in each fluid layer and it is dissimilar to its neighbouring layers (*i.e.* shear flow). Each fluid layer is separated distinctively by an interface as shown in Figure 2.3. The instabilities are initiated by the dissimilar velocity of two parallel layers (or streams) and this induces a vorticity at the interface between the layers. As a result, the interface becomes an unstable vortex sheet and it rolls up into a spiral, eventually forming a vortex.

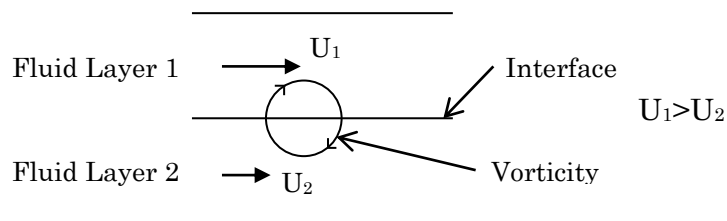


**Figure 2.3: Illustration of the discontinuous velocity in the shear layers that leads to vortex sheet roll-up.**

After the rolling of vortex sheet is initiated by KHI, the forming vortex (the rolling shear layer) is gaining its energy – vorticity from the boundary layer, as shown in Figure 2.4. Ideally, the vortex will continuously drain vorticity from the boundary layer, up to a level where it can no longer withstand anymore, then the vortex detaches from the boundary layer as a rolled-up shear layer. The

shedding of vortex ring from a nozzle, as described by Dabiri and Gharib (2005), exhibits this type of shedding process.

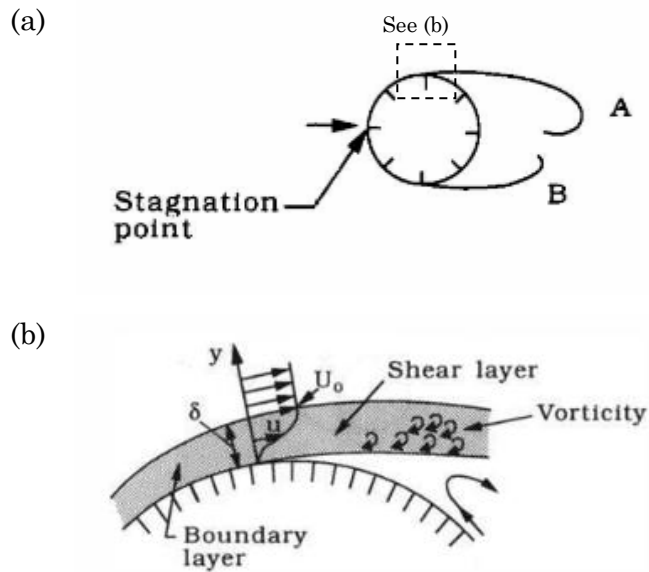


**Figure 2.4: (a) Vortex formation on circular cylinder; (b) zoomed-view at the location of separation where Vortex A (in (a)) forms (Sumer & Fredsøe, 1997).**

In the case of flow past a blunt body such as a circular cylinder, the shedding process has an additional interruption – the formation of an opposing vortex. When Vortex A gains sufficient strength, it will draw the opposite vortex – Vortex B – across the wake, as illustrated in Figure 2.5(a). Since both Vortex A and B are in the opposite swirling direction (opposite sign), the vorticity in Vortex B tends to cut off the vorticity supply of Vortex A, which is illustrated as the arrow in the figure. Once the supply is stopped, the boundary layer and shear layer are disconnected, and Vortex A is shed. After Vortex A had shed off, Vortex B continues to gain vorticity from the boundary layer, and its strength grows. Meanwhile, a new vortex is forming at the side of the cylinder where Vortex A was located, namely Vortex C. As Vortex B becomes stronger, it draws the Vortex C across the wake, and the process described earlier repeats itself. In addition, it is important to mention that the vortex shedding from a normal flat plate exhibits a similar process.

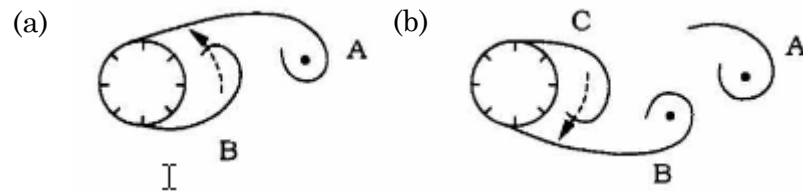


**Figure 2.5: Vortex shedding from a circular cylinder (Sumer & Fredsøe, 1997).**

In this research, a moving cantilever (the flexible vortex generator) is involved. It is expected that the vortex shedding process may undergo a slightly different process with respect to the one discussed earlier. Therefore, in light of this event, it is important to understand the typical vortex shedding process of a rigid and stationary cylinder, so that it can serve as a benchmark to identify any uncommon and/or abnormal shedding behaviour when a moving cylinder/cantilever is studied. This also implies that the identification of the vortex shedding process can provide useful insight into the vortex dynamics in the case of moving cylinder/cantilever, which will be studied in this research.

## 2.5 Vortex Generation Methods

In many engineering applications, turbulence enhancement has become a popular approach or strategy to improve its performance. Various turbulence enhancement methods had been reviewed by Steinke and Kandlikar (2004), which the authors addressed those methods in term of heat transfer enhancement techniques. In fact, many researchers in this area, including Steinke and Kandlikar, have addressed passive heat transfer enhancement as *“breaking of boundary layers that improve mixing and promotes flow transition”*. As *“The breaking of boundary layer”* is generally referring to vortex formation and shedding, the quote generally means turbulence enhancement via vortex generation. Besides, in this study, those enhancement methods are referred as turbulence enhancement methods, where this term accounts the mixing and heat transfer enhancement at the same time.

There are mainly two turbulence enhancement methods: the active methods and the passive methods (Gentry and Jacobi, 1995). According to Gentry and Jacobi (1995), active enhancement methods require external power sources. The most common example of active enhancement method used in the industry is motored-agitator that acts as a homogenizer to stir the fluid in the system. In some occasion, an ordinary pump can act as a turbulence generator

as well. However, active methods required extra cautions such as additional control system and monitoring that add additional cost. Despite that, its implementation is also restricted by the geometry or size of the devices and the space requirement. On the other hand, passive enhancement methods do not require an external power supply and usually can be done by a surface modification that is much cheaper compared to active methods. As a result, passive methods are much favourable in engineering applications.

Among many passive methods listed in Gentry and Jacobi (1995) and Steinke and Kandlikar (2004), vortex generation is one of the passive enhancement methods that is gaining much interest from the industries. Gentry and Jacobi had done an inclusive review on the performance of various vortex generation devices in heat transfer system and documented a promising performance on vortex generation methods. There are two types of vortex generators, namely the protuberance based and protrusion based generators, as shown in Figure 2.6. Protuberance based generators use bump-like (usually short) structure embossed on the surface that generates horseshoe vortex; whereas, protrusion based generators are usually wing-like (long) structure erected on the surface that generates tip vortex and some are associated with horseshoe vortex as well Gentry and Jacobi (1995); it is often known as the wing based method as well. The details of each vortex generator types are summarized in Table 2.2.

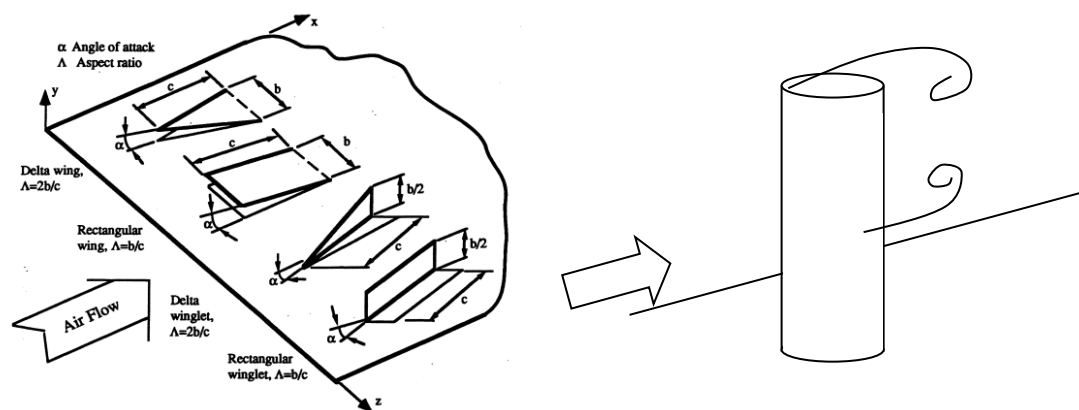


**Figure 2.6: (Left) Protuberance based generators (Gentry & Jacobi, 1995); (right) protrusion based generator.**

**Table 2.2: The features, vortex generation ability and the applicability of protrusion-based and protuberance-based VG.**

	<b>Protuberance-based</b>	<b>Protrusion-based</b>
Features	i. Bump-liked ii. Small in height	i. Wing-liked ii. Long in height
Vortex generation	Horseshoe vortex only	Longitudinal tip vortex, Kármán vortex and horseshoe vortex
Applicability	Application with space limitation	Application that requires great turbulence

This research focuses on turbulence enhancement through a protrusion based vortex generator due to its high capability in turbulence enhancement by generating multiple vortex structures such as tip vortex, Kármán vortex and horseshoe vortex. Besides, when the protrusion based vortex generator is applied in heat transfer system, it also holds the benefit of heat transfer as it generally serves as the extended surface that can promote heat transfer, effectively. Apart from these general properties, a protrusion based vortex generator is also slender, which allows it to adopt an additional property – flexibility. This additional property is crucial in this research as it allows the vortex generator to deform or vibrate with large amplitude.

A cantilever erected in a current of fluid can be regarded as one of the simplest protrusion based vortex generators; thus, this configuration/setup will be used in this research work as the vortex generator.

## 2.6 Vortex-Induced Vibration

Vortex-Induced Vibration (VIV) plays an important role in this research. It is the driving source that initiates the oscillating motion of the Flexible Vortex Generator (FVG), which is postulated to have positive impacts on turbulence generation. The VIV is one of its bigger family – the Flow-Induced Vibration (FIV) that groups the motion of submerged body that is caused by a various type of flow features.

As mentioned in Chapter 1, VIV happened due to the alternating forces exerted on the object during vortex shedding. In fact, to be precise, VIV can be initiated by two types of vortex shedding, namely the symmetric vortex shedding and Kármán vortex shedding. The type or mode of vortex shedding determines the vibrating mode of VIV. Symmetric vortex shedding induces an in-line

vibration, namely the in-line VIV, by shedding away a pair of symmetrical vortices. This type of shedding may occur at lower flow velocity compared to Kármán vortex shedding (Nakamura *et al.*, 2013). Kármán vortex shedding, on the other hand, refers to alternating (or non-symmetric) vortex shedding from the cylinder. Kármán vortex shedding is responsible for inducing cross-flow VIV, where the vibration is in the transverse direction. The VIV responses with respect to the shedding mode are demonstrated in Figure 2.7. In this study, Kármán vortex shedding is expected to be the dominant vortex shedding aside from tip vortex shedding. Therefore, a cross-flow VIV should be the dominating oscillation mode unless the direction of motion is restricted by certain criteria. For example, flat plate cantilever erected normal to the flow will not vibrate in cross-flow VIV, due to its large second moment of inertia that resists its motion in that direction.

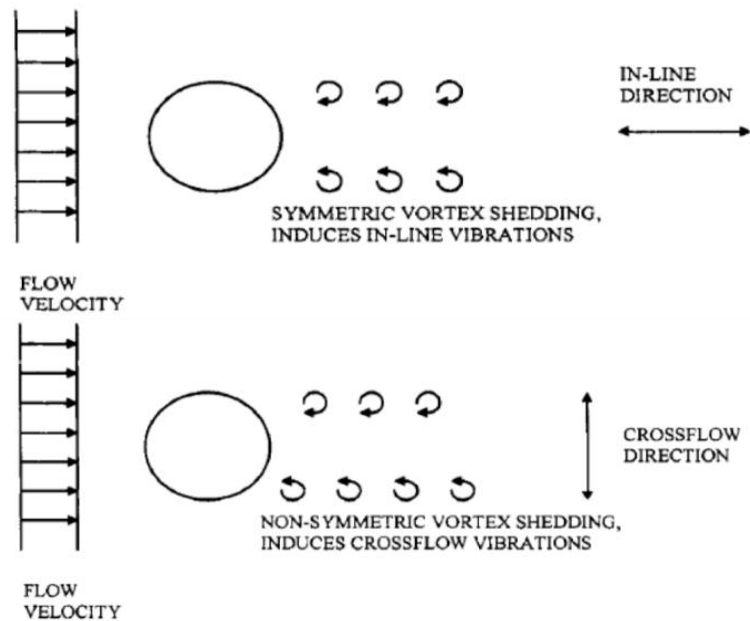


**Figure 2.7: (Top) In-line VIV by symmetric vortex shedding; (bottom) cross-flow VIV by non-symmetric vortex shedding. (Bai & Bai, 2005).**

### 2.6.1 Lock-in

There is a special regime of VIV where the vibration behaves so differently compared to its normal or common condition. It happens when the vortex shedding frequency ( $f$ ) matches the natural frequency ( $f_n$ ) of the vibrating object, where the vibration frequency takes over the vortex shedding frequency and the amplitude of the vibration increases significantly compared to the typical VIV responses (Xie *et al.*, 2011). This special condition is termed as the

lock-in condition. Figure 2.8 illustrates the amplitude response of a circular cylinder that undergoes VIV. From the figure, it clearly shows that there is a peak amplitude occurred when the reduced velocity is approximately 6. With reference to the frequency ratio ( $f/f_n$ ), the peak amplitude happened exactly when the ratio is in unity. In fact, the “lock-in” is a term that describes the resonance happened in VIV.

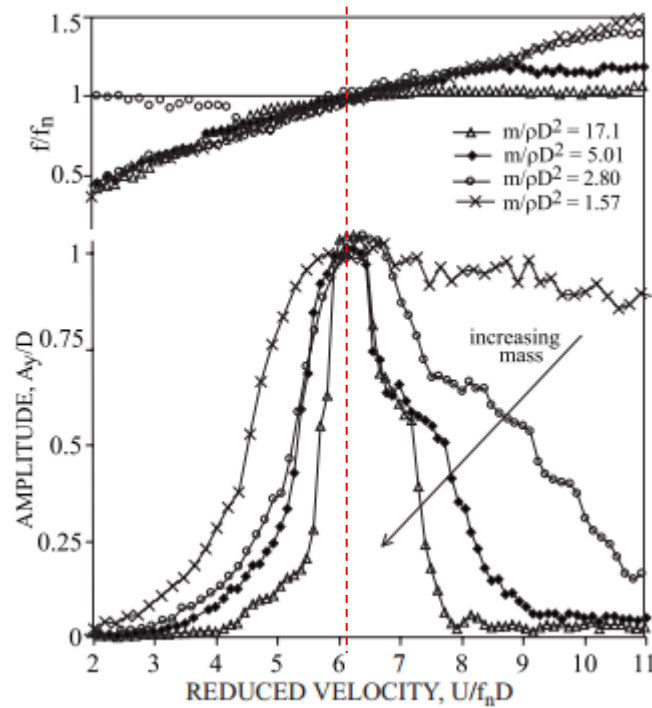


**Figure 2.8: The amplitude plot of a cylinder that undergoes VIV versus the reduced velocity (Blevins & Coughran, 2009).**

It is interesting to note that, in Figure 2.8, the range of lock-in is getting narrower when the mass ratio (expressed as  $m/\rho D^2$  in the graph) is increased. The mass ratio ( $m^*$ ), which is defined by the ratio of oscillating mass ( $m_{osc}$ ) to the mass of displaced fluid ( $m_{disp}$ ), is one of the most important aspects in the study of VIV. The narrowing of lock-in range may due to the fact that high mass ratio system requires more energy to accelerate due to the fact that heavy cylinder has greater inertia (Newton’s 1<sup>st</sup> Law of motion). Let consider the delivered energy is a function of  $f/f_n$  and it reaches its maximum when the  $f/f_n$  approaches unity (when the vortex shedding response superimposes with the structural frequency that can deliver a greater amount of energy). So, it takes a more precise  $f/f_n$  relationship (closer to unity) to initiate the large vibration as a greater energy is required to accelerate a heavy object.



However, in this research, the mass ratio does not play a significant role due to two reasons. First, the proposed FVG system does not consist of additional components other than the cylinder that can induce an inconsistent mass ratio. Secondly, through simplifying the definition of mass ratio, it denotes the ratio of the density of vibrating structure's material to the density of the surrounding fluid (as shown below). Note that this definition is valid if and only if no addition masses (such as springs, damper and *etc*) are involved in the system (the mass contributors are always the vibrating structure and fluid, nothing else). Since the same material and fluid will be used in the same study, the mass ratio does not play a significant role, as shown below.

$$m^* = \frac{m_{osc}}{m_{disp}} = \frac{\rho_s \times \text{Volume of structure}}{\rho_f \times \text{Volume of structure}} = \frac{\rho_s}{\rho_f} = \text{constant}$$

When an object is undergoing a locked-in VIV, it can induce several impacts to the flow behaviour. According to Faltinsen (1993), the consequences of lock-in are:

- i. The increase of correlation length
- ii. The increase of vortex strength (or circulation)
- iii. The increase of lock-in bandwidth
- iv. The maximum relative amplitude increases, to approximate  $A/D \approx 1$  (as shown in Figure 2.8)

Among these consequences, Point ii – *The increase of vortex strength* is the aspect that concerns this research work. As mentioned in Chapter 1, the current work aims to enhance turbulence by employing flexible vortex generator that vibrates in large amplitude when fluid flows past it. The main contributor of mixing and heat transfer enhancement is, in fact, the vortices in the flow. Therefore, a vortex with greater strength signifies a better turbulence quality.

Furthermore, based on Faltinsen's arguments, it can be deduced that these consequences are, perhaps, happened once large-amplitude vibration is achieved as it is the major characteristic described by lock-in condition. Therefore, it is believed that the described influences are not limited to lock-in condition only; as long as there is a large-amplitude vibration, these consequences shall occur. In other words, these consequences can also present when a large-amplitude vibration is attained by employing the FVG, even though the frequency ratio is not in unity. This will be the greatest benefit of using a FVG where a large-amplitude vibration can be achieved effortlessly

without concerning the frequencies. Besides, its vibration amplitude may also be relatively larger than the conventional rigid vortex generator ( $A/D > 1$  instead of  $\approx 1$ ) depending on its material and cross-section shape (the effects of these parameters on the deflection rate will be discussed in the next section).

In short, a FVG is capable of mimicking large-amplitude vibration that is only achievable in the locked-in condition when a rigid structure is used. For instance, a large-amplitude vibration is possible at lower velocity when a FVG is used instead.

## 2.7 The Flexible Vortex Generator (FVG)

There are two ways to create a FVG, which is by introducing elasticity and/or flexibility to the VG. Both *flexibility* and *elasticity* define the ability to deform; but precisely, they define the ability to deform due to a different characteristic. So both terms should be treated differently. Consider a simple system consists of a cantilever as shown in Figure 2.9:

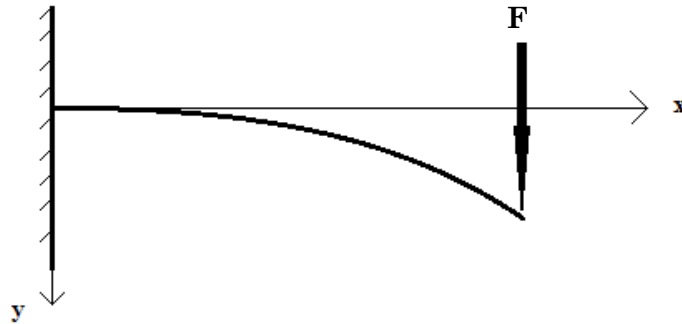


**Figure 2.9: Bending of a cantilever beam with applied force  $F$ .**

The equation that describes the  $y$ -deflection,  $d_y$  is:

$$d_y = \frac{Fx^2}{6EI}(3L - x) \quad (2.7)$$

By comparing Equation 2.7 with the Hooke's Law equation, the spring stiffness ( $k$ ) is found to be:

$$k = \frac{6EI}{x^2(3L - x)} \quad (2.8)$$

The  $k$  is known as the ease for the structure to deform under certain loading. From above expression, it can be clearly seen that the  $k$  is a function of  $E$ ,  $I$ ,  $L$

and position  $x$ ;  $k = f(E, I, L, x)$ . These variables can be further categorised into two categories: a) material properties; and b) structural characteristic.

Among the variables listed in Equation 2.8, the elastic modulus (or Young's modulus)  $E$  is the only variable that represents the material properties, therefore, it is categorised under (a). This indicates that the change in spring stiffness can be achieved by varying the elastic modulus, *i.e.* changing the material of the deflecting beam. Alternatively, the second moment of inertia  $I$ , and the length of the cantilever  $L$  represent the structural characteristic (category (b)). A flexible structure can be constructed when low  $I$  geometry and large  $L$  design is adopted. While  $x$  is the position along the beam and it helps in representing the local stiffness. Therefore, the  $x$  does not belong to both categories.

Based on the identified parameters discussed in the previous paragraph, a large deflection can be achieved when the cantilever beam is made by introducing a highly elastic material (low  $E$ ) and/or adopting a design with high flexibility (low  $I$ ) and/or increasing the length of the beam (Large  $L$ ).

### 2.7.1 The Working Principle of the FVG

As discussed previously, the FVG has to create a greater turbulence production in order to improve the performance ratios (*turbulence enhancement to the pressure drop ratio*) and also the efficiency ratio (Equation 2.5). Fortunately and coincidentally, both improvements can be achieved by improving the turbulence generation. This has reduced the aim of the FVG to a more specific one – to generate more turbulence with respect to a RVG.

How does a FVG work? This is an important question to ask before the research has actually started. First of all, the FVG is capable of oscillating due to its elasticity and/or flexibility. The FVG undergoes two phases during oscillation, *i.e.* Phase I – it bends and Phase II – it recovers from bending. In Phase I, the energy from the mean flow is extracted and stored in the form of potential energy as the FVG is bent. Then, the stored energy is returned to the mean flow through shape recovery from bending; Phase II (see Figure 2.10). This process allows the energy, that is originally damped if a rigid VG is used, to be recycled and returned to the flow, hence increasing the efficiency of vortex generation. Besides, the generated turbulence is also expected to be greater than that generated by a rigid vortex generator since the flow has greater energy content. This mechanism is also assumed to be the cause of the increasing

vortex strength in locked-in VIV condition that was identified by Faltinsen (1993). Consequently, the FVG may provide a strategy to improve both performance ratio and the efficiency ratio with respect to a regular rigid vortex generator.

\*The circle with  $E$  represents the energy in the flow and its size represents the intensity of the energy  
 \*The blue arrows represent the energy transfer.

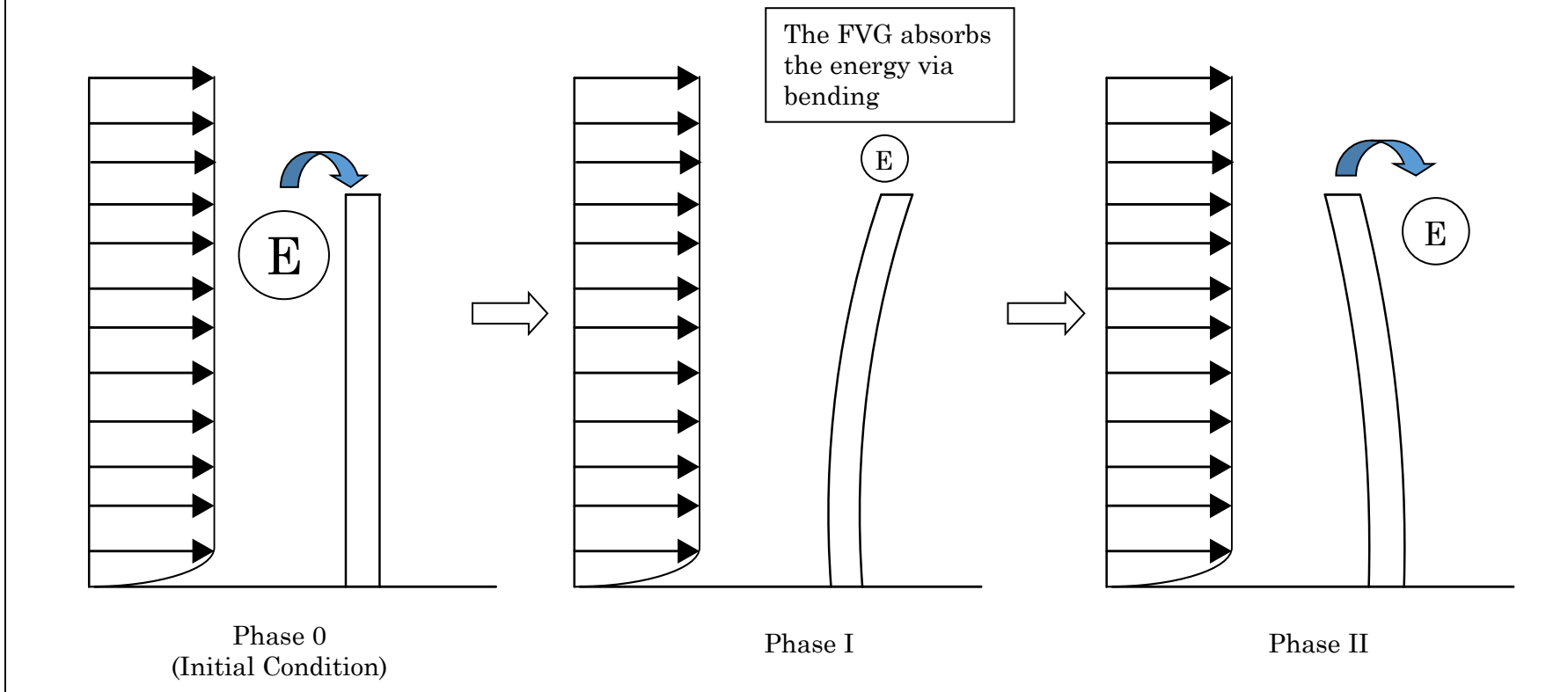


**Figure 2.10: Schematic of the energy transfer between the fin and the flow.**

## Summary of Chapter

This chapter has introduced the essential background theories that allow one to comprehend the problem statement and the objectives of the current research. Firstly, the basic concept to identify turbulent flow is introduced. It is then followed by introducing the Kinetic Budget Equations to discuss the fundamental problems associated with turbulent flow. By studying the equations, it is recognised that turbulent flow is accompanied by an unavoidable viscous loss. It has later been identified that, in order to improve the performance of a vortex generator, the turbulence production of a VG under the same flow condition has to be improved. Besides, the pressure loss problem associated with the vortex generator, which has been introduced briefly in Chapter 1, is discussed with its technical aspects and published evidence.

A solution – the flexible vortex generator (FVG) – has been introduced in Chapter 1 to overcome the discussed problems of the conventional rigid vortex generator (RVG). Since the targeted solution is clear, the basic theories that form the working principle of the VG and FVG are discussed. These include the discussion of the vortex generation method, followed by the phenomenon that initiates the motion of the FVG, *i.e.* the vortex-induced vibration. Lastly, the anticipated working principle of the FVG is discussed as well.

In the next chapter, the literature review will be presented.

## Chapter 3: Literature Review

In this chapter, relevant literature that helps to construct the understanding of the present state-of-art is reviewed. Firstly, since the vortex generators (VGs) used in this research work are basically a cantilever, the literature that studied on the flow behaviour around a cantilever is reviewed as well. Furthermore, the studies that investigated the flow dynamics around a moving object are reviewed to provide further insight on the phenomena that could be expected from the current study. From the literature, the performance and problems of vortex generators (VGs) in recent studies are identified. In addition, the research gaps are addressed based on the review on current research focus.

### 3.1 Flow Past a Cantilever

The present study uses cantilever as the vortex generator. Unlike typical flow past a blunt object, flow past a cantilever possess distinct flow characteristics – three-dimensionality – that emerge from the free end of the cantilever; it is known as the free end effect or tip effect. However, when a cantilever surpasses a critical length, the free end effect become spatially insignificant. This long cantilever is referred as “infinite” cylinder as it is free from the three-dimensional effect arose from the free end. According to Fox and West (1993), a condition that resembles an “infinite” cylinder can be established at a distance of 20 diameters from the free end. Some of the following literature is selected based on the length criterion defined above to ensure that the distinctive flow characteristics of a cantilever are involved.

#### 3.1.1 The Flow Field around the Cantilever

One of the earliest proposed flow models behind a cantilever is illustrated in Figure 3.1, which was proposed based on experimental observations.

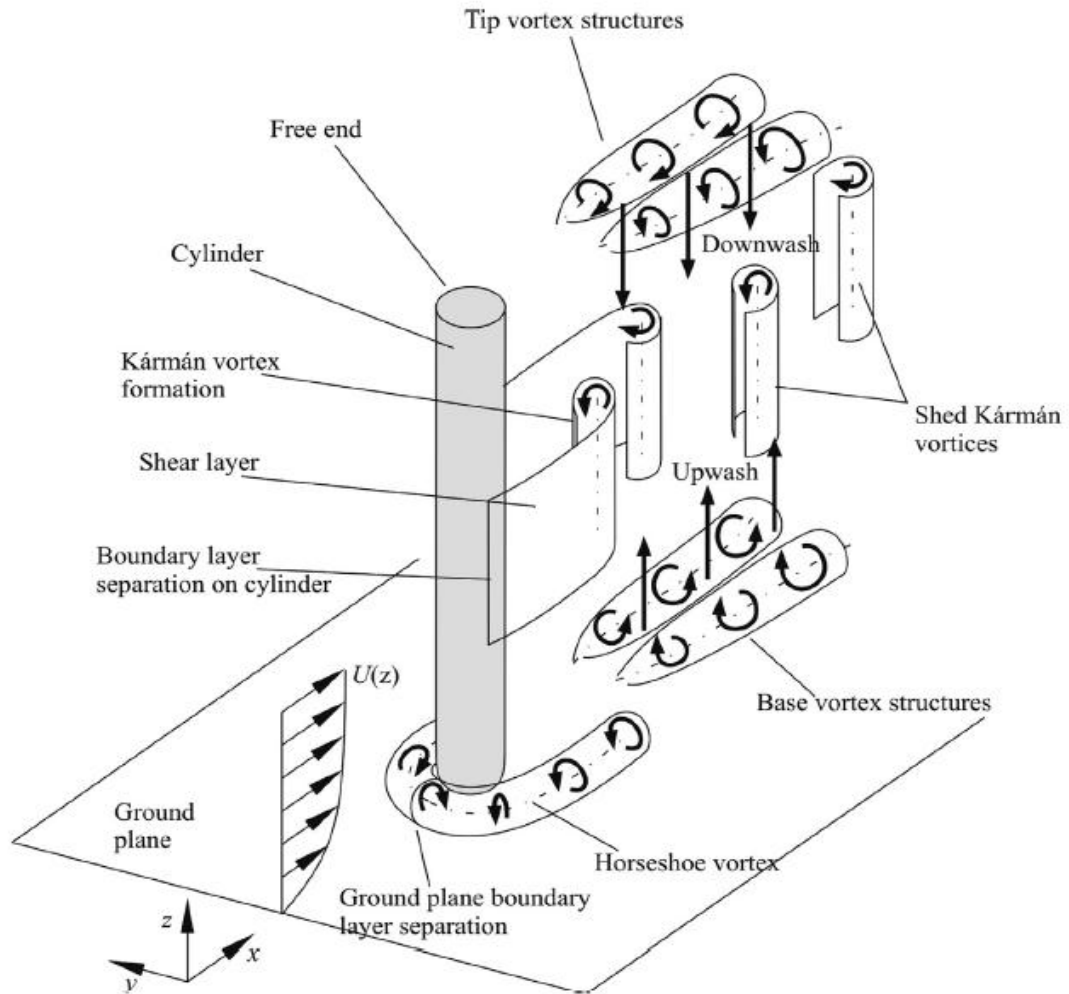


**Figure 3.1: Schematic of flow structures around a circular cantilever (Sumner, 2013).**

Based on the figure, the flow field around a finite circular cylinder is composed of different vortical structures. Apart from the regular Kármán vortices that are shed from the sides of the cylinder along its span, a pair of tip vortices is formed at the free end of the cylinder. In addition, a horseshoe vortex is generated at the root of the cylinder – the cylinder-wall junction, where the boundary layer is rolled up due to the presence of the cylinder. It is worth mentioning that the existence of these vortical structures is less interesting without interacting with each other. In fact, it is the interaction of these vortical structures that gives rise to the complex three-dimensionality of the flow field.

There is a second theory, as discussed in Heseltine (2003), describes a different wake structure pattern behind a cantilever. Instead of having a distinctive vortex structure as shown in Figure 3.1, the trailing vortex (the tip vortex labelled in Figure 3.1) is said to be not existing. Besides, the formation and shedding of the Kármán vortex at the free end is suggested to be delayed,



whereas the region far away from the free end exhibit an ordinary formation and shedding process. It is worth to note that, in this theory, the delayed Kármán vortex (formed at the free end) is connected to the Kármán vortex at the lower span. This causes the vortex filament or vortex tube to incline while the Kármán vortex at the free end is still attaching to the free end, as illustrated in Figure 3.2. The existence of this inclined vortex is later confirmed by Johnston *et al.* (1998) through conducting flow visualisation experiments. Since a vortex tube cannot end itself within a fluid, the vortex must attach to a boundary or fluid surface. In this case, the inclined end of the vortex tube must attach with the cylinder's surface while the other end attaches to the ground plane (Okamoto & Yagita, 1973).

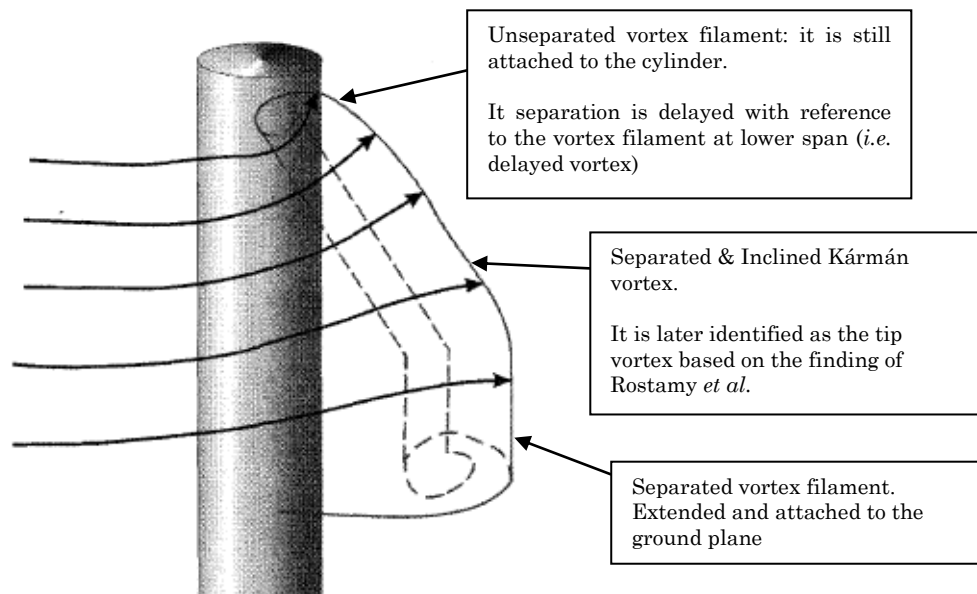


**Figure 3.2: The inclined vortex tube model (Heseltine, 2003).**

It was later found that, by Rostamy *et al.* (2012), the turbulence intensity and Reynolds stresses around the free end is greater than another region. Hence, it further differentiates the inclined vortex from an ordinary Kármán vortex. By considering, jointly, the finding of Rostamy *et al.* and the wake structure that is illustrated in Figure 3.2, it suggests that the inclined part of the vortex tube is actually a tip vortex that is connected to the Kármán vortex, due to the law of nature that a vortex tube cannot end in a fluid, generated from the side of the cantilever.

These theories were still in debate, at the time Heseltine constructed his thesis, due to the lack of visualisation techniques and instruments. However,

Heseltine (2003) was able to identify that the wake structure in his study exhibited the form described by the second theory, purely through constructing the 2-dimensional vorticity contour at the downstream. Fortunately, owing to the availability of better instrumentations and the development in computational fluid dynamics, the second theory has been confirmed by many other studies, which are summarised in Table 3.1.

**Table 3.1: The type of wake visualisation method(s) that confirm the validity of the second theory.**

Author(s)	Visualisation Method	Remarks
Afgan <i>et al.</i> (2007)	Vorticity iso-surface	The vortical structure resembles the form described by the second theory, even though different visualisation method was used.
Palau-Salvador <i>et al.</i> (2010)	1) Iso-surface of minimum pressure 2) 3D stream traces	
Krajnović (2011)	1) Visualising vortex core 2) Q-criterion iso-surface – a type of mathematical scheme that defines a vortex	

However, with the exception of Krajnović (2011), the methods used by Afgan *et al.* (2007) and Palau-Salvador *et al.* (2010) to visualise the wake structure are immature on identifying vortical structure. These methods, as highlighted by Jeong and Hussein (1995), are of intuitive definition and it may not be able to represent the vortical structure thoroughly. Therefore, this research also hopes to provide further insight regarding the wake structure by visualising the wake structure through the mathematical scheme developed by Jeong and Hussein – the Lambda2 criterion (the mathematical definition of this criterion will be discussed in Chapter 5).

Apart from these vortical structures, there are some other interesting flow features that can be observed in the flow field around a finite cylinder. Firstly, an upwash can be observed at the near upstream from the cantilever's free end, as illustrated in Figure 3.3. Interestingly, the flow field at the immediate downstream of the free end responds with a downwash, which is also shown in Figure 3.3. These flow features have been constantly observed in most studies, including Park and Lee (2000). Furthermore, it is well-agreed that the downwash occurs due to the presence of a low-pressure region behind the

cantilever. The occurrence of the upwash, on the other hand, receives little attention and a well-acceptable cause is not available. It is speculated that its formation is due the fact that the fluid has a third possible path to flow, besides going around the cantilever's side surfaces, which is to flow over the cantilever from the above (its free end).

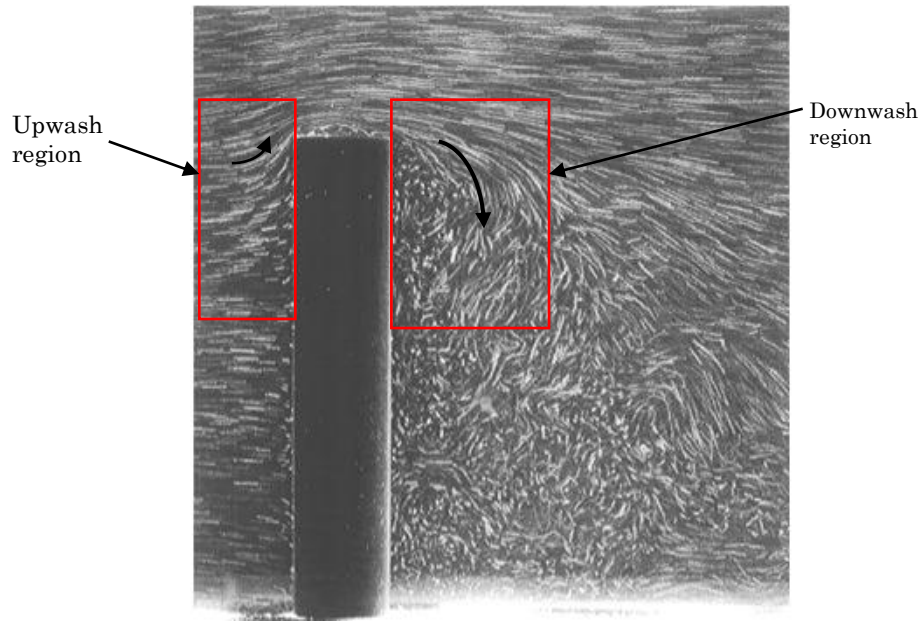


**Figure 3.3: An instantaneous velocity field that demonstrates the upwash and downwash region near the free end of a cantilever (Park & Lee, 2000).**

In this section, the vortical structures and the flow features around a finite cylinder are presented. Moreover, it is worth noting that these vortical structures and flow features with differing magnitude and strength are present in the flow field around a flat plate cantilever as well.

The following review focuses only on studies that investigated on a flow, or precisely, a uniform flow past a cantilever mounted on a flat surface with its free-end exposes to the flow. Since the major difference between the “infinite” cylinder and the cantilever is the exposure and involvement of the free end in the flow behaviour, the free end effects will be the reviewed primarily the following section.

### 3.1.2 Drag Reduction on Cantilever

First of all, the drag experienced by the cantilever is usually lesser than that of an “infinite” circular cylinder. Several studies have been conducted to identify the cause of the reduction. Kawamura *et al.* (1984) investigated this

problem and found that the reduction of drag coefficient is due to the decreasing separation velocity at the side wall compared to a 2-dimensional cylinder case. The reduction of separation velocity can lead to a delayed separation, which allows the pressure to recover. Luo *et al.* (1996) stated that the free end flow can delay the flow separation along the span of the cylinder, which leads to a less negative wake pressure. The conclusion made by Luo *et al.* has agreed well with the insight provided by the results of Kawamura *et al.* In contrast, Afgan *et al.* (2007) argued that such less negative wake pressure is due a strong pressure recovery brought by the downwash presents at the immediate downstream of the free end. Similar pressure recovery mechanism was identified by Liu *et al.* (2005) and Okamoto and Yagita (1973) via examining the local pressure distribution.

In short, according to the reviewed studies, the reduction of drag experienced by a cantilever, compared to an “infinite” cylinder, is caused by the pressure recovery brought by the downwash (or free end flow) from the free end. Therefore, the drag reduction can be considered as one of the free end (or tip) effects.

### 3.1.3 Vortex Shedding

Apart from the decreasing of the local and overall drag, the free end flow also plays a role in interfering the vortex shedding behaviour in the neighbourhood of the free end.

Palau-Salvador *et al.* (2010) observed, through numerical visualisation, that the vortex shedding becomes irregular and somehow suppressed at a certain distance away from the free-end. Similar findings were obtained by Okamoto and Yagita (1973) through experiment. But instead of using flow visualisation technique, they measured the vortex shedding frequency at the immediate downstream of the free end. According to their result, no peak was present in the power spectra plot, which denotes no vortex shedding frequency was captured during the measurement. Hence, they concluded that there was no vortex shedding within two diameters from the free end. Meanwhile, they measured an intermittent vortex shedding was present in between 2 diameters and 4 diameters region. Ayoub and Karamcheti (1982) observed a similar result at high Re flow (high subcritical to supercritical Re) as they detected an intermittent vortex shedding frequency near the free end.

Likewise, Lee and Wang (1987) observed a similar behaviour as they found no dominant frequency (or peak) within  $3.5D$  of a cantilever with an aspect ratio (AR) less than 7. They further concluded that the vortex shedding was suppressed in the measured region. Furthermore, vortex shedding was detected with a consistent frequency (*i.e.*  $St=0.14$ ) at a distance beyond  $3.5D$  from the free end, which indicated that the vortex shedding had retained a normal form at a spanwise location beyond  $3.5D$  from the free end.

Park and Lee (2000) had done the measurement in the wake of circular cantilevers with  $AR=6, 10$  and  $13$  at  $Re=2\times 10^4$ . They reported a weakening vortex shedding frequency when the free end is approached. This result agrees well with the previous literature and it strongly suggests that the regular vortex shedding is weakened and ultimately suppressed as approaching the free end.

However, the cause of the suppression of vortex formation at the free end was not identified. The suppression may be due to the interference originated from the vortical structure formed at the free end – the tip vortex, where it interrupts the roll-up process of regular Kármán vortex (Kawamura *et al.*, 1984; Luo *et al.*, 2005; Lee & Wang, 1987; Farivar, 1981). In this case, the downwash is supporting the suppression by transporting the tip vortex towards lower span region. As a result, the regular Kármán vortex is suppressed within  $3\sim 4D$  from the free end, as observed in the reviewed literature.

Additionally, it is important to note that the vortex is still forming at the suppression zone based on the proposed wake structure shown in Figure 3.2. If so, an important question will be “*why no vortex shedding frequency can be detected in those experiments?*”. Since the wake structure will be visualised in the current study, it is hoped that a clue can be obtained to answer the question.

#### 3.1.4 Span of Free End Effect and Critical Aspect Ratio

Despite the influential effects of the free end’s flow, it does not govern the whole flow field of a finite cylinder; in other words, it has a span limit.

Okamoto and Yagita (1973) had experimentally investigated, particularly, on a  $Re=1.3\times 10^4$  uniform flow pass finite circular cylinders with aspect ratios (AR) ranging from 1 to 15. They observed that the effect of the free end on the near wake structure is limited up to 3 diameters from the free-end via analysing the velocity profile at the downstream of the cantilever. They identified the location where the velocity profile has zero gradients as the end of free end effect.

A similar observation was obtained both numerically and experimentally by Afgan *et al.* (2007) and Heseltine (2003) respectively.

In addition, by studying the rear pressure coefficient, Kawamura *et al.* (1984) reported that the effect of free-end is limited up to 4 diameters away from the free-end. The span of free end effect is summarised in Table 3.2.

However, it can be seen that the findings are not consistent with a span of free end effect (although the values were quite close) ranging from  $2.5D$  to  $4D$ . Apart from different flow conditions were concerned, this may be due to the fact that different methods have been used in their studies to interpret the data. This also shows that a well-established method of identifying the span of free end effect is required.

In addition, in some occasions, the free end flow can overtake the whole flow field behind a finite cylinder. It is referring to the flow field that is mainly consisting of the free end flow (when the free end flow is spatially dominant). It normally happens when the cylinder has a low aspect ratio. Many studies (Okamoto & Yagita, 1973; Adaramola *et al.*, 2006; Sakamoto & Arie, 1983; Sumner *et al.*, 2004) reported the existence of critical aspect ratio, in which the flow field possess a completely different and distinct character when the cylinder's AR is lower than the critical value. Kawamura *et al.* (1984) found that no regular vortex shedding was present when the AR is dropped below the critical AR, which in their case was  $AR=4$ . They attributed this behaviour to the extension of free end effect up till the root of the cylinder. In other words, the free end flow is covering the whole span of the cylinder. Okamoto and Sunabashiri (1992) addressed a similar critical AR ( $AR=4$ ), as they observed a change in flow pattern when the AR is greater than 4. Apart from that, Adaramola *et al.* (2006) and Heseltine (2003) observed a slightly different critical value that is  $AR=3\sim 5$  and  $AR=2.5\sim 3$ , respectively. Nevertheless, Okamoto and Yagita (1973) drawn a completely different conclusion where they marked  $AR=6$  as the critical AR as they observed a change in pressure coefficient when the cylinder's AR is less than 6. Their vortex shedding measurements also agree with this conclusion as no regular vortex shedding was observed behind the cylinder with AR less than 6.

Sumner (2013) addressed the fact that the critical AR is differing significantly in numerous studies is caused by the influences from the Re, AR of the cylinder, the approaching velocity profile and the boundary layer thickness.

Sumner argued that the critical AR is ranged from 1 to 7 depending on the condition of the experiment and it is, in particular, sensitive to the boundary layer thickness of approaching flow. According to Liu *et al.* (2005), when the AR of the cylinder is greater than the critical AR, a 2-dimensional region exists. However, this region decreases in size if the Re increases, which has indirectly highlighted the influence of Re on altering the value of critical AR.

The critical AR is summarised in Table 3.2. Kawamura *et al.* (1984) had directly shown that the critical AR increases as the boundary layer thickness increases. In light of these observations, it is not hard to notice that the increment of the critical AR with the increasing Re and boundary layer thickness is due to the increasing span of the free end effects. At higher Re and boundary layer thickness, the critical AR increases because a larger AR is needed to sustain the 2-dimensional region. To put it differently, the flow behind a finite cylinder with AR lower than the critical value simply means that the 2-dimensional region is suppressed by the overwhelming and spatially dominating free end effects.

**Table 3.2: The summary of the span of free end effect and the critical AR.**

Author(s)	Methodology	Condition	Span of free end effect	Critical AR
Okamoto and Yagita (1973)	Experimental (hot-wire anemometer)	$Re=1.33 \times 10^4$ ; $AR=5 \sim 15$	3~4D from free-end	$AR=6$
Sakamoto and Arie (1983)	Experimental (hot-wire anemometer)	$Re=4128 \sim 7332$ ; $AR=1 \sim 8$	N/A	$AR=2.5$
Kawamura <i>et al.</i> (1984)	Experimental (hot-wire anemometer)	$Re=3.2 \times 10^4$ ; $AR=5 \sim 15$	4D from free-end	$AR=4$
Okamoto and Sunabashiri (1992)	Experimental (surface embedded pressure holes/probes; hot-wire anemometer)	$Re=2.5 \times 10^4 \sim 4.7 \times 10^4$ ; $AR=0.5 \sim 23.75$	$AR=4$	$AR=4$
Heseltine (2003)	Experimental (7-holes pressure probe measurement)	$Re=6 \times 10^4$ , $AR=3 \sim 9$	2.5~3D from free-end	$AR=2.5 \sim 3$
Adaramola <i>et al.</i> (2006)	Experimental (Hot-wire measurement in wind-tunnel)	$Re=6 \times 10^4$ ; $AR=3 \sim 9$	N/A	$AR=3 \sim 5$
Afgan <i>et al.</i> (2007)	Numerical (LES model)	$Re=2 \times 10^4$ ; $AR=6 \& 10$	3D from free-end	N/A
Rostamy <i>et al.</i> (2012)	Experimental (PIV velocity field measurement)	$Re=4.2 \times 10^4$ ; $AR=3 \sim 9$	3D from free-end	$AR=3 \sim 5$



## 3.2 Flow Past an Oscillating Object

Due to the lack of literature that resembles the condition of the current work, the studies of the elastically mounted cylinder with VIV are also reviewed in this section. Besides, since the current work attempts to study the flow dynamics around an oscillating FVG (oscillation caused by VIV), this review focuses on the flow dynamics aspect of VIV, which includes the flow field, the wake structure and the turbulence behind a vibrating object. In other words, the structural dynamics will not be considered in this review.

### 3.2.1 Wake Structure behind an Oscillating Object

One of the earliest experiments on studying the relationship between the vortex shedding and the displacement of a self-excited cylinder (in  $Re$  ranging from 2500 to 7000) was conducted by Angrilli *et al.* (1972) by tracing the location of the (centre of) vortex. The vortex trajectories are as shown in Figure 3.4. They concluded that: (1) the vortex trails of a cylinder with small oscillation (Figure 3.4a) does not show a significant difference compared to those produced by a stationary cylinder; (2) for large oscillation, the vortex trajectories must cross each other to establish a stable wake. Besides, it is also noticed that P+S mode vortices were present at far downstream (refer to the dashed boxes in the figure), but it is not addressed in their work.

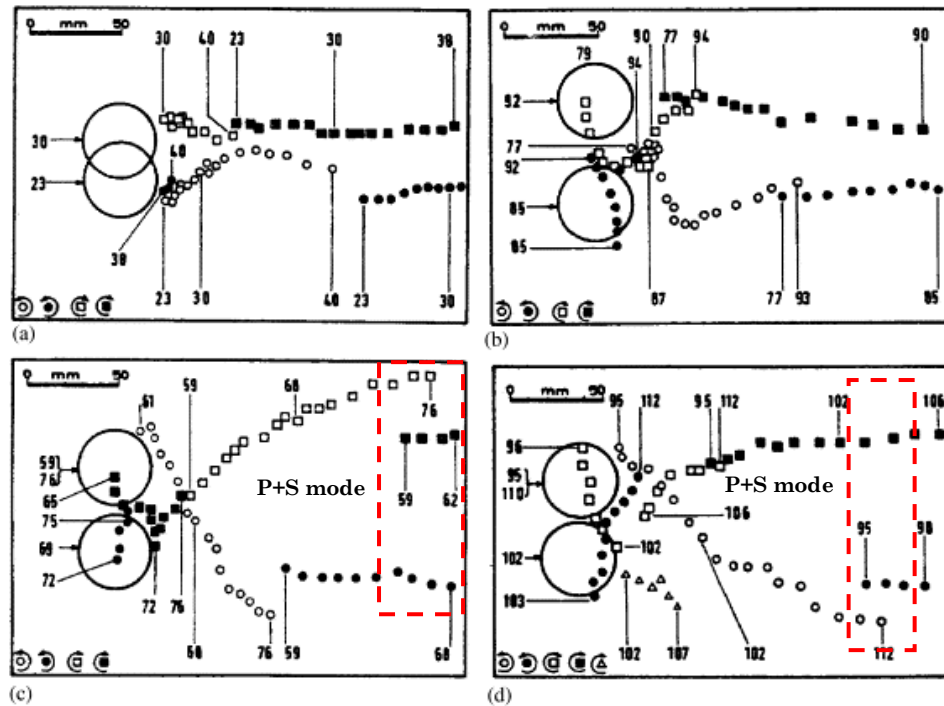


**Figure 3.4: The vortex trajectories behind the oscillating cylinder in various amplitude. (a) Small amplitude oscillation; (b-c) large amplitude oscillation; (d) unstable configuration (Angrilli *et al.*, 1972).**

The existence of P+S mode vortex pattern was later confirmed by William and Roshko (1988) where a wide spectre of vortex pattern was mapped based on the relationship between the oscillation amplitude and the frequency ratio as well as the reduced (or normalised) velocity, as shown in Figure 3.5 (it is, hereafter, referred as the W-R's map). The W-R's map shows that when the cylinder is oscillating in high amplitude, the wake is probably comprising a P+S vortex pattern (it is depending on the reduced velocity as well), which agrees well with the observation of Angrilli *et al.* (1972).

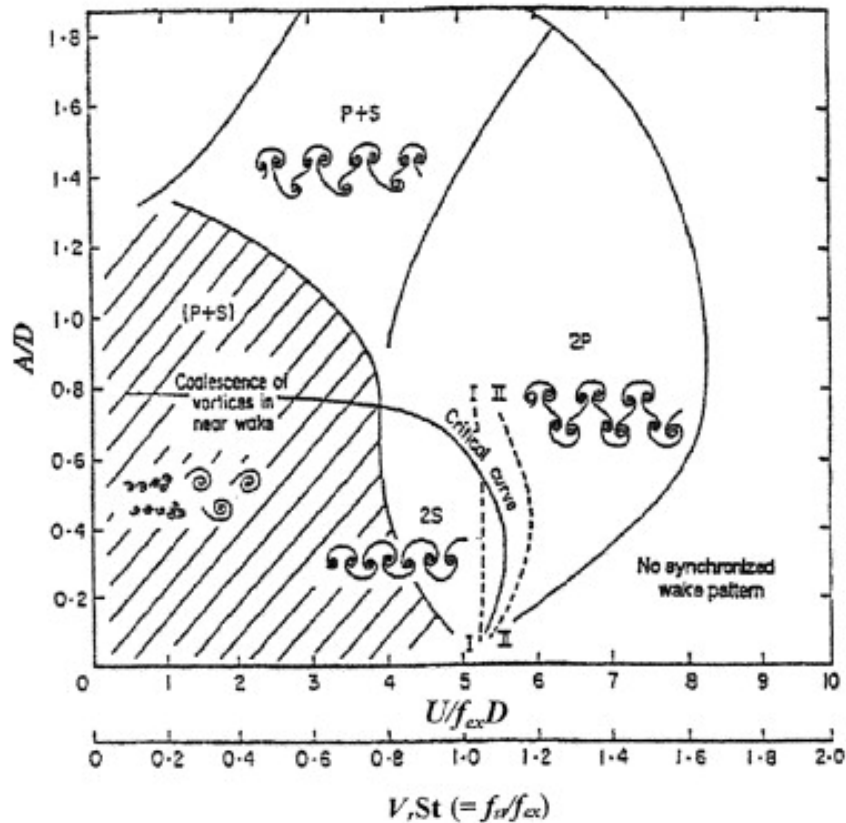


**Figure 3.5: Map of vortex pattern at different amplitude responses ( $A/D$ ) and reduced velocity ( $U/f_{ex} D$ ) – the W-R's map (William & Roshko, 1988).**

Lam *et al.* (2010) conducted an experimental study on the mechanism of vortex formation and its pattern behind an oscillating cylinder in a slow uniform flow. The flow field was measured using Particle Image Velocimetry (PIV) method. Based on their experiments, they concluded that: (1) the 2S vortex was formed at relatively smaller amplitude ( $A/D < 0.5$ ) and it was convected in the wake at locations close to the wake centerline; (2) the 2P vortex pattern was formed at higher amplitude ( $A/D \approx 1.5$ ); (3) P+S occurred at a high amplitude ( $A/D \approx 1.5$ ) as well, but in contrast to the 2P formation, the reduced velocity has to be low. A very similar result was obtained by Govardhan and Williamson (2001) using Digital Particle Image Velocimetry (DPIV). The findings agree well with the W-R's map, which has shown a great consistency in the understanding of vortex pattern behind an oscillating cylinder. In addition, the reliability of the map is also boosted since one of the most reliable flow measurement techniques – PIV/DPIV was used.

The previous literature review focuses mainly on an elastically mounted rigid circular cylinder, where the oscillation response is uniform along its length. Those cases are considered as 2-dimensional. In the present work, the 3-

dimensional flow field behind an oscillating cantilever (the FVG) will be studied; thus, it is expected that the information gained from the previous review may not be sufficient to represent the present research. Unfortunately, the study of a three degree-of-freedom VIV problem, not to mention flow past an oscillating cantilever, is rare; there are countable amount of paper discussed in these cases.

Fujarra *et al.* (2001) studied the flow past a circular cantilever, made of elastomeric material, embedded with a thin flexible aluminium plate in its core to confine the motion in the transverse direction. They reported that a vortex-induced vibrating cantilever exhibits similar response modes as found for the elastically mounted rigid cylinder that is discussed above. Although the motion of the flexible cantilever was limited into transverse direction, the study has established a connection between the responses of the elastically mounted rigid cylinder and the oscillating cantilever. Regrettably, the flow dynamics around the flexible cylinder is not considered in their study.

Inspired by Fujarra *et al.*, Yamamoto *et al.* (2004) furthered the study by numerically modelled a flow past a flexible cantilever and investigated the wake of the cantilever via numerical wake visualisation. In their study, two cases were investigated, each with a different reduced velocity. They observed that the vortex pattern exhibited a 2S mode near the cylinder-wall junction; and a 2P mode near the free end. They regarded this as a hybrid mode as two vortex patterns existed simultaneously. Since there were two vortex patterns along the cantilever's span, a transition point (the point where the 2P mode was converted into the 2S mode or *vice-versa*) must exist. They further found that the location of this transition point is dependent on the reduced velocity. When the reduced velocity is increased, the transition point shifted towards the cylinder-wall junction. The vortex pattern and the relationship between the transition point and the reduced velocity are summarised in Figure 3.6. Although the relationship of vortex pattern transition and the reduced velocity was discussed, the reason(s) behind the formation of a different vortex pattern along the cantilever's span was not addressed.

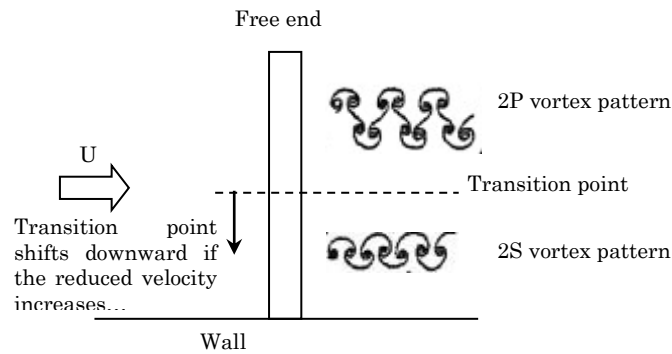


**Figure 3.6: Vortex pattern along a cantilever.**

Based on the previous review, it is known that the vortex pattern is a function of the amplitude response. Since Fujarra *et al.* has confirmed that flexible cantilever exhibits similar responses with the reviewed elastically mounted rigid cylinder, the reviewed W-R's map shall be used to evaluate the vortex pattern behind a flexible cantilever.

First of all, it is clear that the local displacement/amplitude along the cantilever's span is always different; the greatest displacement happened at the free end and no displacement occurred at the base (the cylinder-wall junction). By relating this fact with the W-R's map, there is no surprise that the vortex near the free end exhibits a 2P mode and a 2S mode at the region near the base as it has a small amplitude. Figure 3.7 is presented to aid on this statement. As demonstrated in the figure, the near free end region belongs to the 2P regime and the near-junction region belongs to the 2S regime. Besides, the figure also illustrates and explains the shifting of transition point when reduced velocity is changed. As the reduced velocity increases, the location that exhibited a 2S vortex pattern surpasses the critical curve and entered the 2P regime. At the same time, the transition point also shifts towards the base of the cantilever as it follows the critical curve. As a result, the region that generates 2P vortices expanded as observed by Yamamoto *et al.* (2004).

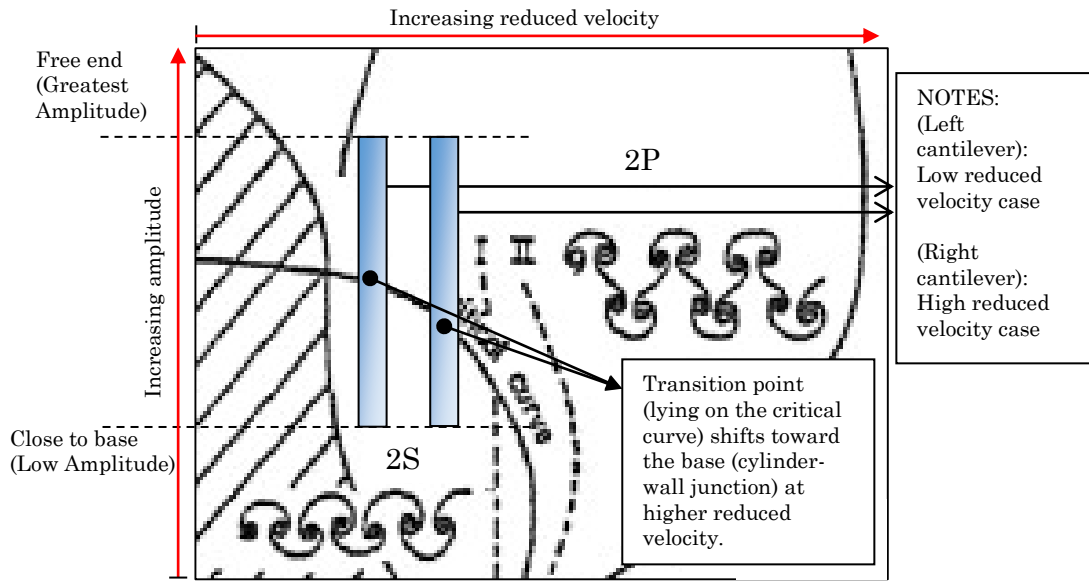


**Figure 3.7: Vortex pattern behaviour of an oscillating cantilever. Modified from Figure 3.5. (Check the unmodified figure for the covered details).**

Techet *et al.* (1998) conducted experiments to study the flow behind an oscillating tapered cylinder. Firstly, they observed the existence of 2S-2P hybrid vortex pattern behind the cylinder via visualisation, which shows a certain degree of similarity with the observation obtained by Yamamoto *et al.* (2004). In addition, they plotted the amplitude and the respective reduced velocity on the W-R's map and showed a great agreement in their results with the W-R's framework. Lastly, based on the visualised flow field, they suggested a vortex connection topology that describes their findings (see Figure 3.8).

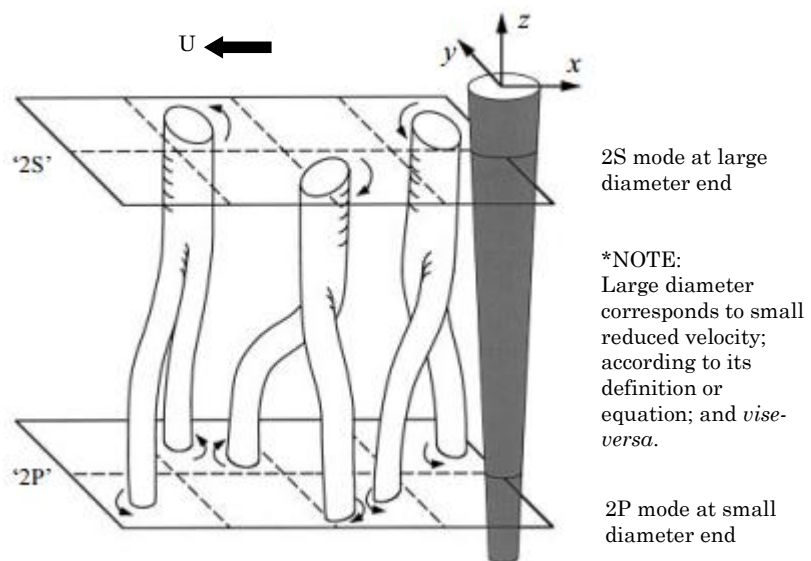


**Figure 3.8: A sketch of the hybrid (2P+2S) vortex pattern behind an oscillating tapered cylinder (Techet *et al.*, 1998).**

Based on the evaluation, the vortex pattern behind a flexible cantilever is well-explained by the vortex pattern map originated from William and Roshko (1988). Therefore, it suggests that the current understanding of vortex pattern formed behind an elastically mounted rigid cylinder can be applied directly to the case with a flexible cantilever where the evaluation has to be based on the local displacement amplitude of the cantilever. However, it is important to mention that the visualisation methods used in the reviewed literature are mainly on displaying the flow field or vorticity contour. If other visualisation methods (such as the  $\Lambda^2$  criterion used in the present study) are used, the interpretation of the vortex pattern might be different, though it is expected that the vortex structure will resemble a pattern similar to the one sketched in Figure 3.8.

Lastly, it is important to note that the understanding of the vortex structure behind an oscillating cylinder is based on the studies at low  $Re$ . Bearman (2011) has published one of the most recent review papers regarding VIV and the author urged to conduct further study on VIV at higher  $Re$  (especially at high subcritical values) since many practical applications are operating in this regime. Besides, the study on three-dimensional and three degree-of-freedom VIV are also lacking.

### 3.2.2 Velocity Field and Turbulence Characteristic behind an Oscillating Object

Unlike the wake structure behind the oscillating cylinder, which is sufficiently established (although the number of literature is limited, but consistent observations are constantly obtained), the velocity field around an oscillation cylinder has received an unsatisfactory attention from the researchers; not to mention the lacking study on the turbulence characteristic behind the oscillating cylinder that is usually based on the velocity field. Govardhan and Williamson (2001) stated that the only paper that had studied on the wake velocity, at the time their paper was written, is the work of Griffin (1971). This marks an approximately 30-years gap between both publications and, according to them, there is no other relevant work published in between. This has strongly shown the ignorance from the researchers on the topic. However, the lack of interest in the topic is justifiable since the concern of VIV was mainly on suppressing the destructive motion in the earlier years.

The earliest study on the velocity field behind a forced oscillating cylinder can be dated back to Griffin (1971). In their experiment, hot-wire anemometer was used to measure the flow with  $Re=120$  and  $350$ . They observed that the velocity fluctuation was generally greater than a stationary cylinder, which signifies a greater turbulence in the wake. Besides, it was identified that the velocity fluctuation is influenced by the frequency and amplitude of the oscillation. The presented results strongly indicate that the involvement of oscillation can improve turbulence production. However, it is worth to highlight that this improvement was achieved by forced oscillation, instead of self-excitation caused by vortex shedding. Therefore, the relation mechanism of the turbulence production phenomena may not be applicable to self-excited oscillation, such as the one that the present work concerns.

Govardhan and Williamson (2001) demonstrated a significant qualitative change in the velocity field of an elastically mounted rigid cylinder (at  $Re=3000-4000$ ) oscillating transverse to a flow. The velocity was measured using Digital Particle Image Velocimetry (DPIV). They observed that the Reynolds Stresses in the wake of the oscillating cylinder have increased for approximately  $100\sim 485\%$  compared to the stationary cylinder values, which strongly evident the improvement of turbulence quality.

In the meantime, when the present work is conducted, there are two papers that are working on a very similar concept with the present study have been published, both are from the same research team. In their study, the performance of the flexible flat plate vortex generators (they named it as the FVG as well) were numerically studied. However, their study is mainly 2-dimensional and the flow is laminar.

Ali *et al.* (2015) had numerically studied a series of tilted winglets (they named it as FVG) that was installed in a channel. They quantified the mixing quality by investigating the transport of a passive scalar and the FVGs managed to achieve  $97\sim 98\%$  enhancement in mixing compared to the rigid case with the exact similar flow condition and configuration. Since the mixing quality is closely related to the turbulence level, their results have indirectly demonstrated that the turbulence level generated from the FVGs is greater than that of the RVGs, although the turbulence characteristics are not evaluated explicitly in their studies.



They furthered their study on the effects of different FVGs configuration in Ali *et al.* (2016). They concluded that the mixing quality can be affected by the FVGs' configuration, including the distance between each subsequent FVG, because the oscillation behaviour is affected by the other FVGs.

However, both Ali *et al.* (2015) and Ali *et al.* (2016) have mainly provided a descriptive discussion on the performance of the FVGs; the physics behind the mixing (turbulence) enhancement is not addressed in detail. Besides, since multiple FVGs were considered in their studies, it is hard to extract the pure physics behind the enhancement because every FVG can interact with the other FVGs (as demonstrated in Ali *et al.* (2016)). Therefore, it is essential to study the turbulence enhancement ability of a single FVG. This allows one to comprehend the underlying physics without external interruptions, and eventually gain sufficient knowledge to control the flow.

To the best of the author's knowledge, there is no other literature, apart from the reviewed literature, has reported the turbulence characteristic behind an oscillating cylinder. Although the study of vortex formation and vortex pattern behind the oscillating cylinder (such as those discussed in the previous section) can somehow justify the turbulence characteristic of the flow, its quantitative measure – the vortex strength (or circulation) – is not discussed in the literature.

### **3.3 Role of Vortex and Vortex Generator on Heat Transfer**

In this section, the role of vortex in heat transfer performance is reviewed. Wang and Zhao (2015) had conducted a test to examine the heat and fluid flow characteristic when a small-diameter circular cylinder is subjected in a flow as a vortex generator. They reported that the existence of the cylinder has improved the heat transfer performance by manipulating the flow structure, mainly by the cylinder wake. This study has clearly shown that the presence of vortex generator, even on a small scale, is sufficient to alter the flow structure and ultimately improve the heat transfer.

Li *et al.* (2015) studied the effects of longitudinal vortex generator (LVG) in the heat exchanger. The heat transfer performance and the pressure drop penalty of such system were investigated. In their study, rectangular and delta winglets were used as the LVGs. From their study, they concluded that by implying LVGs into the system, the heat transfer performance is improved. This

result was observed by studying the Nusselt Number, where the Nusselt Numbers increase up to 20% comparing with the system without LVGs. These improvements were, mainly, due to the generation of secondary vertical structures at the leading edge, trailing edge and the holes. Besides, it was observed that, in general, rectangular winglet was performing better than that of delta winglets. However, the direct correlation between the formed vortices by winglet with different geometries and the heat transfer characteristic, *i.e.* the Nusselt Number are not addressed in their work. Understanding this relationship can be helpful to manipulate the heat transfer performance by controlling the vortex formation.

Khoshvaght-Aliabadi *et al.* (2015) did a similar study on a heat exchanger with vortex generators. In their study, transverse vortex generator was used. Similar to the observations obtained by Li *et al.*, Khoshvaght-Aliabadi *et al.* (2015) concluded that rectangular winglet has the best overall heat transfer performance of about 58.3% and 26.2% when compared to the triangular and trapezoidal winglets, respectively. However, the associated pressure loss is also higher. Moreover, the cause of the difference between the heat transfer performance between the rectangular winglet and the other winglets is not addressed clearly. It is suspected that the difference is caused by the varying vortex strength generated from vortex generator with different shape and geometry.

In the perspective of fluid dynamics, Abdollahi and Shams (2015) stated that vortex generators enhance the heat transfer due to the generation of vortical motions (vortex) and secondary flows at the leading edges of the vortex generator. This vortical motion entrains nearby fluid molecules towards the heat transfer surfaces, thus encouraging the heat transfer process to take place. Similarly, Lotfi *et al.* (2014) addressed that a better heat transfer can be achieved when a large area of a vortex generator is facing the flow that can induce strong streamwise vortices. These statements have strongly suggested the important role of vortex in heat transfer processes, *i.e.* stronger vortex can escalate the heat transfer rate. With reference to the above statement, it is suspected that the vortex generated from the rectangular winglet has greater strength than the triangular and trapezoidal winglets. However, a stronger proof or evidence is needed.

Based on the reviewed literature, it can be seen that those studies reported similar outcomes. Firstly, vortex generator is useful for enhancing heat transfer. Secondly, the results from these studies suggest that the strength of the generated vortex plays an important role in enhancing the heat transfer rate, in which a vortex with greater strength is favourable. This review encourages the present work to evaluate the heat transfer process via the vortex strength, which is uncommon in the available studies. Furthermore, the review provides a strong insight that the FVG can improve the heat transfer performance since the FVG is expected to generate stronger vortices.

### **3.4 Effects of Oscillating Structure on the Heat Transfer Performance**

The following reviews do not cover only the studies on the passively-excited oscillation, the studies on the forced-oscillation are also reviewed to provide further insight on the current study.

Sreenivasan and Ramachandran (1961) had experimentally studied the effect of vibration on heat transfer of a horizontal cylinder normal to air stream. They concluded that the heat transfer coefficient has no appreciable change at a vibrational velocity around 20% of the flow velocity.

Saxena and Laird (1978) had experimentally investigated the transversely-oscillating cylinder in an open water channel. However, in contradict to the conclusion drawn by Sreenivasan and Ramachandran, Saxena and Laird observed the increment of heat transfer to be about 60%. They stated that the amplitude and the frequency have about the same contribution to the increases in local heat transfer coefficient.

Cheng *et al.* (1997) had experimentally investigated heat transfer around a heated forced-oscillating circular cylinder. The nature of this study is not completely the same with the present study (the present study focuses on a passively-oscillating object). However, it should provide some useful insight that allow a better understanding to the topic. Cheng *et al.* found that the heat transfer enhances significantly upon the employment of forced-oscillating cylinder. They also concluded that the enhancement of heat transfer is proportional to the magnitude of oscillating frequency and amplitude of the circular cylinder. Leung *et al.* (1981) and Gau *et al.* (1999) also conducted a

similar study with forced-oscillating cylinder and they have drawn a similar conclusion.

In addition, Gau et al. (1999) attributed the heat transfer enhancement to the instability mode in the wake and shear layer, which is strongly related to the turbulence of the flow. Regrettably, further elaboration about these instabilities in terms of turbulence is not found in their discussion.

Karanth et al. (1994) had numerically studied the flow over a transversely oscillating cylinder. They found that the heat transfer rate of the oscillating cylinder increases with the increasing of velocity.

Fu and Tong (2002) conducted a numerical study on the heat transfer from a heat oscillating cylinder in a cross-flow. Their results show that the heat transfer rate increased significantly as the oscillating frequency approaches the natural vortex shedding frequency. This shows that the greatest heat transfer enhancement is achieved when the cylinder is in lock-in condition (as described in Chapter 2, lock-in refers to a state where large amplitude oscillation mode is attained when the oscillating frequency and the natural shedding frequency is in unity). Moreover, they also concluded that the heat transfer rate is increased when the oscillation velocity and the  $Re$  are increased.

The two papers who have studied on a similar concept with the present work, *i.e.* Ali *et al.* (2015) and Ali *et al.* (2016) that are reviewed in Section 3.2, have evaluated the heat transfer performance of the FVG as well.

In Ali *et al.* (2015), a series of (2D) flexible tilted winglets was used in a system as the vortex generator. The results show that the heat transfer enhancement have increased significantly. The heat transfer was examined by evaluating the local and overall Nusselt Number. The FVG is able to improve the heat transfer up to 97% and 134% for local and overall heat transfer respectively, when comparing to the rigid case. Then, they furthered their study by investigating the effect of different FVG configurations in the system, as presented in Ali *et al.* (2016). They found that different configurations can affect the oscillation behaviour of the FVG and hence, it is affecting the heat transfer performance.

However, they have mainly provided a descriptive and a performance-based discussion in their papers, *i.e.* they only described and compared the performance between the FVG and RVG, the physics behind the observed data are not fully addressed.

Based on the review, most of the studies show a positive likelihood that an oscillating cylinder can enhance the heat transfer rate in a system. However, apart from the works done by Ali *et al.*, most of the reviewed studies were working on rigid structure attached with springs to facilitate motion. Although Ali *et al.* have been working on a flexible structure – a FVG, but their studies are in 2-dimensional and also the bulk flow is laminar (according to the given bulk flow  $Re$ ). In the present study, a 3-dimensional flexible structure will be studied. Besides, the flow around the RVG and FVG in the present work is ensured to be within the subcritical Reynolds range, as described in the Objectives written in Chapter 1, to ensure the wake is turbulent. In light of this, a turbulence model is integrated into the current model, whereas the model used by Ali *et al.* is solving an incompressible laminar flow.

### 3.5 Numerical Approaches and Modelling

A fluid-structure interaction (FSI) problem, such as the VIV problem, is complex, even in an experimental framework. Its numerical strategy is also challenging and varies diversely depending on the computational cost, type of FSI and others. In this section, the numerical approaches and models used in a VIV study are reviewed. The numerical strategy to simulate a VIV problem is mainly by coupling a flow model with a structural model, which solve the fluid motion and structural motion respectively.

Constantinides and Oakley (2006) solved the finite element 3-dimensional Navier-Stokes (NS) and the turbulence was modelled using the Reynolds Average Navier-Stokes (RANS) model. They stated that their model was able to reproduce the strain (displacement) that matches with the experimental data. However, the details of their structural model were not mentioned; the available details only cover the procedure of obtaining the displacement, *i.e.* perform surface forces integral on the cylinder in each time step to determine the motion of the cylinder. The body dynamics were determined by computing the 1 or 2 degree-of-freedom (DoF) differential equation of motion.

Huang *et al.* (2007) used a 2-dimensional RANS code along with  $k-\omega$  (SST) turbulence model to simulate a 2 DoF elastically mounted cylinder. Their results were compared with experimental results for validation.

In the model of Willden and Graham (2001), the incompressible 2-D NS equation was solved. For the structural model, a spring-mass-damper model was used to simulate the 1 DoF transverse vibration of an elastically mounted circular cylinder. Furthermore, the structural model was solved explicitly while the flow model was solved implicitly.

Pan *et al.* (2007) simulated a 2-dimensional VIV problem by solving an unsteady RANS equation through finite volume method. In their flow model, the  $k-\omega$  (SST) model was selected as the turbulence model. The fluid force obtained via solving the mentioned equation was used to determine the motion of the cylinder. The classical equation of motion was used to characterise the structural motion. Their model has successfully reproduced, with a certain degree of similarity, the vortex pattern behind an oscillating cylinder reported by Govardhan and Williamson (2000). They concluded that the model is capable of predicting the vortex mode with a good agreement with the experimental results. Lastly, as described by Pan *et al.*, a similar numerical strategy was attempted by Guilmineau and Queutey (2004). Other studies (including Zhao & Cheng, 2010; Zhao & Cheng, 2011) also employed the  $k-\omega$  (SST) turbulence model to study the VIV of a circular cylinder and they reported satisfactory results were obtained.

Furthermore, the unsteady RANS (URANS) model was used extensively by Prof. Bernitsas's team to numerically study the dynamics of elastically mounted circular cylinder Ding *et al.* (2013). The results serve as an important input for their famous VIVACE project. The model was used along with the Spalart-Allmaras one-equation turbulence model. As for the structural model, a classical spring-mass-damper model was used to describe the cylinder motion. The model was verified with experimental results and a good agreement was demonstrated. In addition, according to the authors, URANS is widely used to simulate flow past cylinder problem and the results obtained from URANS model agree well with other numerical and experimental results.

Despite this, they also extended the application of the model to simulate flow past an elastically mounted cylinder with a roughen surface as the passive turbulence control Ding *et al.* (2015). They claimed that URANS is capable of predicting the flow with a great agreement with the experiments. A similar study was performed by Wu *et al.* (2011). They have also reported the excellent

performance of URANS model, in which the frequency ratio, vortex patterns, transitional behaviours and lifts were well predicted by the model.

Wanderley *et al.* (2008) solved the 2-dimensional RANS to study stationary and VIV of an elastically mounted circular cylinder. K-epsilon turbulence model was used to simulate the turbulence. They claimed that their numerical results agree well with other numerical and experimental results at  $Re < 1000$ .

Catalano *et al.* (2003) performed a simulation on flow past a cylinder at  $Re = 10000$  and  $50000$ , which are relatively greater in many order compared to Wanderley *et al.* (2008). They had tried both LES and RANS models in their study. They reported that the RANS results followed the same tendency, with tolerable accuracy, compared with the LES results while the computational time was much quicker than the LES model.

The 2-dimensional URANS with the  $k-\omega$  (SST) turbulence model were used in the model of Cui *et al.* (2015) as well. However, unlike the literature discussed before, they applied the model on an elastically mounted rectangular/square cylinder instead of a circular cylinder. On the other hand, the structural motion of the cylinder was computed by solving the classical equation of motion, which in this case only accounted for 1 DoF vibration. The equations were solved by the Arbitrary Lagrangian Eulerian (ALE) scheme to avoid excessive mesh distortion. The model was validated with the experimental results of flow past a stationary and a vibrating square/rectangular cylinder with different aspect ratios. The comparison showed a promising agreement.

Other than the RANS (or URANS) model, the work that uses a more reliable turbulence model such as LES shall be reviewed. However, Breuer *et al.* (2012) have reported that the LES model is still not well established in the FSI context up to now. According to Breuer *et al.*, the problem arises from the mesh quality inconsistency occurs in FSI simulation due to the involvement of moving mesh as the demands on the mesh quality are higher for LES than for RANS model. Furthermore, Breuer *et al.* also mentioned that the mesh movement in the ALE formulations that is applied in most FSI simulation causes the filter scale to vary throughout the simulation, resulting in additional commutation errors.

Even though the use of LES model in FSI simulation requires additional care, there are researchers who have minimised the risk and successfully

perform the numerical study through applying specific procedures. Nguyen and Nguyen (2016) used DES approaches to avoid the aforementioned modelling difficulties. In their study, the DES model was used to solve an incompressible NS flow over a moving cylindrical structure. DES formulation allows RANS model to be used at near wall and LES model to resolve the wake dynamics. Their model was validated against several experimental data of fixed cylinder as well as a cylinder with VIV, and the numerical results were in good agreement with the experimental studies, *i.e.* the 1 DoF and 2 DoF studies showed that the model can capture the fundamental VIV characteristics.

Wei (2013) had numerically studied the turbulent flow around a forced moving circular cylinder using LES and DES turbulence models. Their model was validated briefly by comparing the simulated results of a fixed cylinder case with its respective experimental results. Regrettably, no validation on the forced oscillating cylinder case had been done in this study. Hence, the work is unable to justify the reliability of their model on FSI problem.

Feymark *et al.* (2010) used LES approach to study the flow around an (streamwise sinusoidal) oscillating cylinder with a steady approaching flow. They reported that the model was sufficient to provide accurate predictions of the hydrodynamic loads acting on the oscillating cylinder when compared to experimental data.

Feymark *et al.* (2012) then furthered their study using the same model to investigate the hydrodynamics forces on a fixed and an oscillating circular cylinder. Both cases were validated with experimental data, and good agreements with the experimental data were reported by the authors, especially for the case of fixed cylinder. However, the validation of oscillating cylinder case did not cover the flow properties such as the mean flow field, fluctuating flow field and vorticity field due to the lack experimental data; and it was also out of their study's scope that focused on hydrodynamic forces. Therefore, the presented data is unavailable to provide information regarding their LES model's reliability on the mean (shear) flow that is relevant to the present interest. In addition, they also named the huge computational cost of LES model to be its main shortcoming that hinders its usage over the industrial widely adopted URANS model.

Murrin (2007) had developed a model that utilised LES model to simulate VIV on marine risers at high Re. The validation was performed by



comparing the eddy formation length, Strouhal Number and Separation bubble size of a low Re ( $Re=100$ ) fixed circular cylinder with its respective experimental data. Moreover, the velocity field was compared qualitatively as well. Regrettably, no validation has been done on the turbulence flow properties such as the fluctuating velocity components and, most importantly, it does not cover the mean (shear) flow that is relevant to the needs of current work.

In the doctoral dissertation of Yin (2013) who had used LES to model a circular cylinder undergoing VIV. The author reported that the numerical results were generally agreeing well with the experimental results, although some discrepancies were observed as well. Yin argued that these discrepancies can be attributed to the model optimisation, Re dependence, vortex shedding mode transition and the orbit shape of the oscillation. No flow relevant properties were discussed by Yin, except the visualisation of the vorticity field for qualitative representation of vortices.

Apart from solving the classical NS Equation, some of the researchers employed a different model to solve the fluid motion. Meneghini *et al.* (2004) used the Discrete Vortex Method (DVM), a Lagrangian numerical scheme, for simulating two-dimensional incompressible and viscous flow. A finite element model based on the Euler-Bernoulli Beam Theory was coupled with the flow model to simulation the structural motion. The similar structural model was used by Ferrari (1999) as well. The same model was used in Yamamoto *et al.* (2004), which the results have been discussed in the previous section. In addition, Sarpkaya and Shoaff (1979) also used DVM in their study to simulate the flow past a long flexible cylinder. The authors claimed that their model achieved a reasonable success in prediction the dynamics.

In summary, solving the classical NS equations is still the most common approach used in simulation oscillating cylinder, although there are other alternative models such as the DVM. Moreover, the use of different turbulence models, such as LES and URANS models, have been constantly reported. Although LES is expected to outperform other turbulence models, its usage in FSI problem is still limited due modelling difficulties that involve moving mesh; while good results computed from the URANS model are constantly reported. For the structural model, the most common strategy used in the literature is by solving the equation(s) of motion (some papers refer it as the spring-mass-

damper equation(s)). The number of the equation involves in the model depends on the DoF.

### **Summary of chapter**

This chapter covers the literature reviews on similar studies that provide further in-depth insight and understanding towards the current project. Since the cantilever is selected as the rigid and flexible VGs in the current study, the studies on the flow past a cantilever are reviewed. The review focuses on the flow characteristics behind a cantilever are identified and the free end effect.

Next, the most important aspect of the current study – flow past an oscillating object is reviewed. Most of the published works that involved flow dynamics behind an oscillating object discuss the vortex pattern behind the structure. However, the respective influences on the turbulence aspect are not discussed in those papers. Only two papers that discuss the velocity field and turbulence aspects (which are the field-of-interest to the current work) are found. Despite this, these two papers have shown the potential of a submerged oscillating object in turbulence enhancement.

The role of vortex on heat transfer is reviewed as well. Based on the review, it is understood that the vortex plays an important role in heat transfer processes. Many researchers have acknowledged that stronger vortex has improved the heat transfer performance in their study.

Lastly, the numerical strategies and approaches used in the previous researches are reviewed.

# Chapter 4: Numerical Modelling

This chapter consists of two main sections. The first section introduces the governing equations that shape the basis of the modelling used in this work. The presented equations cover both structural and CFD models. Furthermore, the fluid-structure coupling method is also introduced and discussed in the first section.

In the second section, the simulation domain of the present work is presented. The domain adopted the mathematical models discussed in the first section of the chapter. The setup of the model and the mesh will be discussed in this section as well. Besides, the validation of the model's physics is also presented to verify the reliability of the model.

## 4.1 Governing Equations

### 4.1.1 Structural Model

The governing equation for a structure in motion can be described by the equation of motion:

$$m\ddot{x}_i + q\dot{x}_i + kx_i = \sum F_i \quad (4.1)$$

Where  $m$ ,  $q$  and  $k$  are the mass, damping, and stiffness matrices respectively;  $x$ ,  $\dot{x}$ , and  $\ddot{x}$  are the displacement, velocity, and acceleration respectively.  $\sum F_i$  represents the summation of forces such as drag force, buoyant force, structural weight and others in the  $i$ -direction; the equation accounts for the other dimensions, which is represented in the  $j$ - and  $k$ -direction.

### 4.1.2 Fluid Flow Model

Fluid flow can be described analytically by Continuity equation (Equation 4.2) and Navier-Stokes equation (Equation 4.3). In the present work, the flow is assumed to be incompressible, which is a common assumption based on the previous literature review.

The Continuity equation states that the mass is conserved. This equation is also known as the conservation of mass equation.

For Incompressible flow and no external mass input:

$$\frac{\partial u}{\partial x} + \frac{\partial v}{\partial y} + \frac{\partial w}{\partial z} = \frac{\partial u_i}{\partial x_j} = 0 \quad (4.2)$$

Continuity equation always cooperates with the Navier-Stokes (NS) equations in order to compute the velocity tensors in all directions. The NS equations are also known as the conservation of momentum, which is originated from Newton's second law. This describes that the momentum is conserved as long as there is no external force. As mentioned earlier, the fluid is assumed to be incompressible in this work. Thus, the incompressible NS equation is used.

Incompressible Navier-Stokes Equation:

$$\rho \left[ \frac{\partial u_i}{\partial t} + u_j \frac{\partial u_i}{\partial x_j} \right] = - \frac{\partial p}{\partial x_i} + \mu \frac{\partial^2 u_i}{\partial x_j^2} + \rho g_i + S_{m,j} \quad (4.3)$$

where the  $S_{m,i}$  denotes the source terms in the  $i$ -component.

### 4.1.3 Turbulence Model

In CFD simulation, the turbulent models need to be introduced and integrated into the model in order to simulate the effect of turbulence. There are few turbulence models available, which include Reynolds-Averaged Navier-Stokes (RANS) model, Large Eddy Simulation (LES) and Detached Eddy Simulation (DES).

As mentioned in the research aim, the current research focus is to study the mean flow's shear (*i.e.*  $\frac{dU_i}{dx_j}$  that governs the boundary layer, shear layer and the vortex). With reference to this, the unsteady RANS (URANS) coupled with the SST k- $\omega$  model is selected in the present work because the model is known to be able to predict the mean flow well without excessive computational power. Besides, based on the literature review on LES model, the model possesses certain modelling difficulties when it is used in FSI problem. This also encourages URANS model to be selected over LES model. In addition, good results are constantly reported with the use of URANS model as discussed in the Literature Review.

#### 4.1.3.1 Unsteady Reynolds-Averaged Navier-Stokes Equations

RANS model is the most popular among those three models stated previously. The selection of a steady or unsteady RANS equation is crucial. If a steady RANS is used to solve an unsteady problem, such as the one solved in the current work, the result will be inaccurate. Since vortex shedding, which is an

unsteady phenomenon, is involved in the present work, the unsteady RANS (URANS) formulation is selected.

URANS equation is derived from conventional Continuity equation (Equation 4.2) and Navier-Stokes equation (Equation 4.3) by introducing the double decomposition on every instantaneous term, which includes the terms that cover the velocity and pressure components. Equation 4.4 and 4.5 express the double decomposition of instantaneous velocity and pressure, respectively. The term in the capital form is the mean term and the primed term is the fluctuation term.

$$u_i = U_i + u'_i \quad (4.4)$$

$$p = P + p' \quad (4.5)$$

Equation 4.4 and 4.5 are inserted into Equation 4.2 and 4.3 and the mean of the whole equation is taken. An important assumption or concept is applied during the averaging, which is the mean of the fluctuating part is equal to zero. This leads to the following definitions:

$$\overline{u_i} \equiv U_i \text{ and } \overline{u'_i} = 0 \quad (4.6)$$

$$\overline{p} \equiv P \text{ and } \overline{p'} = 0 \quad (4.7)$$

Firstly, the continuity equation (Equation 4.2) is rewritten in the following form:

$$\overline{\frac{\partial(u_i)}{\partial x_i}} = \frac{\partial U_i}{\partial x_i} = 0 \quad (4.8)$$

On the other hand, the URANS equation is rewritten in the form as shown in Equation 4.9. Besides, the mass conservation law ( $\partial U_i / \partial x_i = 0$ ) has been incorporated into the equation as well. Note that for an unsteady RANS, the time derivative term ( $\partial \overline{u_i} / \partial t$ ) has to be included; without this term, the RANS is solving for a steady solution.

$$\rho \left[ \frac{\partial U_i}{\partial t} + U_j \frac{\partial U_i}{\partial x_j} \right] = -\frac{\partial P}{\partial x_i} + \rho g_i + \frac{\partial}{\partial x_j} \left[ \mu \frac{\partial U_i}{\partial x_j} - \rho \overline{u'_i u'_j} \right] + S_{m,i} \quad (4.9)$$

In Equation 4.9, an additional term appears in the equation that describes the turbulence properties. This term is known as the Reynolds Stress ( $\overline{\rho u'_i u'_j}$ ) and it has introduced extra unknown quantities to the equation. Since no additional equations are available, the system described by the URANS equation is not a close system. Therefore, the Reynolds Stress needs to be modelled in order to

close the system. The most common approach is by introducing the eddy viscosity or turbulent viscosity ( $\mu_t$ ). This is known as the eddy viscosity models and it includes the famous k-epsilon and k-omega models.

#### 4.1.3.2 (SST) K-Omega Model ( $k-\omega$ )

Based on the review discussed in Chapter 3, regarding the numerical approaches in simulating the FSI problem, the SST  $k-\omega$  model has been used extensively with an accuracy beyond the acceptable range. In light of its promising ability, the current work will use the model to simulate the turbulence scale in the problem.

The SST  $k-\omega$  model is developed by Menter (1994), which model the turbulent viscosity in order to describe the characteristic of turbulent flow that denotes by the Reynolds stresses in URANS equation. Unlike standard  $k-\omega$  model, the SST  $k-\omega$  model integrates standard  $k-\epsilon$  and standard  $k-\omega$  models by introducing a blending function. The standard  $k-\omega$  resolves the flow in the near wall region while standard  $k-\epsilon$  is used to resolve free-stream turbulence. Furthermore, it has good accuracy in predicting the adverse pressure gradient on a surface, which is crucial in the current work to compute the hydro/aerodynamic forces, boundary layer separation and vortex formation.

SST  $k-\omega$  model is a two-equation eddy-viscosity model that models the kinematic eddy viscosity ( $\nu_t$ ) through the turbulence kinetic energy equation (Equation 4.10) and the specific dissipation rate equation (Equation 4.11).

$$\frac{\partial k}{\partial t} + u_i \frac{\partial k}{\partial x_j} = P_k - \beta^* k \omega + \frac{\partial}{\partial x_j} \left( (\nu + \sigma_k \nu_\tau) \frac{\partial k}{\partial x_j} \right) \quad (4.10)$$

$$\frac{\partial \omega}{\partial t} + u_i \frac{\partial \omega}{\partial x_j} = \alpha S^2 - \beta \omega^2 + \frac{\partial}{\partial x_j} \left( (\nu + \sigma_k \nu_\tau) \frac{\partial \omega}{\partial x_j} \right) + 2(1 - F_1) \sigma_{\omega 2} \frac{1}{\omega} \frac{\partial k}{\partial x_i} \frac{\partial \omega}{\partial x_i} \quad (4.11)$$

#### 4.1.4 Heat Transfer Model

In Chapter 7 of this thesis, the application of the Flexible Vortex Generator is extended to heat transfer process to examine its ability in facilitating heat transfer. Therefore, in order to compute the heat transfer, an additional energy equation is included into the model described earlier, apart from continuity equation and URANS equation, to account for the heat transfer process. For incompressible flow, the energy equation is expressed by the following equation:

$$\frac{\partial E}{\partial t} + u_j \frac{\partial E}{\partial x_j} = \Phi + \frac{1}{\rho} \frac{\partial}{\partial x_j} \left( k \frac{\partial T}{\partial x_j} \right) \quad (4.12)$$

where  $E$  is the internal energy per unit mass,  $\Phi$  is the viscous dissipation function per unit mass, which can be expressed by the following equation:

$$\Phi = \frac{\nu}{2} \left( \frac{\partial u_i}{\partial x_j} + \frac{\partial u_j}{\partial x_i} \right) \left( \frac{\partial u_i}{\partial x_j} + \frac{\partial u_j}{\partial x_i} \right) \quad (4.13)$$

#### 4.1.5 The Coupling – Fluid-Structural Interaction (FSI)

In this study, the fluid flow model is solved by the commercial CFD software – STAR-CCM+; on the other hand, the structural model is solved by a commercial FEA software – Abaqus. STAR-CCM+ solves the fluid flow governing equation via the finite volume method (FVM) while Abaqus uses finite element method on the structural equation to compute its solution. Once the solvers for the fluid flow and structural models have been identified, the remaining issue will be the way to couple both solvers or models to simulate the complex Fluid-Structure Interaction (FSI). In this work, the Abaqus Co-Simulation Engine is used to couple the two models.

There are two types of FSI coupling, namely the one-way and the two-way couplings. One-way coupling is normally used when the fluid dynamics plays little role in the solution. So basically, what is one-way coupling? First of all, it is important to mention that since two solvers are involving in a FSI simulation, the structural and the fluid flow models have to work in a sequence. The starting solver in the simulation is known as the leading solver while the following solver is known as the lagging solver. As demonstrated in Figure 4.1, the coupling is considered as a one-way coupling when the leading solver is the only solver that transfers the computed data to its partnering solver; *i.e.* the data is transferred in one-way. Once the data is transferred to the partner solver, the computed values are assigned to the cells/elements accordingly; this process is known as the mapping process and it is one of the most crucial procedures in FSI simulation. Then, the lagging solver uses the imported data as part of its input and runs. Once the lagging solver finishes the calculation, no data will be transferred to the leading solver.

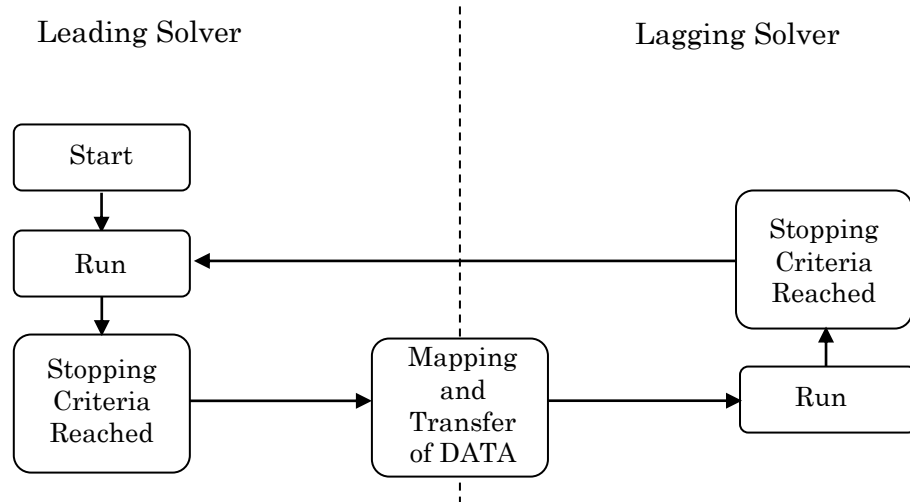


**Figure 4.1: The flowchart of one-way FSI simulation (for a single time step).**

That major difference that distinguishes a two-way coupling from a one-way coupling is the fact that the leading solver is accepting the information from the lagging solver, as shown in Figure 4.2. The two-way coupling can be further categorised into strongly coupled and weakly coupled two-way coupling. A strongly coupled method exchanges information (the data) implicitly; in other words, it exchanges data iteratively. Conversely, a weakly coupled method exchanged data explicitly, *i.e.* data is exchanged only at the end of each calculation (it exchanges only when the iteration has ended).

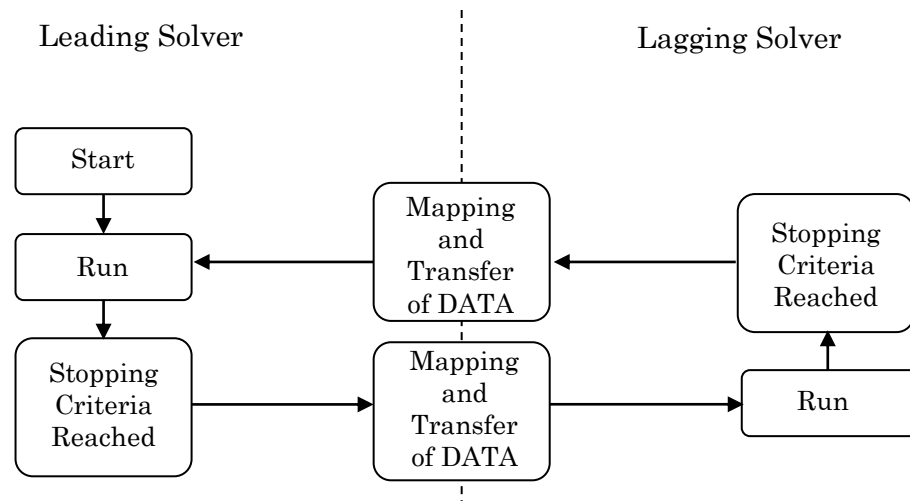


**Figure 4.2: The flowchart of two-way FSI simulation (for a single time step).**

In the present work, a strong two-way coupling method is used. The leading solver is the structural solver – Abaqus. First, it gains the simulation



inputs (pressure and wall shear stress) from the initial boundary condition of the simulating domain and computes the solution for the structural model via solving Equation 4.1. Then, the computed solution – the variables such as the displacement and structural velocity – are exported to the fluid flow model. Mapping is conducted immediately after the exportation of the data. Next, the fluid flow model is solved based on the imported variables from the structural model, plus the other variables that characterise the flow properties. Finally, the essential variables (pressure and wall shear stress) are exported from the fluid flow model to the structural model to complete a simulation routine. The routine is repeated until the solution is converged, then it proceeds to the next time-step. Figure 4.3 is used to illustrate the simulation routine.

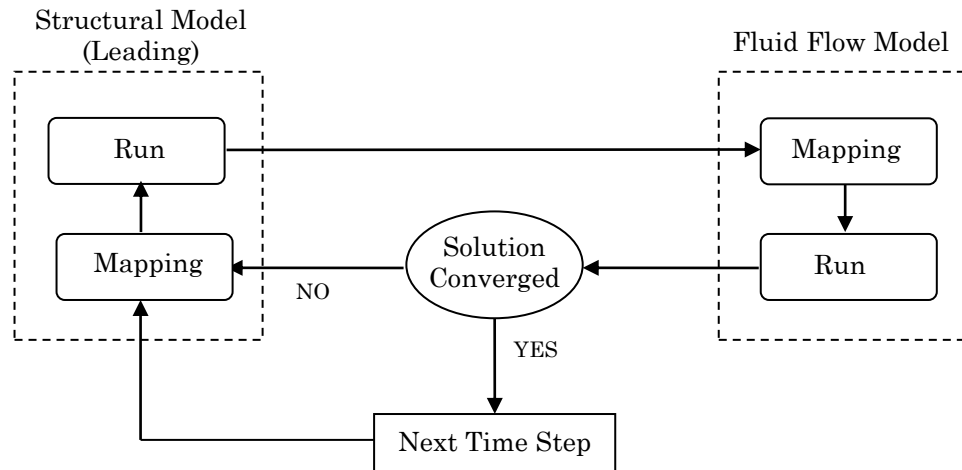


**Figure 4.3: Flowchart of the strongly coupled two-way FSI simulation used in the present study.**

A two-way FSI solution shows several advantages than the one-way coupling method. Firstly, it is more accurate. Besides, it is more suitable in the case when a large deflection is involved and/or the fluid domain is strongly influenced by the structural changes. It is also more stable (Vassen *et al.*, 2011). According to Benra *et al.* (2011), two-way coupling also guarantees the energy conservation at the interface (the boundary that experiences the import and export of the solutions). However, it is computationally more expensive than one-way coupling method.

#### 4.1.5.1 Morphing – The mesh/grid deformation scheme

The last important aspect will be the fluid mesh/grid deformation, which is referred as morphing in this context. It also plays an important role in the

coupling discussed earlier. Since the deformation is involved in the simulation, the mesh configuration of the fluid domain is expected to distort throughout the simulation process to account for the structural deformation.

In the present model, the strategy used for the mesh deformation is via adopting the morphing feature that is available in the Star-CCM+. The morphing process in Star-CCM+ is achieved by solving the URANS equation via the Arbitrary Lagrangian Eulerian (ALE) technique. It allows the deformation of the fluid mesh's vertices in a manner to conform to the solid structure and maintain the quality of the fluid grid within a reasonable border.

## 4.2 Numerical Model

### 4.2.1 Simulation Domain

As presented in Section 4.1.3, the incompressible URANS equations are solved along with the  $k-\omega$  (SST) model in the present study. A schematic diagram of the fluid domain is shown in Figure 4.4.

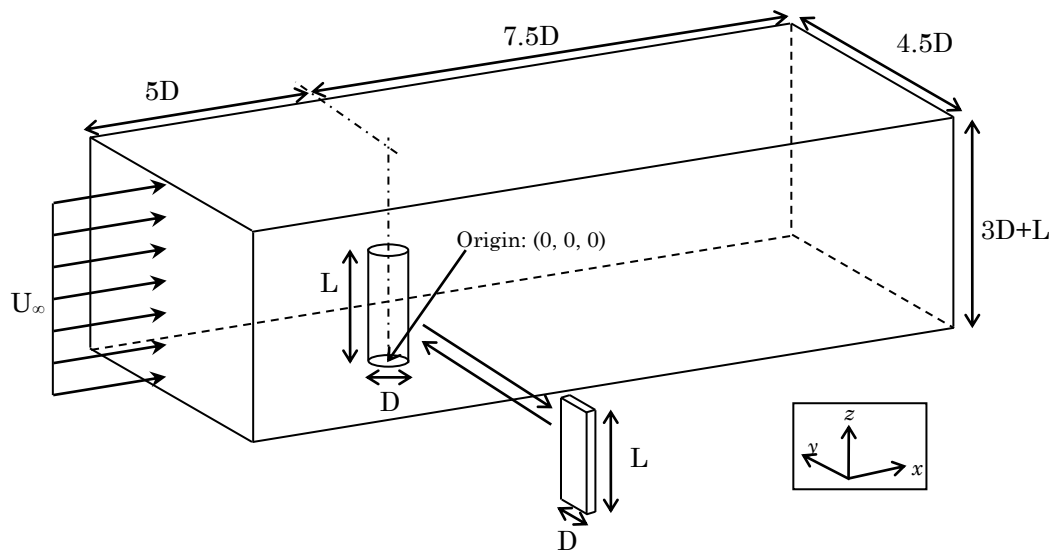


**Figure 4.4: Schematic of the fluid domain (Not to scale).**

In the present work, a cantilever is used as the VG. Therefore, the flow past a cantilever (either circular or flat plate cantilever) is simulated. A uniform flow,  $U_\infty$ , is approaching the cantilever from the inlet. The boundary conditions are tabulated in Table 4.1.

**Table 4.1: List of boundary conditions.**

<b>Surface</b>	<b>Boundary type</b>
Inlet	Velocity Inlet
Outlet	Pressure Outlet
Bottom surface	Non-Slip Wall
Cylinder	Non-Slip Wall; Co-simulation Interface (flexible)
Top surface	Symmetry Plane
Side surfaces	Symmetry Plane

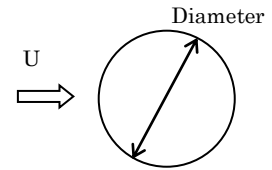
The setup of each case will be introduced in the next section. Before proceeding to the introduction of the simulation setup, it is important to mention that the purpose of considering VG with two different geometries is to extract more information from the phenomena that may be hidden if only one case is considered. Therefore, the results generated from each case will not be compared to each other (result from circular VGs will not be compared quantitatively with the result from flat plate VGs). Besides, the flow condition of both cases does not match with each other. This is because different geometries and materials are used. These induce different loading forces and oscillation response that discourage comparison among different cases. The details of each setup choices will be explained in each sub-section later.

#### *4.2.1.1 Case description: Circular VGs*

The fluid, flow and structural properties in the case that involves circular VGs (both RVG and FVG) are summarised in the following table. Since circular cross-section can induce a large second moment of inertia, water is used in this case to create a greater force (due to its large density) to deform the FVG. Furthermore, in order to facilitate greater deformation, an elastic material – silicon foam – is used as the circular FVG's material. The fluid, flow and structural properties used in the study of circular VGs are summarised in Table 4.2.

**Table 4.2: The fluid, flow and structural properties used in circular R/FVG simulation.**

<b>Fluid Properties</b>	
Fluid	Water
Density	998.2 kg/m <sup>3</sup>
Dynamic viscosity	1.002×10 <sup>-3</sup> Pa·s
<b>Flow Properties</b>	
Reynolds Number	~3500
Inlet Velocity	0.35 m/s
Inlet Turbulence Intensity	0.5%
<b>Structural (VG) Properties</b>	
Cross-sectional geometry	Circular
Diameter	0.01m
Aspect Ratio	6, 8 and 10
Second Moment of Inertia	4.91×10 <sup>-10</sup> m <sup>4</sup>
Material	Silicon Foam
Young's Modulus	486927 Pa
Density	676.78 kg/m <sup>3</sup>
Poisson ratio	0.4

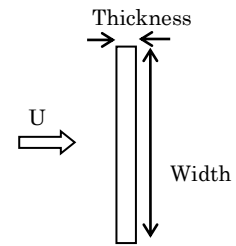


#### 4.2.1.2 Case description: Circular Flat Plate VGs

The fluid, flow and structural properties in the case that involves flat plate VGs (both RVG and FVG) are summarised in Table 4.3. Special care should be taken in simulating flow past a flat plate VG. Based on the results from Lee *et al.* (2012), the flat plate does not undergo oscillation when the flow has high viscosity. Owing to this fact, water is not used in the simulation of flat plate FVG; instead, air will be used. However, since air has low density, the flow velocity has to be increased to allow sufficient force to bend the flat plate FVG. With these considerations, the Reynolds number of the case is increased sufficiently. It is also the considerations that discourage the comparison between circular case and flat plate case because an identical flow behaviour is difficult to achieve without compromising the structural dynamics.

**Table 4.3: The fluid, flow and structural properties used in flat plate R/FVG simulation.**

<b>Fluid Properties</b>	
Fluid	Air @20°C
Density	1.1842 kg/m <sup>3</sup>
Dynamic viscosity	1.855×10 <sup>-5</sup> Pa·s
<b>Flow Properties</b>	
Reynolds Number	~11500
Inlet Velocity	4.5 m/s
Inlet Turbulence Intensity	0.5%
<b>Structural (VG) Properties</b>	
Cross-sectional geometry	Thin Flat Plate
Width	0.04m
Thickness	0.002m
Aspect Ratio	4, 5 and 6
Second Moment of Inertia	2.67 ×10 <sup>-11</sup> m <sup>4</sup>
Material	Teflon
Young's Modulus	5.0×10 <sup>-8</sup> Pa
Density	2200 kg/m <sup>3</sup>
Poisson ratio	0.46



## 4.2.2 Mesh

### 4.2.2.1 Fluid Domain

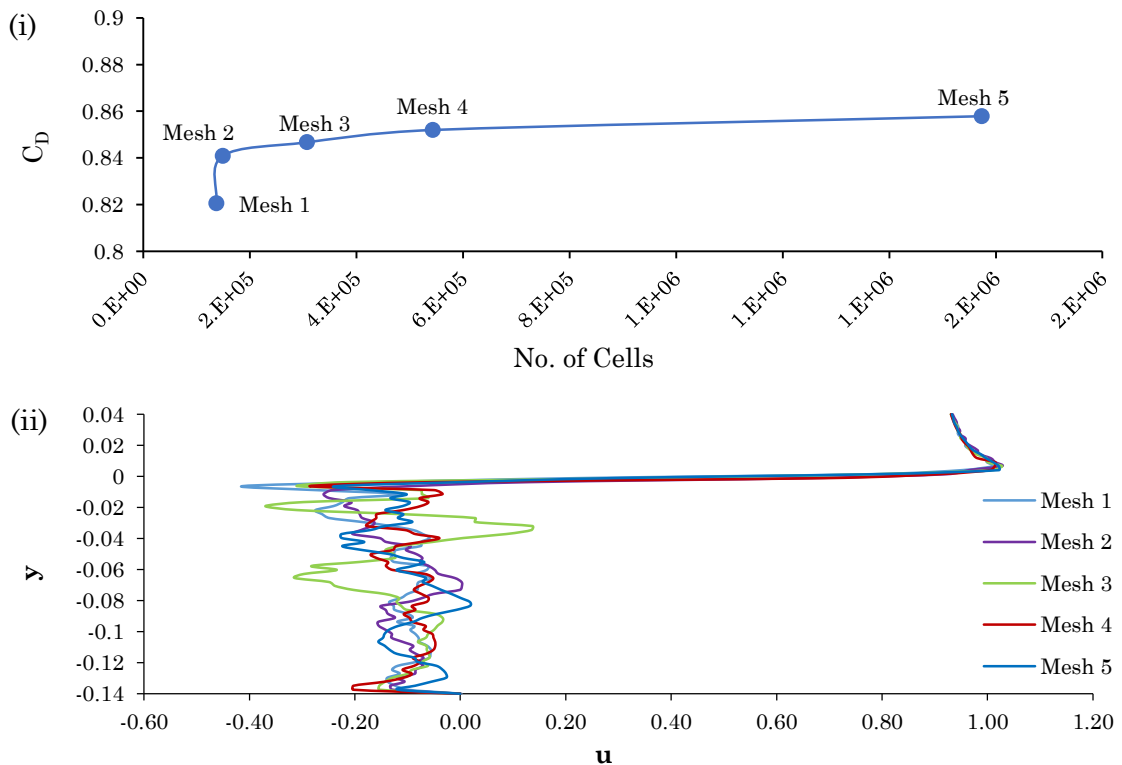
Before performing the actual numerical validations, the mesh independence was checked. Ideally, the accuracy of simulation increases with a smaller mesh. However, the increase in accuracy becomes negligible when the mesh exceeds a certain density. On the other hand, the computational time increases significantly when the mesh size decreases, due to the significant increase in the calculation loads. Therefore, typical CFD's procedures included mesh independency studies to obtain a threshold mesh size, where further refinement will have minimal effects on the results. The purpose is to obtain the optimum mesh size with the optimum accuracy to simulate the case.

Six different meshes with various mesh size, as shown in Table 4.4, were used in this study. Furthermore, the mesh size is identified with relative to the characteristic length scale, in this case, it is the diameter of the cantilever. This identification method allows the mesh size to be universally identified (*i.e.* the outcome of the mesh independence study will always be applicable for a similar configuration, even if the diameter is different). The mesh around the cylinder is refined, and a slow growth rate is allowed beyond the refined zone. Lastly, an unstructured polyhedral mesh is used in this study.

**Table 4.4: Summary of meshes and its respective information.**

Mesh No.	Targeted Max. Mesh Size	Targeted Min. Mesh Size	Cylinder's Surface Mesh	Number of Cells	Obtained Max. $y^+$
Mesh 1	$0.6D$	$0.150D$	$0.150D$	136979	3.63
Mesh 2	$0.5D$	$0.125D$	$0.125D$	149176	3.58
Mesh 3	$0.4D$	$0.100D$	$0.100D$	306901	3.34
Mesh 4	$0.3D$	$0.075D$	$0.075D$	543050	3.63
Mesh 5	$0.2D$	$0.050D$	$0.050D$	1573239	3.71

To choose the most suitable mesh, the drag coefficient, pressure profile and velocity profile were monitored. The results of the analysis are compiled and presented in Figure 4.5. Judging from the drag coefficient ( $C_D$ ), it achieves a nearly constant value starting from Mesh 2. Further reduction in mesh size does not bring significant impact to the  $C_D$ . On the other hand, the velocity profile at  $x/D=0.75$  downstream from the cylinder achieves a consistent pattern starting from Mesh 4. Similarly, the obtained pressure profile at  $x/D=0.75$  downstream, the profiles achieve a nearly consistent pattern starting at Mesh 4. Therefore, based on the overall analysis, Mesh 4 is selected as the most suitable mesh in this work, as shown in Figure 4.6.

**Figure 4.5: For caption see next page.**

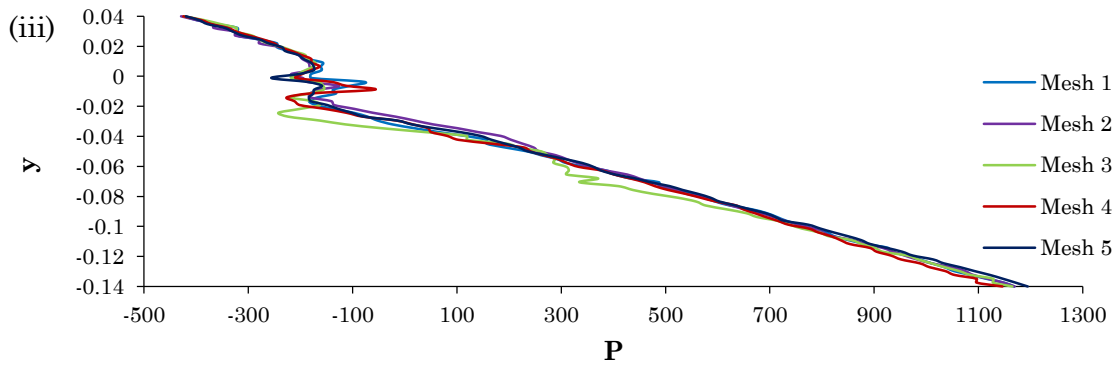


**Figure 4.5: The mesh independency study: (i) the drag coefficient ( $C_D$ ); (ii) The  $x$ -component velocity ( $u$ ) profile at  $x/D=0.75$  downstream from the cantilever; (iii) The static pressure profile at  $x/D=0.75$  downstream from the cantilever.**

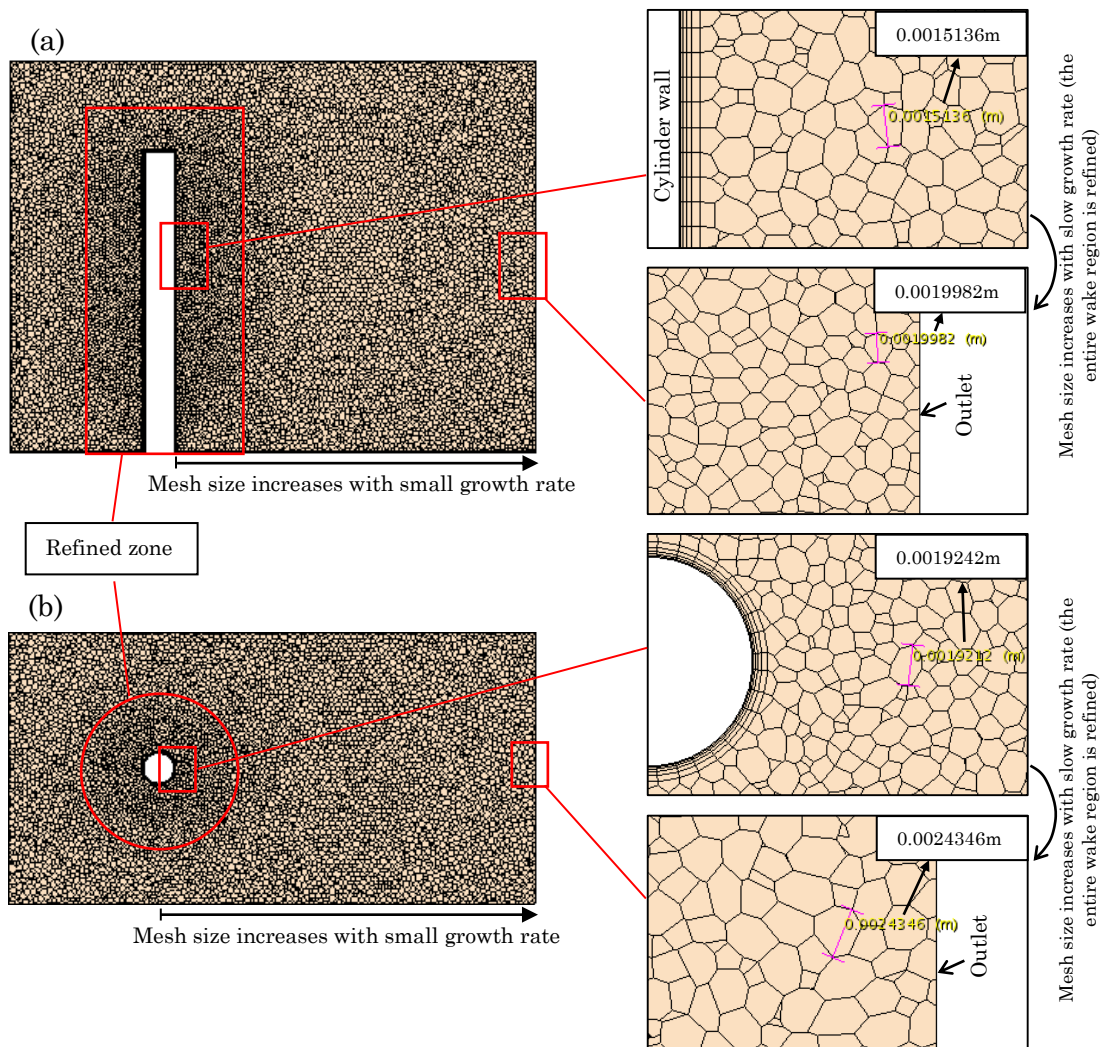


**Figure 4.6: The selected mesh (Mesh 4) on the simulation domain: (a) side view on the plane of symmetry ( $y=0$ ) and (b) top view on the cross-sectional plane.**

#### 4.2.2.2 Structural Domain

For the mesh of the circular and flat plate VG, C3D8R type structured mesh is used, as shown in Figure 4.7. This mesh is used in the FEA analysis to compute the structural deformation caused by the flow.

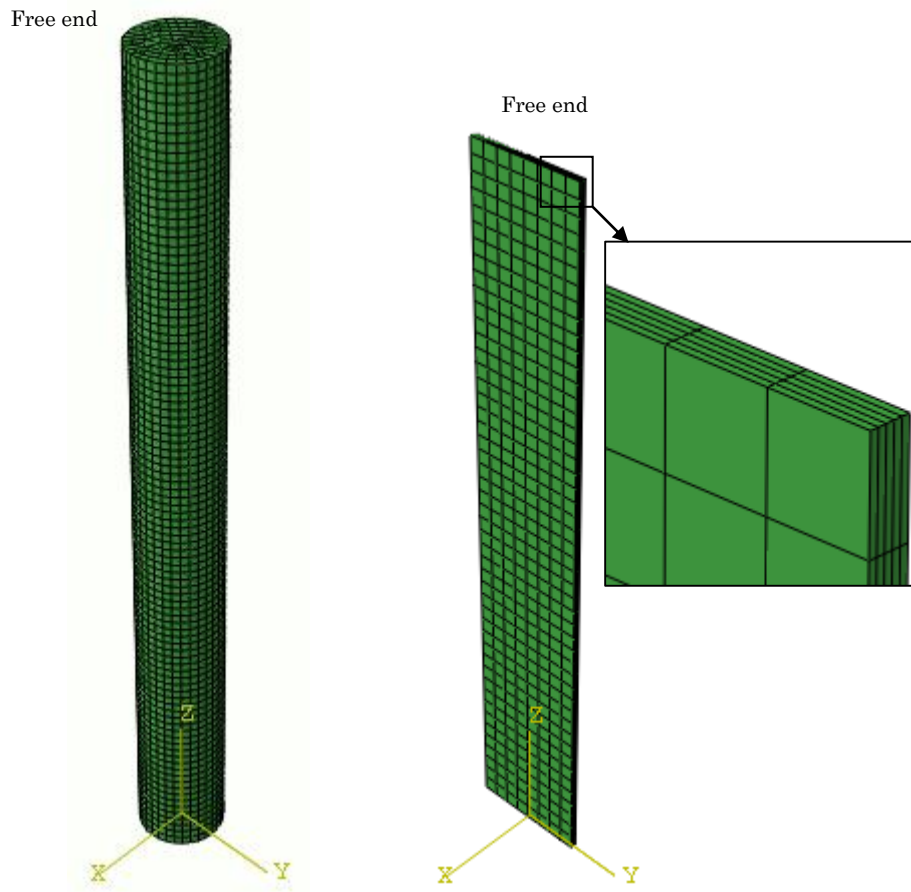


**Figure 4.7: The structured mesh on the (left) circular FVG and (right) flat plate FVG.**

The element size is 0.005m for both cases. This value is obtained from a stand-alone FEA mesh independence study (no fluid flow involved) where a static pressure was applied on the VG to bend it. However, the results do not show significant changes with different mesh size. A similar mesh independency behaviour was observed from the mesh independence study done by Yamamoto *et al.* (2004), where the displacement does not show significant changes with an increasing number of element (or smaller mesh size). This result signifies that the mesh on the FEA analysis of the FVGs is insensitive at the range that has been tested in the current study.



### 4.2.3 Time-step size

The size of the time step ( $\Delta t$ ) is determined from the number of the time step ( $n_{\Delta t}$ ) per shedding cycle. The size of the time step ( $\Delta t$ ) can be calculated by Equation 4.14.

$$\Delta t = \frac{D}{n_{\Delta t}(St \times U)} \quad (4.14)$$

Where  $St$ ,  $D$ , and  $U$  represent the Strouhal Number, cylinder's diameter, and free stream velocity, respectively.

#### 4.2.3.1 Circular VGs

An important guideline in this time-step size calculation is to select a suitable value for  $St$ . For flow past a circular cylinder, the maximum possible  $St$  is 0.21, which happens when the flow is dynamically 2-dimensional. When 3-dimensionality is considered, the  $St$  experienced by a circular cantilever is approximately 0.14~0.18 (Sumner *et al.*, 2004). Since the  $\Delta t$  is an inversely proportional to  $St$ , selecting the maximum  $St$  will result in a smallest time-step size. Furthermore, it is also the safest value to be used. For instance, since the shedding frequency varies along the cantilever span (slower shedding near the free end, faster shedding at a location far away from the free end), selecting the maximum  $St$  in the calculation allow the resulting time step size to be able to account for all shedding frequencies along the cantilever.

It is suggested that at least 20~25 time-steps per shedding cycle are needed to capture vortex shedding correctly. In this work, ~100 time-steps per shedding cycle are used; *i.e.*  $n_{\Delta t}=100$ ; so that the shedding can be captured precisely. Thus, by using Equation 4.14,  $\Delta t \approx 0.001s$  is computed and this value is used in this study.

#### 4.2.3.2 Flat Plate VGs

A similar technique is used for flat plate cantilever case as well. The maximum  $St$ , in this case, is ~0.16. By applying similar  $n_{\Delta t}$ , which is ~100 steps per shedding cycle, the resulting time-step size is  $\Delta t \approx 0.0005s$ .

### 4.2.4 Model Validations

This sub-section discusses the efforts used to validate the model employed in this work. In this section, various flow conditions have been simulated and compared to the corresponding experimental data for validation.

Each respective flow conditions shall be addressed in its corresponding subsection. Different properties such as the aerodynamic forces (Drag coefficient), the shedding frequency (Strouhal Number), and the velocity flow field behind the cylinder are included in this study and it is examined accordingly with the different experimental setup. The experimental data is obtained either from self-conducted experiments or from various publications.

#### 4.2.4.1 Aerol/Hydrodynamic Force and Shedding Frequency Validation

In this part, the ability of the model to predict and compute the aerodynamic forces is examined. A  $Re \approx 2.5 \times 10^4$  flow past a fixed-fixed end cylinder was simulated and the result was compared with the experimental data. Therefore, it is considered as a 2-dimensional case. The benefit of simulating a 2-dimensional case is to examine the fundamental ability of the model to compute the hydrodynamic forces without the interference from the third-dimension component. Besides, the data for the two-dimensional case is also well established to allow fair validation. The schematic of the experiment setup is as shown in Figure 4.8.

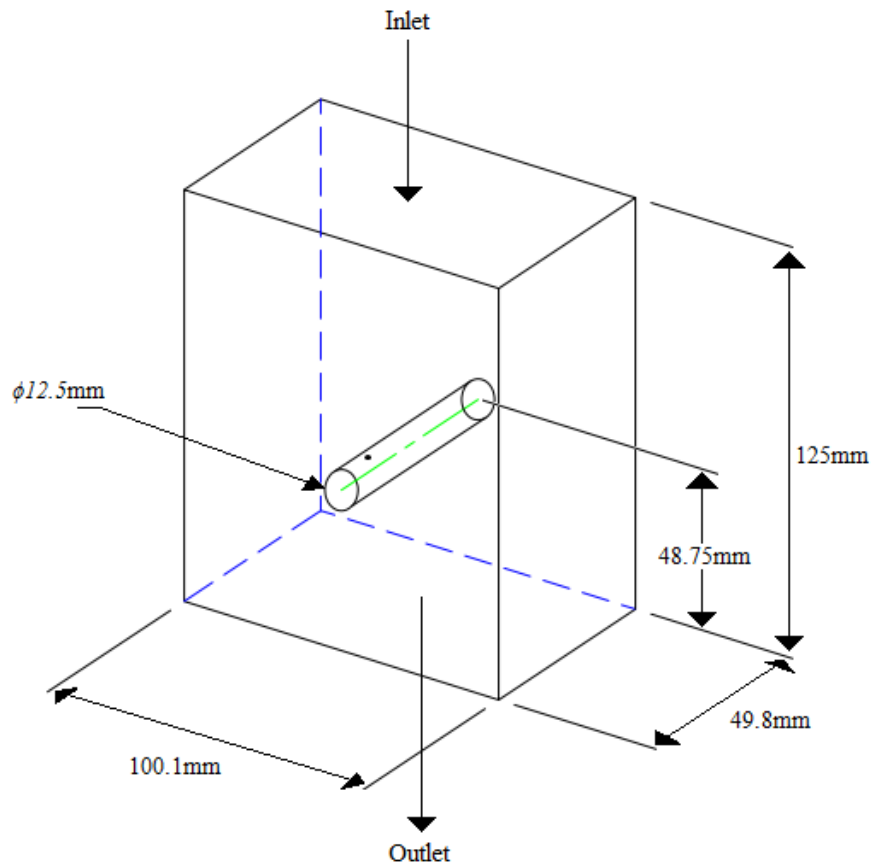


**Figure 4.8: Schematic of the experiment setup with dimensions (Not to scale).**

The experiment was conducted to collect the pressure distribution around the cylinder's surface. The local pressure was measured by the Surface Pitot tube that is located at 0.0071m away from the centre of the cylinder's span, which is represented by a black dot in Figure 4.8. The velocity was calculated based on the static pressure collected at two locations in the wind tunnel. The computed flow velocity and the local Reynolds Number were 34.074m/s and 25345.249 respectively. From the Reynolds Number, it can be seen that the flow was in the subcritical regime. Then the drag coefficient  $C_D$  was calculated by using Equation 4.15.

$$C_D = \int_0^{2\pi} C_p \cos\theta \delta\theta \quad (4.15)$$

On the other hand, the experiment was mimicked by using CFD approach. The upstream flow velocity was measured and used as an input boundary condition in CFD approach. The computed results were compared with the experimental result from for validation. Furthermore, Detached Eddy Simulation (DES) was also used to simulate the case. The consideration of many turbulence models in this test is to check the validity of the model, which can be helpful in the selection of the final turbulence model. The summary of the study is tabulated in Table 4.5.

**Table 4.5: Details of experimental and CFD comparison.**

	$C_D$	% differences of $C_D$ compared to experimental data	Strouhal Number, $St$
Experiment	0.9937	-	0.2 (Theoretical Value @ $Re=2.5 \times 10^4$ )
$k-\omega$ (SST) – Mesh 4	1.0189	2.49%	0.2038
$k-\omega$ (SST) – Mesh 5	1.0018	0.81%	0.2021
DES – Mesh 4	0.8018	-19.31%	0.2168

Based on the study,  $k-\omega$  (SST) achieves the lowest discrepancy compared to DES. The error between experimental and numerical results modelled by  $k-\omega$  (SST) is less than 2.49% and 0.81% for Mesh 4 and Mesh 5, respectively; while *DES* achieves a high - 19.31% discrepancy. In order to generate a result with greater accuracy in DES model, a smaller mesh size should be considered. Throughout the validation, it is learned that the  $k-\omega$  (SST) model computes a promising prediction, compared the DES model, even though the same mesh configuration is used.

Moreover, this study also confirms that Mesh 4 is sufficient and capable of simulating the desired problem since the discrepancy obtained is <3%, which is within an acceptable range. The validation has supplemented the mesh independence study presented previously. On the other hand, Mesh 5 has ~2.89 times more cells compared to Mesh 4. As a result, its computational time is approximately 1.8 times of the Mesh 4, although it has achieved a low 0.81% differences. However, a 1.8% improvement in accuracy is, perhaps, unsatisfactory for an extra ~1.8 times computational time, given the fact that Mesh 4 is already capable of producing an acceptable result. Therefore, it is concluded that, for the current numerical setup, Mesh 5 has over-refined the mesh configuration that leads to an inefficient simulation experience. Therefore, Mesh 5 is less recommended in this work.

#### 4.2.4.2 *Flow Field Validation (Upstream and Downstream flow field)*

Besides, to further proof the reliability of the model, the flow field of the simulated AR=5 circular cantilever was compared with the visualisation image, under the same flow condition (*i.e.*  $Re=2\times 10^4$ ), captured by Park and Lee (2000), as shown in Figure 4.9. It is important to note that the current comparison is focus on the mean flow features such as the flow direction and the flow pattern (*i.e.* upwash, downwash and flow recirculation).

Based on the comparison, it can be seen that both flow fields show a high similarity. In addition, some distinct flow features can be distinguished and identified. These features are grouped accordingly with boxes in different shapes and box number, as shown in Figure 4.9.

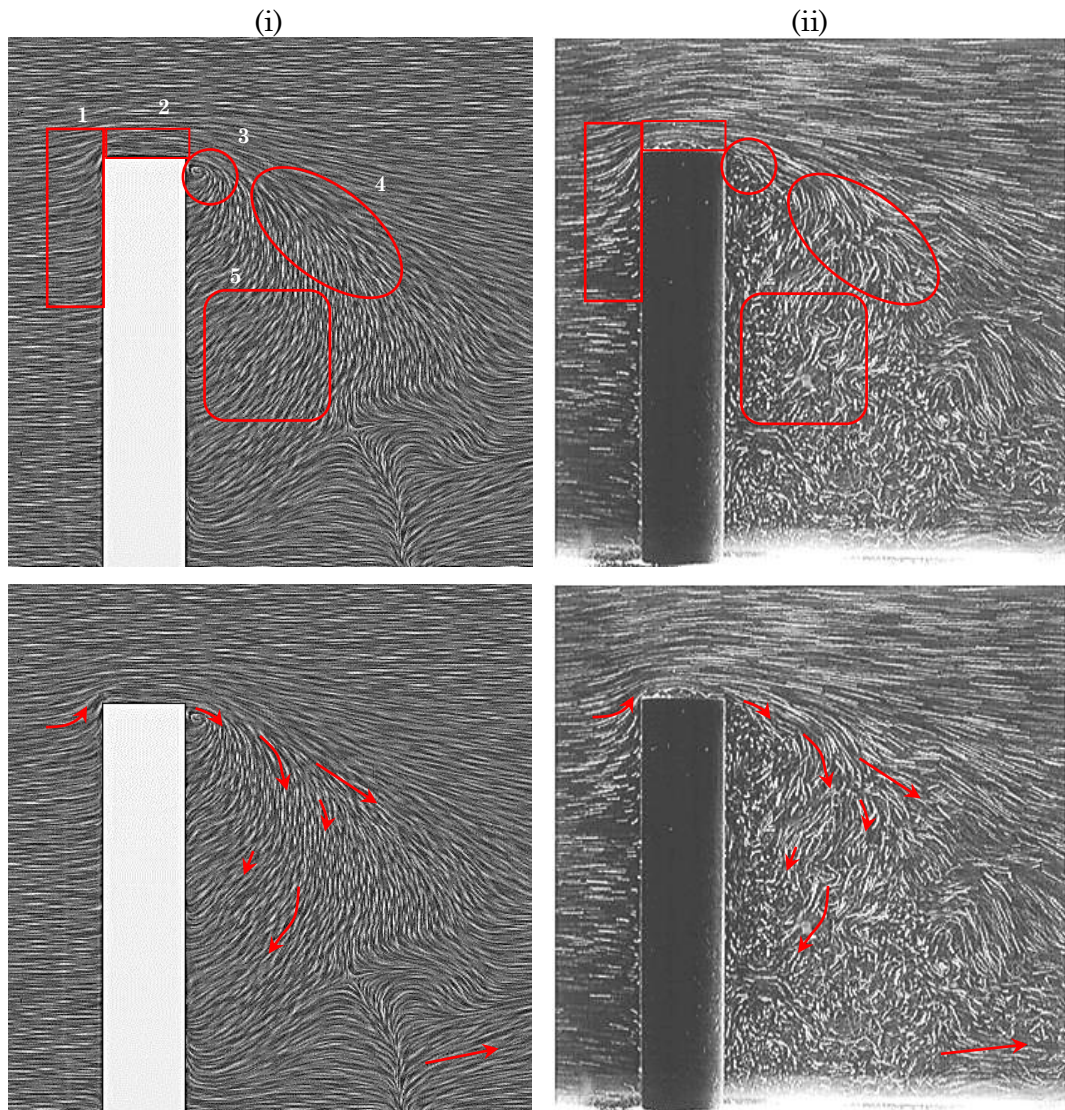


**Figure 4.9: The instantaneous flow field comparison (at the plane of symmetry) of the CFD result with the experimental result: (i) Streamline from CFD ( $k-\omega$  (SST) – Mesh 4); (ii) experimental visualisation (Park & Lee, 2000).**

The first identical feature noticed from the comparison is the upwash flow that is present near the free end of the cylinder (labelled as Box no.1). This upwash is a product of the acceleration of the flow when it is approaching the leading edge of the free-end surface. Apart from the work done by Park and Lee (2000), many literature (Rostamy *et al.*, 2012; Afgan *et al.*, 2007; Palau-Salvador *et al.*, 2010; Kawamura *et al.*, 1984; Liu *et al.*, 2005) have investigated a similar cantilever cylinder setup, by a mean of numerical and experimental approaches under various  $Re$ , and they have reported the same flow feature in the same region.

Secondly, it is noticed that there are two recirculation zones location right above the surface of the free-end (Box no.2) and right after the trailing edge of the free-end (Box no.3). However, it is difficult to view the recirculation zone in the visualisation image captured by Park and Lee. Therefore, the CFD result is compared with another literature, which has studied, specifically, the flow field around the free-end.

In this case, a circular cantilever with  $AR=7$  in a  $Re_D=4.4\times 10^4$  flow case is used for this comparison. The purposes of selecting a cylinder with a different  $AR$  in this validation, are (i) to match the flow condition that was used in the work of the literature (it is  $Re_D=4.4\times 10^4$  done by Sumner *et al.* (2013)); ii) to test the reliability of the model under different flow conditions. The comparison of the flow field above the free-end surface is shown in Figure 4.10.

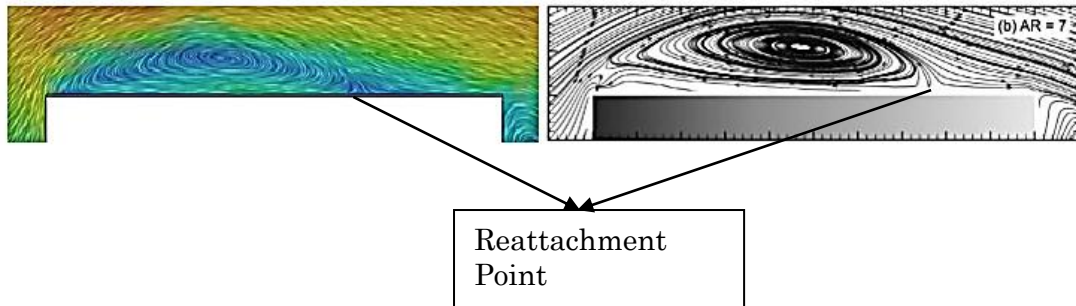


**Figure 4.10: Flow field comparison of the recirculation zone above the free end surface (at the plane of symmetry). (Left) Instantaneous velocity field computed by CFD approach ( $k-\omega$  (SST) – Mesh 4); (Right) Mean Streamlines obtained through experimental approach done by Sumner *et al.* (2013).**

As shown in the figure above, the model has predicted the recirculation zone with a good agreement with the experimental result studied by Sumner *et al.* (2013). Furthermore, the location of reattachment point, which is regarded as one of the important flow feature at the free-end surface, obtained through CFD approach is also close to the experimental result.

#### 4.2.4.3 Velocity Profile

In addition to flow field validation, the velocity profile of both experimental and CFD case is compared as well. In this part, the velocity profile obtained through CFD approach was validated with the experimental data from Okamoto and Yagita (1973). Okamoto and Yagita conducted a study in early 70's to address the flow behaviour behind a finite cylinder. The velocity profile behind an  $AR=5$  circular cantilever in a  $Re=6700$  flow is used as the

experimental data in this validation. The velocity profiles are plotted in Figure 4.11.

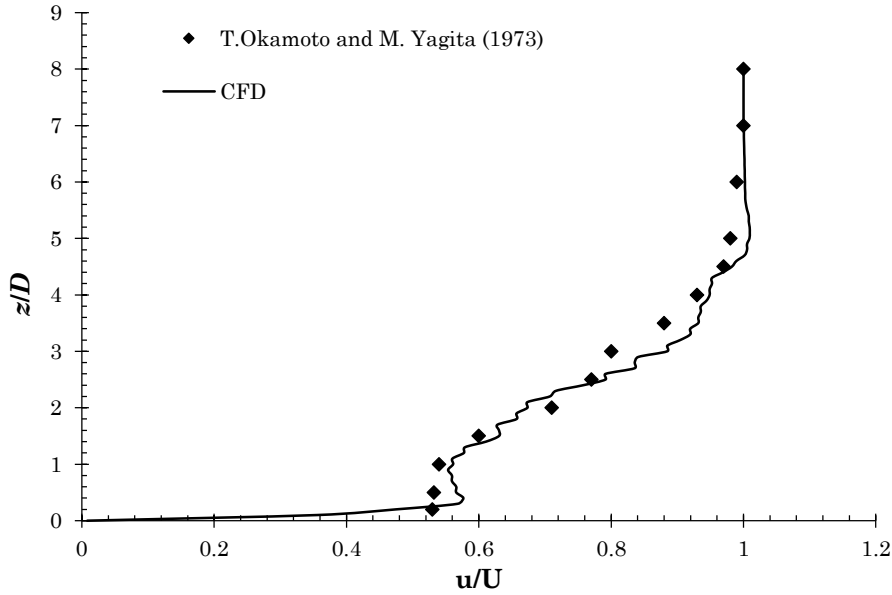


**Figure 4.11: The velocity profile at the plane-of-symmetry ( $y/D=0$ ), located at  $x/D=6$ .**

Based on the figure, it is clear to see that the numerical solution has successfully predicted the trend and most importantly, it is able to capture the key feature of the velocity profile – the gradient of the curve. The velocity gradient plays an important role in this study because it is the main component in calculating the vorticity of the flow field. The vorticity of the flow is an important aspect in circulation calculation. The circulation, also known as the strength of the vortex, is used to examine the properties of the flow such as the mixing ability. Therefore, the ability to predict the velocity gradient correctly is crucial in this case.

There is a small discrepancy located at the root of the cylinder ( $0 < z/D < 1$ ). The discrepancy may be caused by the difference of boundary layer thickness. There is no specific boundary layer thickness mentioned in the work of Okamoto and Yagita. Therefore, a small boundary layer thickness (*i.e.*  $\delta/D=0.7$ ) is used when simulating the case. The reason for selecting a small boundary layer thickness is to minimise its effect toward the flow field.

#### 4.2.4.4 FSI Coupling

This section verifies the capability of the model in simulating the FSI problem by reproducing the published result. The result from Tian *et al.* (2014)



is selected as the benchmark to verify the current numerical approach. It is because one of the problems solved in the published work resembles a great similarity with the scope of the present work.

Before proceeding to the discussion of the validation, the work that was done by Tian *et al.* will be introduced. Their work focused on the numerical studies of FSI that involves large deformations. They have developed a FSI model via adapting the Immersed-Boundary Method and have done a series of benchmarking by simulating different cases with their model. The major objective of their work was to validate the reliability of their model. The performance of the model is promising.

Among many cases, one of their validations was working on the deformation of a flexible plate in a cross flow, which resembles an almost identical condition with the current scope of study. Their results were validated with the experimental results conducted by Luhar and Nepf (2011). An important note has to be taken on the fact that the buoyant effect was taken into account in the experiment conducted by Luhar and Nepf. Therefore, Tian *et al.* has cooperated a source term to model the buoyant force. By taking into account the ~10% experimental error, that was identified by Luhar and Nepf, the result obtained by Tian *et al.* agree well with the experimental value.

After the validation, Tian *et al.* performed a series of simulation to expand the database of this problem for further benchmarking purposes. However, these benchmarks neglect the effect of buoyancy by disabling the buoyancy source term. In the current validation, one of the benchmarks will be reproduced.

In addition, it is important to note that Tian *et al.* only provided the details (including the boundary conditions) of their simulation in the form of dimensionless parameters. Therefore, it is impossible to obtain the exact value of the parameters that they had used in their simulation. One of the examples will be the density of the fluid and the material of the flat plate; only density ratio was given by them (*i.e.*  $\rho^* = \rho_s / \rho_f = 0.678$ ). With only the ratio, there is no other possible ways to compute the exact value of the densities as there are an infinite number of combinations to get the exact same ratio. Since it is known that Tian *et al.* was reproducing the result from Luhar and Nepf, the missing parameters such as the flow velocity ( $U_\infty$ ) and others are referred from Luhar and Nepf, instead (Please refer to Appendix I for the calculations). However,



most of the values described by Luhar and Nepf are associated with uncertainty. Thus, the values may differ, within certain margin, with those used by Tian *et al.*. The necessary properties to construct the simulation are tabulated in Table 4.6. Moreover, Mesh 4 is used in this validation as well.

**Table 4.6: Structural and Fluid flow properties of the FSI-coupling validation.**

<b>Structural (Silicon Foam flat plate) Properties</b>	
Width, ( $D$ )	0.01m
Thickness ( $t$ )	0.002m
Length ( $L$ )	0.05m
Young's Modulus ( $E$ )	486927.4Pa
Density ( $\rho_s$ )	676.78kg/m <sup>3</sup>
<b>Fluid (water) flow Properties</b>	
Re	1600
Flow velocity ( $U_\infty$ )	0.16m/s
Density ( $\rho_f$ )	998.21kg/m <sup>3</sup>

The results of the simulation are tabulated in Table 4.7. The drag coefficient ( $C_D$ ), force and normalised  $x$ -displacement are compared to validate the model. Firstly, the comparison of  $C_D$  shows a large discrepancy. However, it is later found that, in fact, Tian *et al.* calculated the  $C_D$  with a less accurate method, which used the frontal area of the pre-deformed flat plate in the calculation. It is certain that the frontal area of the flat plate will reduce during deformation; in other words, their  $C_D$  is under-predicted. In light of this matter, their calculation is reversed to obtain the force exerted on the plate and the force is used to compare with the simulated value. The comparison shows that the simulated value is 4.7% greater than benchmark's value. Besides, the normalised  $x$ -displacement is also obtained and compared with the benchmark's value. The comparison shows a 4.1% difference between both values. Figure 4.12 visualises the bending of the flat plate.

**Table 4.7: Comparison between the results of the CFD simulation and the benchmark.**

	$C_D$	Force (N)	Normalised $x$ -displacement ( $x/D$ )
CFD	1.19	0.00645	2.53
Tian <i>et al.</i>	0.94	0.00616	2.45
Error (%)	n/a	4.7%	4.1%

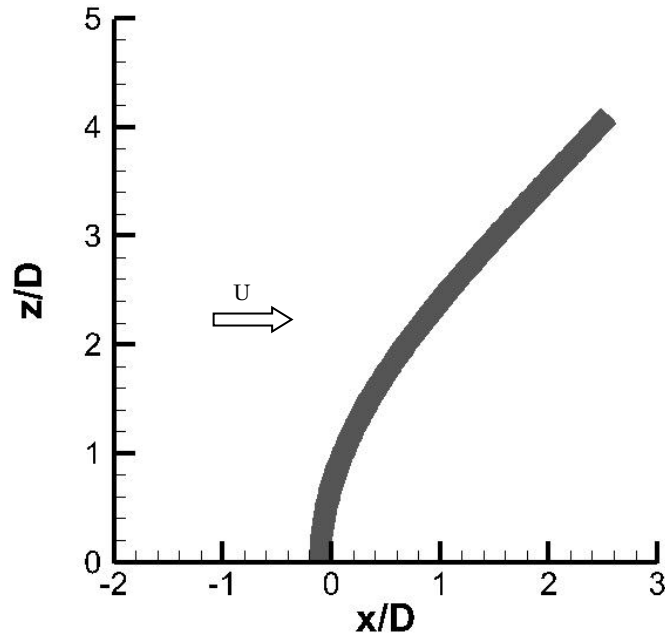


**Figure 4.12: The bending of the flexible flat plate in a cross flow.**

Before concluding this discussion, it is important to mention that the input parameters and boundary conditions used in the present validation are not identical to the values used by Tian *et al.* The input values are associated with the uncertainty that is within the range described by Luhar and Nepf. Owing to this fact, part of the computed error is actually caused by the slight variant in assumption assumptions on the initial conditions and governing parameters. This is to say that the computed errors (*i.e.* the 4.7% and 4.1% error) comprise the uncertainties. In other words, the actual modelling error is less than 4.7% and 4.1% for the computed force and  $x$ -displacement.

It can be concluded that the numerical approach is capable of simulating the FSI problem – the bending of a flexible flat plate in a cross flow – that resembles a great similarity with the present simulation case. The computational errors lie below 5%, inclusive of the uncertainty in the input parameters, which is within the acceptable range.

### Summary of chapter

In this chapter, the all the governing equations of both fluid and structural domains are presented. Furthermore, a coupling scheme that connects the fluid and structural domains is presented. Apart from this, an additional turbulence model is introduced as well. In the present model, the SST  $k$ - $\omega$  model is used.

Secondly, the numerical setup of the model is discussed in this chapter. The simulation domain is introduced along with the boundary conditions and the input parameters. Once the model is configured, the mesh independence study is conducted to obtain the optimal mesh settings.

Next, the model is put into several tests to validate its validity. In this study, various flow condition and AR were simulated by a predetermined numerical model and the results are compared the corresponding experimental data for validation. It is important to note that the optimum mesh obtained from mesh independency study was used throughout the entire validation works.

In the next chapter, the simulated results will be visualised for virtual analyses.

# Chapter 5: Numerical Visualisation

This chapter discusses flow past a Flexible Vortex Generator (FVG) through flow visualisation. The wake structure will be the main focus of this discussion. Comparisons with the respective Rigid Vortex Generator (RVG) are made to emphasise the effects of FVG.

This chapter starts with visualising the wake structure; first on the wake of the circular VGs (RVGs and FVGs), followed by the wake of the flat plate VGs. The differences between the wake behind a RVG and a FVG are, then, identified. Next, the underlying mechanism that leads to the observations is identified and discussed.

In addition, the strength of the vortical activities behind the VGs is discussed based on the first-hand information gained from wake visualisation; this discussion is purely on observing and speculating the dynamics behind the VGs. The discussion provides a preliminary insight on the improvement of turbulence generation achieved by employing the FVG.

The reader is advised to refer to Appendix II, which covers the  $x$ - and  $y$ -displacement monitors, prior to proceeding to the chapter. This allows the comprehension of the oscillation responses of the FVGs that is useful to grasp the information discussed in this chapter.

Besides, an abbreviation is introduced to simplify the description of R/FVG in different ARs, as shown below. With this abbreviation, the lengthy “AR=6 flat plate RVG” can be written as 6<sub>PR</sub> accordingly.

$$\delta_{CF}$$

└─ F: **F**VG or R: **R**VG

└─ C: **C**ircular or P: **F**lat **P**late

└─ The Aspect Ratio: AR = **8**

## 5.1 Wake of the FVG and RVG ( $x$ - $z$ plane)

The study of wake plays a crucial role in understanding vortex generation. A wake is a flow region that can be observed behind a blunt body; such as a vortex generator; that is submerged in a flow. It is composed of highly recirculated structures (*i.e.* vortices) and vorticity involves heavily in this region.

There are several aspects that can be studied from the wake, one of the most important aspects will be the spatial/dimensional aspect, *i.e.* the size of the wake. In general, the wake is often regarded as the “body” of turbulence, where turbulence effects (such as mixing) are expected to take place in this region. In short, the wake represents the effective region where most of the turbulent activities occur. So, the dimensions of the wake structure can directly demonstrate the effectiveness of the wake in facilitating those turbulence events (larger wake means more turbulence activities). Since the objective of current research is to study the turbulence enhancement ability of the FVG, the spatial aspect of the wake is definitely an important aspect to examine.

As described in Chapter 4, FVG with different cross-sectional shape – circular and flat plate – are considered in the present work. However, it is important to mention that the purpose of studying different geometry is not for qualitative and quantitative comparison (the flow condition is not the same). Since the physics should behave the same in any given condition, the main idea of including two geometries is to extract additional useful information that may not be revealed if only one geometry is studied.

Lambda2 criterion ( $\lambda_2$ ) will be used to visualise the vortical structure – the vortex. This mathematical description of vortex is developed by Jeong and Hussein (1995) after identifying the lack of capability of the common vortex identification methods. Lambda2 criterion defines vortex boundaries as regions bounded by the negative value of the second eigenvalue of the symmetric tensor –  $S^2 + \Omega^2$ , where  $S$  and  $\Omega$  are the strain-rate tensor and spin tensor respectively, which represent the symmetric and anti-symmetry portions of the velocity tensor. When the value of Lambda2 is positive, it does not carry any physical interpretation.

In the following discussion, the observations obtained from the VGs’ wake visualisation will be presented, first. Once the wake behaviours are identified, the cause(s) to the observed wake behaviours are studied.

### 5.1.1 Wake of the Circular VGs ( $x$ - $z$ plane)

Figure 5.1 and Figure 5.2 show the 3-dimensional wake structures behind the circular RVGs and FVGs respectively, which is represented by the iso-surfaces defined by  $\lambda_2$  equals to -100. In other words, the figures portray the vortical structures (*i.e.* the vortices) that are present in the wake.

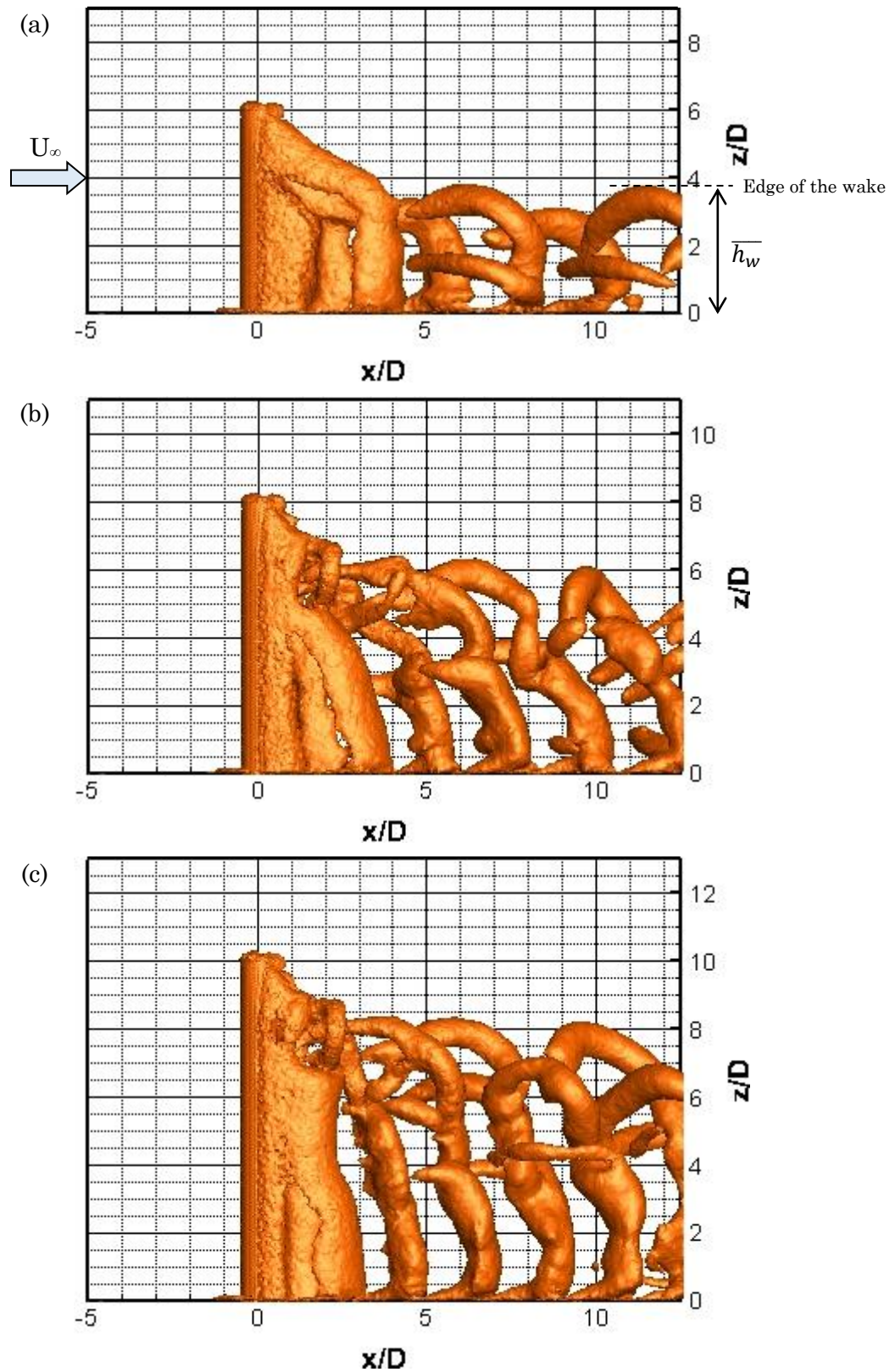


Figure 5.1: The  $\lambda_2$  ( $\lambda_2$ ) iso-surface,  $\lambda_2=-100$ , in the  $z$ - $x$  plane, of the circular RVG with (a) AR=6, (b) AR=8, and (c) AR=10.

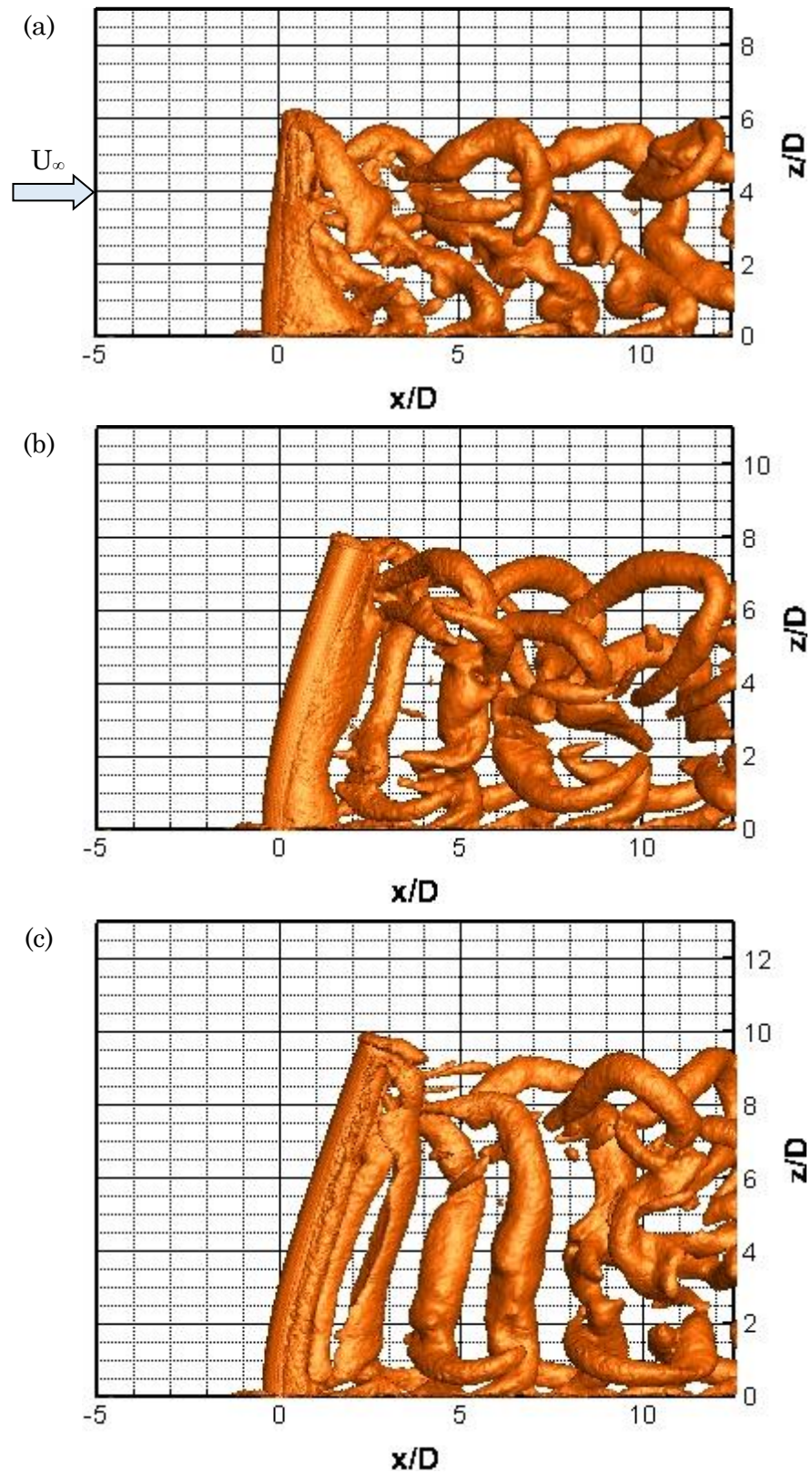


Figure 5.2: The  $\lambda_2$  ( $\lambda_2$ ) iso-surface,  $\lambda_2=-100$ , in the  $z$ - $x$  plane, of the circular FVG with (a)  $AR=6$ , (b)  $AR=8$ , and (c)  $AR=10$ .

First of all, based on the figures, the average wake height ( $\overline{h_w}$ ) of the RVGs are generally  $2D$  shorter than its AR, *i.e.*  $\overline{h_w}_{(RVG)} \approx AR - 2D$ . No vortex can be observed at the region outside of the wake ( $\overline{h_w}_{(RVG)} > AR - 2D$ ), as shown in Figure 5.1. The result agrees well with the the finding of Okamoto and Yagita (1973), where they observed no vortex shedding from the free end up to 2 diameters from it. Based on Figure 5.1, it can be seen that the vortex formed at the free end is convected downward/toward the floor before it travels to the downstream. This explains why previous researches are unable to measure any dominant vortex shedding frequency at the direct downstream of the free end while the theory shows that there are vortices forming at the free end.

On the other hand, it appears that the vortex formed at the FVG's free end does not experience the downward convection/motion, as shown in Figure 5.2. The vortex travels downstream right after it shed off. As a result, the wake has almost equivalent height with the FVG's length, *i.e.*  $\overline{h_w}_{(FVG)} \approx AR$ .

By comparing the wake behind both RVG and FVG, it is clear that the wake of FVG has greater height; it is approximately  $1.5D \sim 2D$  higher than the wake behind the RVG with the same AR. As the wake represents the effective region that facilitates the turbulence activities, the larger wake of FVG is able to facilitate more turbulence activities than the wake of RVG. Hence, the FVG can generate more turbulence, in term of spatial scale, than the RVG.

The average wake height ( $\overline{h_w}$ ) of the circular VGs is summarized in Table 5.1. The height increment achieved by employing the FVG is calculated and tabulated in the table as well.

**Table 5.1: The summary of wake height ( $\overline{h_w}$ ) behind the circular VGs.**

Circular:	Average wake height ( $\overline{h_w}$ )		
	RVG	FVG	Increment (%)
AR=6	$\sim 3.7D$	$\sim 6.0D$	$\sim 62.2$
AR=8	$\sim 6.0D$	$\sim 7.5D$	$\sim 25.0$
AR=10	$\sim 8.0D$	$\sim 9.5D$	$\sim 25.0$

### 5.1.2 Wake of the Flat Plate VGs ( $x$ - $z$ plane)

Likewise, Figure 5.3 and Figure 5.4 show the  $\lambda_2 = -100$  iso-surface that display the vortex structures behind the flat plate RVG and FVG, respectively.



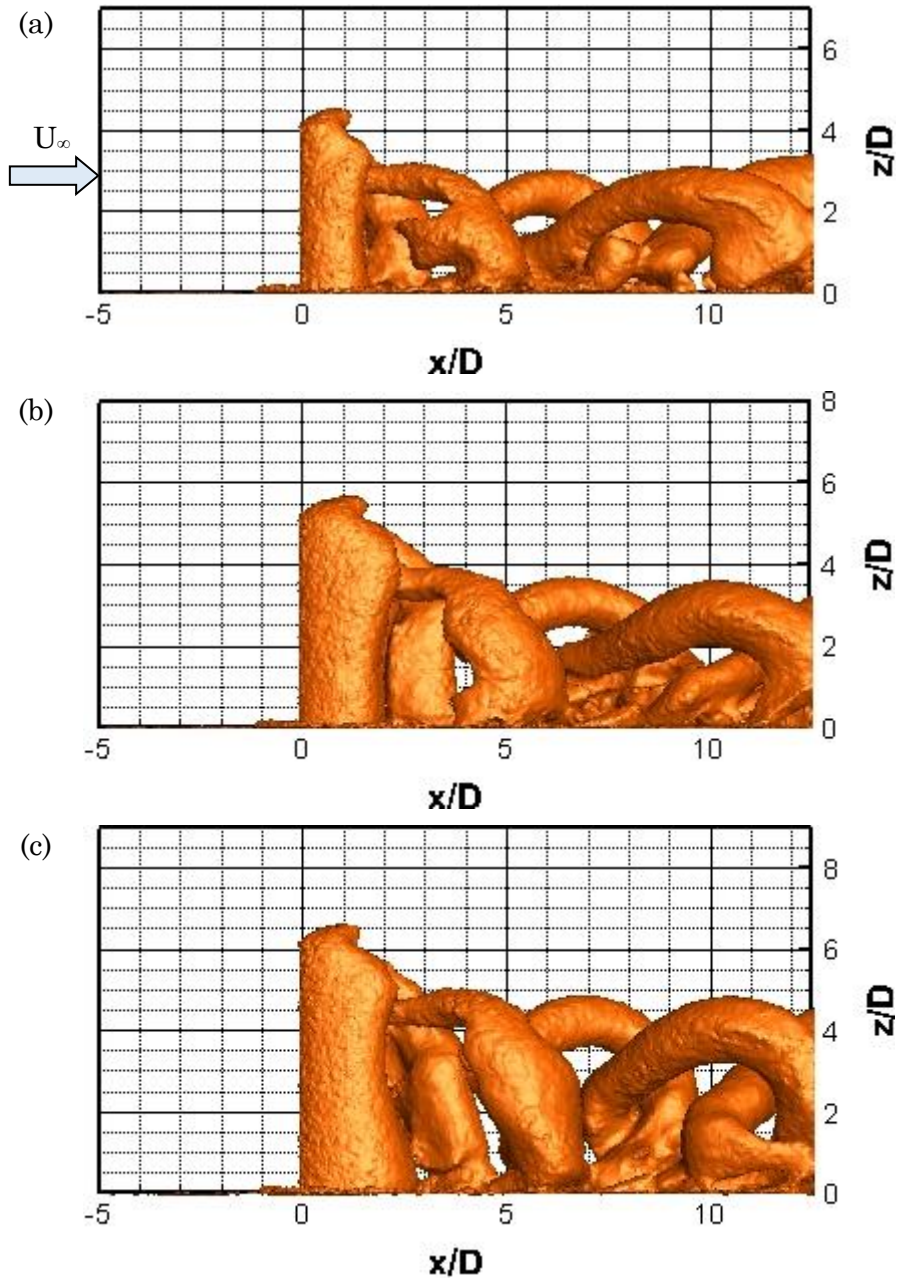


Figure 5.3: The  $\lambda_2$  ( $\lambda_2$ ) iso-surface,  $\lambda_2=-100$ , in the  $z$ - $x$  plane, of the flat plate RVG with (a)  $AR=4$ , (b)  $AR=5$ , and (c)  $AR=6$ .

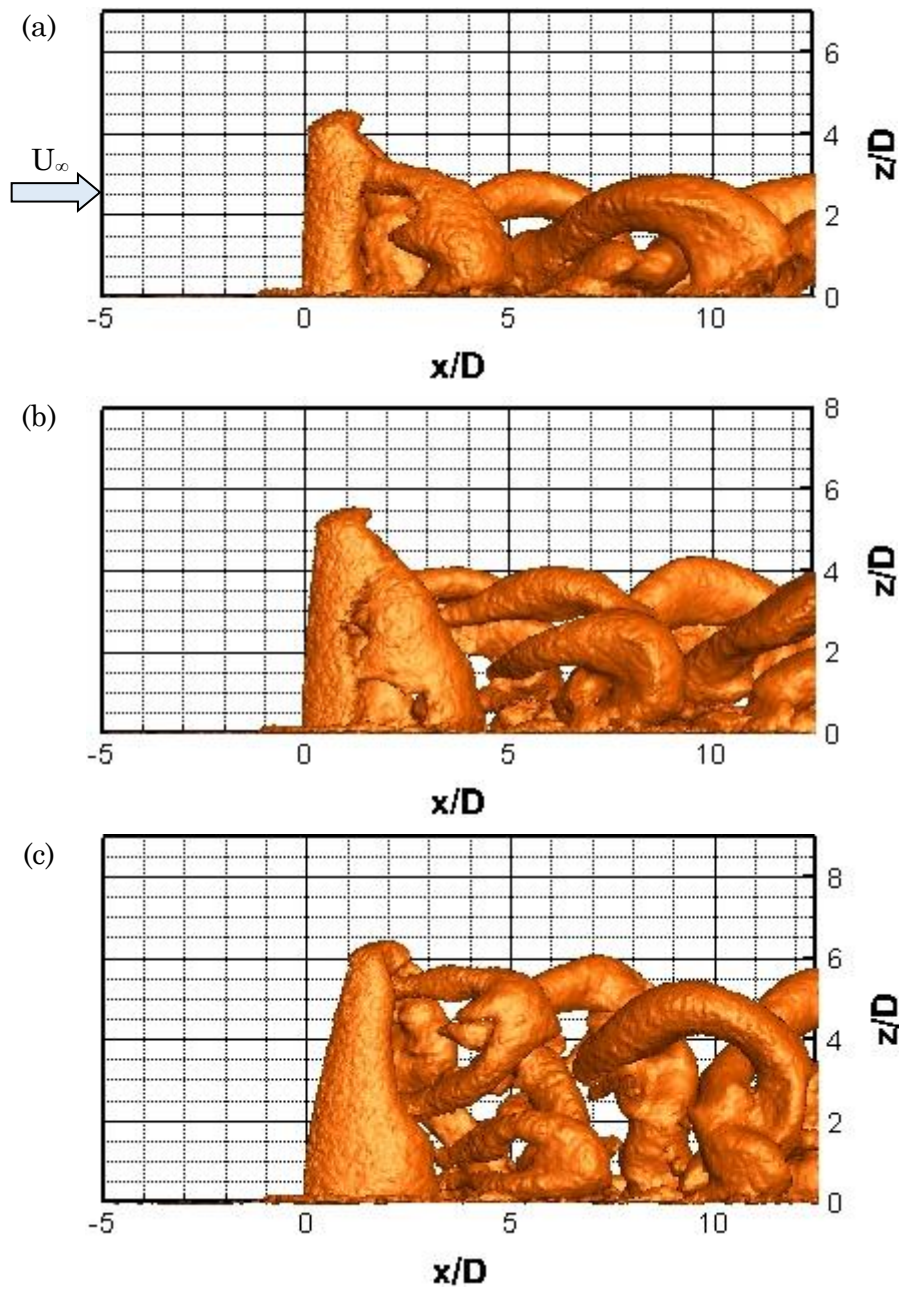


Figure 5.4: The  $\lambda_2$  ( $\lambda_2$ ) iso-surface,  $\lambda_2=-100$ , in the  $z$ - $x$  plane, of the flat plate FVG with (a)  $AR=4$ , (b)  $AR=5$ , and (c)  $AR=6$

The wake behind a flat plate RVG has similar behaviour to the wake of the circular RVG; where the vortex formed at the free end is washed downward before it travels downstream horizontally. Consequently, the  $\overline{h_w}$  of the RVG is shorter than the its AR; *i.e.*  $\overline{h_w}_{(RVG)} \approx AR - 1D$  up to  $\overline{h_w}_{(RVG)} \approx AR - 2.5D$ .

However, unlike the circular FVG where the  $\overline{h_w}$  is approximately the same with the FVG's AR, the wake behind the flat plate FVG experiences different wake height that seems to be varying with the AR. The vortex formed near the free end of the flat plate FVG still experiences the downward motion, but with a different rate depending on the AR. At low AR, the downward motion is strong, causing the vortex to travel closer toward the floor before it is transported downstream; at higher AR, the downward motion is weaken/vanished, thus the vortex is transport downstream without getting much influence from the downward motion.

In this case, the wake of the 4<sub>PF</sub> is 1D shorter than its AR, which denotes that it has the same  $\overline{h_w}$  with its respective rigid counterpart. Meanwhile, the wake of the 5<sub>PF</sub> is approximately 0.5D greater than the rigid case. Last but not least, the wake of the 6<sub>PF</sub> is the only case in this study that resembles a completely similar observation with the one obtained from the circular FVG; the  $\overline{h_w}$  of the 6<sub>PF</sub> is nearly equivalent to the FVG's AR, which signifies a circa 1D height difference compared to its rigid counterpart. The average wake height ( $\overline{h_w}$ ) of the flat plate VGs and its percentage of increment are summarized in Table 5.2.

**Table 5.2: The summary of wake height ( $\overline{h_w}$ ) behind the flat plate VGs**

Flat Plate:	Average wake height ( $\overline{h_w}$ )		
	RVG	FVG	Increment (%)
AR=4	$\sim 3.0D$	$\sim 3.0D$	0
AR=5	$\sim 3.5D$	$\sim 4.0D$	$\sim 14.3$
AR=6	$\sim 4.7D$	$\sim 5.7D$	$\sim 21.3$

### 5.1.3 Effects of Oscillation and Deflection on the Wake Structure ( $x$ - $z$ plane)

Based on the observation, the wake size of the RVG is generally shorter than the AR. However, this is not a new observation; a similar flow pattern has been reported constantly in the literature (Okamoto & Yagita, 1973; Afgan *et al.*, 2007; Liu *et al.*, 2005; Sumner *et al.*, 2004). Based on Figure 5.1 and Figure 5.3,

it can be concluded that the wake height of RVG is reduced because the generated vortex is drawn toward the floor. In Chapter 3, it has been discussed and identified that there is a downwash right behind the free end of a cantilever. In this case, the downwash is the key flow feature that causes the vortex near the free end to flow towards the floor. As a result, the wake has a lower height. By examining the mean velocity field at the plane of symmetry ( $y/D=0$ ) as shown in Figure 5.5 and Figure 5.6, it shows that the travelling path of the vortices coincides with the streamline in the figures, which agrees with the mentioned postulation.

With reference to the above argument, since the vortex behind the FVG is not convected toward the floor, it is suggesting that the downwash has become weaker or it has vanished in the case of FVG (apply for both circular and flat plate cases). Similarly, the mean velocity fields of the flow behind the FVGs are examined in order to provide a better illustration to this event. Figure 5.7 and Figure 5.8 show the streamlines of the mean velocity magnitude at the plane of symmetry of the circular and flat plate FVG, respectively. With no surprise, the results do not diverge too much from the speculation; based on the streamline plots, it appears that the downwash behind the circular FVGs has vanished; while the downwash behind the flat plate FVGs is weakened (except 4PF).

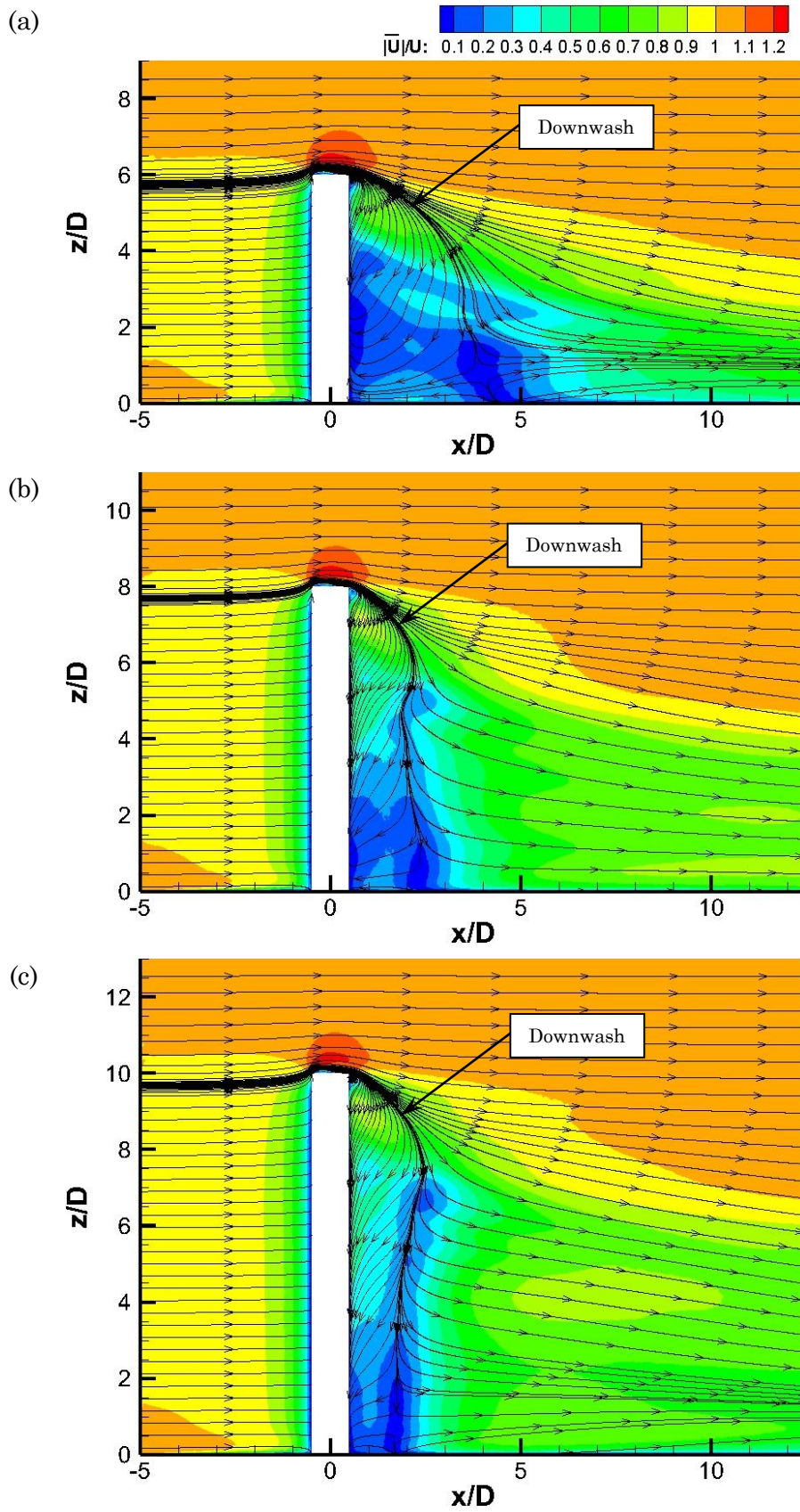
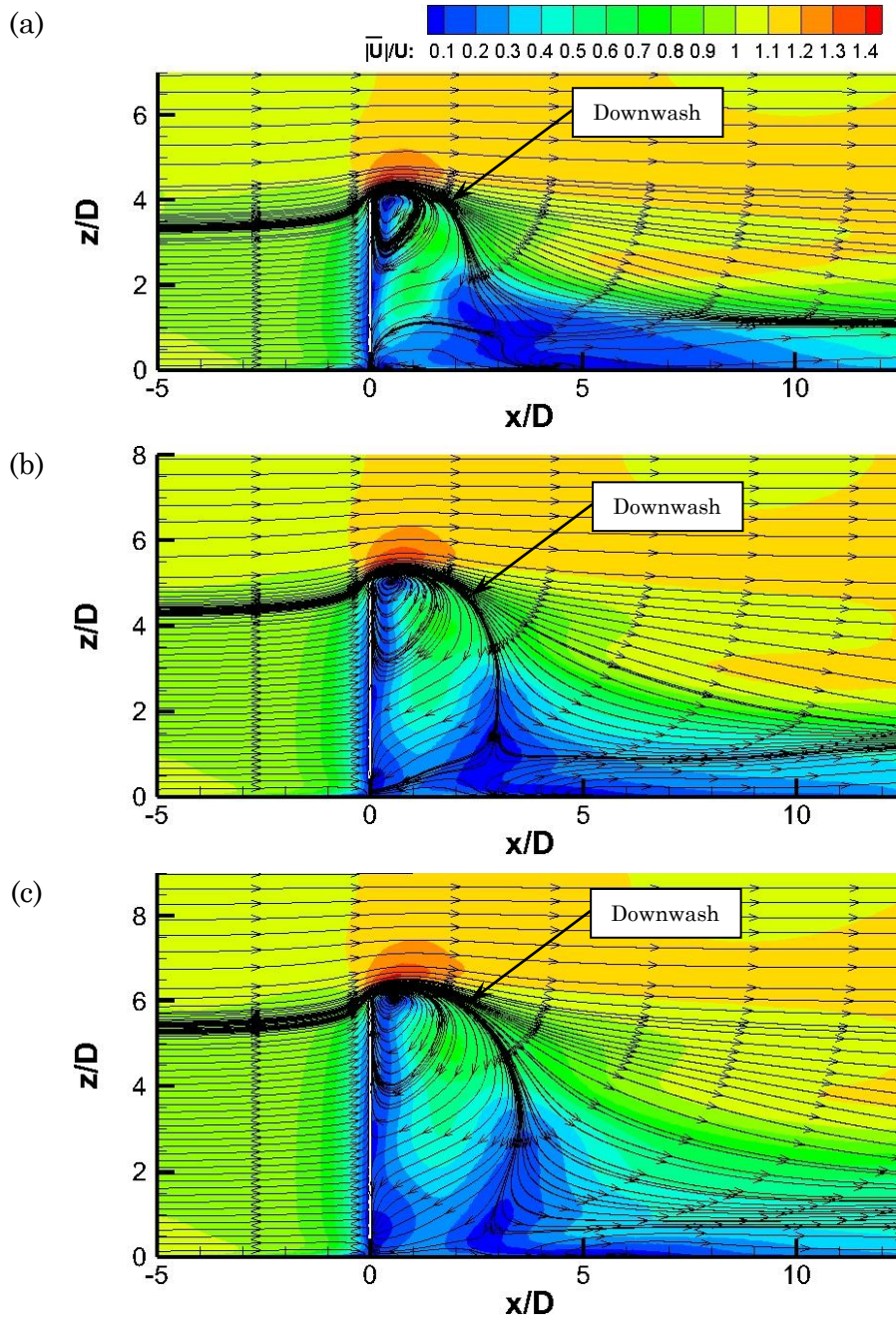


Figure 5.5: The streamlines of the normalised mean velocity magnitude at the plane of symmetry ( $y/D=0$ ) of the circular RVG with (a) AR=6, (b) AR=8, and (c) AR=10.





**Figure 5.6: The streamlines of the normalised mean velocity magnitude at the plane of symmetry ( $y/D=0$ ) of the flat plate RVG with (a)  $AR=4$ , (b)  $AR=5$ , and (c)  $AR=6$**

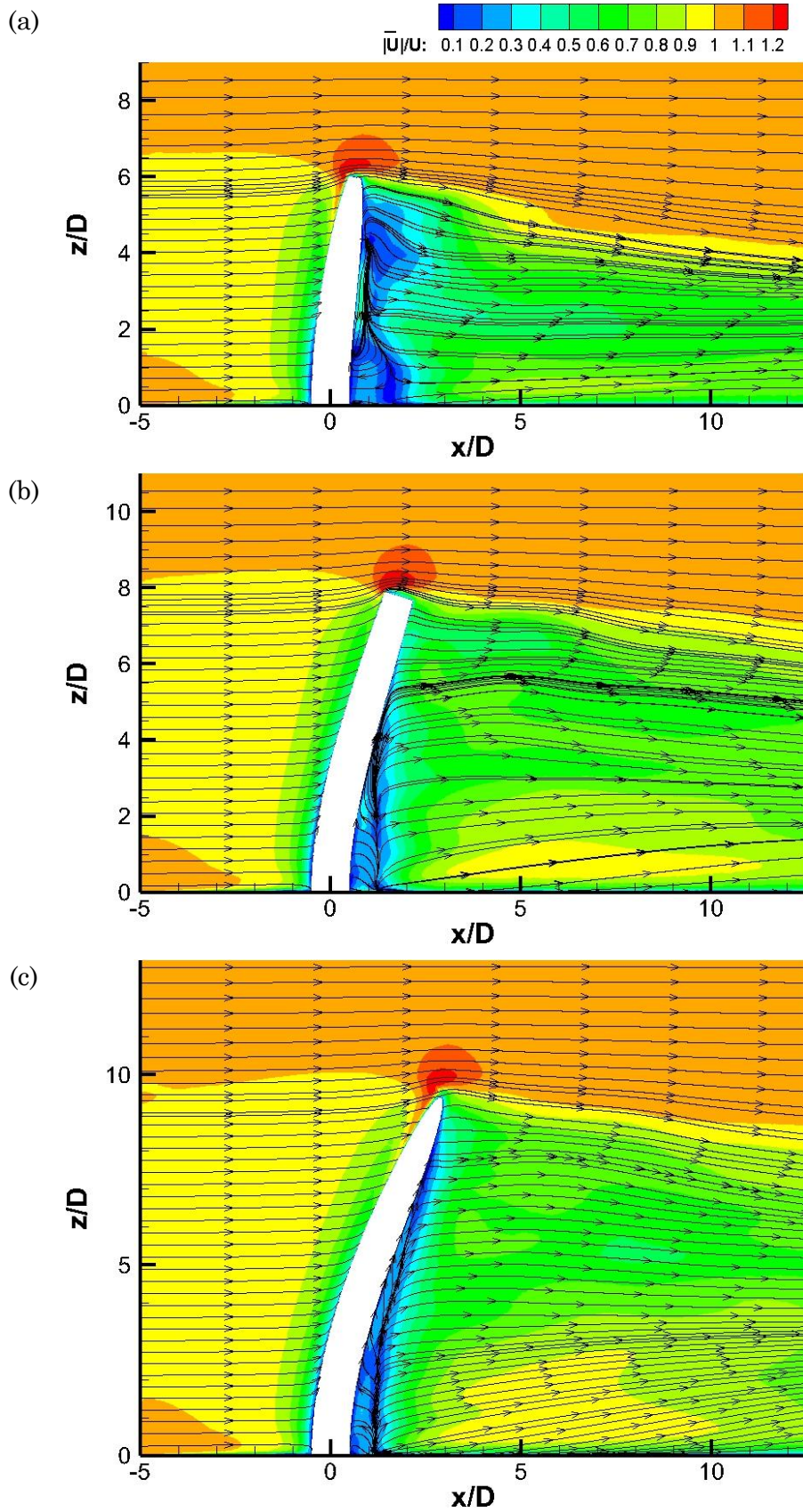
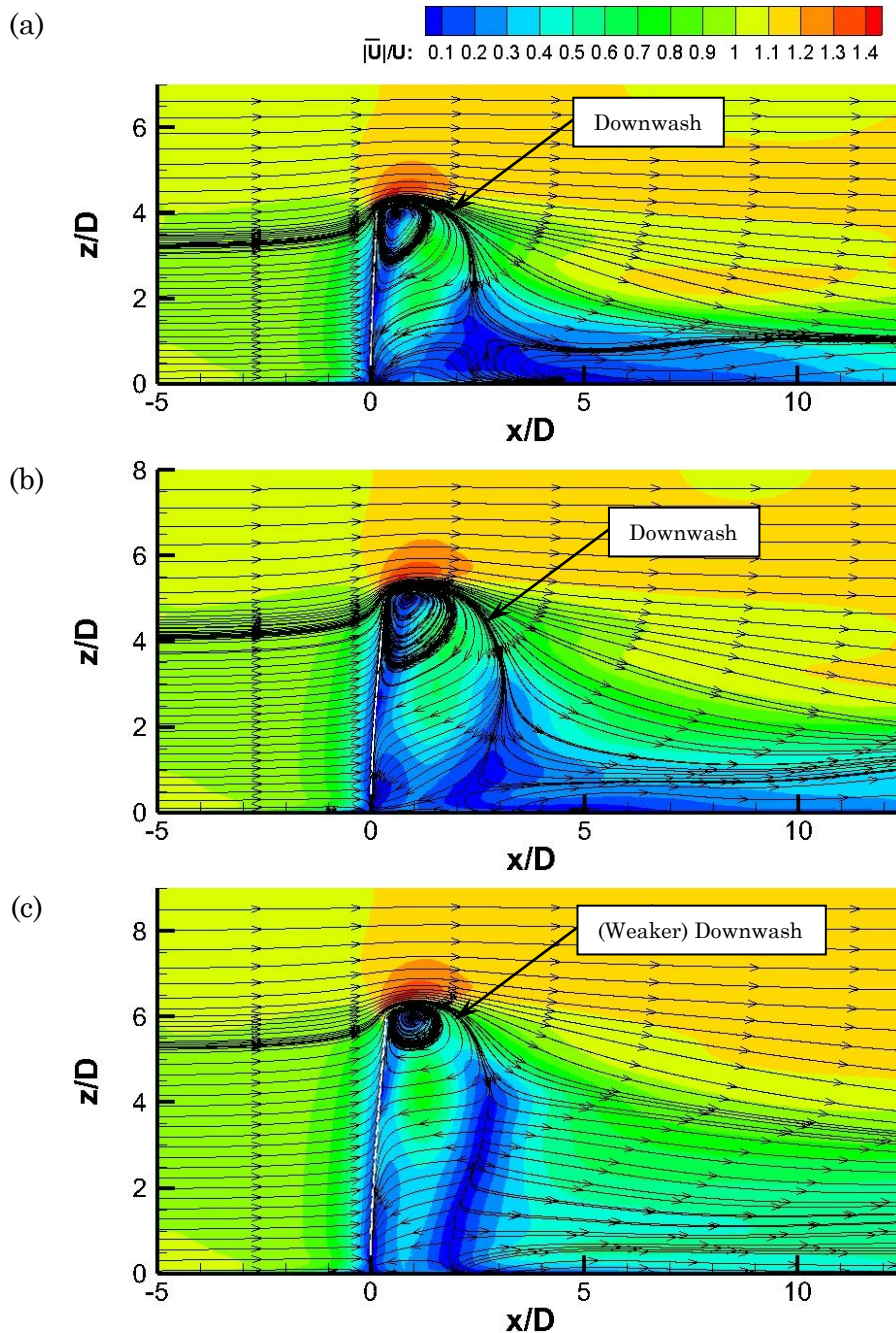


Figure 5.7: The streamlines of the normalised mean velocity magnitude at the plane of symmetry ( $y/D=0$ ) of circular FVG with (a) AR=6, (b) AR=8, and (c) AR=10.





**Figure 5.8: The streamlines of the normalised mean velocity magnitude at the plane of symmetry ( $y/D=0$ ) of flat plate FVG with (a)  $AR=4$ , (b)  $AR=5$ , and (c)  $AR=6$ .**

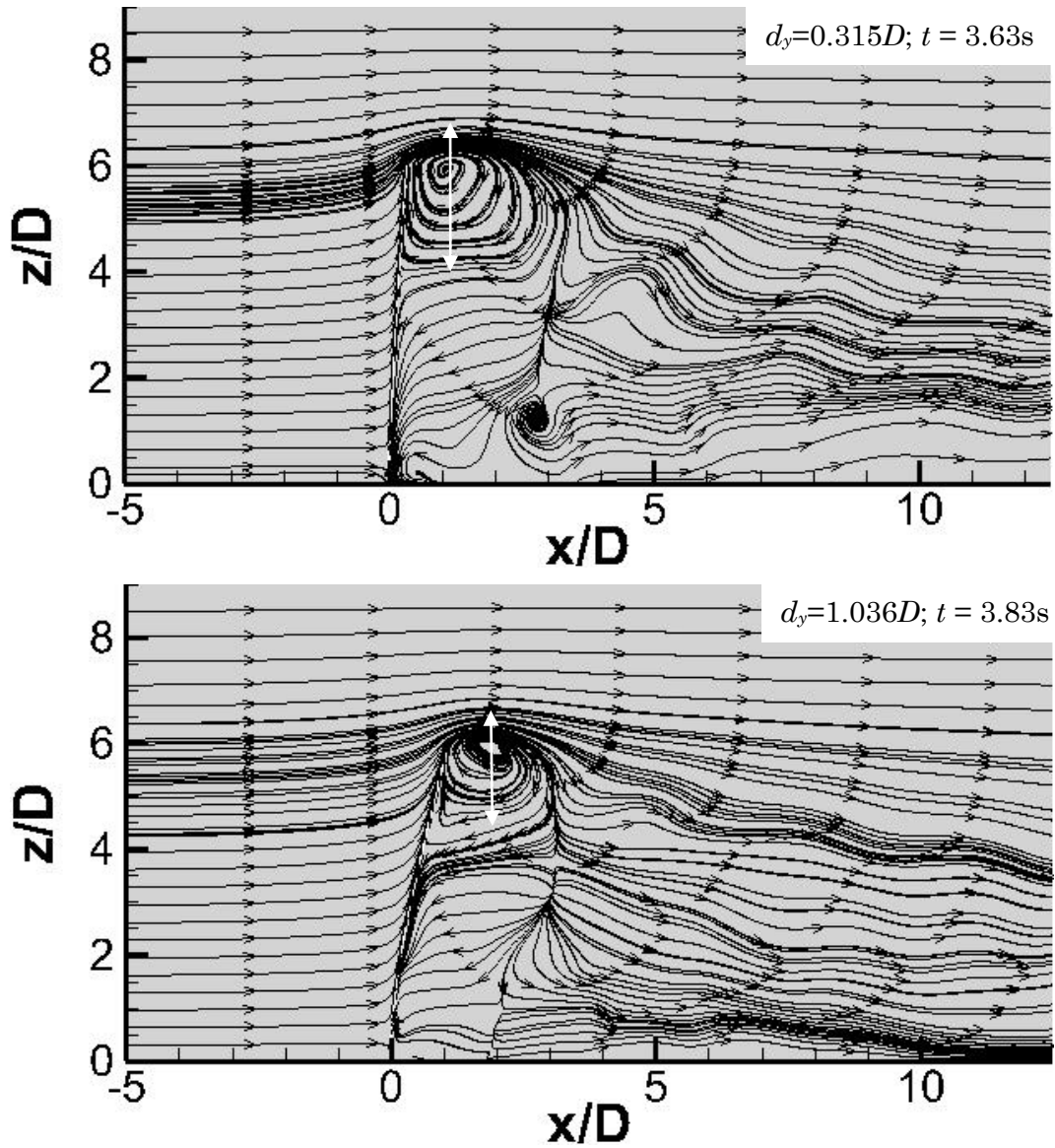
Now, it is known that the downwash behind a FVG is vanished/weaker, but what has caused the phenomenon? There are two important facts that need to be considered in order to answer the question. First, the oscillating FVG consists of two major aspects that distinguish itself from a RVG, *i.e.* the degree of deflection (that describes the magnitude of bending) and the oscillation responses (that includes the frequency, the peak-to-peak amplitude and others).

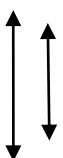


Secondly, an oscillating FVG must have a certain degree of deflection; in contrast, a deflected FVG may not have oscillation (it can be a steady deflection). Therefore, it is important to identify whether the vanishing or weakening downwash is caused by the deflection or the oscillation. This is important as it provides an insight to control the flow behaviour.

Firstly, considering the wake behaviour of the circular FVG, the previous discussion shows that the downwash behind the circular FVG has vanished regardless of its AR and most importantly, the wake of the considered circular FVGs have equivalent height with the FVG's AR (*i.e.*  $\overline{h_{w(FVG)}} \approx AR$ ) regardless of AR. However, from the  $x$ - and  $y$ -deflection responses, which are attached in Appendix II, it shows that the FVGs have varying oscillating frequency and peak-to-peak amplitude. In short, the wake of circular FVG is behaving the same even though each case has its own distinctive oscillation response. The result suggests that the weakening of downwash behind the FVGs is not a product of FVG's oscillation. If the disappearance/weakening of downwash is due to the oscillation, the wake behind the low AR circular FVG will not behave the same as the high AR case. To put it differently, the  $6_{CF}$  should not have a similar wake behaviour with the  $10_{CF}$  since they have different oscillation responses (*i.e.* different oscillating frequency and peak-to-peak amplitude). Due to this fact, the phenomenon must be caused by other factors. More information has to be evaluated for understanding this phenomenon.

Meanwhile, by evaluating the flow field behind the flat plate FVGs, it is noticed that the downwash remains its size at  $4_{PF}$  and its size decreases in the case with higher AR. Since it is known that the downwash is unaffected by the oscillation-related parameters as discussed in the previous paragraph, it is suspected that the second characteristic of the FVG – the deflection is the cause of the phenomenon. For this purpose, the evolution of the streamlines plot at the plane of symmetry of the  $6_{PF}$  is examined to search for the evidence of the mentioned speculation. The streamline evolution is illustrated in Figure 5.9. Based on the figure, as the  $x$ -deflection increases, the effect of recirculation becomes weaker and its size decreases; in contrast, when the  $x$ -deflection decreases, the recirculation regains its size. This observation has shown that the degree of deflection has a direct relationship to the presence and characteristic of the downwash.




 These arrows are the copies (with exact same size) that are used in the figures to mark the size of the recirculation zone in the figures. The arrows are placed side-by-side: (left) represents the top figure; (right) represents the bottom figure respectively, to show the size difference between the two recirculation zones.

**Figure 5.9: The streamlines plot at the plane of symmetry ( $y/D=0$ ) of AR=6 flat plate FVG at (top)  $t = 3.63\text{s}$  and (bottom)  $t = 3.83\text{s}$ .**

The postulation above is also capable of providing an answer to the question “*why the downwash survives behind the low AR flat plate FVG but it vanishes behind a low AR circular FVG?*”. It is known that the pressure drop – that lead to the formation of the downwash – behind a flat plate cantilever is always greater than that behind a circular cantilever (it can be seen by comparing their drag coefficients: the drag coefficient of flat plate is always greater than circular cylinder under the same flow condition). Therefore, a flat plate cantilever has to bend more (to reduce its angle of attack in order to attain a streamlined body) compared to circular cantilever to weaken the pressure drop between the upstream and downstream. Consequently, a small deflection of flat plate cantilever (such as the 4PF) is not capable of weakening the pressure drop, so the downwash still occurs. On the other hand, the condition is less critical for the circular cantilever; so minimal bending should be able to work out sufficiently to weaken the downwash.

As a result, it has been shown that the weakening/vanishing of the downwash that leads to a higher wake is a production of deflection. The effect becomes more significant if the magnitude of the deflection increases. Besides, it is important to note that only the deflection in the direction of flow (positive  $x$ -deflection) is capable of inducing this phenomenon. In order to further confirm this speculation, a separate study is recommended to study on a flow past a rigid, non-oscillating bent cylinder so that the effect of oscillation can be completely eliminated and the pure effect of the bent cylinder can be examined.

## 5.2 Wake of the FVG and RVG ( $x$ - $y$ plane)

The previous discussion focuses on the height of the generated wake. Since the circular FVG is oscillating in the  $y$ -direction as well, the width of the wake may also be affected. Since the location of vortex shedding is constantly shifting, in the  $y$ -direction, the wake width of the circular FVG is expected to be greater, according to the amplitude of the oscillation, than the RVG’s. Note that only the wake width of the circular RVG and FVG are discussed in this section. Flat plate cases are not considered because it does not involve any motion in the  $y$ -direction.

Similar to the previous discussion, the  $\Lambda_2$  iso-surface as shown in Figure 5.10 and Figure 5.11 is used to demonstrate the vortical structures in the wake, but it is viewed from the top instead (focusing on  $x$ - $y$  plane). Based on the

figure, it is found that the wake width between the FVG and RVG does not differ significantly. In fact, the final width (at  $x/D=12.5$ ) is approximately the same between the RVG and FVG, for all ARs. Only the near wake (*i.e.*  $x/D < 5$ ) of the FVG has slightly wider wake. The result suggests that the mentioned cause that may lead to a wider wake is only affecting the near wake.

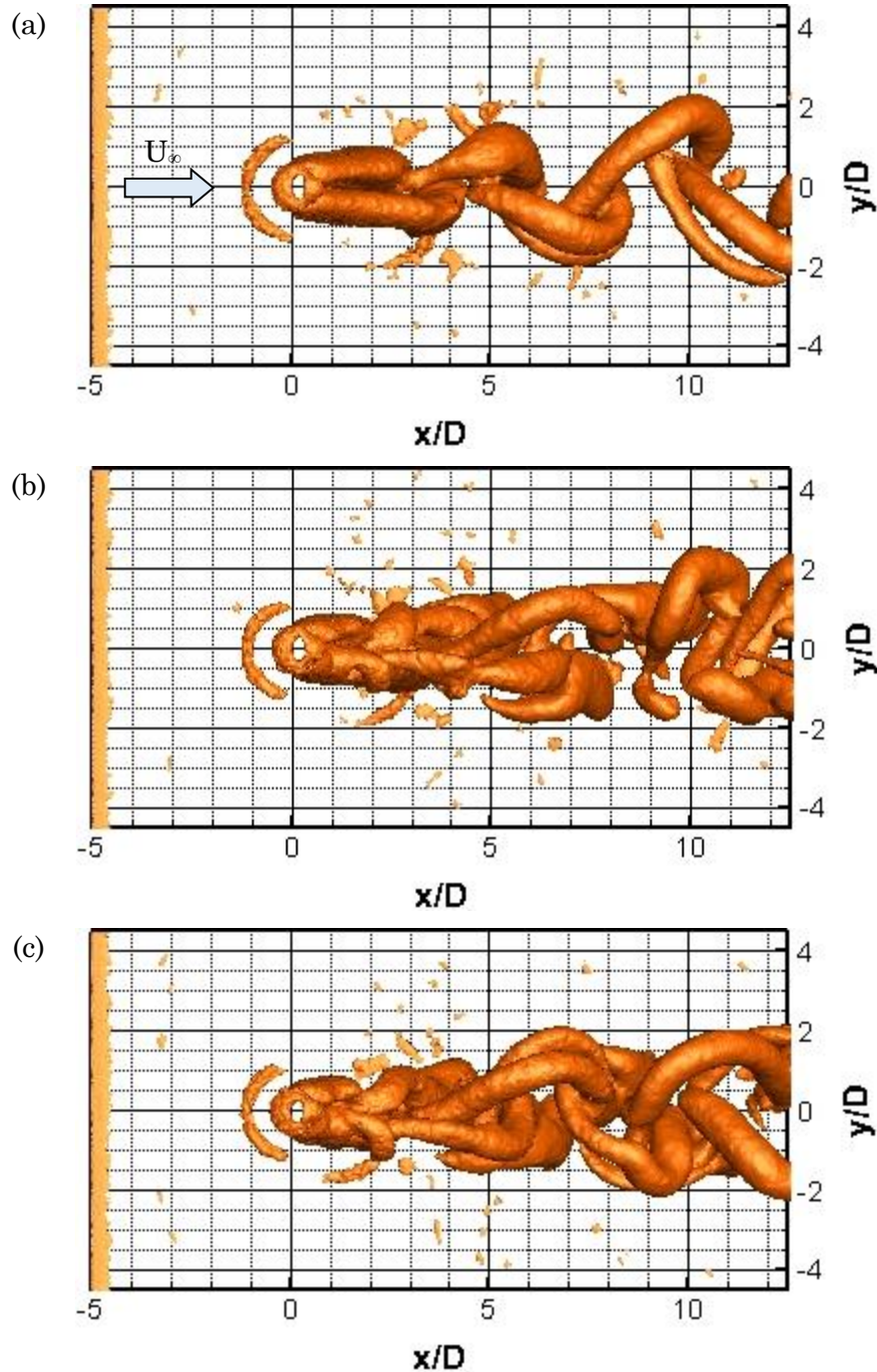


**Figure 5.10: The  $\lambda_2$  ( $\lambda_2$ ) iso-surface,  $\lambda_2=-100$ , in the  $x$ - $y$  plane, of the circular RVG with (a) AR=6, (b) AR=8, and (c) AR=10.**

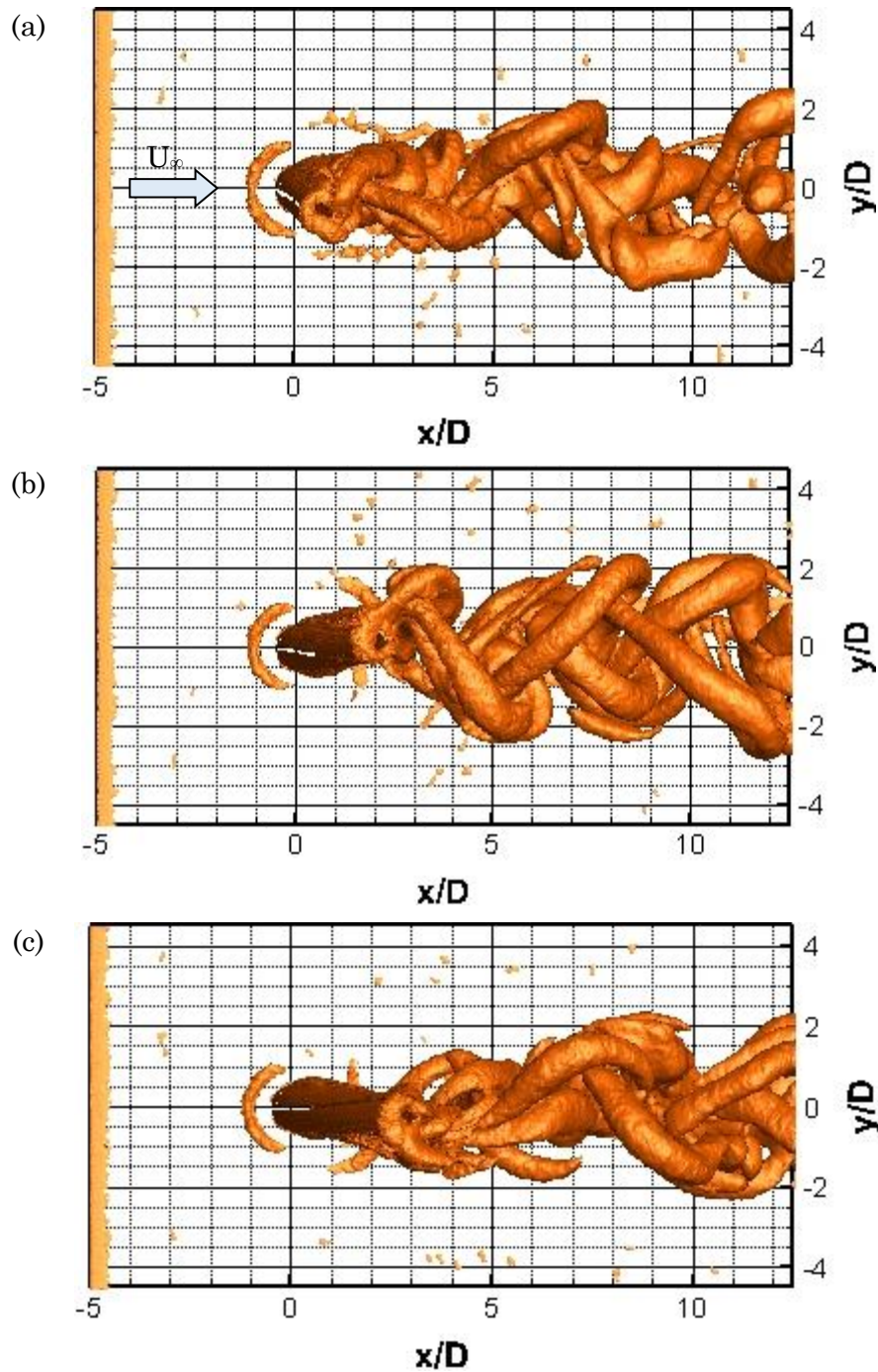
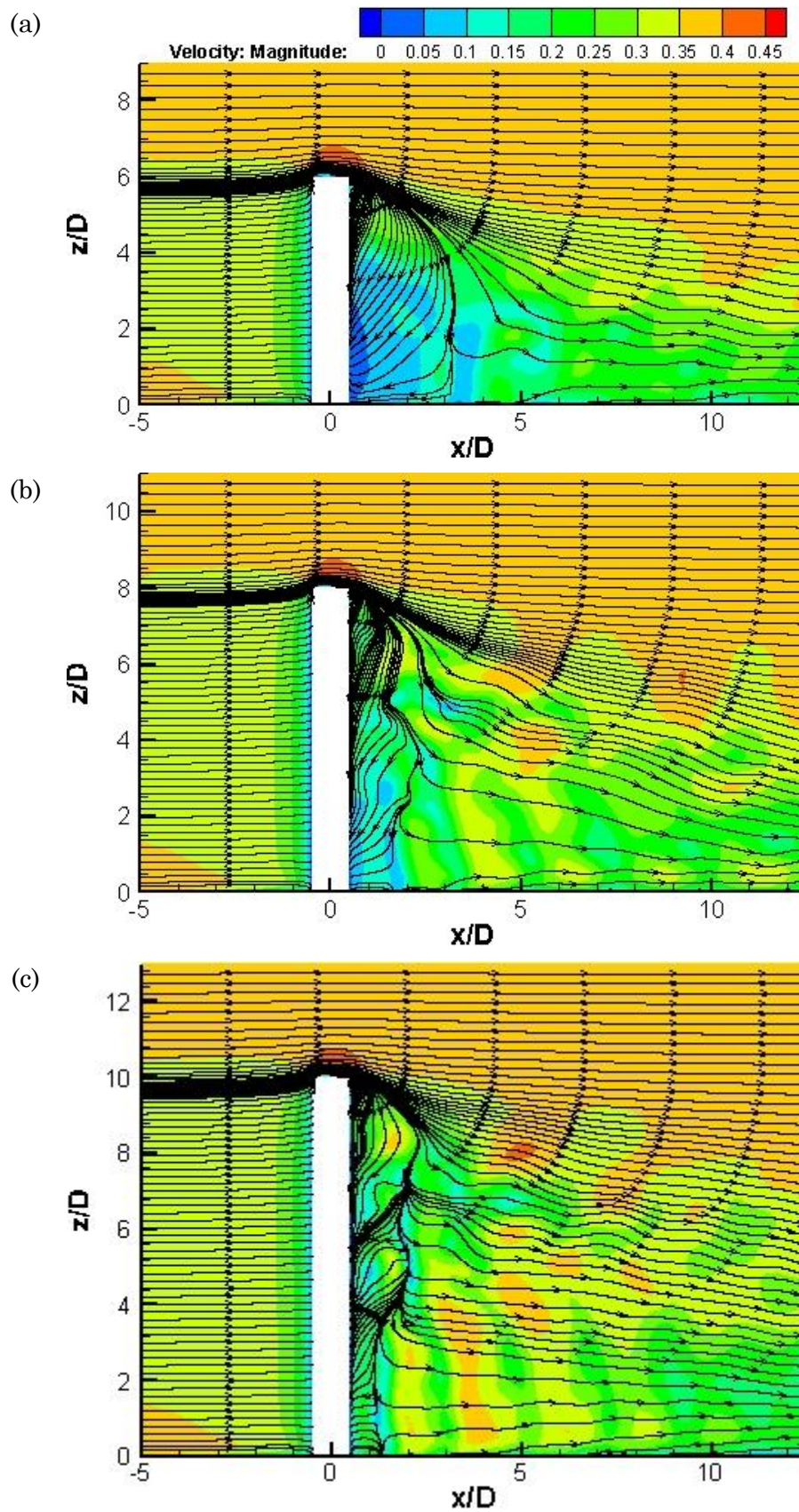


Figure 5.11: The  $\lambda_2$  ( $\lambda_2$ ) iso-surface,  $\lambda_2=-100$ , in the  $x$ - $y$  plane, of the circular FVG with (a)  $AR=6$ , (b)  $AR=8$ , and (c)  $AR=10$ .

### 5.3 Vortical Activities Analysis

Apart from the size difference, the visualisation of the instantaneous streamline can also provide an insight regarding the flow dynamics in the wake. The instantaneous streamline plots at the plane of symmetry are shown in Figure 5.12 to Figure 5.15.





**Figure 5.12: The instantaneous streamlines at the plane of symmetry ( $y/D=0$ ) of circular RVG with (a)  $AR=6$ , (b)  $AR=8$ , and (c)  $AR=10$ .**

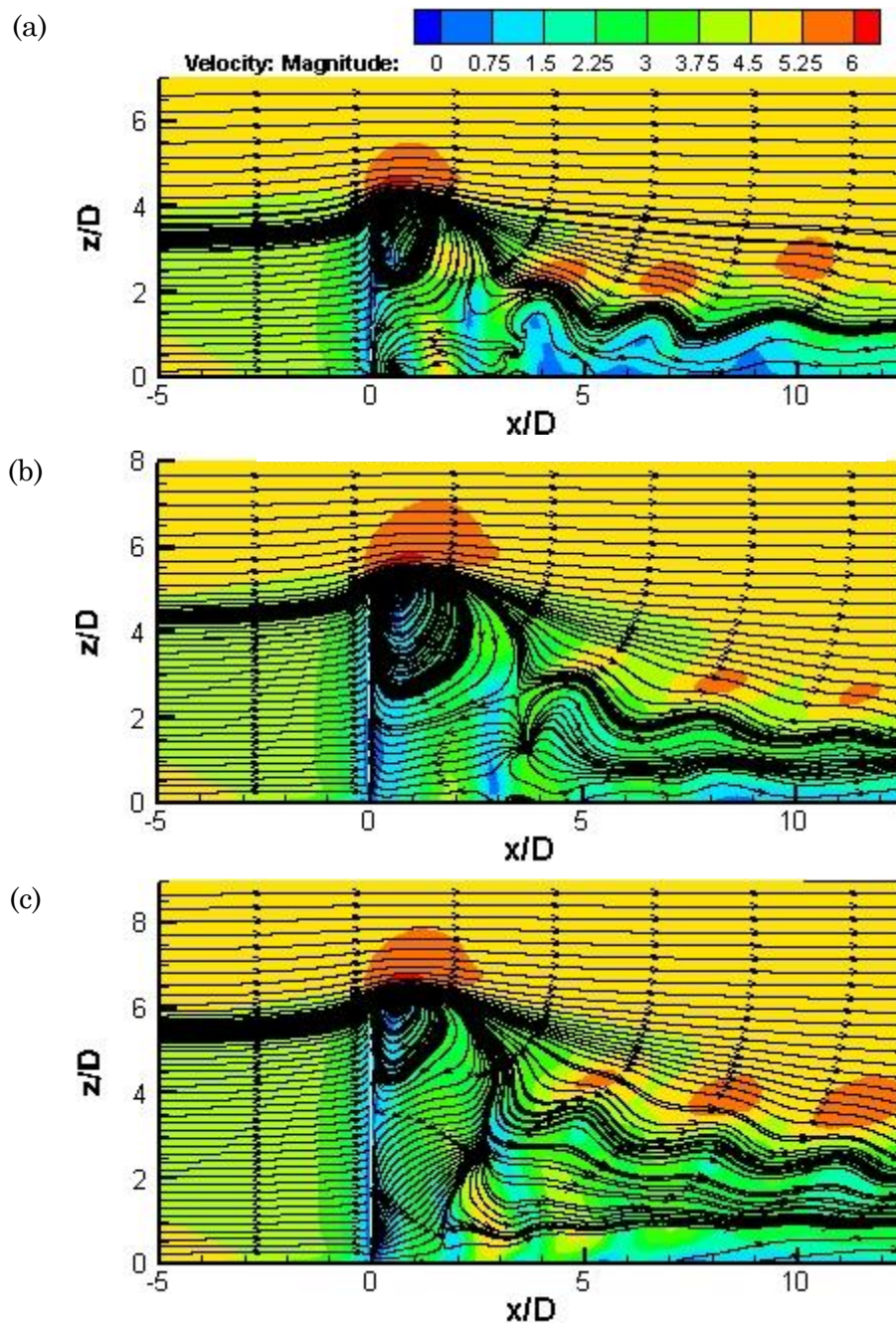


Figure 5.13: The streamlines at the plane of symmetry ( $y/D=0$ ) of flat plate RVG with (a)  $AR=4$ , (b)  $AR=5$ , and (c)  $AR=6$ .



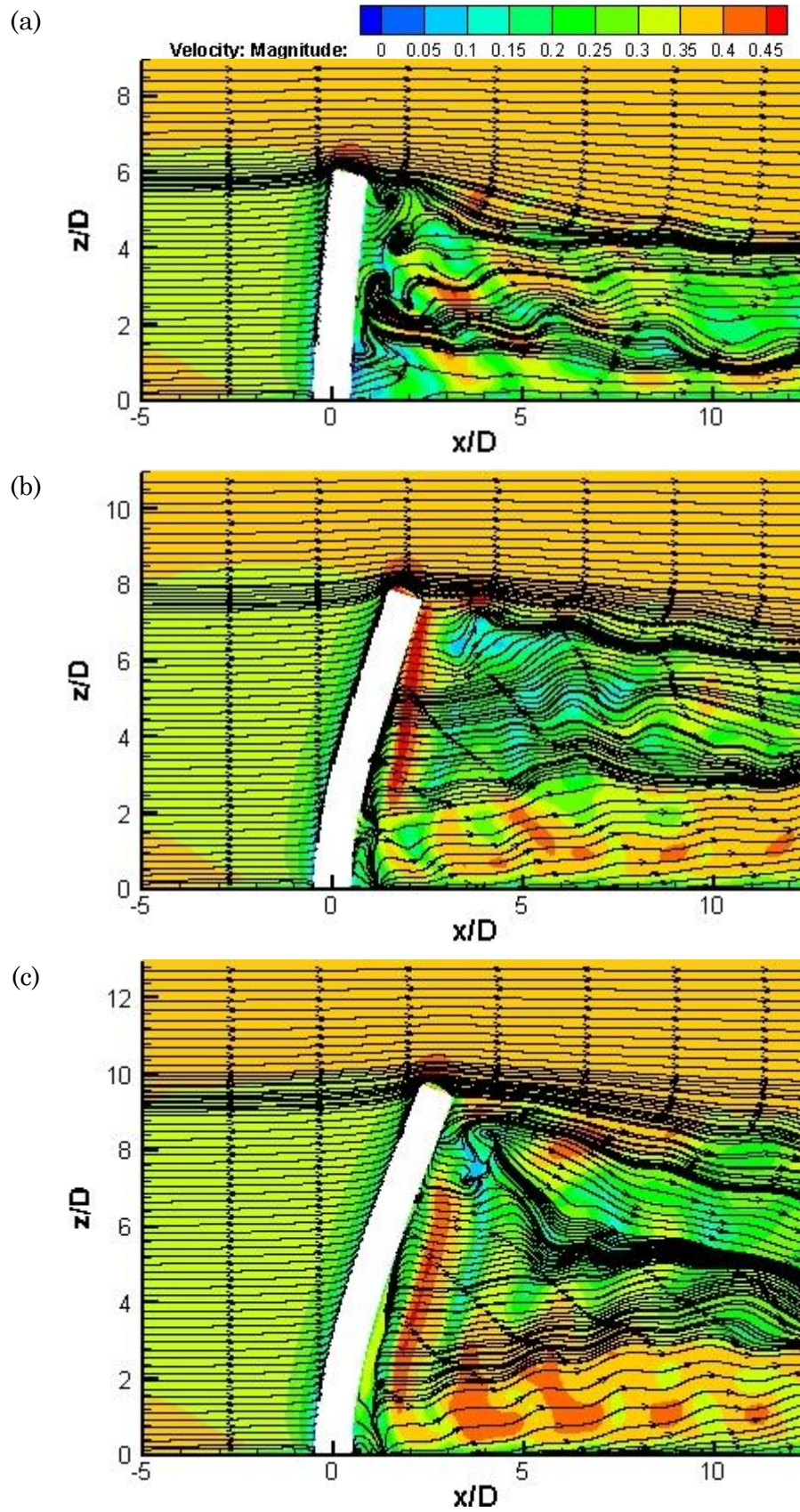


Figure 5.14: The instantaneous streamlines at the plane of symmetry ( $y/D=0$ ) of circular FVG with (a) AR=6, (b) AR=8, and (c) AR=10.



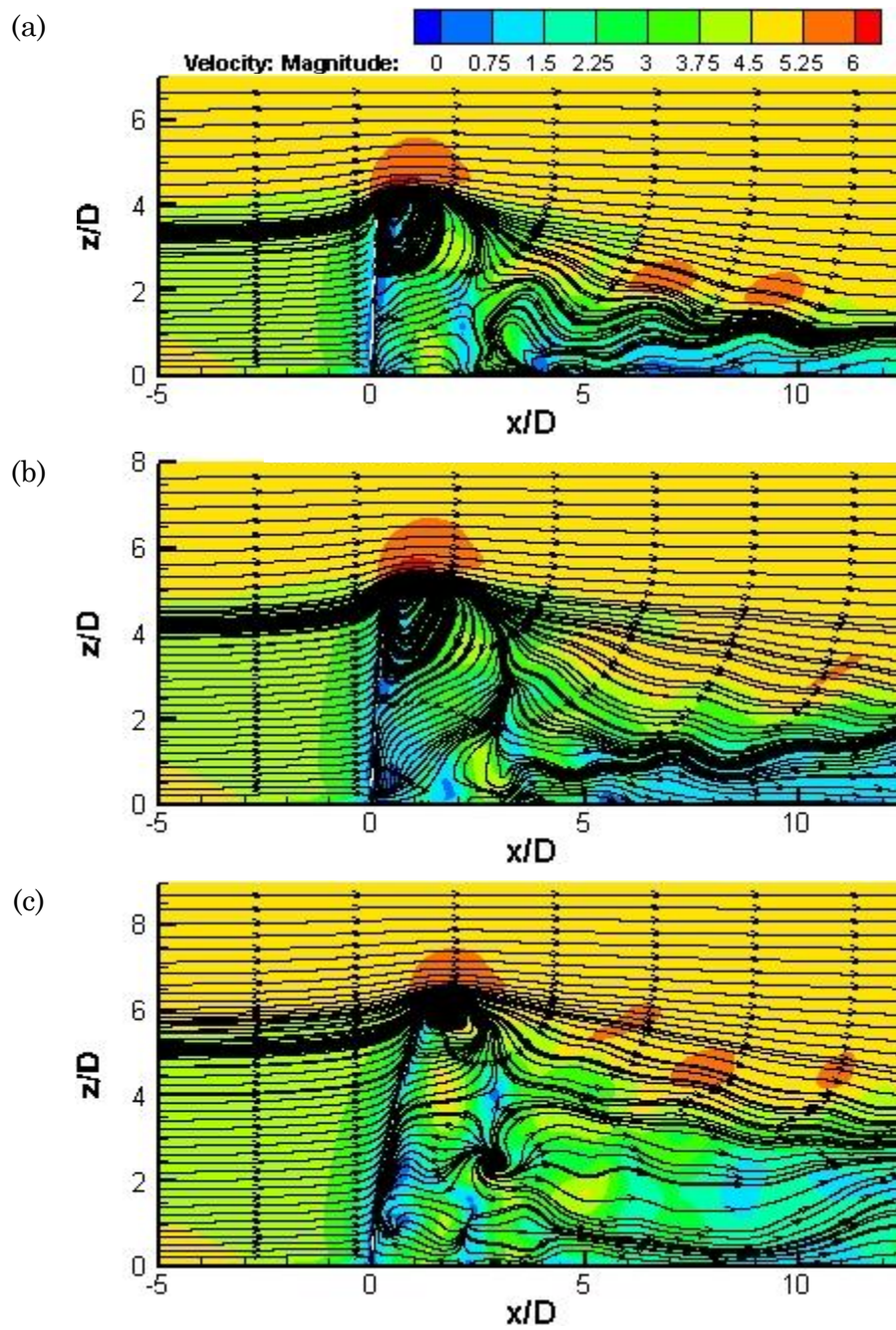
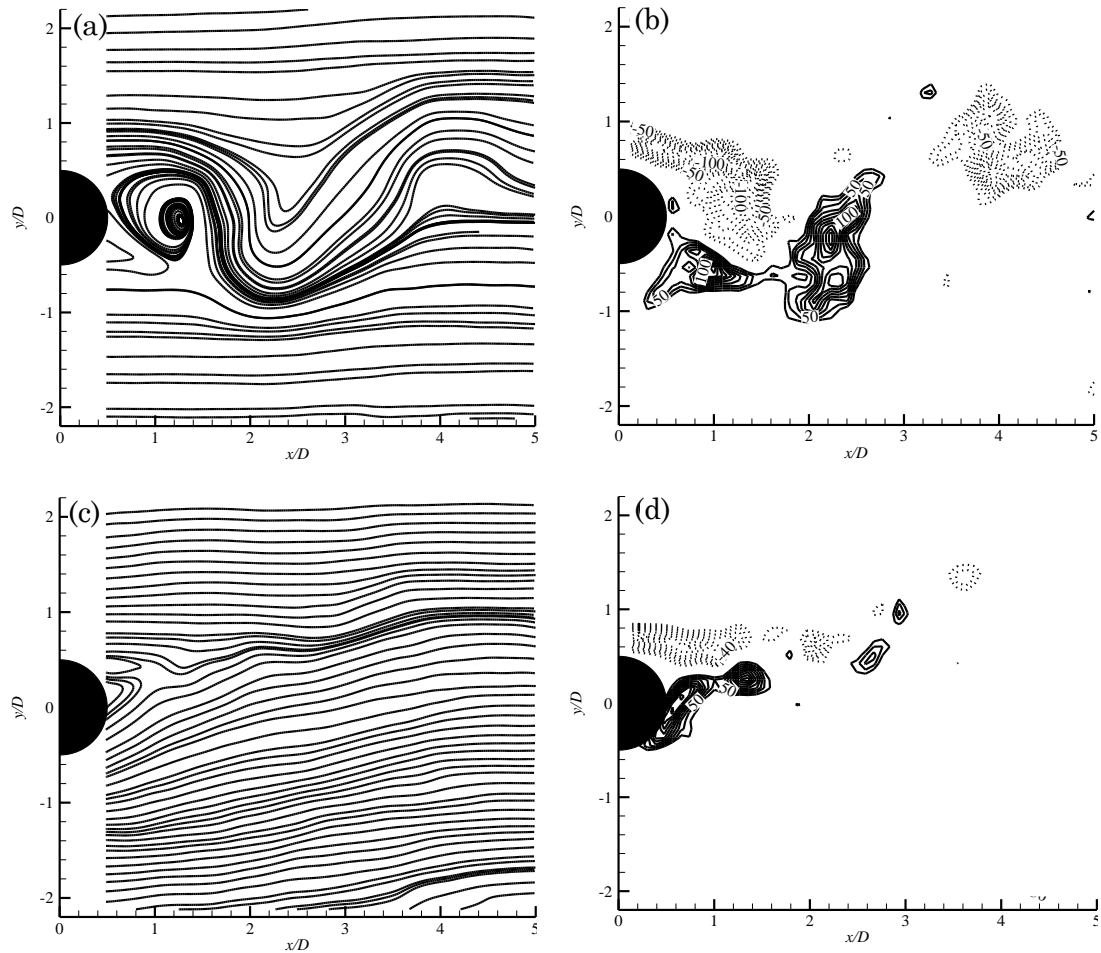


Figure 5.15: The streamlines at the plane of symmetry ( $y/D=0$ ) of flat plate FVG with (a) AR=4, (b) AR=5, and (c) AR=6.

First of all, it can be observed that the degree of waviness of the streamlines in the wake of the FVGs are greater than that in the wake of the RVGs. This waviness of streamline is known to be a signature of vortical activities presenting in the flow field. Thus, it is capable of providing a simple, yet a straightforward evidence of the quality of vortical activities in the wake. A published work is used to justify this statement.

According to Dol *et al.* (2008), the waviness appears to be more significant when strong vortical motion is present in the flow field (the results obtained by Dol *et al.* are presented in Figure 5.16). Figure 5.16(a) and (b) depict the streamlines plot behind a stationary circular cylinder and its instantaneous vorticity contour, respectively. Based on the figures, it can be clearly observed that the streamlines curve according to the presence of vorticity in the field. On the other hand, the flow behind a rotating cylinder behaves differently compared to that of a static cylinder. In this case, the rotating cylinder serves as a strategy of vortex suppression (Dol *et al.*, 2008). Therefore, as expected, the vortical activities behind the rotating cylinder were actively suppressed, which can be seen from the vorticity contour plotted in Figure 5.16(d). It is important to note that the streamlines lost most of its waviness simultaneously; as shown in Figure 5.16(c). These results have clearly displayed the correlation between the streamlines and the vorticity, where a greater waviness is shown if stronger vortical activities are present.

Based on the discussion above, it suggests that the wake of FVGs has stronger vortical structures than that of a RVGs. This postulation shall be justified, quantitatively, in the next chapter.



**Figure 5.16: (a) Streamline plot behind a stationary circular cylinder; (b) Instantaneous vorticity behind a stationary cylinder; (c) Streamline plot behind a rotating circular cylinder; (d) Instantaneous vorticity behind a rotating cylinder. (a) to (d) are adapted from Dol *et al.* (2008).**

### Summary of Chapter

In this chapter, a qualitative discussion is presented by analysing the visualised wake behind the FVGs and the RVGs. The major conclusion that can be drawn from this chapter is the size difference between the wake of the FVGs and the wake of RVGs. Based on the analysis, the wake of a FVG is generally larger than the wake of a RVG. A larger wake denotes a larger effective region where turbulence events can take place. Thus, the size increment of the wake can be translated into a direct evidence of turbulence enhancement. Besides, it is speculated this wake modification is caused by the deflection (*i.e.* the bending) of the FVG instead of the oscillating motion. A separate study can be conducted to examine the wake behind a rigid, non-oscillating bent cantilever to further confirm this speculation. Besides, the width of the wake is found to be similar between the FVG and RVG, regardless of AR.

Furthermore, through analysing the waviness of the streamlines in the flow field of FVGs and RVGs, it is noticed that the wake of the FVGs contains stronger vortical activities compared to the wake of RVGs. This observation will be justified in the next chapter.

In the next chapter, the turbulence quality of FVG shall be examined and discussed, quantitatively, through examining the shear component of the flow field.

## Chapter 6: Turbulence Characteristics

This chapter analyses and discusses the turbulence characteristic generated by the FVGs. According to the kinetic energy budget equations, which has been discussed in Chapter 2, it is clear that the flow shear has been an important aspect of turbulence generation. Therefore, the analysis method that is discussed in this chapter will focus on various types of shear. The importance and significance of focusing on shear in this analysis will be identified.

The results obtained from the shear analysis serve as a measure to identify the turbulence enhancement generated by the FVGs and RVGs. By comparing the results, it also provides an insight on the modifications in performance by replacing RVG with the FVG.

A similar abbreviation, which is introduced in the previous chapter, is used in this chapter to simplify the description of R/FVG in different ARs, as shown below.

$$\begin{array}{l} \delta_{CF} \\ \left\{ \begin{array}{l} \text{F: FVG or R: RVG} \\ \text{C: Circular or P: Flat Plate} \\ \text{The Aspect Ratio: AR = } \delta \end{array} \right. \end{array}$$

### 6.1 The shear rate in boundary layer: Wall shear stress

As discussed previously, flow's shear is the main focus of the current research. First of all, the shear in the VG's boundary layer can be studied in a rather straightforward approach. It can be done by analysing the wall shear stress ( $\tau_w$ ) – Equation 6.1 – that defines the shear stress exerts on a solid wall (in this case, on the VGs).

$$\tau_{w,i} = \mu \frac{\partial U_i}{\partial x_j} \quad (6.1)$$

According to the equation, it can be seen that the  $\tau_w$  is the product of the shear rate and the dynamic viscosity ( $\mu$ ) of the flowing fluid. Since the dynamic viscosity is constant for a given fluid, the equation has directly shown that the wall shear stress is a direct linear function of the shear rate. So, it scales directly to the shear rate at the wall.

It is worth to mention that  $\tau_w$  is a vector, which means that there are at least two  $\tau_{w,i}$  components exerting on a surface, where the third component may be zero if the surface is normal to a primary axis, *i.e.*  $x$ -,  $y$ - or  $z$ -direction. However, this also means that a single  $\tau_{w,i}$  component is incapable of providing the full picture of the  $\tau_w$  distribution. Since the direction of the  $\tau_w$  is less important in the current study, the  $\tau_w$  magnitude is examined instead, which allows one to determine the  $\tau_w$  behaviour on all walls at once.

In this discussion, the observations of circular and flat plate VGs will be presented first, followed by examining the cause of the observed behaviour.

### 6.1.1 Wall Shear Stress on the Circular RVG and FVG

Figure 6.1 depicts the wall shear stress ( $\tau_w$ ) contour on both circular RVG and FVG. As shown in Figure 6.1a, the local maximum wall shear stress ( $\tau_{w,max}$ ) occurs in the vicinity of the RVG's free end. A Similar observation can be seen on FVGs as well, as shown in Figure 6.1b, where the maximum wall shear stress is also located in the vicinity of the FVG's free end. That is the region where the flow accelerates over the top of the free end, hence creating shear concentration point in both cases.

Next, by comparing the RVG's  $\tau_w$  contour in different ARs, it is found that the  $\tau_w$  contour does not differ significantly with varying AR. This observation suggests that the magnitude of the wall shear stress is not influenced by the variation of AR. Thus, the effect of the geometrical factor can be eliminated from the analysis. With reference to the observation discussed above, if the  $\tau_w$  contour on FVG case is found to be altered at different AR (it is, in fact, changing with different AR), it is suggested that it is not caused by the changing of geometrical parameters such as length or diameter. Indeed, it is due to the structural dynamics factors, such as the degree of deflection and oscillation, which scale with the AR. In structural dynamics, a cantilever (e.g. the FVG) with a larger AR experiences greater deflection and oscillation. To be specific, it scales with the increasing length and/or decreasing diameter of the cantilever that leads to the reduction of structural stiffness ( $k$ ). Consequently, the cantilever experiences greater deflection and oscillation. In short, the  $\tau_w$  is less dependent on the geometrical aspects defined by AR; instead, it is strongly linked to the structural dynamics aspects induced by varying AR.

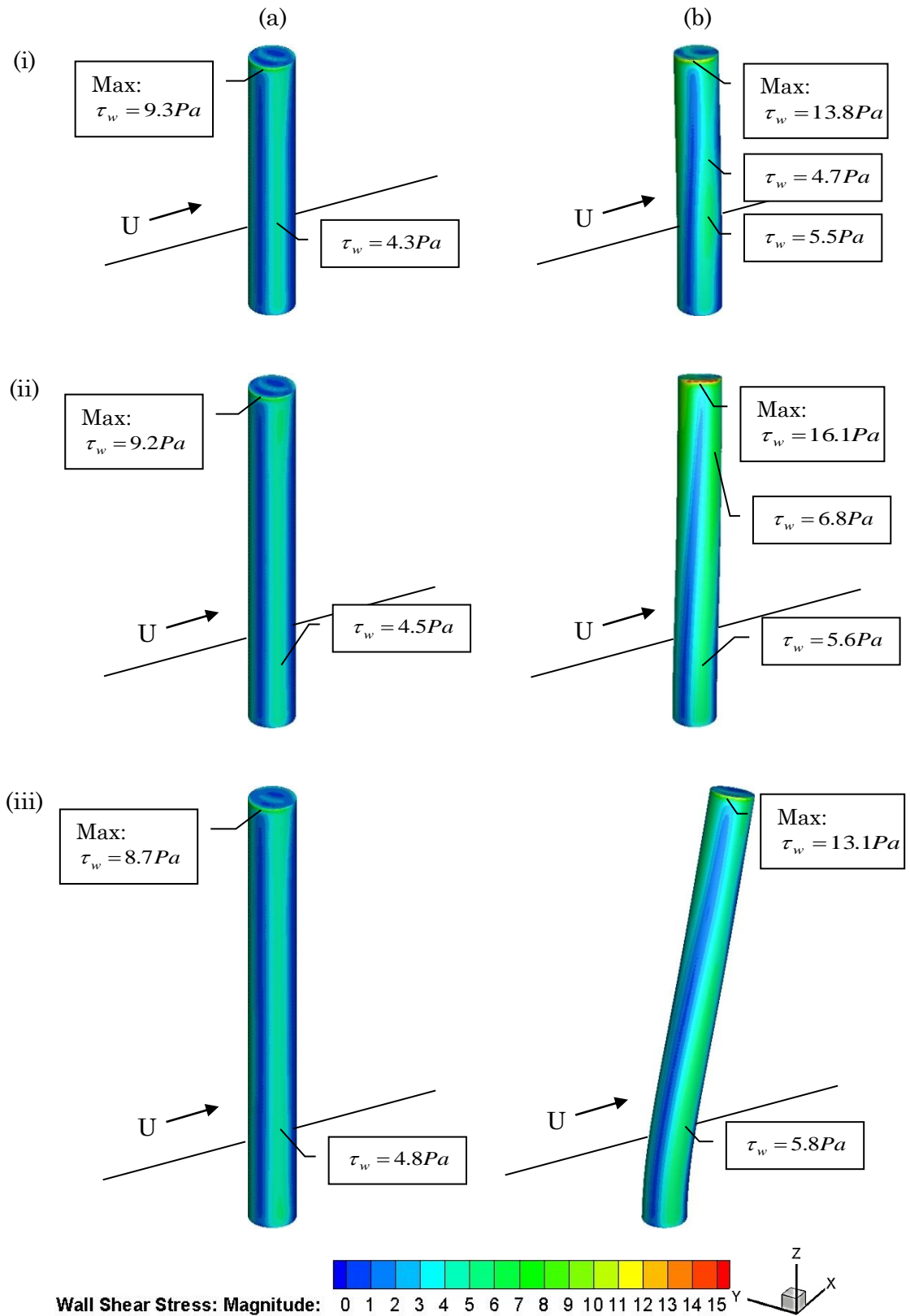


**Figure 6.1: Instantaneous wall shear stress magnitude (Pa) contour on (a) the circular RVG and (b) the circular FVG with (i) AR=6, (ii) AR=8 and (iii) AR=10.**

On the other hand, a distortion of  $\tau_w$  contour on the FVGs is noticed. This distortion is mainly caused by the motion of the FVGs, which is evidenced by the shifting of the stagnation point (the local minimum of  $\tau_w$  that is facing the flow). The  $\tau_w$  contour can signify different part of the fluid structure on the cylinder cantilever. As the fluid is flowing across the surface, a boundary layer is formed where a band of higher wall shear stress is present (refer to Figure 6.2). Vorticity is formed in the boundary layer as the fluid travels further downstream and eventually, this vorticity is fed to the forming vortex. When the forming vortex gains sufficient vorticity, or when it is interrupted by other fluid structures such as an opposition vortex, it sheds away. The shedding of the vortex leaves a sudden drop of wall shear stress on the surface, which can be seen in Figure 6.2. In other words, the end of the high wall shear stress band also signifies the separation point of the flow.

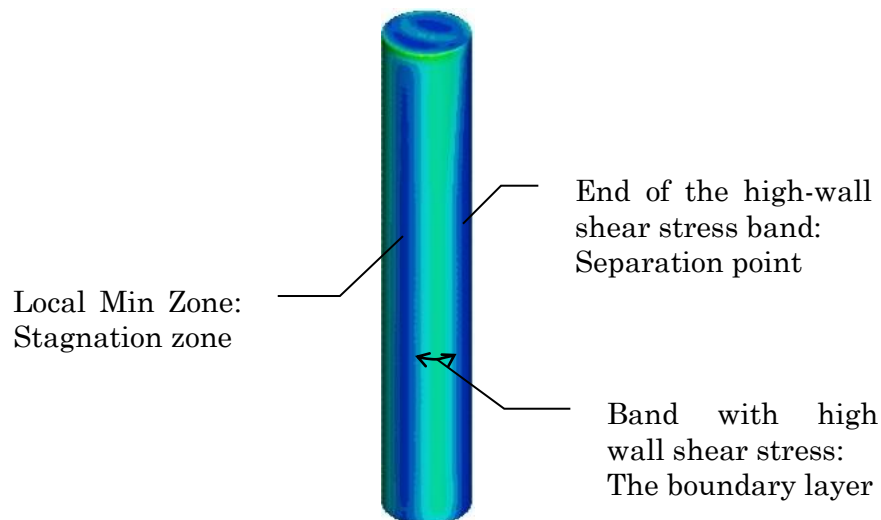


**Figure 6.2: Labels of flow zones based on wall shear stress contour.**

Apart from the change of the  $\tau_w$  contour distribution pattern between RVGs and FVGs, the difference in the  $\tau_w$  magnitude between the RVG and FVG can also be observed. In fact, this magnitude difference is one of the important measures that helps to distinguish FVGs from RVGs, in term of turbulence generation. Based on Figure 6.1, it is observed that the  $\tau_w$  on the FVGs is greater in magnitude than its respective rigid counterpart. By replacing RVGs with the FVGs, the  $\tau_{w,max}$ , which is located at the free end, increases approximately 48.4%, 75.0%, and 50.6% for AR=6, 8 and 10 respectively. Apart from this, the localised  $\tau_w$  on the surface of the FVG also experiences an



increment, ranging from 9.3% to 44.7% compared to its respective rigid counterpart. These magnitudes are labelled accordingly in Figure 6.1.

### 6.1.2 Wall Shear Stress on the Flat Plate VG and FVG

Likewise, the  $\tau_w$  on the flat plate RVG and FVG is examined in this section to investigate their shear production. The  $\tau_w$  contour on the flat plate RVGs and FVGs are demonstrated in Figure 6.3. Similar to the previous discussion, the  $\tau_w$  on the flat plate FVG is generally greater than that on a RVG with the same AR. Besides, the distribution of  $\tau_{w,\max}$  contour is also nearly independent to the varying AR; the same goes for its magnitude. Moreover, the  $\tau_{w,\max}$  – which is located at the sharp corners of the VGs – has increased 5.0%, 10.3% and 6.6% for AR=4, 5 and 6 respectively, by replacing the RVG to a FVG with the same AR.

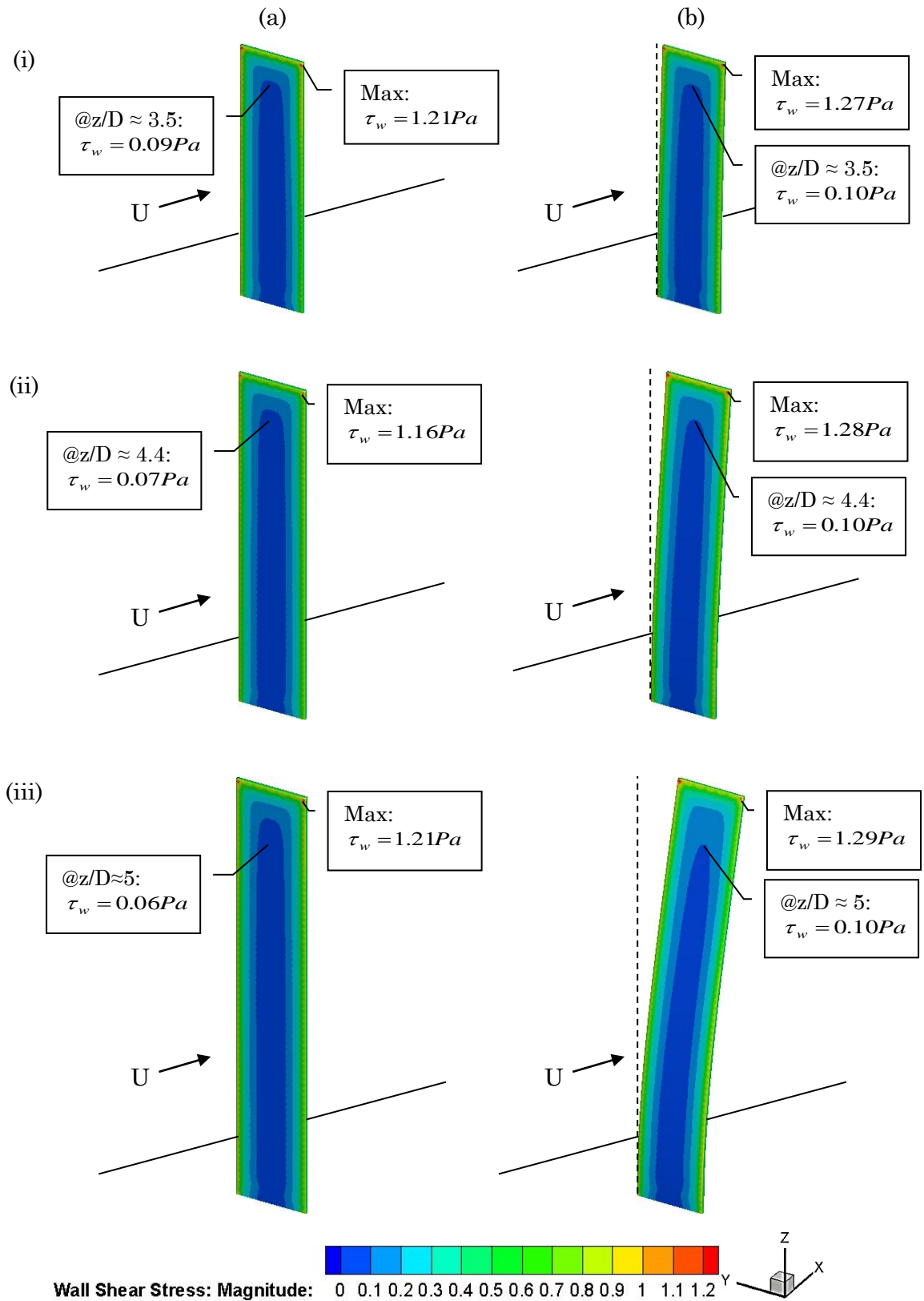


Figure 6.3: Wall shear stress magnitude (Pa) contour on (a) the flat plate RVG and (b) the flat plate FVG with (i) AR=4, (ii) AR=5 and (iii) AR=6.

Furthermore, the localised  $\tau_w$  at the region other than the free end is probed and compared between the rigid and flexible cases to quantify the improvement achieved by FVG. It is important to note that approximately the same location, on both RVG and FVG, is probed and compared in this study. The probed values are labelled in Figure 6.3. From the comparison, the computed improvements are 11.1%, 42.9% and 66.7% for AR=4, 5 and 6, respectively.

Unlike circular FVGs, the distortion of wall shear stress contour is missing in the case of flat plate FVGs. This is mainly due to the different mode of motion compared to the circular FVG. The flat plate FVGs always oscillates in the direction parallel to the flow; only  $x$ -deflection occurs. As a result, most portion of the flat plate FVG's surface remains perpendicular to the flow. Thus, the stagnation zone on the flat plate FVG does not shift its position.

### 6.1.3 Effects of Oscillation and Deflection on Wall Shear Stress Magnitude and Distribution

Based on the observation presented earlier, it is clear that the  $\tau_w$  magnitude on the FVGs is greater than the RVG's. However, the cause of this escalation is yet to be identified. For this purpose, the evolution of  $\tau_w$  contour (the time series) on the FVGs is studied to provide further insight into the cause of the escalation. The time series of the  $\tau_w$  of the circular FVG and flat plate FVG are demonstrated in Figure 6.4 and Figure 6.5 respectively.

#### 6.2.3.1 *The Effect of Oscillation*

From Figure 6.4, it can be seen that the magnitude of the  $\tau_w$  increases when the FVG is deflecting away from its initial position (when the FVG is in motion). However, when the FVG has attained its maximum deflection (when the FVG stops), the magnitude of the  $\tau_w$  reduces. The evolution of  $\tau_{w,max}$  at the free end shows the clearest changes as there is the location that experiences the greatest motion. A similar result is obtained in the flat plate FVG.

The result suggests that the increment of the wall shear stress magnitude is caused by the oscillation or the motion of the FVG instead of its degree of deflection. If this phenomenon is caused by the degree of deflection, then the  $\tau_{w,max}$  should have achieved its greatest scale when the FVG hits its maximum deflection magnitude. Since the evolution of the  $\tau_w$  does not behave in this way, it is strongly evident that the increasing shear rate happens only when the FVG is in motion.

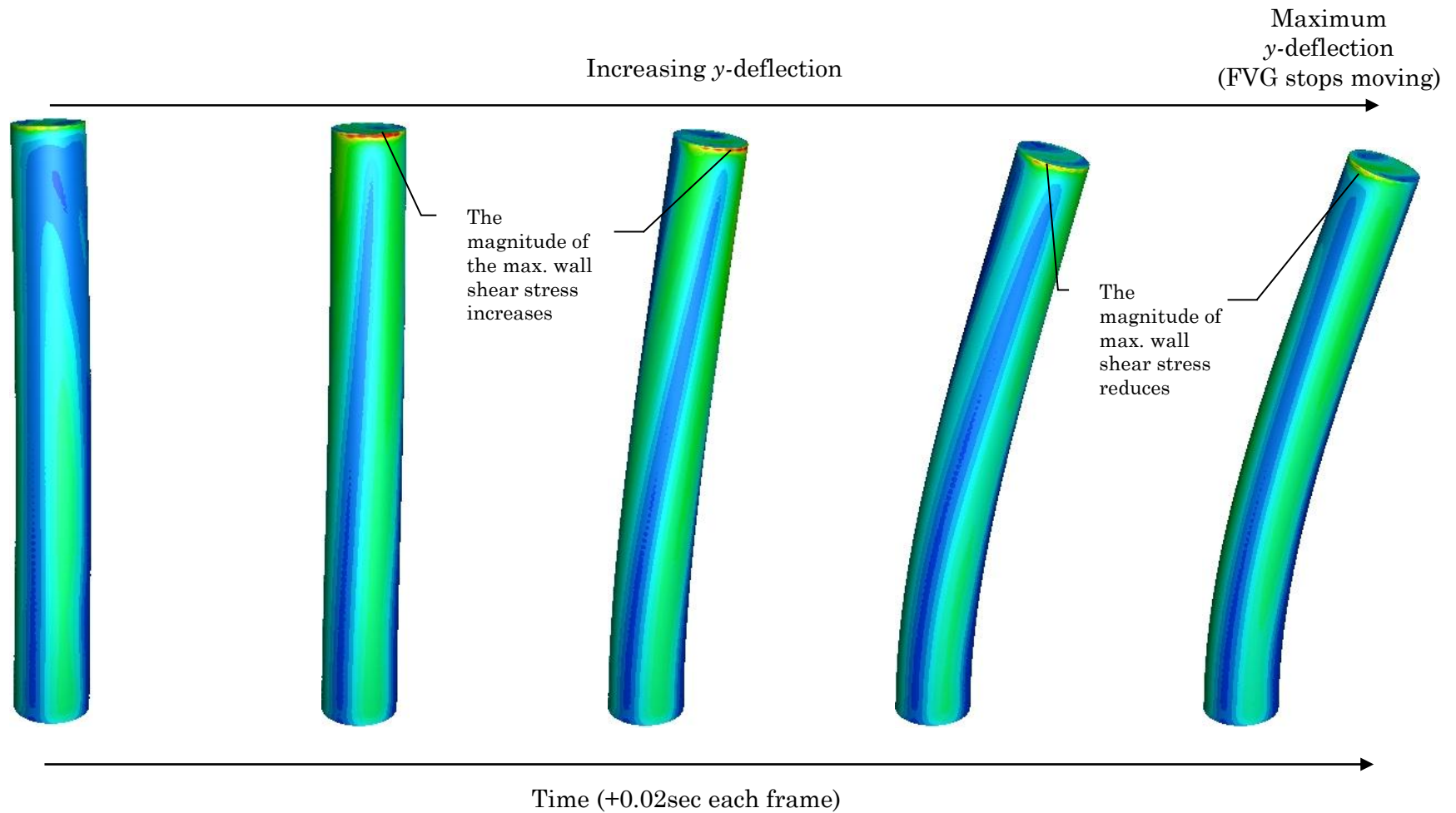


Figure 6.4: The change of wall shear stress contour on an AR=8 circular FVG as it deflects.

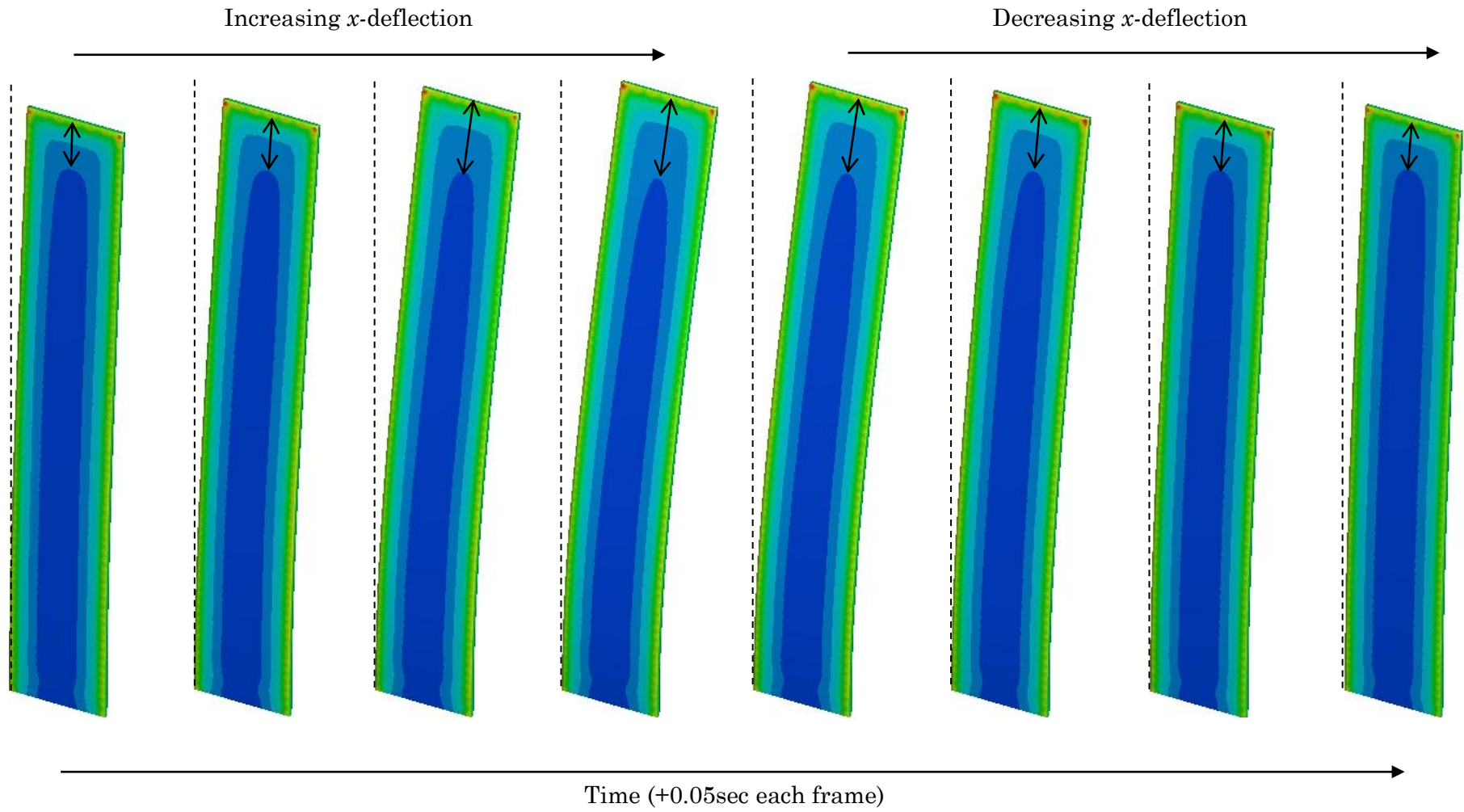
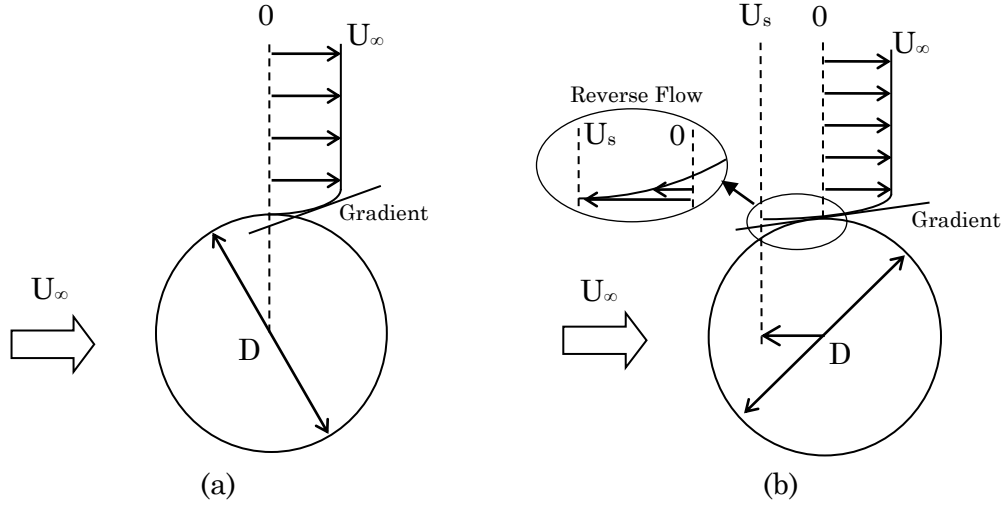


Figure 6.5: The change of wall shear stress contour on an AR=6 flat plate FVG as it vibrates.

A flow model is developed to explain this phenomenon, theoretically, by considering the relationship between the moving FVG and the velocity gradient around it. Figure 6.6 is presented to aid the explanation.



**Figure 6.6: Velocity gradient on the surface of a submerged structure: (a) stationary (b) moving against the flow with velocity  $U_s$ .**

First of all, the dynamic of a static structure is presented as a control that serves to distinguish the dynamics of a moving structure from a static one. When the structure is in static, the wall has zero velocity due to non-slip condition assumption (see Figure 6.6a). Moreover, the properties of the flow near the surface, *i.e.* the boundary layer properties, can be studied by computing the local Reynolds Number ( $Re_D$ ):

$$Re_D = \frac{\rho U_R D}{\mu} \quad (6.2)$$

where all the variables represent the same definition with those that are defined in the regular  $Re_D$  (see Equation 2.1 in Chapter 2), except  $U_R$  that represents the relative velocity experienced by the flow or structure, *i.e.*  $U_R = U_{flow} - U_{Structure}$ . So, for a static structure (Figure 6.6a), it has zero structural velocity ( $U_{Structure} = 0$ ). Then, the  $U_R$  is:

$$U_R = U_{flow} - U_{Structure} = U_{\infty} - (0) = U_{\infty}.$$

Thus,

$$Re_D = \frac{\rho U_R D}{\mu} = \frac{\rho U_{\infty} D}{\mu},$$

which is in the exact same form with the regular  $Re_D$  that has been defined in Chapter 2.

For an instance when the structure is moving in a flow, the dynamics behaves differently. In this case, the velocity of the moving structure is denoted by  $U_S$ . Let consider the case when the structure is moving in the direction against the flow's direction as shown in Figure 6.6b, then  $U_{Structure} = -U_s$  (assuming the velocity of the flow is positive,  $U_{flow} = U_\infty$ ). This negative velocity leads to a non-zero velocity at the wall of the structure and hence, drastically increases the velocity gradient at the wall. As a result, the  $\tau_w$  increases (note and compare the gradients drawn in Figure 6.6). For a moving structure (Figure 6.6b), the  $U_R$  is:

$$U_R = U_{flow} - U_{Structure} = U_\infty - (-U_s) = U_\infty + U_s.$$

Thus,

$$Re_D = \frac{\rho U_R D}{\mu} = \frac{\rho(U_\infty + U_s)D}{\mu}.$$

By comparing the  $Re_D$  of both cases, it is clear that the  $Re_D$  of the case involving moving structure is greater, *i.e.*

$$\frac{\rho(U_\infty + U_s)D}{\mu} > \frac{\rho U_\infty D}{\mu}.$$

This comparison signifies that the boundary layer of a moving object is more turbulent than that of a static object. Besides, it also shows that the escalation of  $\tau_w$  on FVG has no relationship to the degree of deflection; it is mainly depending on the travelling velocity (it is named as the structural velocity ( $U_s$ ) in this thesis) of the FVG.

### 6.2.3.2 The Effect of Deflection

Apart from the effect of oscillation, the degree of deflection should play a role in wall shear stress enhancement as well. The effect of the degree of deflection is reflected in term of its streamline-ness of the geometry that changes the behaviour of flow around a deflected FVG.

In fact, its effect can be observed from the dimensional and spatial changes of the wall shear stress contour. For instance, considering the distance between the edge of the free end (Point A in Figure 6.7) and the edge of the contour before it achieves the lowest scale (Point B in Figure 6.7), it is found that this distance is longer in the case of FVG compared to the RVG. The

observation suggests that the contour field has been modified. Furthermore, Distance AB is observed to be scaled with the AR of a FVG, *i.e.* Distance AB becomes longer (as the contour “spreads” further) when the FVG has a greater deflection.

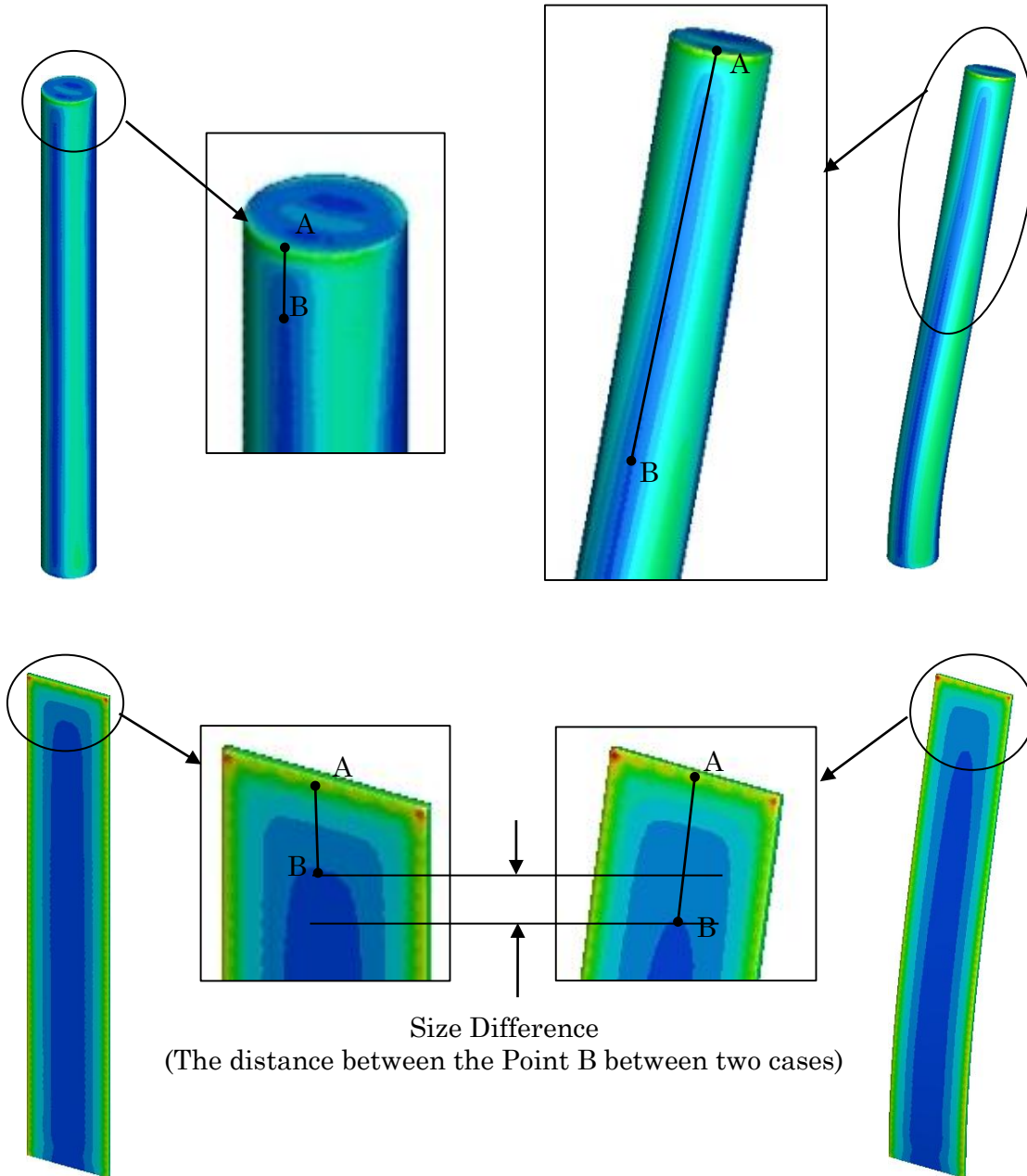


**Figure 6.7: The size difference between the wall shear stress contours of the (left) RVG and (right) FVG: (top) AR=10 circular VG and FVG and (bottom) AR=6 flat plate RVG and FVG.**



The argument above can be confirmed by examining the evolution of wall shear stress contour as illustrated in Figure 6.4 and Figure 6.5. However, the effect is less noticeable in the case of circular FVG. This is because circular FVG barely vibrates in the  $x$ -direction, thus, the distance between A and B does not change significantly (the effect of deflection is nearly constant due to minimal changes in  $x$ -deflection). Plus, the contour on circular FVG experiences severe distortion caused by  $y$ -deflection. As a result, the effect of deflection on circular FVG is overshadowed by other factors. Fortunately, the contour on flat plate FVG does not experience distortion and the degree of its deflection changes sufficiently to allow this discussion. Based on Figure 6.5, it can be seen that Distance AB increases with the increasing deflection and it reaches its maximum when the flat plate FVG attains its maximum deflection. Then, Distance AB decreases as the FVG restores from the deflection. This result serves as a strong evidence that the spatial scale of wall shear stress contour changes, directly, in response to the degree of deflection.

### 6.3 The Shear Rate in a Vortex: Circulation

The analysis of the wall shear stress in the previous section sheds light on the improving strength of the vortex generated from a FVG compared to that generated from a RVG. Furthermore, the analysis on the streamline waviness in Chapter 5 has also provided a similar insight, where the strength of the vortex in the wake behind a FVG is greater than that behind a VG. These results seem to agree with each other. To further confirm these speculations, the shear rate in the vortex shall be investigated.

The shear rate of a vortex can be examined through studying the vorticity content in a vortex. The vorticity of a region of fluid can be expressed by Equation 6.3.

$$\omega_k = \frac{1}{2} \left( \frac{\partial u_i}{\partial x_j} - \frac{\partial u_j}{\partial x_i} \right) \quad (6.3)$$

From the equation, it can be seen that the vorticity is a function of shear rate in two dimensions; for example, the vorticity in  $k$ -component is a function of shear rate in  $i$ - and  $j$ -component. In short, the vorticity is able to express the shear rates on a plane-of-interest.

However, computing and studying vorticity, alone, is not capable of expressing the strength of the vortex. Using an analogy from pipe flow, the flow velocity is rarely used to represent the effectiveness of a flow system. This is

because it does not only dependent on the flow velocity, it is also reliant on the diameter of the pipe used. For instance, given that the operating flow velocity of a pipe system remains unchanged, the output can be increased, directly, by manipulating the diameter of the pipe. This is because the parameter that determines the delivery capability of a pipe flow system is the flux (or strength) of the flow instead of the flow velocity. In fact, mass flow rate and volumetric flow rate (see Equation 6.4 and 6.5) are commonly used in the industry to identify the effectiveness of a flow system. A similar idea applies in electromagnetism, *i.e.* the electric flux or magnetic flux as well.

Mass Flow Rate (Mass flux):

$$\dot{m} = \int \rho \mathbf{U} \cdot d\mathbf{A} \quad (6.4)$$

Volumetric Flow Rate (Velocity Flux):

$$Q = \int \mathbf{U} \cdot d\mathbf{A} \quad (6.5)$$

Likewise, the effectiveness of a vortex does not depend only on its vorticity level. It is also a function of its size, in particular, its cross-sectional area. Therefore, the flux of the vorticity has to be calculated in order to quantify the strength of a vortex. This simply means that the influences of the cross-sectional area of the vortex have to be taken into account. The flux of vorticity is known as the circulation or vortex strength. Circulation ( $\Gamma$ ) in any closed loop in a fluid is the line integral of the velocity:

$$\Gamma = \oint_s \vec{U} \cdot d\vec{S}. \quad (6.6)$$

By applying Stoke's theorem, the equation is redefined to the following form:

$$\Gamma = \iint_A \nabla \times \vec{U} \cdot d\vec{A}_v = \iint_A \nabla \times \vec{U} \cdot \vec{n} dA_v. \quad (6.7)$$

It is important to note that the area ( $\vec{n}dA$ ) written in the equation refers to an area of a bounded surface that is normal to the direction of the integrand – the  $\nabla \times \vec{U}$ . It is known that the curl of velocity,  $\nabla \times \vec{U}$  represents the vorticity in the field, hence, the equation can be rewritten in the following form:

$$\Gamma = \int \omega \cdot \vec{n} dA_v, \quad (6.9)$$

which is, now, in the equivalent form with the mass flow rate and volumetric flow rate equations that have been defined earlier. In this study, the line integral method (Equation 6.6) is used to calculate the circulation.

$\Gamma$  has always been a useful tool to justify the capability of a vortex. In fact, it is constantly used in studying vortex dynamics. However, this is only

limited in two-dimensional flow. When a vortex is in a highly three-dimensional flow, the localised vorticity at different points will no longer have a unified direction due to the influences from the flow field. Thus, the job of defining the vortex area ( $dA_v$  in Equation 6.7 and 6.8) that is completely normal to the direction of its vorticity becomes extremely difficult. Consequently, to the best of the author's knowledge,  $\Gamma$  has not been used in the three-dimensional flow.

This problem arises in the present work, as well, due to the great three-dimensionality triggered by the VG's free end (as discussed in Chapter 3). To resolve this problem, the circulation in the primary axis (*i.e.*  $\Gamma_x$ ,  $\Gamma_y$  and  $\Gamma_z$  with respect to  $y$ - $z$ ,  $x$ - $z$  and  $x$ - $y$  plane accordingly) is computed to overcome the difficulty in defining the vortex cross-section, *i.e.*  $dA_v$ . However, this strategy does not overcome the issue completely as it omits the effect from the third dimension (for example, it neglects the influence from  $y$ -direction if the  $x$ - $z$  plane is considered).

With reference to this issue, the newly shed vortex (at the near wake region) is targeted in the calculation. At this stage, the vortex is behaving "more 2-dimensionally" because it has yet to be significantly contaminated by the third-dimensional flow. Figure 6.8 is presented for the purpose to support this statement. From the figure, as the vortex travels further downstream, the  $x$ -velocity ( $u$ ) and  $y$ -velocity ( $v$ ) start to fade in strength, while otherwise happens on the  $z$ -velocity ( $w$ ). It is also worth mentioning that the scale of  $w$  is weaker compared to  $u$  and  $v$  in the near wake region that signifies its weak effect in that region. In short, the influence of the third dimension velocity ( $w$  in this case) is at its weakest at near wake and it gains its strength gradually at further downstream. Consequently, the  $z$ -circulation at downstream region becomes unreliable and insufficient to represent the strength of that vortex, not to mention the effect of decaying circulation when it travels downstream.

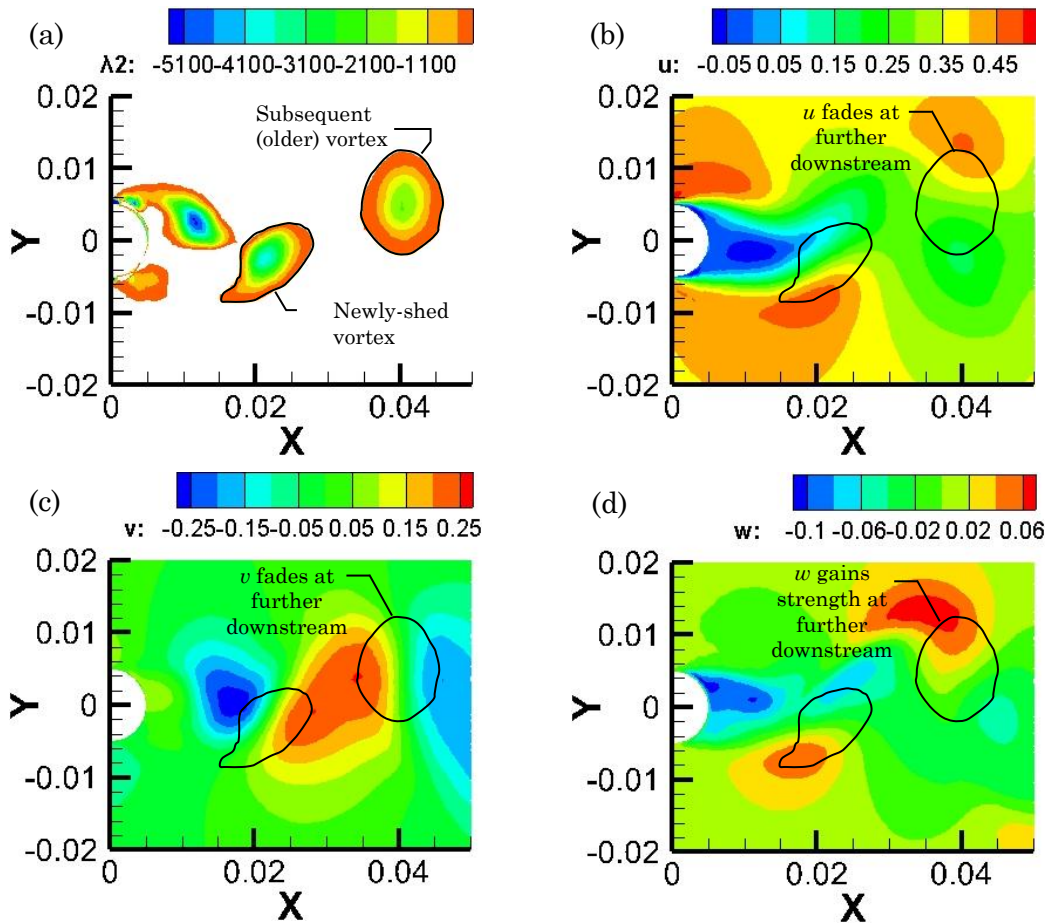


**Figure 6.8: (a) The  $\Lambda_2$  ( $\Lambda_2$ ) contour; (b) the  $x$ -velocity ( $u$ ) contour; (c) the  $y$ -velocity ( $v$ ) contour; and (d) the  $z$ -velocity ( $w$ ) contour that covers the newly shed vortex and a downstream vortex.**

As a result, for the purpose of analysing the effect of vibrating FVG on vortex generation, computing the  $z$ -circulation of the newly-shed vortex is, by far, the most suitable approach to study the vortex dynamics. Besides, it can also demonstrate the pure vortex strength generated from the FVG before it experiences a decay caused by internal dissipation, diffusion and vortex-to-vortex interaction.

### 6.3.1 $z$ -circulation ( $\Gamma_z$ )

This section strictly discusses on the  $z$ -circulation (the Kármán vortex in  $x$ - $y$  plane only), the circulation of the planes where tip vortex is involved are not considered in the analysis. This is because the tip vortex has high three-dimensionality that can reduce the accuracy of the analysis. Besides, tip vortex normally has greater strength compared to the regular vortex. Thus, the result will be inconsistent if Kármán vortex is compared with it. The  $z/D$  planes where tip vortices are involved, completely, are isolated. The isolated region will be labelled in the figures that are presented later.

#### 6.3.1.1 *Circular VGs*

First of all, the  $z$ -circulation in the rigid case is discussed to set a benchmark, so that the difference in FVG can be distinguished easily. From Figure 6.9, it is observed that the  $\Gamma_{z,RVG}$  decreases at higher  $z/D$  (except for  $\Gamma_{z,RVG}$  at “ $z/D=4$  of  $8_{CR}$ ” and “ $z/D=6$  of  $10_{CR}$ ”, which will be discussed shortly). This is a sign where the identity of the Kármán vortex is fading at higher  $z/D$  location.

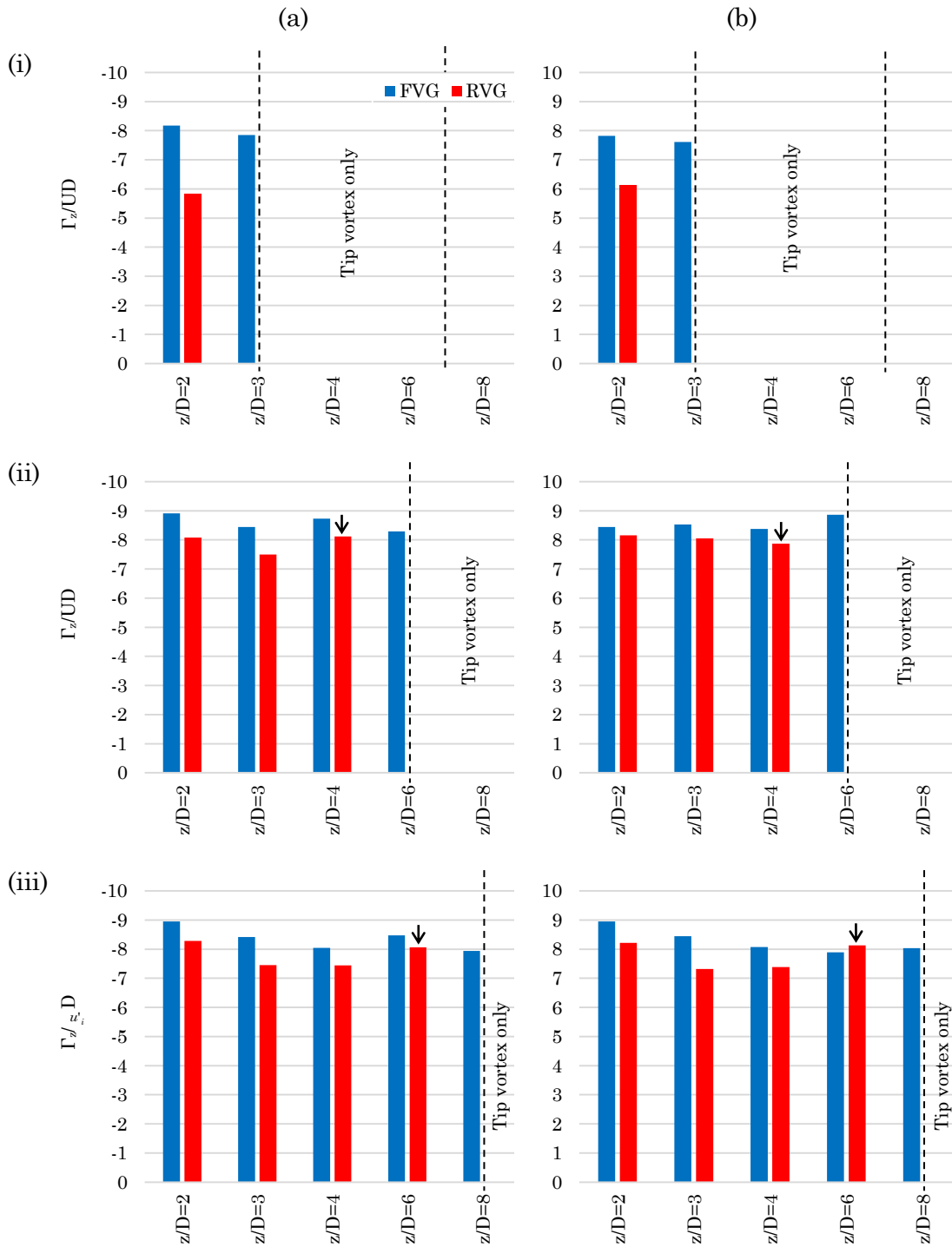


**Figure 6.9: The (a) negative and (b) positive initial z-circulation for (i) AR=6, (ii) AR=8 and (iii) AR=10 circular RVG and FVG ( $\blacktriangledown$  marks the location where tip vortices are partially involved in the calculation).**

According to Okamoto and Yagita (1973), Palau-Salvador *et al.* (2010), Lee and Wang (1987), the formation of tip vortex can suppress the formation of the Kármán vortex, which is considered as one of the tip effects. A similar phenomenon can also be seen in the wake of RVG that has been discussed in Chapter 5; it is labelled and re-plotted as Figure 6.10. The figure clearly shows that at the region near the tip, only tip vortex is shed and the shedding of Kármán vortex at the same region is suppressed. Conversely, the Kármán vortex reappears below the aforementioned suppression region. At the spanwise location below this suppression region ( $z/D$  lower than  $3D$  from the free end; at  $z/D < AR-3D$ ), the strength of tip effect becomes weaker and it is no longer capable of suppressing the formation of Kármán vortex. However, the results of  $\Gamma_{z,RVG}$  suggests that the tip effect is still existing, which is reflected by the decreasing  $\Gamma_{z,RVG}$ . Since (to the best of the author's knowledge)  $\Gamma_z$  has not been used to analyse the vortex behind a circular cantilever (equivalent to the circular RVG in this case), the reduction of circulation at a location closer to the cantilever's free end has not been directly identified before.

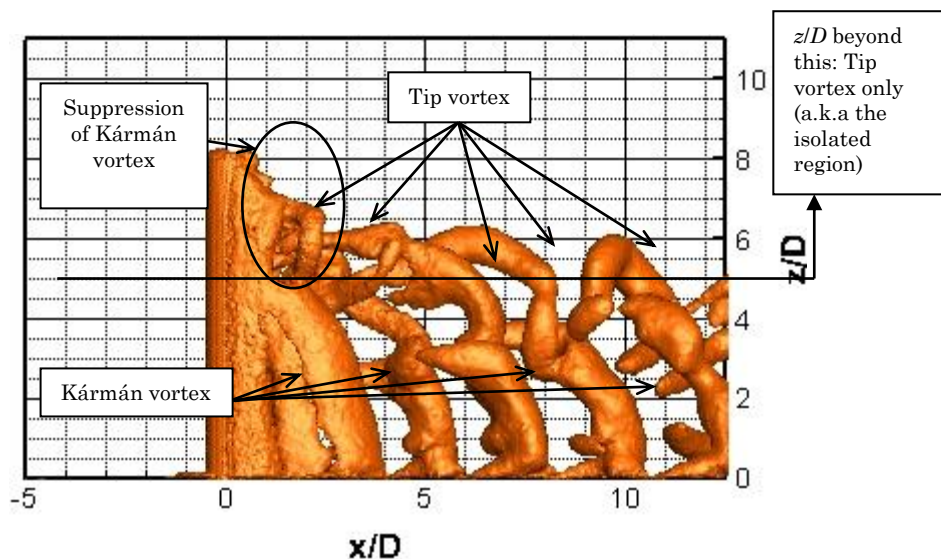


**Figure 6.10: Tip vortices and Kármán vortices behind a RVG.**

As mentioned earlier, the calculated  $\Gamma_{z,RVG}$  at “ $z/D=4$  for  $8CR$ ” and “ $z/D=6$  for  $10CR$ ” are found to be increasing instead of the anticipated reduction, which has violated the discussed suppression effect. This sudden increment of  $\Gamma_{z,RVG}$  is actually originated from the tip vortex that had accidentally “slipped” into the measuring plane. The location near the isolated region will normally stand greater chance to detect an unwelcomed tip vortex. This inconsistency happens

due to the irregular downwash that is transporting the tip vortex to the measuring plane. Since the tip vortex is always stronger than the Kármán vortex, so whenever a tip vortex is involved, the calculated  $\Gamma_{z,RVG}$  shows an abnormal increment.

The suppression effect caused by the tip effect applies in the FVG as well. Due to the vanishing downwash as identified in Chapter 5, the tip vortex behind the FVG is not being washed to the region-of-analysis. Hence, none of the calculated  $\Gamma_z$  in FVG case involves tip effect; no sudden increment of  $\Gamma_z$  is spotted at higher  $z/D$ . However, the Kármán vortex still experiences the tip effect. But the effect and its rate are relatively weaker than that of the RVG case. Consequently, the  $\Gamma_{z,RVG}$  is reducing slowly with at higher  $z/D$ .

Next, by comparing the  $\Gamma_z$  of the FVG and RVG cases, the results show that the  $\Gamma_{z,FVG}$  is, in general, stronger than the  $\Gamma_{z,RVG}$  (except the location where the tip vortex is involved). The result agrees fairly with the prediction made wall shear stress analysis. However, the scale of improvement is not in the same order with the improvement obtained from the wall shear stress analysis. Since, the energy in the source, *i.e.* turbulence in the boundary layer has become stronger, the strength of the generated vortex should have increased on a similar scale. The result suggests that there is something happening in between the feeding phase and the shedding phase of a vortex.

To examine this speculation, the time series (evolution) of the Lambda2, which covers the evolution of a vortex from its formation to the moment of shedding, as shown in Figure 6.11 is studied. It is important to mention that the process demonstrated in the figure is repeating itself for every cycle. Hence, it can be considered to have reached a periodically-steady state. Based on the figure, it shows that the vortex is “peeled off” from the VG instead of following a typically shedding process as discussed in Chapter 2. This indicates that the vorticity feeding process is interrupted. Therefore, it is believed that the vortex is detached from the boundary layer (that is feeding the vortex) before it has gained sufficient vorticity. In short, the vortex is shed before attaining its maximum circulation capacity. A similar shedding process is observed in the case of 10<sub>CF</sub> as well. Therefore, the  $\Gamma_{z,FVG}$  in 8<sub>CF</sub> and 10<sub>CF</sub> display an improvement that is lower than expected.



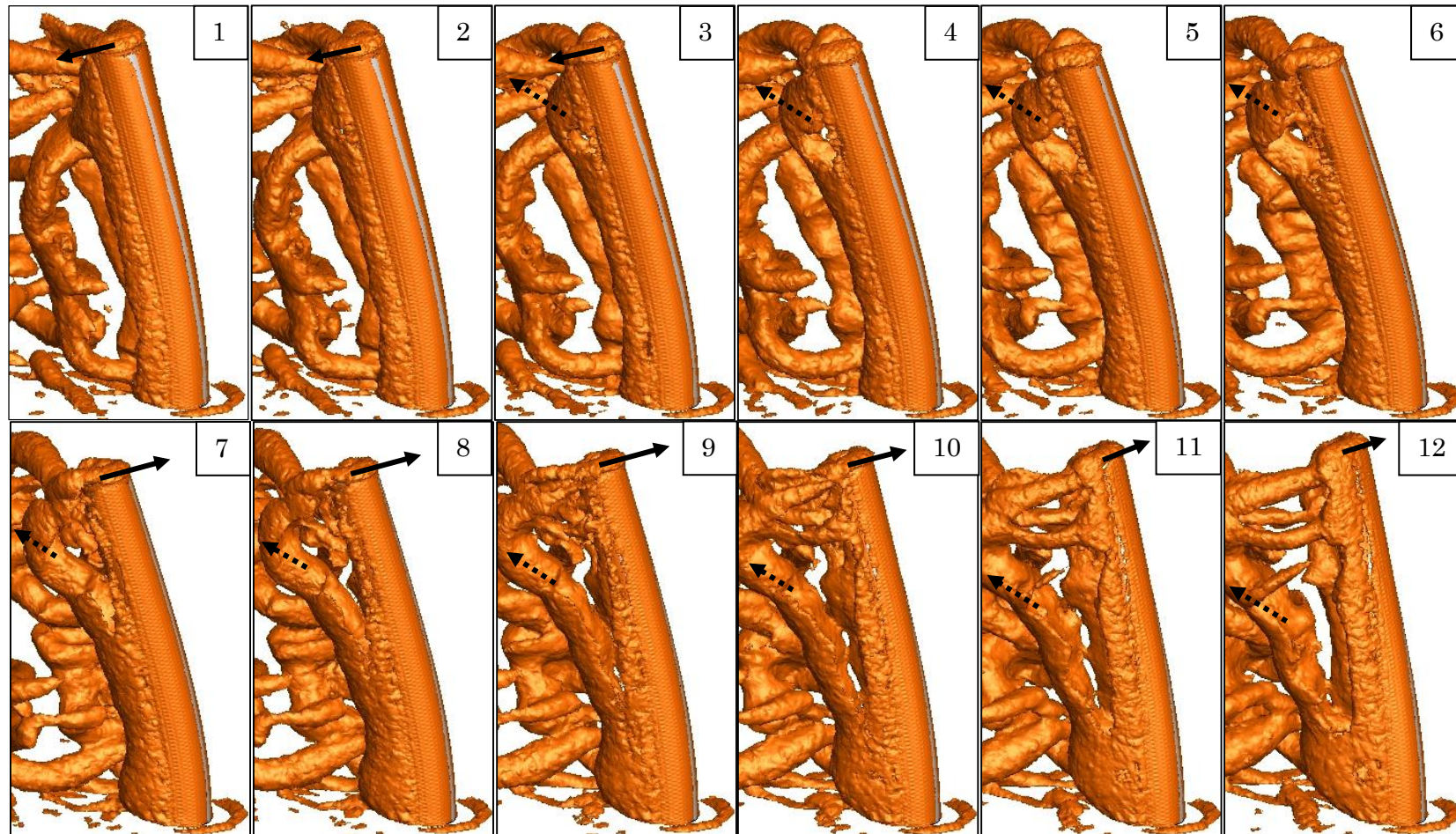


Figure 6.11: Time series of  $\Lambda_2$  - vortex forming and shedding: (1-3) vortex formation; (4-6) shedding of tip vortex and; (7-12) “peeling” of Kármán vortex. Dashed arrows denote the direction that the vortex tube/filament travels; solid arrows denote the direction that the circular FVG moves.

Unlike  $8_{CF}$  and  $10_{CF}$ , the  $6_{CF}$  does not experience the “peel-off” shedding mode. This observation is also reflected in the calculated  $\Gamma_{z,FVG}$  as it has improved approximately 67.2% compared to its rigid counterpart. The result has also echoed the speculation made previously. Fortunately, due to the boundary layer with a relatively greater turbulence production, the strength of the generated vortex is still comparatively stronger than the RVG case.

Furthermore, the  $\Gamma_{z,FVG}$  of circular FVG with different AR is compared with each other to provide further insight into the physics. The  $\Gamma_{z,FVG}$  at  $z/D=3$ , 6 and 8 for  $6_{CF}$ ,  $8_{CF}$  and  $10_{CF}$  respectively are considered in this comparison because these are the highest-possible plane where tip vortex is isolated. Besides, it is also experiencing a higher vibration compared to the low  $z/D$  region. The comparison is summarised in Table 6.1.

It shows that the  $\Gamma_{z,FVG}$  generated from the  $8_{CF}$  is the greatest among the others, followed by  $10_{CF}$ , then  $6_{CF}$ . As discussed in the previous section, the turbulence generation is highly related to the structural velocity. With reference to this, it is predicted that the  $8_{CF}$  will have the greatest structural velocity ( $U_s$ ), followed by  $10_{CF}$ , then  $6_{CF}$ . In order to confirm this postulation, the structural velocities in  $y$ - and  $x$ -directions are computed by differentiating ( $d/dt$ ) the amplitude responses with respect to time. The computed results are plotted in Figure 6.12 and Figure 6.13. From the figure, it is clear that the sequence of the  $U_s$  in term of its scale are the same as the predicted order. To further illustrate the structural velocity in a statistical way, its root-mean-square is computed and tabulated in Table 6.1. This finding can also serve as a strong evidence for the proposed flow model, which has successfully predicted, with certainty, the behaviour of turbulence generation from a moving object in a flow.

**Table 6.1: The normalised mean  $z$ -circulation ( $\Gamma_{z,FVG}$ ) at the highest considering plane and the normalised r.m.s. of structural velocity ( $U_{s,(rms)}$ ) associated to the  $6_{CF}$ ,  $8_{CF}$  and  $10_{CF}$ .**

	$z/D$	$\Gamma_{z,FVG}/U_\infty D$ (negative)	$\Gamma_{z,FVG}/U_\infty D$ (positive)	$U_{s,y(rms)}/U_\infty$	$U_{s,x(rms)}/U_\infty$
$6_{CF}$	3	-7.85	7.61	$\pm 0.42$	$\pm 0.13$
$8_{CF}$	6	-8.29	8.86	$\pm 0.77$	$\pm 0.17$
$10_{CF}$	8	-7.94	8.04	$\pm 0.50$	$\pm 0.14$

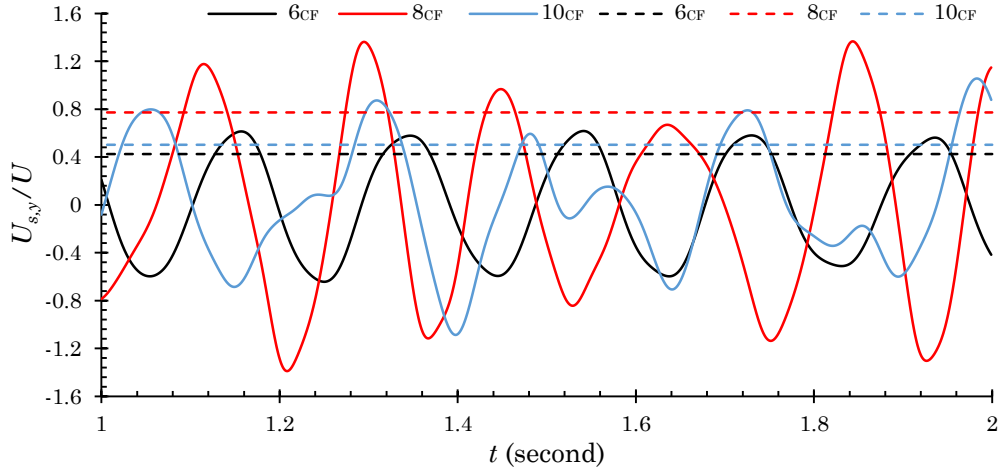


**Figure 6.12: The normalised structural velocity in the  $y$ -direction ( $U_{s,y}/U_\infty$ ) of the circular FVG with different AR. The solid line represents the instantaneous component; dash line represents its r.m.s.**

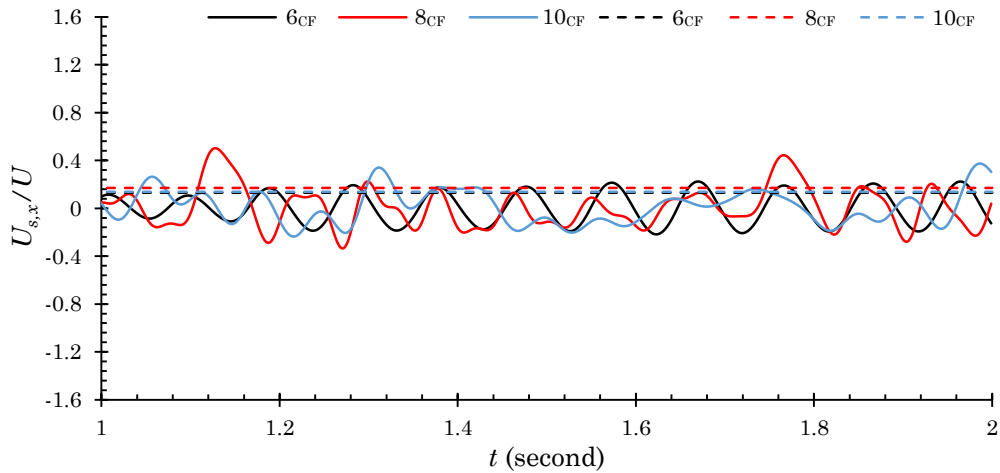


**Figure 6.13: The normalised structural velocity in the  $x$ -direction ( $U_{s,x}/U_\infty$ ) of the circular FVG with different AR. The solid line represents the instantaneous component; dash line represents its r.m.s.**

### 6.3.1.2 Flat Plate VGs.

A similar analysis is done on flat plate VGs to study the initial  $z$ -circulation. Figure 6.14 shows the computed normalised mean  $\Gamma_z$  of the vortex formed right behind the RVG and FVG. Note that 4<sub>PR</sub> and 4<sub>PF</sub> are not included in this study because 4<sub>PF</sub> behaves nearly like a rigid object; *i.e.* the wake size of the 4<sub>PF</sub> is approximately the same size with its rigid counterpart and its deflection and oscillation responses are weak too.

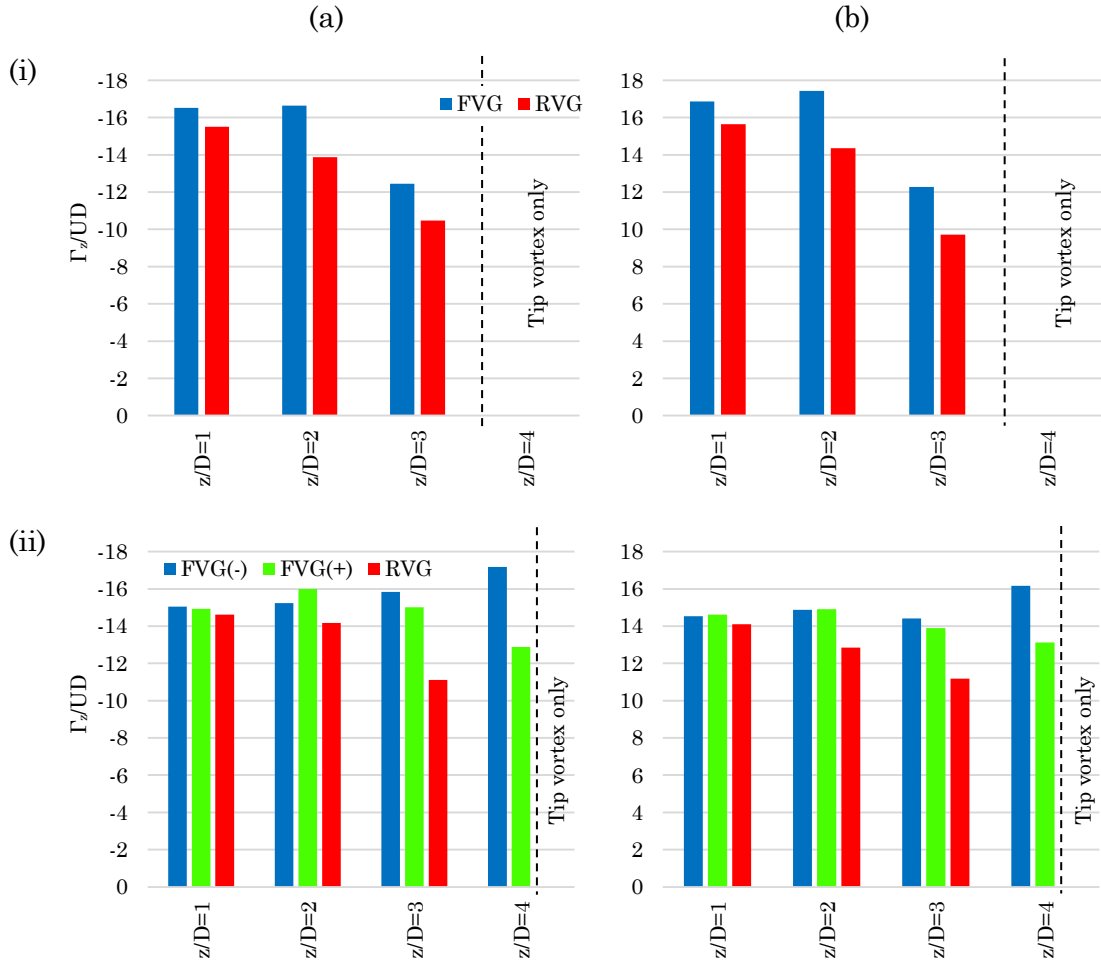


**Figure 6.14: The (a) negative and (b) positive initial  $z$ -circulation for (i) AR=5 and (ii) AR=6 flat plate RVG and FVG.**

Besides, it is also important to mention that two different  $z$ -circulation are calculated in the case of 6PF, *i.e.*  $\Gamma_{z,FVG(+)}$  and  $\Gamma_{z,FVG(-)}$ . The “positive” and “negative” signs symbolise the FVG’s direction of motion when the measured vortex is shed; where the “positive” denotes that shedding occurs when the FVG is deflecting with the direction of the flow (hence, in positive  $x$ -direction) while the “negative” means otherwise.

According to the flow model developed in the previous discussion, the structural velocity ( $U_s$ ) that is opposing the flow’s direction can boost the shear production. It also suggests that the opposite would happen if the FVG travels in the direction of the flow – the shear production is reduced. This postulation can be examined at a higher  $z/D$  location but not too high that covers the tip vortex. In this case,  $z/D=4$  of 6PF will be the best location to describe the phenomenon as that is the highest  $z/D$  location that experiences a high  $\pm U_s$  without involving any tip vortex. By comparing the  $\Gamma_{z,FVG(+)}$  and  $\Gamma_{z,FVG(-)}$  at the

mentioned  $z/D$  location, as shown in Figure 6.14(ii), the  $\Gamma_{z,\text{FVG}(-)}$  shows a greater strength compared to  $\Gamma_{z,\text{FVG}(+)}$ , which has once again confirmed the earlier prediction. Note that this effect happens at  $z/D=3$  as well, but in a smaller scale due to the weak difference between  $+U_s$  and  $-U_s$ . At  $z/D \leq 2$ , this mechanism does not happen because the FVG barely oscillates at the mentioned  $z/D$  range. Thus, the calculated  $\Gamma_{z,\text{FVG}(+)}$  and  $\Gamma_{z,\text{FVG}(-)}$  are nearly the same at  $z/D \leq 2$ . Besides, it is important to mention that this aspect is not examined in the previous circular FVG's analysis because it oscillates transversely towards the flow's direction; its motion is always against the flow.

In addition, based on Figure 6.14, it can be seen that the  $\Gamma_{z,\text{RVG}}$  reduces along the  $z/D$  direction. The cause of this inverse relationship is the same as the cause discussed in circular RVG; where there is a tip effect that suppresses and interrupts the formation of the Kármán vortex. Since the phenomenon is behaving in a similar pattern, it will not be discussed further in this section. Hence, the following discussion will be on the flat plate FVG.

However, it is worth to note that the  $\Gamma_{z,\text{FVG}}$  behaves slightly different compared to the circular case, especially for the low AR case. As discussed in Chapter 5, the flat plate FVG experiences inconsistency wake size due to differing downwash strength. Accordingly, the span of the tip effect differs as well. For instance, the span of the tip effect can extend further when a FVG has small deflection. So, it is important to consider the span of tip effect with reference to the FVG's deflection when analysing the  $\Gamma_{z,\text{FVG}}$  of flat plate FVG.

With reference to the observation made in Chapter 5,  $5_{\text{PF}}$  experiences a stronger downwash than  $6_{\text{PF}}$  due to its relatively weaker deflection. This signifies that the tip effect will have a greater span (because of the greater downwash) in the  $5_{\text{PF}}$  compared to the  $6_{\text{PF}}$ . In this study, the strength of tip effect experienced by the FVG is reflected in term of the reduction rate of  $\Gamma_{z,\text{FVG}}$  along the  $z/D$  direction as shown in Figure 6.14. According to the figure, it can be observed that the  $\Gamma_{z,\text{FVG}}$  of  $5_{\text{PF}}$  has experienced a significant suppression at  $z/D=3$ , which is close to the region that fully filled with tip vortices. This suppression effect can still be observed even at the lower  $z/D$  location, *i.e.*  $z/D \leq 2$ , which shows that the tip effect is extended down to  $z/D \leq 2$ .

Meanwhile, less tip effect is felt by the  $6_{\text{PF}}$  due to its relatively large deflection (the downwash is significantly weaker than that of the  $5_{\text{PF}}$ ), thus, the

$\Gamma_{z,FVG}$  does not vary significantly along  $z/D$ . Besides, it is important to note that the difference between the  $\Gamma_{z,FVG(+)}$  and  $\Gamma_{z,FVG(-)}$  at  $z/D=4$  of 6PF has no relation to the tip effect. If it does, the  $\Gamma_{z,FVG(-)}$  should have experienced the suppression because the  $\Gamma_{z,FVG(-)}$  was measured when the FVG travels opposing to the flow's direction; its deflection is reducing and the tip effect grows. Since the  $\Gamma_{z,FVG(-)}$  does not suppress (in fact, it gains strength), it is strongly evident that the cause of the difference between the  $\Gamma_{z,FVG(+)}$  and  $\Gamma_{z,FVG(-)}$  at  $z/D=4$  is still depending on the flow mechanism as described in the flow model mentioned earlier. Furthermore, this observation also proves that the tip effect is relatively weak to bring weighty effects on the  $\Gamma_{z,FVG(+)}$  and  $\Gamma_{z,FVG(-)}$  at  $z/D=4$ .

Similar to the analysis on circular FVG, the  $U_s$  is computed to further explain the gain of  $\Gamma_{z,FVG}$  at high  $z/D$  location. The  $\Gamma_{z,FVG}$  at the highest considering location ( $z/D=3$  for 5PF and  $z/D=4$  for 6PF) is tabulated in Table 6.2. In addition, the computed  $U_s$  and its r.m.s. are plotted in Figure 6.15 as well. From the comparison, it is clear that the  $\Gamma_{z,FVG}$  of 6PF is greater than 5PF. With reference to this, the computed  $U_s$  also shows that the 6PF oscillates faster than the 5PF, resulting a greater shear production in the boundary layer. Ultimately, the generated vortex is fed with a greater turbulence energy (the turbulence shear production) that leads to its escalated strength. The result agrees well with the deduced flow model.

**Table 6.2: The normalised mean  $z$ -circulation ( $\Gamma_{z,FVG}$ ) at the highest considering  $z/D$  and the normalised r.m.s. of structural velocity ( $U_{s,(rms)}$ ) associated to the 5PF and 6PF.**

	$z/D$	$-\Gamma_{z,FVG}/U_\infty D$	$+\Gamma_{z,FVG}/U_\infty D$			$U_{s,x(rms)}/U_\infty$
5PF	3	-12.45	12.28			$\pm 0.0086$
		$-\Gamma_{z,FVG(-)}/U_\infty D$	$-\Gamma_{z,FVG(+)} /U_\infty D$	$+\Gamma_{z,FVG(-)}/U_\infty D$	$+\Gamma_{z,FVG(+)} /U_\infty D$	
6PF	4	-17.18	-12.87	16.16	13.12	$\pm 0.0414$

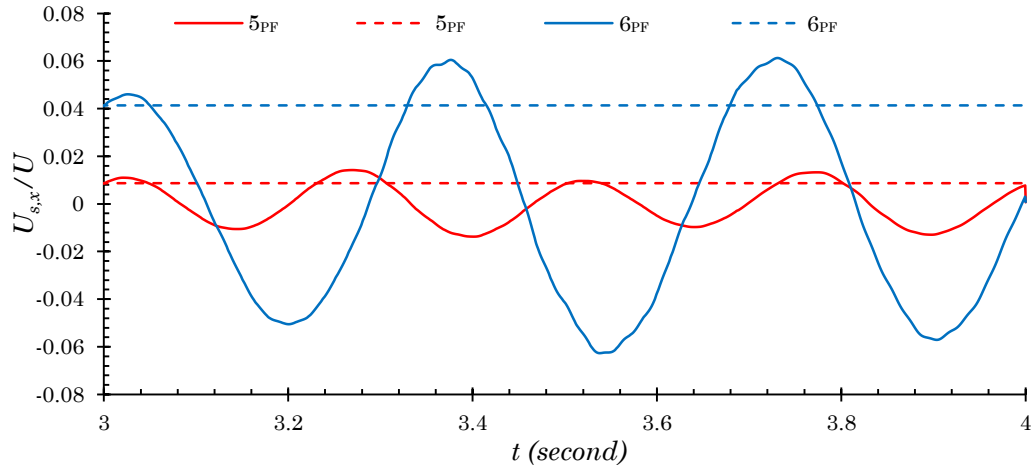


**Figure 6.15: The normalised structural velocity in the  $x$ -direction ( $U_{s,x}/U_{\infty}$ ) of the flat plate FVG with different AR. The solid line represents the instantaneous component; dash line represents its r.m.s.**

#### 6.4 The Pressure Loss on the FVG

Although the main aim of the current study is to investigate the turbulence enhancement generated by the FVG, it is a good practice to check the pressure loss associated with it as well.

The mean pressure profiles in the streamwise direction ( $x$ -direction) in the field around the circular RVG and FVG are plotted and shown in Figure 6.16. In this case, the pressure loss is defined as the pressure different between the direct upstream and downstream of the VG. So, it is basically represented by the sudden drop (the negative pressure slope) in the pressure profiles as shown in the figure.



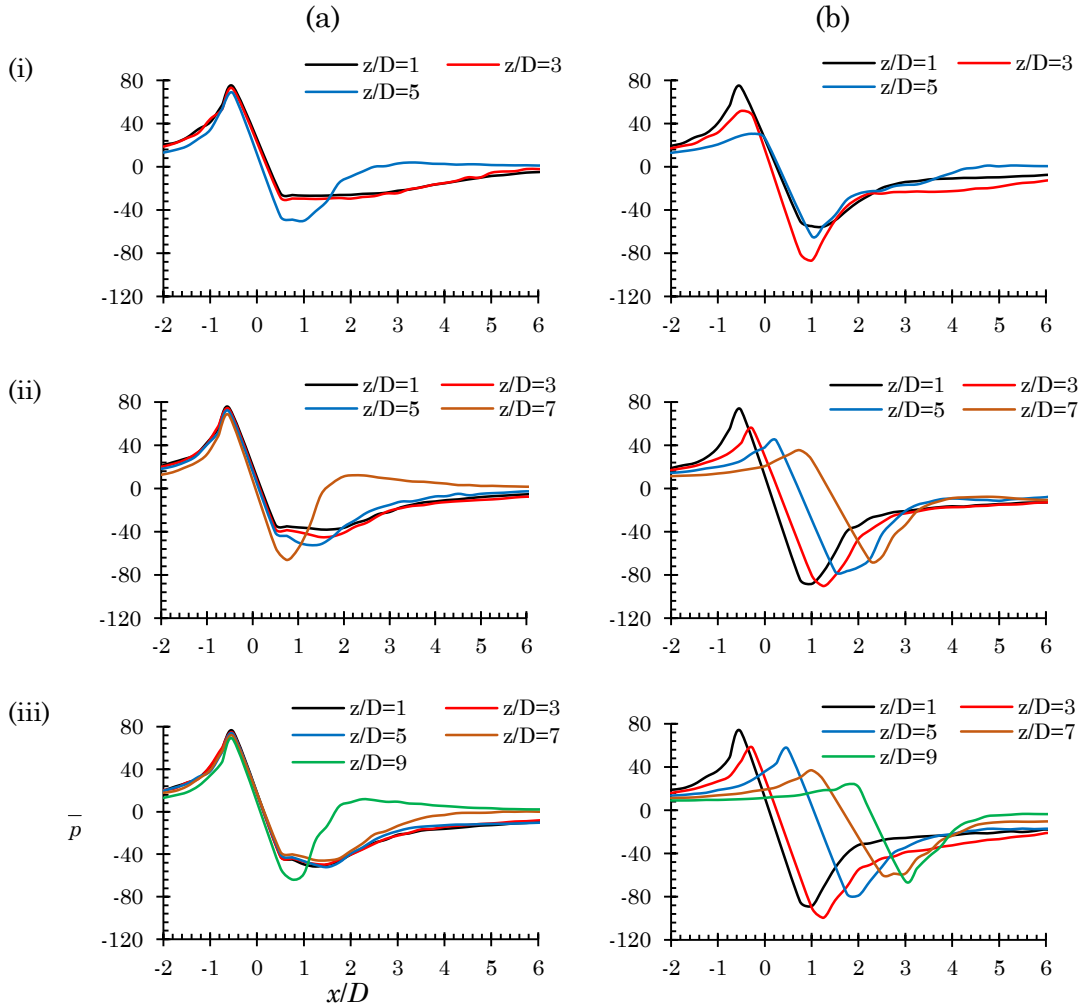


**Figure 6.16: The mean pressure profile, at different spanwise location, in the plane-of-symmetry ( $y=0$ ) of the circular (a) RVG and (b) FVG with (i) AR=6, (ii) AR=8 and (iii) AR=10.**

Based on the figure, it is noticed that the pressure loss has different behavior once the FVG is employed. There are two regions that are experiencing different pressure drop behavior, namely the near-free-end region, and the near-wall-junction region.

At the near-free-end region (high  $z/D$  values or locations), the pressure drop is observed to be lesser in the case of FVG than its rigid counterpart. However, this is not caused by the high downstream pressure that reduces the pressure deficit between the upstream and downstream locations. In fact, this low-pressure drop is caused by the reduction of pressure at the upstream of the FVG.

Furthermore, the reduction of pressure drop near the free end is believed to be the physical cause of the vanishing downwash behind the circular FVG. It is already known that the downwash behind a RVG (the rigid cantilever) is



caused by the strong pressure drop between the upstream and downstream of the RVG. This is because a flow will always have a greater “potential” to flow into a region with a lower pressure than those regions with a relatively higher pressure. In this case, the low pressure region is at the direct downstream of the RVG. Hence, the fluid above the free end is washed into those region, resulting a downwash. Once the pressure drop is reduced, the “potential” of the flow to flow downward is reduced as well. As a result, the downwash is vanished.

However, this finding appears not to be in a disagreement with the previous observation that demonstrates “the deflection is causing the vanishing/weakening of downwash”. In fact, the reduction of pressure drop is originated from the FVG’s deflection because the FVG has developed a slightly streamlined geometry as it deflects.

On the other hand, the pressure loss at the near-wall-junction region (low  $z/D$  values or locations) in the case of FVG is experiencing a greater pressure drop than its rigid counterpart. This happens because the pressure at the direct downstream of the FVG in this region is having a lower pressure than that of the RVG.

In short, although the pressure loss has increased at the near-wall-junction region, the pressure drop at the near-free-end region has experienced a reduction in pressure loss and this reduction has balanced the escalated pressure drop near the cylinder’s root.

Similar observations are found from the mean pressure profiles of the flat plate FVG but the difference of pressure drop between both cases is less noticeable, as shown in Figure 6.17. Since it has been shown that, in the previous studies, the flat plate FVG can generate greater turbulence, this analysis has further highlighted the fact that the flat plate FVG has achieved the turbulence enhancement without sacrificing much on the pressure loss.

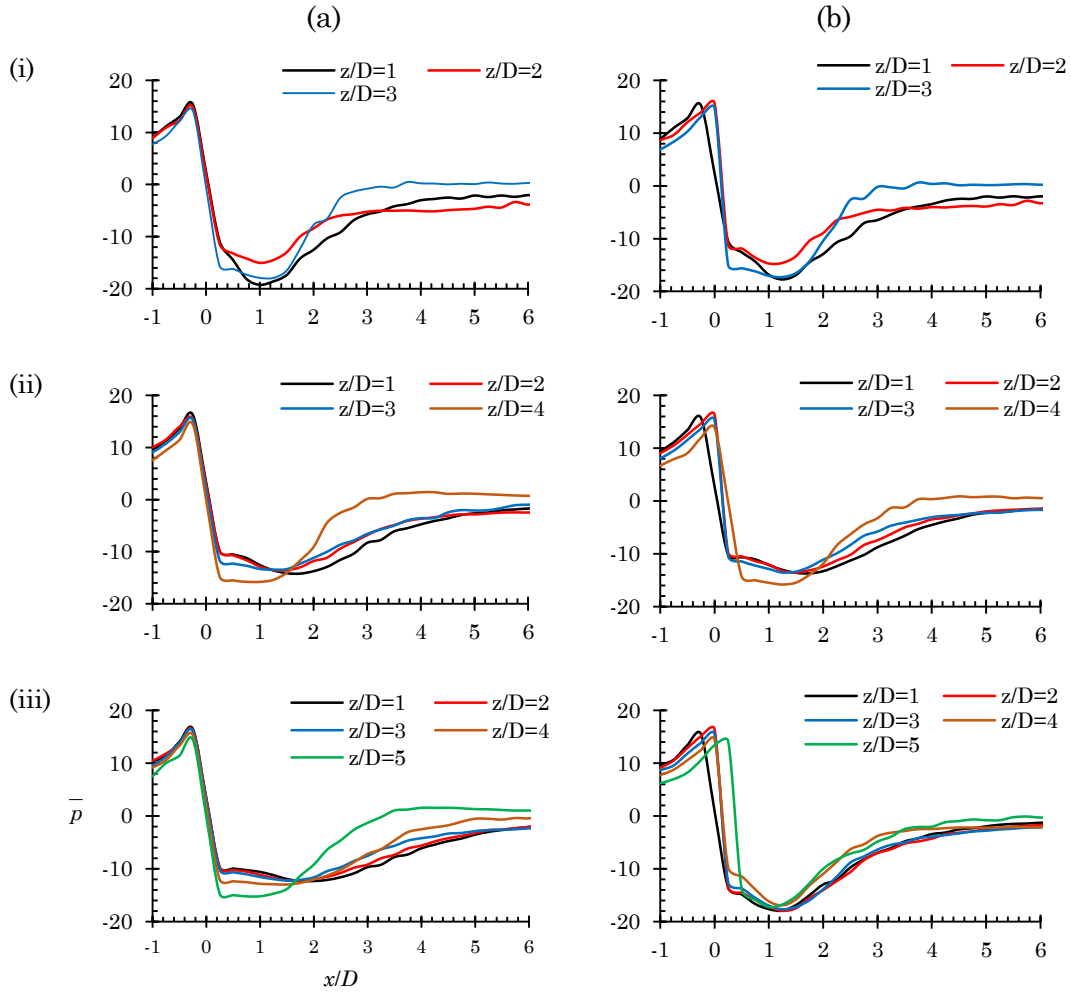


**Figure 6.17: The mean pressure profile, at different spanwise location, in the plane-of-symmetry ( $y=0$ ) of the flat plate (a) RVG and (b) FVG with (i) AR=4, (ii) AR=5 and (iii) AR=6.**

## Summary of Chapter

The present study demonstrated that FVG is capable of generating greater turbulence through examining the shear production, specifically, the shear rate in the flow field. This chapter consists of two parts that discuss the shear rate in different regions.

Firstly, the shear rate in the boundary layer – the region where the vortex gains its energy – was investigated in the form of wall shear stress. The study has demonstrated that the FVG experiences greater wall shear stress than a RVG. Besides, the factors that contribute to this improvement have been identified, *i.e.* (i) the oscillating motion of the FVG increases the magnitude of wall shear stress, and (ii) the deflection generates a better wall shear stress distribution where the area with greater wall shear stress increases. Besides, it is also found that the variable that governs the shear production is the

structural velocity instead of the FVG's degree of deflection nor the oscillation amplitude. A flow model is also proposed to explain the mechanism. Based on these findings, it is expected that the boundary layer around a FVG contains stronger turbulence, which is going to be fed towards the forming vortex.

The previous result suggests that the vortex generated from a FVG may have a greater strength. To prove this, the shear rate in the vortex was investigated. Based on the comparison between the computed initial  $z$ -circulation, it can be concluded that a FVG generally produces a stronger vortex compared to a RVG at the same AR. Furthermore, the circulation results were analysed further to look into the physics of the improvement. Finally, the study confirmed that the flow model proposed at the end of the previous discussion holds true; the strength of the generated vortex is, indeed, dependent on the structural velocity.

This paragraph marks the end of the discussion on the improvement of turbulence characteristic achieved by employing the FVG. In short, the chapter concludes that the FVG is capable of providing a better turbulence enhancement than the conventional RVG, where the rate of enhancement depends on the structural velocity of the FVG.

## Chapter 7: FVG's Heat Transfer Performance

In Chapter 6, the performance of FVG in turbulence enhancement has been identified. The study found that the wake size of a FVG is generally greater than that of a RVG. Since the wake is the effective region that facilitates turbulence activity, the result has directly demonstrated that the FVG has a large turbulence region as indicated by a larger wake. In short, a FVG can generate greater turbulence, in term of its spatial definition, than a RVG. Furthermore, the first-hand analysis on the flow field – the streamlines waviness also shows that the flow field behind a FVG has stronger vortical structures (the vortex) than a RVG.

Apart from the qualitative findings discussed in Chapter 5, the greater turbulence enhancement ability of the FVG has also been quantitatively confirmed via examining the shear component in the flow field, *i.e.* the wall shear stress and the circulation.

With reference to those findings, since it is known that heat transfer rate is closely related to turbulence, the previous results suggest that the FVG may be able to improve the heat transfer process as well. Therefore, this chapter discusses the extended application of the FVG on a heat transfer process. The performance of a FVG is compared with a RVG, which is running in identical flow conditions with the FVG case, to highlight the differences and/or improvement.

### 7.1 Heat Source on the FVG

This section focuses on the effect of FVG on heat transfer when a heat source is applied on the FVG. It is commonly known that the heat transfer process between a solid wall and its surrounding fluid is governed by the characteristic of the boundary layer on the wall. On the other hand, in the previous wall shear stress study, the result shows that the distribution and magnitude of wall shear stress have been altered as the FVG vibrates. This result provides an insight that the velocity gradient of the boundary layer on the heated wall has changed (recall that the wall shear stress is scaled with the velocity gradient, as demonstrated in Equation 6.1). Since the velocity gradient is an important variable that characterises the boundary layer, the result

suggests that the characteristics of the boundary layer on the heated wall have changed. Ultimately, the heat transfer process between the FVG and its surrounding fluid will behave differently compared to conventional RVG case.

### 7.1.1 Case Description

In this study, a constant temperature of 373.15K was applied on the surface of the VG (both RVG and FVG). In contrast, a 293.15K (air) flow was injected into the domain from the inlet. The material used for the FVG in this study is aluminium. The purpose of selecting aluminium is to simulate a real-life condition as metal is commonly used to conduct heat. Besides, it is also because the polymer materials used in the previous studies are technically poor in conducting heat, not to mention its low melting point that discourages its usage in the real application. However, even though aluminium – one of the softest metals – is used, its Young's Modulus ( $E$ ) is still considered high. As a result, the FVG made from an aluminium has high resistance to deformation due to the high stiffness originated from the material. In order to resolve this issue, the FVG is designed to be long and thin, so that the stiffness ( $k$ ) can be sufficiently reduced. In this case, an AR=10 flat plate cantilever is used as the VG.

The heat is expected to be convected toward the flow through the vortex formation process: the vortex draws the heat energy from the VG during its formation. Through shedding, the heat is carried away by the vortex. In the wake, the vortex diffuses and stretches that helps to distribute the heat to the colder region. In the case that employs FVG, it is anticipated that the vortex may have drawn more heat from the heat source (due to the increased circulation discussed in Chapter 6), which improves the heat transfer performance.

Note that all the boundary conditions in the RVG and FVG study will be exactly the same, except in the FVG study, the structural model will be activated to compute the FVG's motion.

Furthermore, the Nusselt Number (Nu) and the temperature of the wake will be examined to justify the heat transfer performance. The Nu is used to quantify the heat transfer between a boundary (surface) and a fluid. It is the ratio of convective to conductive heat transfer across the boundary, which is expressed by Equation 7.1.

$$Nu = \frac{hD_c}{k} \quad (7.1)$$

where  $h$  is the convective heat transfer coefficient of the flow,  $D_c$  denotes the characteristic length and  $k$  is the thermal conductivity of the fluid. The  $k$  of air is used in this study while the characteristic length is the width of the flat plate VG (the same  $D_c$  applies for both RVG and FVG).

### 7.1.2 Results and Discussion

Figure 7.1 and Figure 7.2 illustrate the mean Nusselt Number ( $\overline{Nu}$ ) on the VGs' front and rear surface, respectively. On the front surface (Figure 7.1), the  $\overline{Nu}$  distribution and its magnitude are about the similar for both RVG and FVG cases, which suggests that the motion has minimal effect to the  $\overline{Nu}$  on the frontal surface. On the other hand, a distinct difference is observed between the  $\overline{Nu}$  distributions on the rear surface between two cases, as shown in Figure 7.2. It can be clearly seen that, on the FVG's rear surface, there is a region with greater  $\overline{Nu}$  present near the free end when comparing to the exact same spot of the RVG. The greater  $\overline{Nu}$  denotes a greater heat transfer rate is experienced by the surface.

Based on the wake visualisation discussion presented in Chapter 5, it has been identified that the near wake flow behind a FVG experiences a distinctive change on its flow feature. Firstly, the downwash has become weaker and secondly, the Karman vortex has grown stronger when a FVG is employed. Therefore, the changes in  $\overline{Nu}$  distribution at the rear surface of the FVG can be attributed to the fact that the near wake flow behind the FVG has changed. Since it is known that the flow is responsible for the heat transfer, the greater  $\overline{Nu}$  in the case of FVG suggests that the flow features behind the FVG favour the heat transfer process.

Furthermore, the increased  $\overline{Nu}$  on the FVG's surface suggests that the wake behind the FVG, in particular, the vortex is carrying greater heat compared to the vortex in the case of RVG.

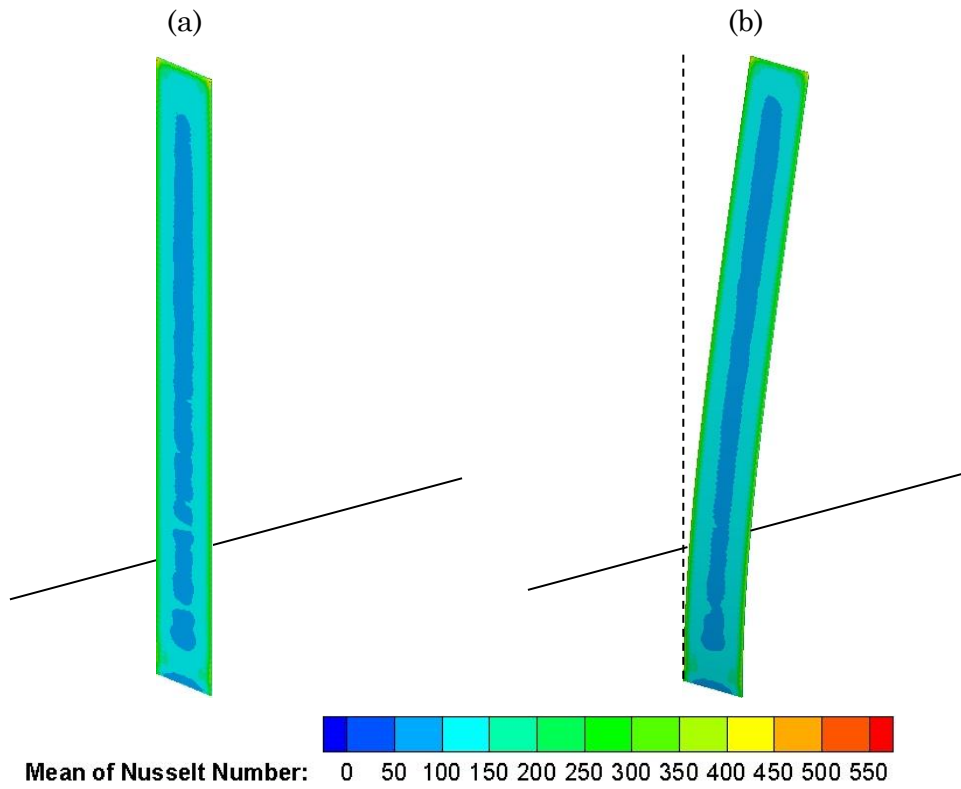


Figure 7.1: Mean Nusselt Number on the frontal surface of the flat plate (a) RVG and (b) FVG.

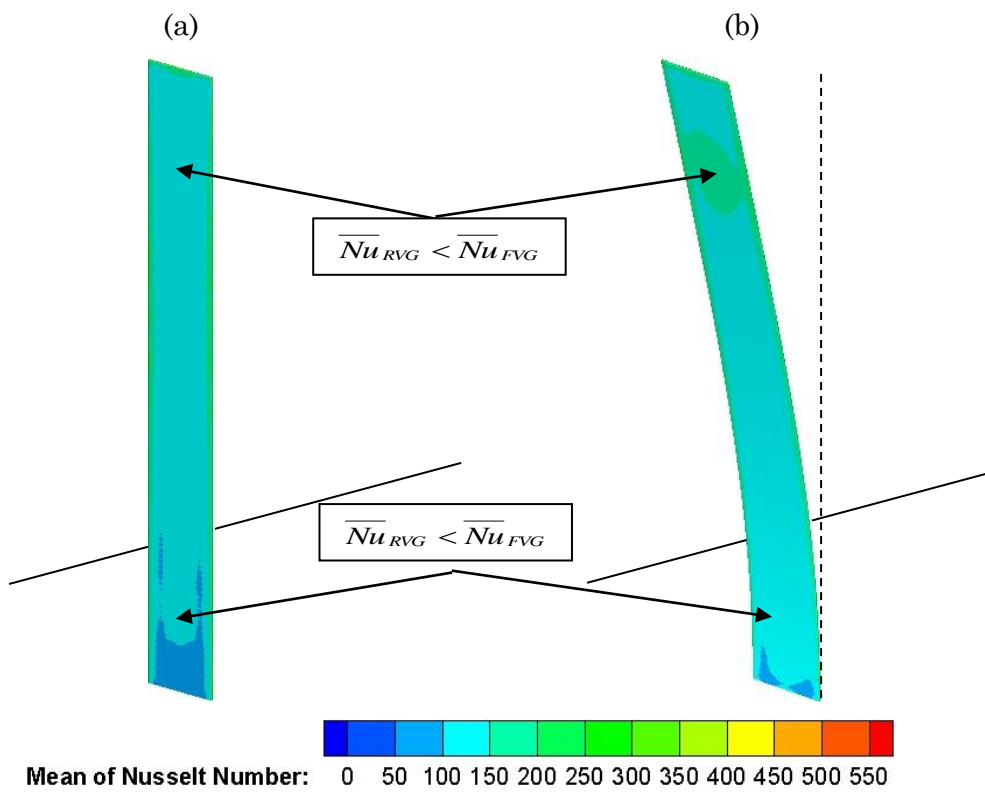


Figure 7.2: Mean Nusselt Number on the rear surface of the flat plate (a) RVG and (b) FVG.

In order to examine the heat carried by vortex, the instantaneous temperature values in the downstream are probed and plotted as well, as shown in Figure 7.3. The reason for monitoring the instantaneous temperature instead of mean temperature will be explained shortly. The locations of the probes used in the temperature measurement are plotted in Figure 7.5 as well.

According to the temperature profiles, the wake of FVG generally has a slightly greater temperature than the RVG's wake. Besides, it can also be observed that most of the temperature profiles in Figure 7.3 resemble a wave-like curve. The crests of the curve symbolise the presence of vortex along the probes as more heat is carried by the vortex. In contrast, the troughs represent the breaks between the vortices, where the heat from the FVG is absent; this argument is reflected by the fact that all troughs have approximately the same temperature, which is around 293.15K – the temperature of inlet flow. The vortex structure behind both RVG and FVG are demonstrated in Figure 7.4, whereas the temperature plots are illustrated in Figure 7.5 to highlight the role of vortex in heat transfer. These observations clearly show that the heat is carried by the vortex generated from the VG. Moreover, this is also the reason for monitoring the instantaneous temperature instead of the mean value where the heat carrying feature of a vortex will be disregarded via averaging.

In contrast with the above observations, the temperature profile at  $z/D=8$  in the RVG case does not possess a wake-like curve. The temperature profile shows a gradual decrease along the streamwise direction. This observation suggests that no vortex is present at  $z/D>8$  in the FVG case. Conversely, the wake-like curve is observed from the profile of  $z/D=8$  (Figure 7.3d) behind the FVG, which shows that vortex is present at that spanwise location. These results are agreeing well with the observation seen in Chapter 5.

On the other hand, no vortex is observed at  $z/D=10$  for both cases. It is important to note that the local maximum is seen in the temperature profile at  $z/D=10$  (Figure 7.3e) in the FVG case (at  $x/D=2.5$ ) is a false temperature peak; it does not represent the existence of a vortex. In fact, this temperature peak is a product of the FVG's deflection. During the deflection, the FVG's free end is bent and it reaches further downstream that is located approximately at  $x/D=2$ . In other words, the probe at  $x/D=2.5$  has detected the heat near the bent FVG that is only  $0.5D$  away from itself, thus resulting a local temperature peak in the



profile (as shown in Figure 7.5b). Therefore, this peak is neglected from the analysis and the temperature profiles in both cases show no vortex is present.

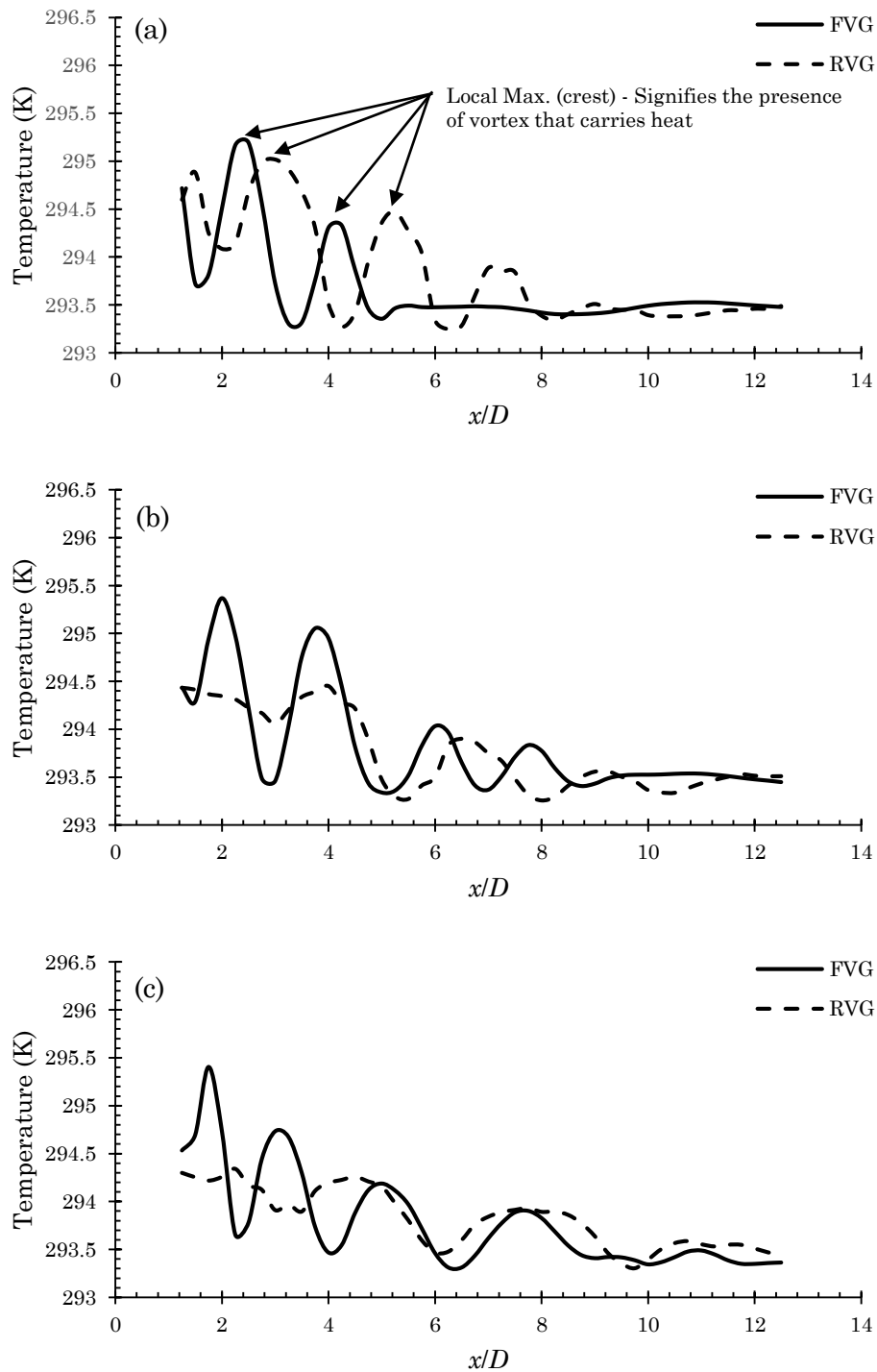


**Figure 7.3:** For caption see the following page.

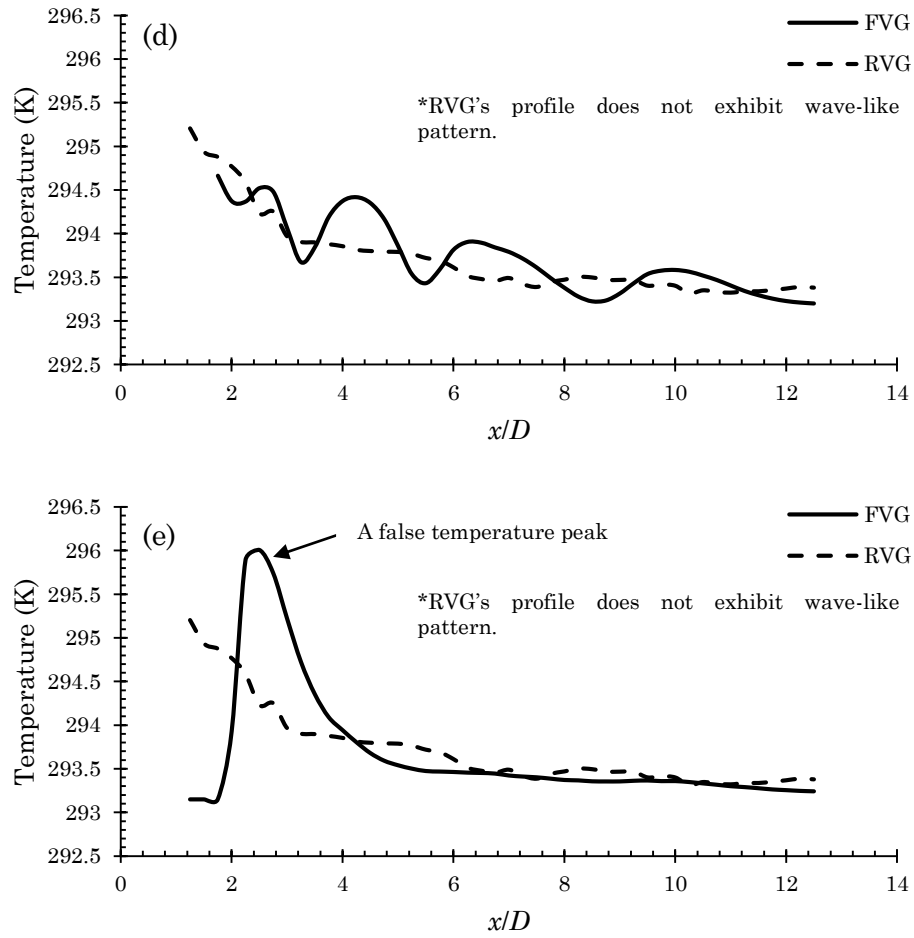


**Figure 7.3: The temperature profile (T), along the  $x/D$  direction. (a) to (e) represent different spanwise locations, *i.e.*  $z/D=2, 4, 6, 8$  and  $10$  respectively.**

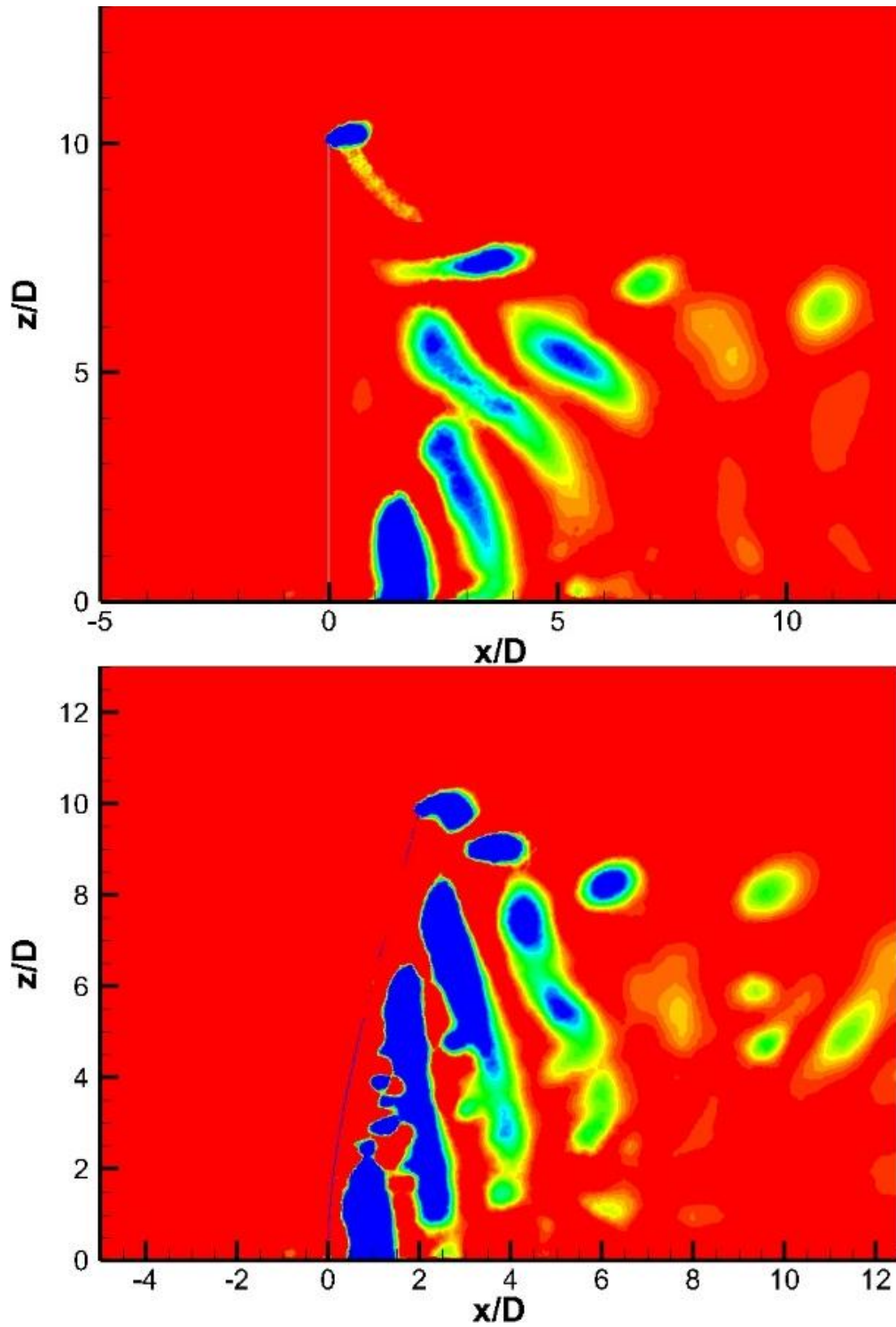


Figure 7.4: The vortex structures ( $\lambda_2 < -100$ ) behind the heated (top) RVG and (bottom) FVG.

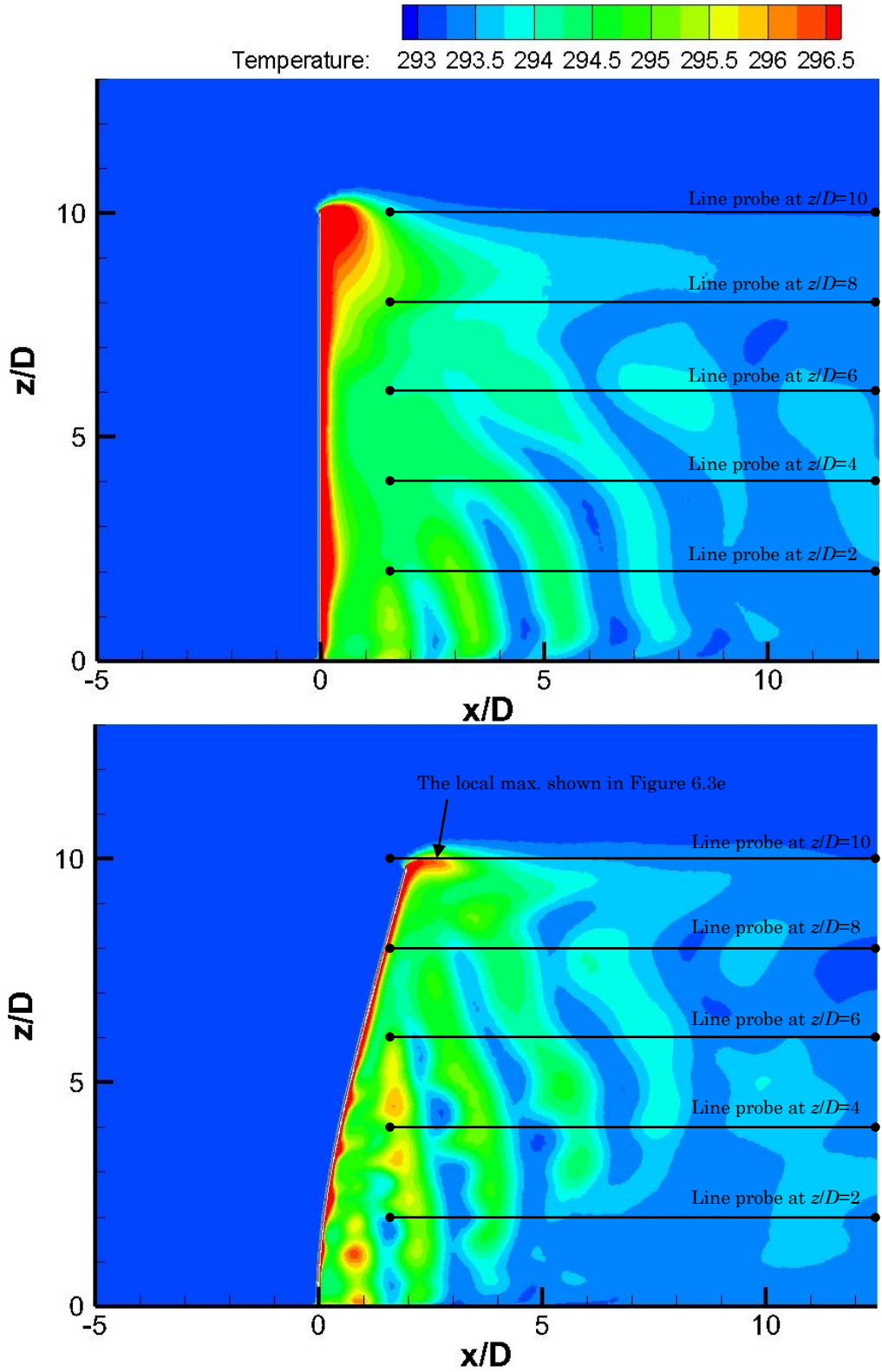


Figure 7.5: Temperature contour at the plane of symmetry ( $y=0$ ) of the (top) RVG and (bottom) FVG. The line probes used are also included.

Besides, based on Figure 7.5, it can be seen that the temperature at the immediate downstream of the RVG is a lot greater than that of the FVG, which is contradicting to the finding obtained from temperature profiles depicted in Figure 7.3. The contour shows that the heat is trapped behind the RVG, probably due to the existence of the stronger downwash as discussed in Chapter 5 and 6, which leads to the formation of the observed high-temperature region. Since the formed vortex is responsible for carrying the heat away from this region, the result has directly demonstrated that the vortex generated from the RVG is ineffective in conveying the trapped heat to the remaining fluid region. This argument can also be supported by the fact that the vortex behind the RVG is carrying less heat (has a lower temperature) than the vortex behind the FVG.

Once again, the results have strongly evidenced the important role of vortex in transporting heat from the VG to the flow. Relating the observations from this study with the findings of Chapter 6, it is believed that a stronger vortex is beneficial to transporting heat from the heated VG to the flow. In other words, the FVG is indeed performing better in heat transfer due to the stronger vortex generated from it.

## 7.2 Heat Source on the Ground Plate

In the second case, the heat source is applied on the ground plate where the VG is placed. This is a common configuration used in the study of VG-induced heat transfer enhancement, including the Shape Memory Alloy VG study conducted by Aris *et al.* (2007).

### 7.2.1 Case Description

A constant temperature of 373.15K was applied on the ground plate while the inlet flow was at room temperature (293.15K). Due to the fact that the heat was not applied on the FVG, Teflon was used as the material of the FVG. However, this selection is accompanied by an assumption, *i.e.* the FVG is assumed to be adiabatic (to reduce the complexity of the mechanism, although it is unreal).

Since the heat transfer is happening only near the ground plate, there is no need to simulate a long FVG because the vortex formed at a higher  $z/D$  location will not reach the ground plate. Conversely, a shorter FVG holds the benefit where the tip vortex can be downwashed depends on the strength of the

downwash (in other words, it is depending on the degree of deflection based on the conclusion drawn in Chapter 5).

Unlike the previous case, the heat transfer mechanism does not only happen during the vortex formation. Instead, the vortex will constantly stimulate the flow near the heated surface to boost the heat transfer process as it is travelling towards the downstream. Therefore, the temperature field will not possess a distinctive vortex pattern as shown in the previous study. In other words, the wave-like temperature profile will not exist in this case.

### 7.2.2 Results and Discussion

The mean Nusselt Number ( $\overline{Nu}$ ) is illustrated in Figure 7.6. Based on the figure, the magnitude of the  $\overline{Nu}$  for both RVG and FVG cases do not show much different. However, there is a distinct difference in its distribution. The discussion of the  $\overline{Nu}$  contour can be classified into two parts, *i.e.* (i) the region around the VG ( $-1 < z/D < 4$ ) and (ii) the downstream region ( $z/D > 4$ ).

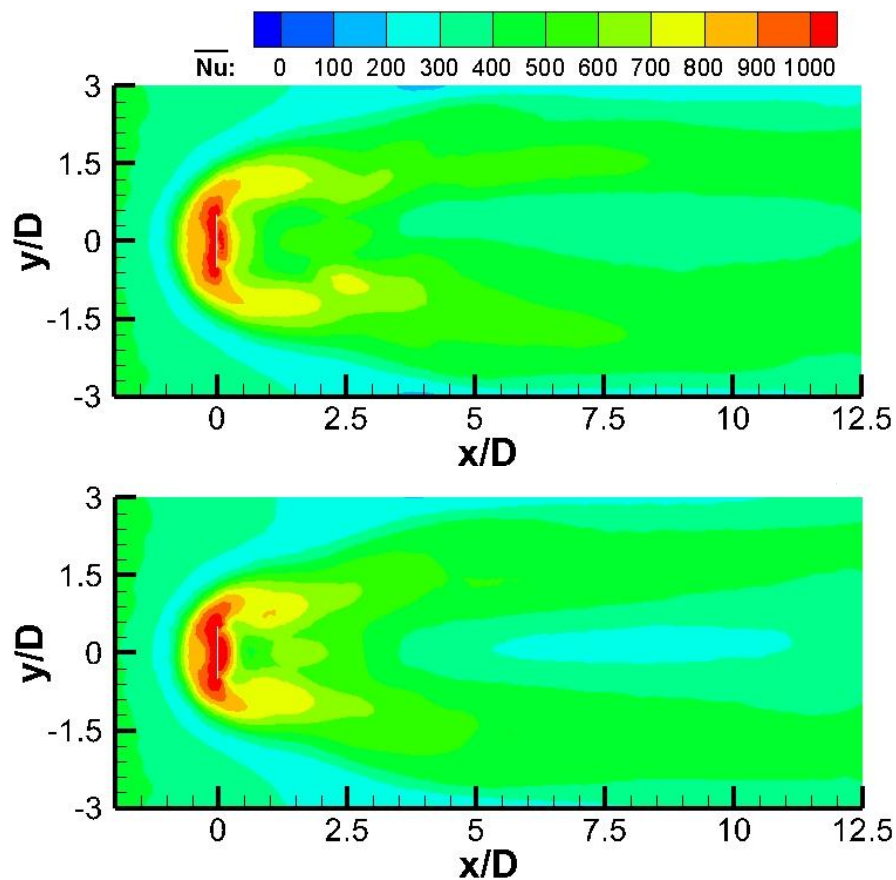
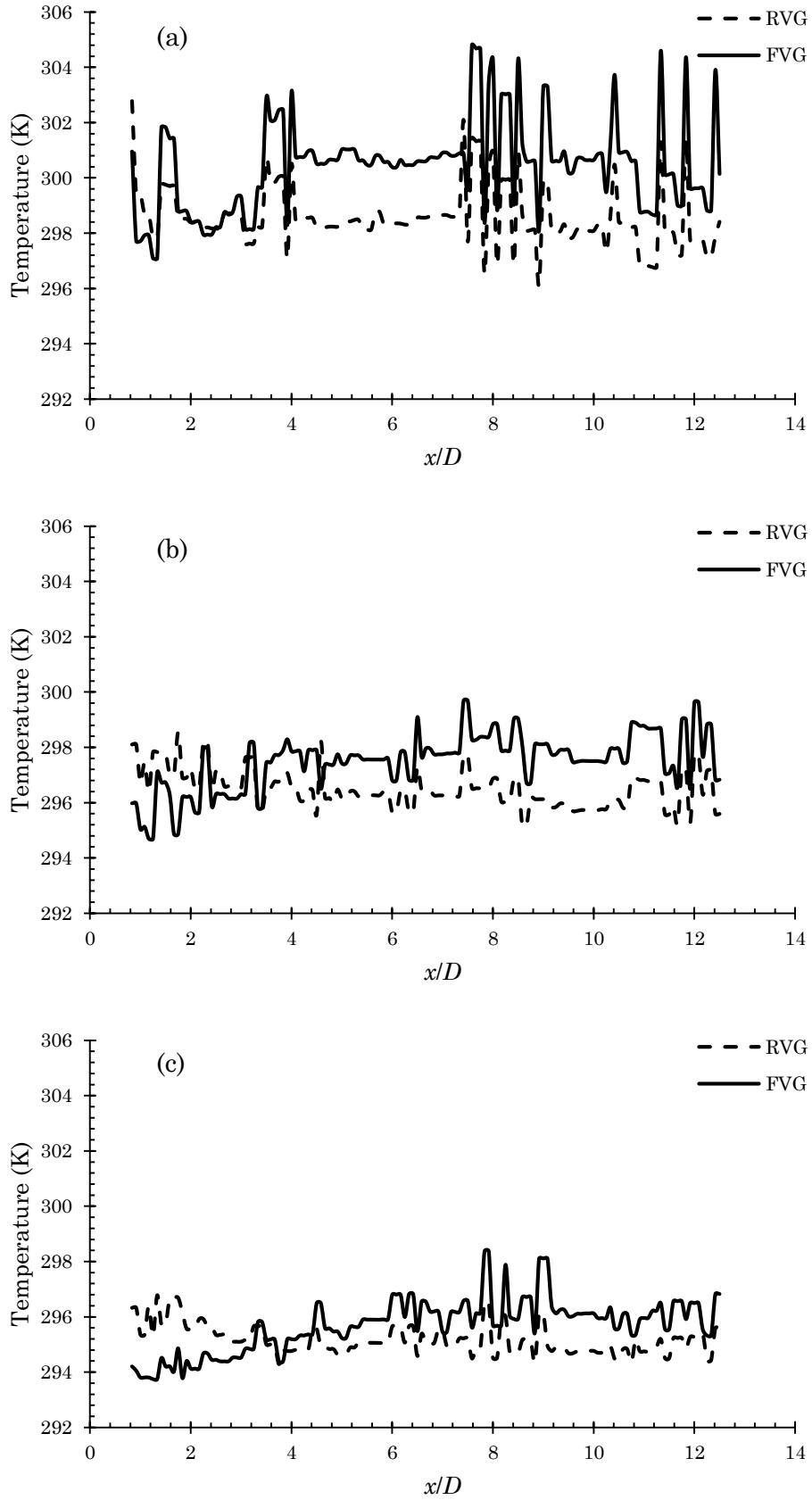


Figure 7.6: The mean Nusselt Number ( $\overline{Nu}$ ) on the ground plate of (top) the RVG and (bottom) FVG.

**Around the VG ( $-1 < z/D < 3.5$ ):** At the region around the VG, it can be seen that the heat transfer rate around the FVG is greater than that of the RVG in term of its spatial distribution (the region with the highest  $\overline{Nu}$  level (■) is spatially larger). Purely based on this observation, it can be said that the FVG has promoted the heat transfer rate and hence, lead to a better heat transfer performance.

**The downstream region ( $z/D > 3.5$ ):** It can be seen that, in the case of RVG, the contour with higher  $\overline{Nu}$  level is extended further downstream than that of the FVG case. The contour suggests that the RVG case has a better heat transfer performance than the FVG case at the downstream region ( $z/D > 3.5$ ). This result is, however, opposing to the previous observation.

By considering both observations, it is difficult to conclude that which case has a better heat transfer performance; additional information is needed. Therefore, the temperature near the heated ground plate is probed and plotted to aid the analysis. The temperature profiles are shown in Figure 7.7. In general, based on the profiles, the temperature around the FVG ( $x/D < 3.5$ ) is lower than that of the RVG. The temperature is increasing gradually and it surpasses the RVG's at further downstream, *i.e.*  $x/D > 3.5$ . The results clearly show that more heat has been transported, at  $x/D > 3.5$ , to the fluid in the case with FVG compared to the RVG case, which is completely opposing the observations seen from the  $\overline{Nu}$  contour that suggest that the RVG provides a better heat transfer performance.



**Figure 7.7:** The temperature profile ( $T$ ), along the  $x/D$  direction. (a) to (c) represent different spanwise locations, *i.e.*  $z/D=1/6$ ,  $1/3$  and  $1/2$  respectively.



However, the temperature profiles have provided an important insight that may result in the presented  $\overline{Nu}$  contour. By examining the definition of Nusselt Number, it is found that the Nusselt Number is strongly dependent on the temperature gradient, as shown in Equation 7.2.

$$Nu = \frac{hD_c}{k} = \frac{\left[ \frac{\partial(T_s - T)}{\partial z} \right]_{z=0}}{\left( \frac{T_s - T_\infty}{D_c} \right)} \quad (7.2)$$

Where  $T_s$  is the temperature of the heated surface,  $T_\infty$  is the temperature of the free stream flow. In the expression, the  $z$ -direction refers to the direction normal to the heated surface. Based on Equation 7.2, the main aspect that drives the heat transfer is the temperature difference between the heated surface and the flow. Furthermore, since the denominator is the same for both RVG and FVG cases (the surface and the flow have an identical temperature in both cases; the  $D_c$  is also the same in both cases), the difference of Nusselt Number shown in Figure 7.6 must be induced by the difference between the numerators (*i.e.* the temperature gradient between the heated surface and the flow).

By relating the temperature profile with the above definition, the reason that causes the distribution shown in the  $\overline{Nu}$  contour has become clear. Figure 7.8 is used to aid the following explanation. The relationship between the temperature profile and the Nusselt Number is also summarised in the figure (in the boxes). The last expression in each box denotes the temperature gradient (temperature difference between the heated surface and the flow). The comparison shows that, at  $z/D < 3.5$ , the gradient of the FVG case is greater than the RVG case. As a result, according to Equation 6.2, the  $\overline{Nu}_{FVG}$  is greater than the  $\overline{Nu}_{RVG}$ , which matches with the observation gained from Figure 7.6. Meanwhile, this relationship is completely inverted at the downstream (at  $z/D > 3.5$ ) as the flow temperature in the FVG case has become greater than that in the RVG case. Consequently, the relationship of the  $\overline{Nu}$  between both cases is inverted as well; where  $\overline{Nu}_{RVG}$  is greater than the  $\overline{Nu}_{FVG}$ .

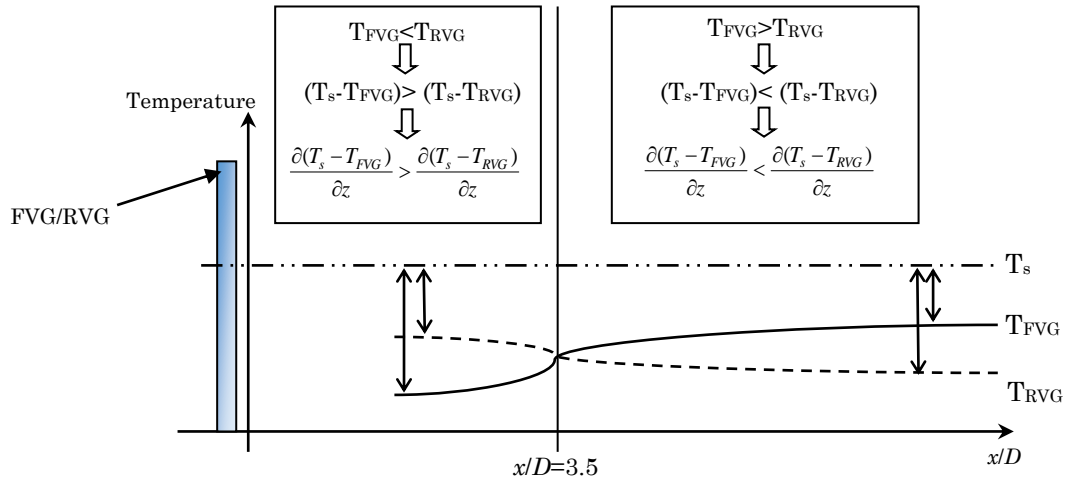


**Figure 7.8: Schematic that illustrates the relationship between the Nusselt Number and the flow temperature.**

In this section, both mean Nusselt Number and temperature profiles are examined to study the heat transfer performance of the case. However, the findings from both analyses have demonstrated a different conclusion. Firstly, based on the Nusselt Number contour, the RVG case is said to have an overall better heat transfer performance. On the contrary, the temperature profiles show that the FVG provides a better heat transfer at its downstream. However, if the ultimate goal of the heat transfer process is to deliver the heat up the fluid that flows in the system, then the FVG can be considered to have a better heat transfer performance.

In addition, in the author's opinion, the heat transfer performance at further downstream does not actually play a significant role in the actual application of the FVG. As commonly known, a heat transfer system is regularly featuring multiple VGs that are arranged in a certain order and/or configuration. In other words, the effective region that a single FVG has to take care will be the region around it before the subsequent FVG overtake the responsibility. Since the  $Nu$  around the FVG is higher than that of the RVG, the FVG allows a relatively efficient heating process at its immediate downstream, thus, it is preferred than the RVG.

Besides, this study also raises another doubt, which is the feasibility of using the Nusselt Number as the direct indicator of heat transfer performance. As seen from the result presented in this section, although the RVG's  $\overline{Nu}$  is, in overall, greater than the FVG's  $\overline{Nu}$ , the FVG plays a better part in conveying the heat towards the fluid. Due to its effectiveness in heating, the flow at the

downstream has already reached a higher temperature. As a result, the temperature difference between the heated surface and the fluid flow decreases, which leads to a slower heat transfer process in that region, hence showing a lower  $\overline{Nu}$ . If the  $\overline{Nu}$  is the only measure used in quantifying the heat transfer process, then the fact that the fluid temperature has reached a higher temperature (such as the result observed in the current study) will not be uncovered. Again, if the ultimate goal of the heat transfer process is to increase the temperature of the fluid, then temperature monitoring should also play a crucial part in justifying the performance of a heat transfer system.

### Summary of Chapter

This chapter has demonstrated the heat transfer performance of the proposed FVG. Comparisons with the typical RVG system were made to justify its performance. First of all, it has been identified, in the first study of the chapter, that the strength of vortex has played a crucial role in heat transfer. Based on the result, a stronger vortex will draw more heat from the heated VG resulting in a better heat transfer process.

In the second study, the flow temperature behind the FVG is higher than the flow behind the RVG. Although the mean Nusselt Number contour shows that the RVG has an overall greater heat transfer rate, it is later identified that the result is caused by the fact that the flow temperature at far downstream of the FVG is greater than that of the RVG case. Due to the decreasing temperature difference between the heated surface and the flow, the Nusselt Number in the case of FVG shows a lower value than the RVG case. However, since the goal of heat transfer process is to heat up the flow, the FVG is considered to have a better performance than the RVG.

In overall, although the difference is not huge, the results have shown that FVG performs slightly better than the RVG in term of conveying heat to the flow. Although the improvement may be small as shown from the result, the total improvement when multiple FVGs are employed can be significant.

Besides, this study has considered only a fraction of the full potential of a FVG in heat transfer. In addition, the current URANS model might not be the perfect model to simulate heat transfer as it is weak in predicting the fluctuation components of turbulent flow due to its isotropic assumption. Therefore, it might not deliver a complete idea of heat transfer process since it is

dependant to the fluctuation components of turbulent flow as well. Further studies, with a proper turbulence model, are required to explore the effects and impacts of employing a FVG or an array of FVGs on heat transfer system.

## Chapter 8: Conclusions and Recommendations

This chapter summarises the key findings on the wake size modification, the turbulence characteristics and the heat transfer performance of the Flexible Vortex Generator (FVG) that are identified and investigated via numerical simulation. This chapter also covers the recommendation for future research in this area.

### 8.1 The Wake Size behind a FVG

The wake size depicts the effective region where turbulence activities occur. Therefore, a vortex generator (VG) that can create a larger wake size demonstrates its better turbulence generation ability. In the current work, the height and the width of the wake are examined.

#### Wake Height

- The wake of a FVG is generally larger than its respective rigid counterpart (the RVG that has the same geometrical properties and is submerged in an identical flow condition with the FVG). Since a larger wake denotes a larger effective region where turbulence activities can take place, this result depicts that a FVG can generate a larger turbulent region. Hence, a FVG has a better turbulence generation ability.
  - The wake height increment happened in both the study of circular and flat plate FVGs.
- The cause of the greater wake height behind a FVG is the vanishing of downwash when the FVG is deflected.
  - Although the downwash vanished completely in all the cases of circular FVG, the study of flat plate FVG shows that the degree of deflection plays a major role to weaken the downwash. In short, the greater the deflection, the weaker the downwash. As a result, the larger wake is formed.

#### Wake Width

- Although the FVG is constantly oscillating in large displacement, the width of the wake does not change significantly after replacing a RVG with a FVG.

## 8.2 Turbulence Characteristics behind a FVG

The shear rate ( $\partial U_i / \partial x_j$ ) is investigated to examine the turbulence production. According to the shear production term in the turbulent kinetic budget, a greater shear rate depicts a greater turbulence production.

### Wall Shear Stress

- The wall shear stress is the source of turbulence that is being fed to the vortex. Based on the result, the wall shear stress on the FVG is generally greater than that on its rigid counterpart. This denotes that the source of turbulence has become greater when a FVG is employed.
- A flow model is proposed to illustrate and explain the mechanism that increases the wall shear stress on a FVG. The figure presented in the respective chapter is included here for the purpose to supplement the conclusion.
  - Based on the flow model, it is concluded that the cause of the escalated wall shear stress on a FVG is the oscillation of the FVG. The key parameter that governs this mechanism is the structural velocity ( $U_s$ ), which is the oscillation velocity of the FVG.

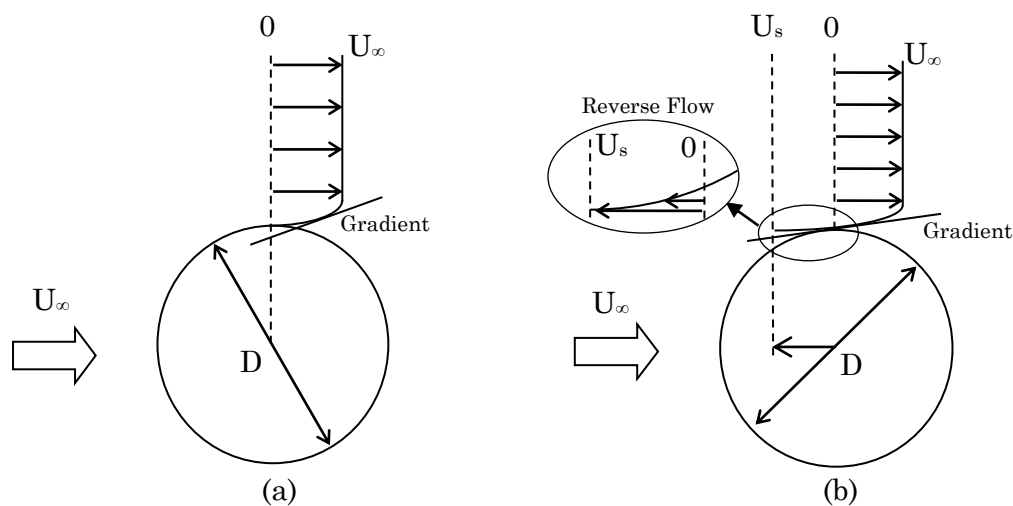


**Figure 8.1: The proposed flow model – showing the velocity gradient on the surface of a submerged structure: (a) stationary, (b) moving against the flow with velocity  $U_s$  (Taken from Chapter 6).**

### Vortex Strength – the Circulation

- Based on the previous wall shear stress analysis, it indicates that the circulation – that depicts the shear rate within a vortex – is becoming

stronger when a FVG is employed because the turbulence source (the wall shear stress) has become stronger.

- The circulation of the vortex behind the RVG and FVG was calculated, and the result showed the vortex generated from a FVG is stronger (the vortex generated from the FVG appears to have greater circulation). This result has clearly demonstrated that the FVG is a better turbulence generator compared to the conventional RVG.
- Besides, the result from the circulation analysis is used to justify the proposed flow model. Based on the flow model, the case with the greatest structural velocity will have the greater circulation. Therefore, the structural velocity is computed and the result shows an excellent agreement with the prediction. This has further confirmed the reliability of the proposed flow model.

### **8.3 Heat Transfer Performance of a FVG**

The FSI model is extended to simulate the heat transfer performance of a FVG. Since a greater turbulence is able to enhance heat transfer significantly, the previous results show that the FVG is capable of improving the heat transfer performance when compared to a conventional RVG. Two cases are considered in this study.

#### Heat Source on the FVG

- When the heat source is on the FVG, the result portrays the significant role of the vortex in delivering the heat towards the flow. From the previous study, it is already known that the vortex generated from the FVG is stronger. As a result, the stronger vortex drew more heat from the heated FVG thus, resulting in a better heat transfer process compared to the case with the RVG. The Nusselt Number and the temperature profiles were examined and the results had confirmed the positive impact of the stronger vortex in heat transfer process.

#### Heat Source on the Ground Plate

- When the heat source is on the ground plate (the surface where the VG is erected), the heat transfer process is quick at the FVG's surrounding. When comparing with the case with RVG, the Nusselt Number is greater around the FVG than the RVG. This result depicts the positive impact of the FVG

in enhancing heat transfer, and it is so effective that the temperature at far downstream of the FVG is significantly greater than that of the RVG case.

#### 8.4 Significance of the Current Work

According to the literature review, it has been clearly demonstrated the lack of interest of studying the turbulence characteristics behind a free-oscillating structure such as the vortex generator – a simple cantilever – used in the current study. As a result of the ignorance, only countable number of papers that focus on the flow dynamic behind a free-oscillating structure are published, not to mention its turbulence aspects. The significance of the present work is the study of the impact of a free-oscillating structure on the flow dynamics, specifically, on the turbulence aspect and/or the vortex dynamics.

On the other hand, it is worth to mention that an enormous amount of studies has been conducted to study the structural dynamics of the same problem. The proposed flow model has reduced the relationship between multiple fluid and structural parameters to a single and clear governing parameter, which is the structural velocity ( $U_s$ ) of the oscillating structure. This finding is acting as a bridge to connect the current understanding of the structural dynamics to the fluid dynamics. However, this is currently applicable only when the turbulence enhancement is the main focus of the problem. In short, all the published papers that discuss the structural dynamics can have a connection to turbulence generation by simply checking on the structural velocity that can be computed from the displacement/amplitude response, which is normally available in those papers.

Besides, it has been frequently demonstrated that the turbulence generated from an oscillating structure is governed by the amplitude and oscillation frequency, *i.e.* Griffin (1971) for its description on velocity fluctuation; Saxena and Laird (1978), Cheng *et al.* (1997), Leung *et al.* (1981) and Gau *et al.* (1999) for their description on the heat transfer enhancement that is originated from the turbulence enhancement. In light of this, the author wishes to emphasis that these observations or remarks are the same with the present conclusion – the turbulence enhancement is governed by the structural velocity,  $U_s$ .

Consider a cylinder oscillates in a sinusoidal response; so its oscillation can be described by the following simple equation:



$$d_y = A \sin(\omega t) \quad (8.1)$$

where  $A$  represents the amplitude of the oscillation and  $\omega$  is the oscillation frequency. The  $U_s$  can be calculated easily by differentiating Equation 8.1. The velocity response is then described by the following equation:

$$U_s = \omega \cdot A \cos(\omega t) \quad (8.2)$$

Since  $\cos(\omega t)$  is just a curve's properties (it does not have a physical meaning other than stating the characteristics of the temporal response of a given quantity, in this case  $A\omega$ ), the  $U_s$  is basically a product of the oscillation amplitude and its frequency. The fact that a greater amplitude and/or frequency can generate greater turbulence, which are described in the aforementioned studies, is also reflected in this equation/relationship. So, once again, this shows the reliability of the proposed flow model. On top of that, the proposed flow model has advanced the current understanding, by providing the relationship between the oscillation amplitude and frequency (*i.e.* the structural velocity,  $U_s$ ) and also its physics in the turbulence enhancement via an oscillating structure.

## 8.5 Recommendations

There are a few recommendations for future research have been identified throughout the course of this study, there are:

- Firstly, in Chapter 5, the result suggests that the vanishing/weakening of the downwash that ultimately lead to the larger wake behind the FVG is caused by the deflection of the FVG. In addition, the degree of deflection plays a direct role as well. Therefore, an actual bent rigid VG should be investigated to prove the above speculation. If it is true that the deflection is the only parameter that causes the vanishing of downwash, then, as long as the wake size is the only concern, there is no need to employ a flexible vortex generator, which is highly unsteady, into the system. The wake size can be altered via controlling the degree of deflection (or angle of attack) of the vortex generator.
- The present study is done thoroughly by considering a system that consists of only a single vortex generator, in both flexible and rigid case. In reality, multiple vortex generators are incorporate into a system to stimulate and facilitate turbulence. So, the future investigation can consider a system consists of multiple FVGs, arranged in different configurations, and investigate the interaction within the array of FVGs. An optimal configuration can be sorted out from this study as well.

- Besides, the current study manipulates the stiffness of the FVG by varying the aspect ratio (the length) of the FVG, so that different oscillation responses (structural velocity, oscillation frequency and others) can be attained. There is another approach that worth a try, which is to change the material of the FVG instead of the length. However, this approach has a series of influences at multiple degrees, such as changing the second moment of inertia ( $I$ ), the structural density, the slenderness factor and others, that increases the complexity of the study. In light of this, additional care has to be spent to understand the complex chained-influences towards the outcome. Despite its complexity, this approach is seen to have greater relevance towards the industry as multiple materials should normally be considered during the design phase to seek for the most suitable material for a specific application.
- In late Chapter 6, it is noticed that the shedding mode has a great impact on the strength of the generated vortex (*i.e.* the impact of the “peeling” shedding mode on the strength of the generated vortex). Based on the observation, the motion of the FVG has forced the vortex filament to be peeled off from the FVG. This action has cut off the supply of vorticity towards the forming vortex. Although the generated vortex is still stronger compared to the vortex generated from a static RVG, this observation has highlighted the possibility that the vortex can attain a greater strength if the shedding mode favours the vortex formation process. Therefore, the relationship between the motion of the FVG and the shedding mode should be investigated. Besides, the effects of shedding mode on the vortex strength should be explored further.
- The heat transfer enhancement ability of the FVG should be explored further as well. In the current study, only two cases were considered due to the limitation in scope of the project. Different heating conditions, oscillation responses, and FVG’s configurations should be investigated to enrich the understanding of the heat transfer performance of FVG(s).

## References

- Abdollahi, A., & Shams, M. (2015). Optimization of shape and angle of attack of winglet vortex generator in a rectangular channel for heat transfer enhancement. *Applied Thermal Engineering*, *81*, 376-387.
- Adaramola, M. S., Akinlade, O. G., Sumner, D., Bergstrom, D. J., & Schenstead, A. J. (2006). Turbulent wake of a finite circular cylinder of small aspect ratio. *Journal of Fluids and Structures*, *22*(6), 919-928.
- Afgan, I., Moulinec, C., Prosser, R., & Laurence, D. (2007). Large eddy simulation of turbulent flow for wall mounted cantilever cylinders of aspect ratio 6 and 10. *International Journal of Heat and Fluid Flow*, *28*(4), 561-574.
- Ağra, Ö., Demir, H., Atayılmaz, Ş. Ö., Kantaş, F., & Dalkılıç, A. S. (2011). Numerical investigation of heat transfer and pressure drop in enhanced tubes. *International Communications in Heat and Mass Transfer*, *38*(10), 1384-1391.
- Ali, S., Habchi, C., Menanteau, S., Lemenand, T., & Harion, J. L. (2015). Heat transfer and mixing enhancement by free elastic flaps oscillation. *International Journal of Heat and Mass Transfer*, *85*, 250-264.
- Ali, S., Menanteau, S., Habchi, C., Lemenand, T., & Harion, J. L. (2016). Heat transfer and mixing enhancement by using multiple freely oscillating flexible vortex generators. *Applied Thermal Engineering*, *105*, 276-289.
- Angrilli, F., Di Silvio, G., & Zanardo, A. (1972). Hydroelasticity study of a circular cylinder in a water stream. *Flow-Induced Structural Vibrations (ed. E. Naudascher)*, 504-512.
- Aris, M. S., Owen, I., & Sutcliffe, C. J. (2007, January). The application of shape memory alloy as vortex generators and flow control devices for enhanced convective heat transfer. In *ASME/JSME 2007 5th Joint Fluids Engineering Conference* (pp. 1465-1470). American Society of Mechanical Engineers.
- Ayoub, A., & Karamcheti, K. (1982). An experiment on the flow past a finite circular cylinder at high subcritical and supercritical Reynolds numbers. *Journal of Fluid Mechanics*, *118*, 1-26.
- Bai, Y., & Bai, Q. (Eds.). (2005). *Subsea Pipelines and Risers: Vortex-induced Vibrations (VIV) and Fatigue*. Elsevier.
- Bearman, P. W. (2011). Circular cylinder wakes and vortex-induced vibrations. *Journal of Fluids and Structures*, *27*(5), 648-658.
- Benra, F. K., Dohmen, H. J., Pei, J., Schuster, S., & Wan, B. (2011). A comparison of one-way and two-way coupling methods for numerical analysis of fluid-structure interactions. *Journal of Applied Mathematics*, *2011*.

- Bernitsas, M. M., Raghavan, K., Ben-Simon, Y., & Garcia, E. M. (2008). VIVACE (Vortex Induced Vibration Aquatic Clean Energy): A new concept in generation of clean and renewable energy from fluid flow. *Journal of Offshore Mechanics and Arctic Engineering*, *130*(4), 041101.
- Biswas, G., & Chattopadhyay, H. (1992). Heat transfer in a channel with built-in wing-type vortex generators. *International Journal of Heat and Mass Transfer*, *35*(4), 803-814.
- Biswas, G., Mitra, N. K., & Fiebig, M. (1989). Computation of laminar mixed convection flow in a channel with wing type built-in obstacles. *Journal of Thermophysics and Heat Transfer*, *3*(4), 447-453.
- Blevins, R. D., & Coughran, C. S. (2009). Experimental investigation of vortex-induced vibration in one and two dimensions with variable mass, damping, and Reynolds number. *Journal of Fluids Engineering*, *131*(10), 101202.
- Breuer, M., De Nayer, G., Münsch, M., Gallinger, T., & Wüchner, R. (2012). Fluid–structure interaction using a partitioned semi-implicit predictor–corrector coupling scheme for the application of large-eddy simulation. *Journal of Fluids and Structures*, *29*, 107-130.
- Catalano, P., Wang, M., Iaccarino, G., & Moin, P. (2003). Numerical simulation of the flow around a circular cylinder at high Reynolds numbers. *International Journal of Heat and Fluid Flow*, *24*(4), 463-469.
- Chen, Y., Fiebig, M., & Mitra, N. K. (1998). Heat transfer enhancement of a finned oval tube with punched longitudinal vortex generators in-line. *International Journal of Heat and Mass Transfer*, *41*(24), 4151-4166.
- Cheng, C. H., Chen, H. N., & Aung, W. (1997). Experimental study of the effect of transverse oscillation on convection heat transfer from a circular cylinder. *Journal of Heat Transfer*, *119*(3), 474-482.
- Constantinides, Y., & Oakley, O. H. (2006, January). Numerical prediction of bare and straked cylinder VIV. In *25th International Conference on Offshore Mechanics and Arctic Engineering* (pp. 745-753). American Society of Mechanical Engineers.
- Cui, Z., Zhao, M., Teng, B., & Cheng, L. (2015). Two-dimensional numerical study of vortex-induced vibration and galloping of square and rectangular cylinders in steady flow. *Ocean Engineering*, *106*, 189-206.
- Dabiri, J. O., & Gharib, M. (2005). The role of optimal vortex formation in biological fluid transport. *Proceedings of the Royal Society of London B: Biological Sciences*, *272*(1572), 1557-1560.
- Ding, L., Bernitsas, M. M., & Kim, E. S. (2013). 2-D URANS vs. experiments of flow induced motions of two circular cylinders in tandem with passive turbulence control for  $30,000 < \text{Re} < 105,000$ . *Ocean Engineering*, *72*, 429-440.
- Ding, L., Zhang, L., Kim, E. S., & Bernitsas, M. M. (2015). URANS vs. experiments of flow induced motions of multiple circular cylinders with passive turbulence control. *Journal of Fluids and Structures*, *54*, 612-628.

- Dol, S. S., Kopp, G. A., & Martinuzzi, R. J. (2008). The suppression of periodic vortex shedding from a rotating circular cylinder. *Journal of Wind Engineering and Industrial Aerodynamics*, 96(6), 1164-1184.
- Dol, S. S., Salek, M. M., & Martinuzzi, R. J. (2014). Energy Redistribution Between the Mean and Pulsating Flow Field in a Separated Flow Region. *Journal of Fluids Engineering*, 136(11), 111105.
- Erickson, P. A., & Liao, C. H. (2007). Heat transfer enhancement of steam reformation by passive flow disturbance inside the catalyst bed. *Journal of Heat Transfer*, 129(8), 995-1003.
- Faltinsen, O. (1993). Sea loads on ships and offshore structures (Vol. 1). Cambridge university press.
- Farivar, D. J. (1981). Turbulent uniform flow around cylinders of finite length. *AIAA journal*, 19(3), 275-281.
- Ferrari, J. A. (1999). *Hydrodynamic loading and response of offshore risers* (PhD Thesis, University of London, UK).
- Feymark, A., Alin, N., Bensow, R., & Fureby, C. (2010). LES of an Oscillating Cylinder in a Steady Flow. In *48th AIAA Aerospace Sciences Meeting Including the New Horizons Forum and Aerospace Exposition* (p. 560).
- Feymark, A., Alin, N., Bensow, R., & Fureby, C. (2012). Numerical simulation of an oscillating cylinder using large eddy simulation and implicit large eddy simulation. *Journal of Fluids Engineering*, 134(3), 031205.
- Fiebig, M. (1995). Embedded vortices in internal flow: heat transfer and pressure loss enhancement. *International Journal of Heat and Fluid Flow*, 16(5), 376-388.
- Fiebig, M., Kallweit, P., & Mitra, N. K. (1986). Wing type vortex generators for heat transfer enhancement. *Heat Transfer*, 1(1986), 909-2.
- Fiebig, M., Kallweit, P., Mitra, N., & Tiggelbeck, S. (1991). Heat transfer enhancement and drag by longitudinal vortex generators in channel flow. *Experimental Thermal and Fluid Science*, 4(1), 103-114.
- Fiebig, M., Valencia, A., & Mitra, N. K. (1993). Wing-type vortex generators for fin-and-tube heat exchangers. *Experimental Thermal and Fluid Science*, 7(4), 287-295.
- Fiebig, M., Valencia, A., & Mitra, N. K. (1994). Local heat transfer and flow losses in fin-and-tube heat exchangers with vortex generators: a comparison of round and flat tubes. *Experimental Thermal and Fluid Science*, 8(1), 35-45.
- Fox, T. A., & West, G. S. (1993). Fluid-induced loading of cantilevered circular cylinders in a low-turbulence uniform flow. Part 1: Mean loading with aspect ratios in the range 4 to 30. *Journal of Fluids and Structures*, 7(1), 1-14.

- Fu, W. S., & Tong, B. H. (2002). Numerical investigation of heat transfer from a heated oscillating cylinder in a cross flow. *International Journal of Heat and Mass Transfer*, 45(14), 3033-3043.
- Fujarra, A. L. C., Pesce, C. P., Flemming, F., & Williamson, C. H. K. (2001). Vortex-induced vibration of a flexible cantilever. *Journal of Fluids and Structures*, 15(3), 651-658.
- Gau, C., Wu, J. M., & Liang, C. Y. (1999). Heat transfer enhancement and vortex flow structure over a heated cylinder oscillating in the crossflow direction. *Journal of heat transfer*, 121(4), 789.
- Gentry, M. C., & Jacobi, A. M. (1995). *Heat transfer enhancement on a flat plate using delta-wing vortex generators*. Air Conditioning and Refrigeration Center. College of Engineering. University of Illinois at Urbana-Champaign..
- Gorji, M., Mirgolbabaei, H., Barari, A., Domairry, G., & Nadim, N. (2011). Numerical analysis on longitudinal location optimization of vortex generator in compact heat exchangers. *International Journal for Numerical Methods in Fluids*, 66(6), 705-713.
- Govardhan, R., & Williamson, C. H. K. (2000). Modes of vortex formation and frequency response of a freely vibrating cylinder. *Journal of Fluid Mechanics*, 420, 85-130.
- Govardhan, R., & Williamson, C. H. K. (2001). Mean and fluctuating velocity fields in the wake of a freely-vibrating cylinder. *Journal of Fluids and Structures*, 15(3), 489-501.
- Griffin, O. M. (1971). The unsteady wake of an oscillating cylinder at low Reynolds number. *Journal of Applied Mechanics*, 38(4), 729-738.
- Guilmineau, E., & Queutey, P. (2004). Numerical simulation of vortex-induced vibration of a circular cylinder with low mass-damping in a turbulent flow. *Journal of fluids and structures*, 19(4), 449-466.
- Heseltine, J. L. (2003). Flow around a circular cylinder with a free end (Master Thesis, University of Saskatchewan, Saskatchewan, Canada). Retrieved from <https://ecommons.usask.ca/handle/10388/etd-07252011-090143>
- Huang, Z. Y., Pan, Z. Y., & Cui, W. C. (2007). Numerical simulation of VIV of a circular cylinder with two degrees of freedom and low mass-ratio. *Journal of ship mechanics*, 11(1), 1.
- Jacobi, A. M., & Shah, R. K. (1995). Heat transfer surface enhancement through the use of longitudinal vortices: a review of recent progress. *Experimental Thermal and Fluid Science*, 11(3), 295-309.
- Jeong, J., & Hussain, F. (1995). On the identification of a vortex. *Journal of fluid mechanics*, 285, 69-94.
- Johnston, C. R., Clavelle, E. J., Wilson, D. J., & Peck, B. J. (1998, June). Investigation of the vorticity generated by flow around a finite cylinder. In

- Proceedings of the 6th annual conference of the computational fluid dynamics society of Canada (CFD'98)*, Quebec City, Canada.
- Kaci, H. M., Lemenand, T., Della Valle, D., & Peerhossaini, H. (2009). Effects of embedded streamwise vorticity on turbulent mixing. *Chemical Engineering and Processing: Process Intensification*, 48(10), 1459-1476.
- Karanth, D., Rankin, G. W., & Sridhar, K. (1994). A finite difference calculation of forced convective heat transfer from an oscillating cylinder. *International journal of heat and mass transfer*, 37(11), 1619-1630.
- Kawamura, T., Hiwada, M., Hibino, T., Mabuchi, I., & Kumada, M. (1984). Flow around a Finite Circular Cylinder on a Flat Plate: Cylinder height greater than turbulent boundary layer thickness. *Bulletin of JSME*, 27(232), 2142-2151.
- Khoshvaght-Aliabadi, M., Zangouei, S., & Hormozi, F. (2015). Performance of a plate-fin heat exchanger with vortex-generator channels: 3D-CFD simulation and experimental validation. *International Journal of Thermal Sciences*, 88, 180-192.
- Krajnović, S. (2011). Flow around a tall finite cylinder explored by large eddy simulation. *Journal of Fluid Mechanics*, 676, 294-317.
- Kundu, P., & Cohen, I. (2008). *Fluid mechanics* 4<sup>th</sup> ed.
- Lam, K. M., Liu, P., & Hu, J. C. (2010). Combined action of transverse oscillations and uniform cross-flow on vortex formation and pattern of a circular cylinder. *Journal of Fluids and Structures*, 26(5), 703-721.
- Laohalertdecha, S., Naphon, P., & Wongwises, S. (2007). A review of electrohydrodynamic enhancement of heat transfer. *Renewable and Sustainable Energy Reviews*, 11(5), 858-876.
- Lee, J. H., & Bernitsas, M. M. (2011). High-damping, high-Reynolds VIV tests for energy harnessing using the VIVACE converter. *Ocean Engineering*, 38(16), 1697-1712.
- Lee, J., Shin, J., & Lee, S. (2012). Fluid–structure interaction of a flapping flexible plate in quiescent fluid. *Computers & Fluids*, 57, 124-137
- Lee, L., & Wang, Y. (1987). Aerodynamics of a circular cylinder of finite length in cross flow. In *Forum on Turbulent Flows- 1987, Cincinnati, OH* (pp. 61-65).
- Lemenand, T., Della Valle, D., Zellouf, Y., & Peerhossaini, H. (2003). Droplets formation in turbulent mixing of two immiscible fluids in a new type of static mixer. *International Journal of Multiphase Flow*, 29(5), 813-840.
- Leung, C. T., Ko, N. W. M., & Ma, K. H. (1981). Heat transfer from a vibrating cylinder. *Journal of sound and vibration*, 75(4), 581-582.
- Leruth, A. (2012). Heat exchanger network self-optimising control: Application to the crude unit at Mongstad refinery.

- Li, L., Du, X., Zhang, Y., Yang, L., & Yang, Y. (2015). Numerical simulation on flow and heat transfer of fin-and-tube heat exchanger with longitudinal vortex generators. *International Journal of Thermal Sciences*, *92*, 85-96.
- Liu, Y., So, R. M. C., & Cui, Z. X. (2005). A finite cantilevered cylinder in a cross-flow. *Journal of fluids and structures*, *20*(4), 589-609.
- Lotfi, B., Zeng, M., Sundén, B., & Wang, Q. (2014). 3D numerical investigation of flow and heat transfer characteristics in smooth wavy fin-and-elliptical tube heat exchangers using new type vortex generators. *Energy*, *73*, 233-257.
- Luhar, M., & Nepf, H. M. (2011). Flow - induced reconfiguration of buoyant and flexible aquatic vegetation. *Limnology and Oceanography*, *56*(6), 2003-2017.
- Luo, S. C., Gan, T. L., & Chew, Y. T. (1996). Uniform flow past one (or two in tandem) finite length circular cylinder (s). *Journal of wind engineering and industrial aerodynamics*, *59*(1), 69-93.
- Meneghini, J. R., Saltara, F., de Andrade Fregonesi, R., Yamamoto, C. T., Casaprima, E., & Ferrari, J. A. (2004). Numerical simulations of VIV on long flexible cylinders immersed in complex flow fields. *European Journal of Mechanics-B/Fluids*, *23*(1), 51-63.
- Menter, F. R. (1994). Two-equation eddy-viscosity turbulence models for engineering applications. *AIAA journal*, *32*(8), 1598-1605.
- Mitra, N. K., & Fiebig, M. (1993). Experimental investigations of heat transfer enhancement and flow losses in a channel with double rows of longitudinal vortex generators. *International Journal of Heat and Mass Transfer*, *36*(9), 2327-2337.
- Murrin, D. (2007). A three-dimensional simulation of Vortex Induced Vibrations (VIV) on marine risers at high Reynolds number using computational fluid dynamics (Doctoral dissertation, Memorial University of Newfoundland).
- Nakamura T, Kaneko S, Inada F, Kato M, Ishihara K, Nishihara T, Mureithi NW & Langthjem, M. A. (Eds.). (2013). Flow-induced vibrations: Classifications and lessons from practical experiences. Butterworth-Heinemann.
- Nguyen, V. T., & Nguyen, H. H. (2016). Detached eddy simulations of flow induced vibrations of circular cylinders at high Reynolds numbers. *Journal of Fluids and Structures*, *63*, 103-119.
- Okamoto, S., & Sunabashiri, Y. (1992). Vortex shedding from a circular cylinder of finite length placed on a ground plane. *Journal of Fluids Engineering*, *114*(4), 512-521.
- Okamoto, T., & Yagita, M. (1973). The experimental investigation on the flow past a circular cylinder of finite length placed normal to the plane surface in a uniform stream. *Bulletin of JSME*, *16*(95), 805-814.



- Palau-Salvador, G., Stoesser, T., Fröhlich, J., Kappler, M., & Rodi, W. (2010). Large eddy simulations and experiments of flow around finite-height cylinders. *Flow, turbulence and combustion*, *84*(2), 239-275.
- Pan, Z. Y., Cui, W. C., & Miao, Q. M. (2007). Numerical simulation of vortex-induced vibration of a circular cylinder at low mass-damping using RANS code. *Journal of Fluids and Structures*, *23*(1), 23-37.
- Park, C. W., & Lee, S. J. (2000). Free end effects on the near wake flow structure behind a finite circular cylinder. *Journal of Wind Engineering and Industrial Aerodynamics*, *88*(2), 231-246.
- Raghavan, K., & Bernitsas, M. M. (2011). Experimental investigation of Reynolds number effect on vortex induced vibration of rigid circular cylinder on elastic supports. *Ocean Engineering*, *38*(5), 719-731.
- Rostamy, N., Sumner, D., Bergstrom, D. J., & Bugg, J. D. (2012). Local flow field of a surface-mounted finite circular cylinder. *Journal of Fluids and Structures*, *34*, 105-122.
- Russell, C. M. B., Jones, T. V., & Lee, G. H. (1982). Heat transfer enhancement using vortex generators. In *Heat Transfer 1982, Volume 3* (Vol. 3, pp. 283-288).
- Sakamoto, H., & Arie, M. (1983). Vortex shedding from a rectangular prism and a circular cylinder placed vertically in a turbulent boundary layer. *Journal of Fluid Mechanics*, *126*, 147-165.
- Sarpkaya, T., & Shoaff, R. L. (1979). *A discrete-vortex analysis of flow about stationary and transversely oscillating circular cylinders*. Monterey, California. Naval Postgraduate School.
- Saxena, U. C., & Laird, A. D. K. (1978). Heat transfer from a cylinder oscillating in a cross-flow. *Journal of Heat Transfer*, *100*(4), 684-689.
- Simpson, R. L. (1989). Turbulent boundary-layer separation. *Annual Review of Fluid Mechanics*, *21*(1), 205-232.
- Singh, S. P., & Chatterjee, D. (2014). Impact of transverse shear on vortex induced vibrations of a circular cylinder at low Reynolds numbers. *Computers & Fluids*, *93*, 61-73.
- So, R. M., Wang, X. Q., Xie, W. C., & Zhu, J. (2008). Free-stream turbulence effects on vortex-induced vibration and flow-induced force of an elastic cylinder. *Journal of Fluids and Structures*, *24*(4), 481-495.
- Sreenivasan, K., & Ramachandran, A. (1961). Effect of vibration on heat transfer from a horizontal cylinder to a normal air stream. *International Journal of Heat and Mass Transfer*, *3*(1), 60-67.
- Steinke, M. E., & Kandlikar, S. G. (2004). Review of single-phase heat transfer enhancement techniques for application in microchannels, minichannels and microdevices. *International Journal of Heat and Technology*, *22*(2), 3-11.

- Sumer, B. M., & Fredsøe, J. (1997). *Hydrodynamics around cylindrical structures* (Vol. 12). World Scientific.
- Sumner, D. (2013). Flow above the free end of a surface-mounted finite-height circular cylinder: a review. *Journal of Fluids and Structures*, *43*, 41-63.
- Sumner, D., Heseltine, J. L., & Dansereau, O. J. P. (2004). Wake structure of a finite circular cylinder of small aspect ratio. *Experiments in Fluids*, *37*(5), 720-730.
- Sumner, D., Heseltine, J. L., & Dansereau, O. J. P. (2004). Wake structure of a finite circular cylinder of small aspect ratio. *Experiments in Fluids*, *37*(5), 720-730.
- Techet, A. H., Hover, F. S., & Triantafyllou, M. S. (1998). Vortical patterns behind a tapered cylinder oscillating transversely to a uniform flow. *Journal of Fluid Mechanics*, *363*, 79-96.
- Tian, F. B., Dai, H., Luo, H., Doyle, J. F., & Rousseau, B. (2014). Fluid-structure interaction involving large deformations: 3D simulations and applications to biological systems. *Journal of computational physics*, *258*, 451-469.
- Tiggelbeck, S., Mitra, N., & Fiebig, M. (1992). Flow structure and heat transfer in a channel with multiple longitudinal vortex generators. *Experimental thermal and fluid science*, *5*(4), 425-436.
- Valencia, A., Fiebig, M., Mitra, N. K., & Leiner, W. (1993). Heat transfer and flow loss in a fin-tube heat exchanger element with wing-type vortex generators. In *INSTITUTION OF CHEMICAL ENGINEERS SYMPOSIUM SERIES* (Vol. 129, pp. 327-327). HEMISPHERE PUBLISHING CORPORATION.
- Vassen, J. M., DeVincenzo, P., Hirsch, C., & Leonard, B. (2011, May). Strong coupling algorithm to solve fluid-structure-interaction problems with a staggered approach. In *7th European Symposium on Aerothermodynamics* (Vol. 692, p. 128).
- Viktorov, V., & Nimafar, M. (2013). A novel generation of 3D SAR-based passive micromixer: efficient mixing and low pressure drop at a low Reynolds number. *Journal of Micromechanics and Microengineering*, *23*(5), 055023.
- Wanderley, J. B., Souza, G. H., Sphaier, S. H., & Levi, C. (2008). Vortex-induced vibration of an elastically mounted circular cylinder using an upwind TVD two-dimensional numerical scheme. *Ocean Engineering*, *35*(14), 1533-1544.
- Wang, J., & Zhao, Y. (2015). Heat and fluid flow characteristics of a rectangular channel with a small diameter circular cylinder as vortex generator. *International Journal of Thermal Sciences*, *92*, 1-13.
- Wei, B. A. I. (2013). Numerical simulation of turbulent flow around a forced moving circular cylinder on cut cells. *Journal of Hydrodynamics, Ser. B*, *25*(6), 829-838.

- White, F. M., & Corfield, I. (2006). *Viscous fluid flow* (Vol. 3). New York: McGraw-Hill.
- Willden, R. H. J., & Graham, J. M. R. (2001). Numerical prediction of VIV on long flexible circular cylinders. *Journal of Fluids and Structures*, 15(3), 659-669.
- Williamson, C. H. K., & Roshko, A. (1988). Vortex formation in the wake of an oscillating cylinder. *Journal of fluids and structures*, 2(4), 355-381.
- Wu, J. M., & Tao, W. Q. (2008). Numerical study on laminar convection heat transfer in a channel with longitudinal vortex generator. Part B: Parametric study of major influence factors. *International Journal of Heat and Mass Transfer*, 51(13), 3683-3692.
- Wu, W., Bernitsas, M. M., & Maki, K. (2011, January). RANS simulation vs. experiments of flow induced motion of circular cylinder with passive turbulence control at  $35,000 < Re < 130,000$ . In *ASME 2011 30th International Conference on Ocean, Offshore and Arctic Engineering* (pp. 733-744). American Society of Mechanical Engineers.
- Xie, F. F., Jian, D. E. N. G., & Zheng, Y. (2011). Multi-mode of vortex-induced vibration of a flexible circular cylinder. *Journal of Hydrodynamics, Ser. B*, 23(4), 483-490.
- Yamamoto, C. T., Meneghini, J. R., Saltara, F., Fregonesi, R. A., & Ferrari, J. A. (2004). Numerical simulations of vortex-induced vibration on flexible cylinders. *Journal of fluids and structures*, 19(4), 467-489.
- Yin, D. (2013). Experimental and numerical analysis of combined in-line and cross-flow vortex induced vibration (Doctoral dissertation, Skipnes Kommunikasjon as).
- Zhao, M., & Cheng, L. (2010). Numerical investigation of local scour below a vibrating pipeline under steady currents. *Coastal Engineering*, 57(4), 397-406.
- Zhao, M., & Cheng, L. (2011). Numerical simulation of two-degree-of-freedom vortex-induced vibration of a circular cylinder close to a plane boundary. *Journal of Fluids and Structures*, 27(7), 1097-1110.

*Every reasonable effort has been made to acknowledge the owners of copyright material. I would be pleased to hear from any copyright owner who has been omitted or incorrectly acknowledged.*

## Appendix I: Structural Parameters Calculation

From Luhar and Nepf (2011), it is known that the structural properties are within the given uncertainty range, shown as follow:

1.  $E = 500 \pm 60kPa$
2.  $\Delta\rho = \rho_f - \rho_s = 330 \pm 50kg/m^3$
3.  $Width = 0.01 \pm 0.0005m$
4.  $Thickness = 0.0019 \pm 0.0001m$

Besides, it is also known that the mean flow velocity is 0.16m/s. To start the calculation, a few initial assumptions have to be made. In this case, it is assumed that the width is equal to 0.01m and thickness is equal to 0.002m; it is assumed that a 20°C water is used in their simulation. Furthermore, the value of Re can be obtained from Tian *et al.* (2014), which is 1600. With the above information, the following calculation can be made:

$$Re = \frac{\rho_f U_\infty D_c}{\mu} = \frac{998.2 \times 0.16 \times 0.01}{1 \times 10^{-3}} = 1597.12 \approx 1600$$

By using the assumed fluid properties, the computed Re is close to 1600. This means the assumed properties of the fluid is correct.

Since the density of the fluid is known, the density of the structural material can be computed based on the density ratio given by Tian *et al.* (2014):

$$\rho^* = 0.678 = \rho_s / \rho_f = \rho_s / 998.2$$

$$\rho_s = 676.78kg/m^3$$

The Young's modulus of the structural material can also be calculated based on the relationship given by Tian *et al.* (2014):

$$E^* = 19054.9 = \frac{E}{\rho_s U_\infty^2} = \frac{E}{998.2 \times 0.16^2}$$

$$E = 486927.4Pa$$

Now, all the essential properties are obtained. The values are checked with the uncertainty range given by Luhar and Nepf (2011) for final confirmation:

1.  $E = 486.92kPa$  [within  $500 \pm 60kPa$ ]
2.  $\Delta\rho = 998.2 - 676.78 = 321.42kg/m^3$  [within  $330 \pm 50kg/m^3$ ]

All properties lie within the given uncertainty range.

## Appendix II: Displacement Responses of FVGs

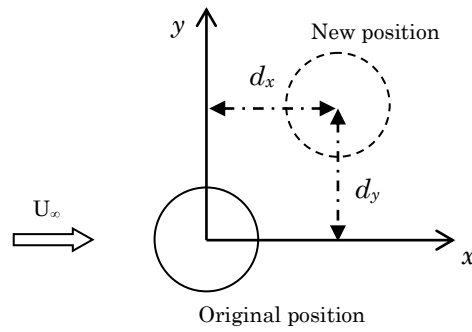
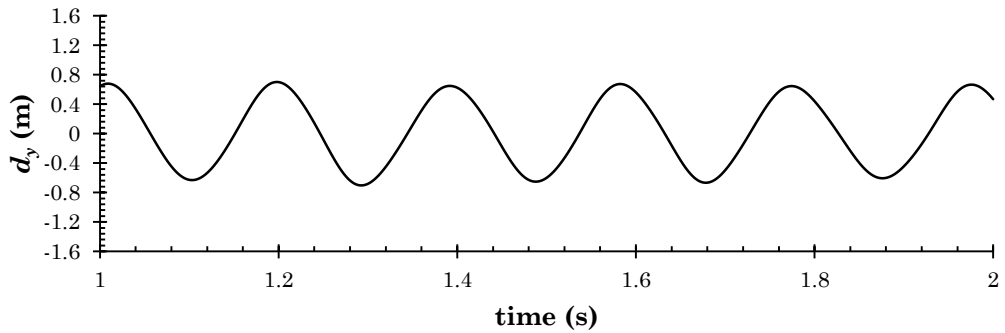


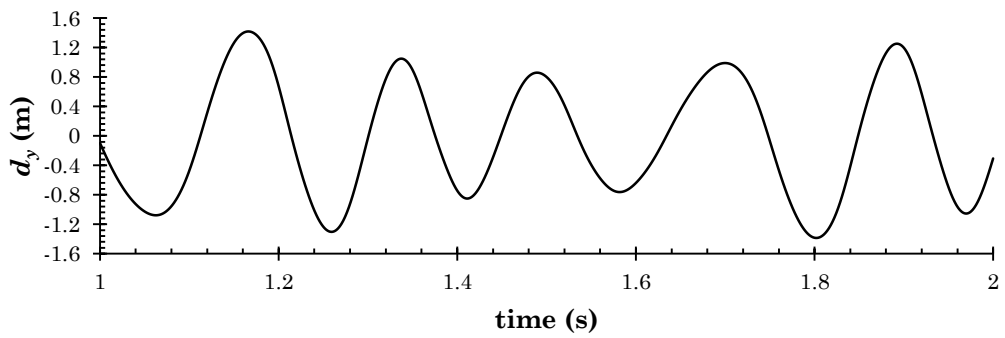
Figure A1: Definition of displacement of RVG due to crossflow with velocity  $U_\infty$ .

### y-displacement vs. time plot of circular FVG:

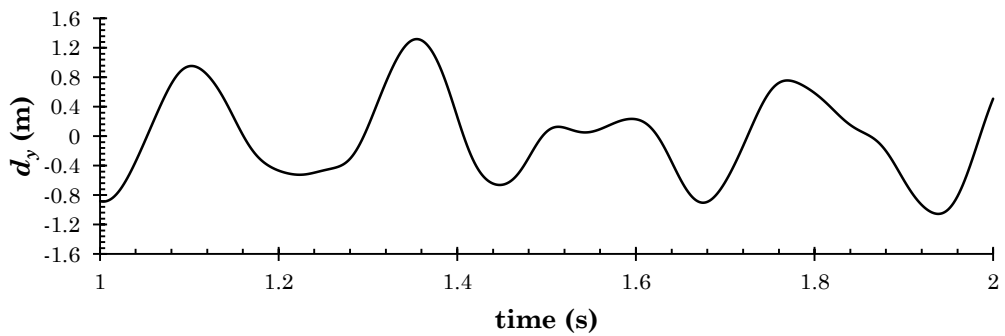
6CF



8CF

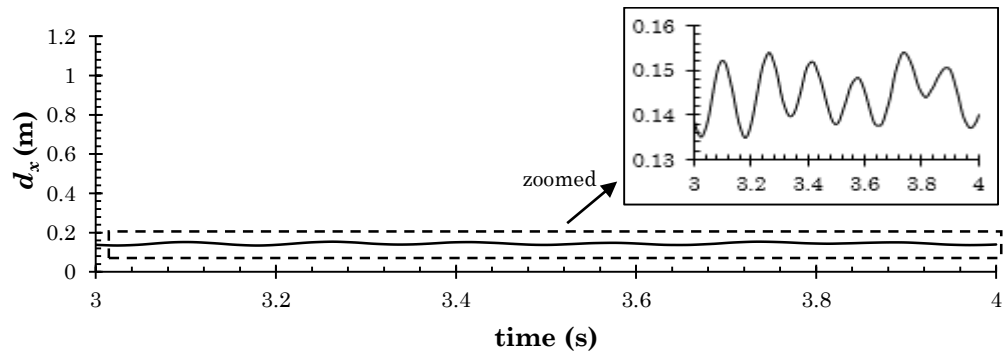


10CF

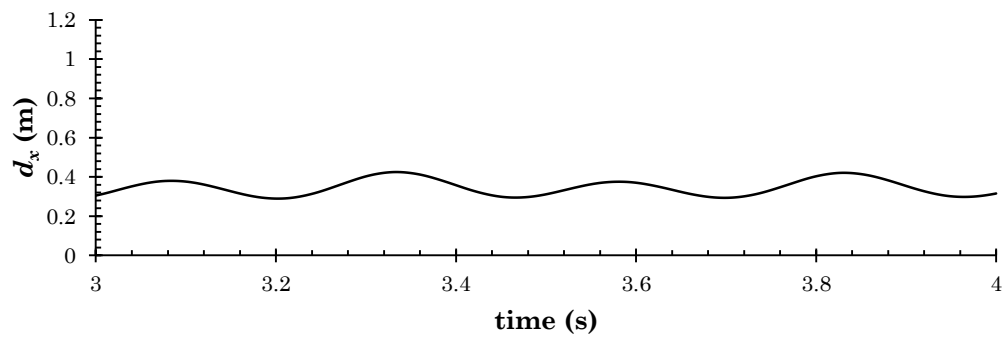


**$x$ -displacement vs. time plot of flat plate FVG:**

4PF



5PF



6PF

